UNIVERSITY OF CAGLIARI

PHD COURSE IN

ELECTRONIC AND COMPUTER ENGINEERING

CLASS XXVII

(ING-IND/32)

MANAGEMENT AND CONTROL OF ENERGY STORAGE SYSTEMS FOR STATIONARY AND AUTOMOTIVE APPLICATIONS

Author: Mario PORRU

PhD Course Coordinator: Prof. Fabio ROLI

Advisors: Prof. Alfonso DAMIANO

Co-Advisor: Dr. Alessandro SERPI

2013 – 2014

PHD DISSERTATION

MANAGEMENT AND CONTROL OF ENERGY STORAGE SYSTEMS FOR STATIONARY AND AUTOMOTIVE APPLICATIONS

Mario PORRU

(ABSTRACT)

The present PhD dissertation deals with management and control of Energy Storage Systems (ESSs) for both stationary and automotive applications. Chapter 1 focuses on the State-of-the-Art of ESS technologies, particularly ESSs are grouped into two main categories at first, i.e. high-energy density and high-power density ESSs. For each category, the most important ESSs are introduced and briefly described, highlighting their main advantages and drawbacks. Subsequently, an overall comparison is performed, together with some details about ESS hybridization and the most promising ESS applications. Chapter 2 regards ESS employment in stationary applications, especially for addressing Renewable Energy Source (RES) exploitation issues and enhancing micro-grid autonomy. In this context, three different scenarios have been considered; the first one regards sizing and management of an ESS fully devoted to increase RES exploitation. For this purpose a scheduling procedure and a real-time control strategy have both been developed and combined appropriately in order to provide both energy buffering and forecasting error compensation. In the second scenario, similar issues are addressed resorting to Vehicle to Grid technology (V2G). Thus, an Electric Vehicle (EV) fleet is introduced, whose mobility needs are appropriately taken into account by developing a suitable mathematical model of the mobility system. Subsequently, a V2G management system is developed in order to increase RES penetration level as much as possible, thus avoiding the employment of devoted ESSs. The last scenario regards the development of an optimal EV charging strategy for increasing micro-grid autonomy. This goal has been achieved resorting to the Optimal Control Theory with the aim of reducing the energy exchanged by micro-grids with the main grid, thus increasing their self-consumption. The results obtained at system level have highlighted some criticalities in the use of EV batteries for both propulsion and power system management. In this context, an Hybrid Energy Storage System (HESS) may represent a viable and suitable solution. Hence, in conclusion, Chapter 3 refers to the design and management of a novel hybrid energy storage system configuration for Electric Propulsion System (EPS). Particularly, HESS management should hold the battery current as constant as possible in order to reduce its stress, thus extending the driving range and improving battery lifetime. This requires ultra-capacitors to assist the battery by handling large and sudden power fluctuations, as those occurring over acceleration and regenerative braking. Thus, mathematical modelling of each EPS unit is introduced at first, subsequently their corresponding control systems are carefully designed and integrated to each other. Finally, extensive and detailed simulation studies have been carried out, which highlight the effectiveness of the proposed HESS in reducing the peak current drawn from EV batteries.

MARIO PORRU gratefully acknowledges Sardinia Regional Government for the financial support of his PhD scholarship (P.O.R. Sardegna F.S.E. Operational Programme of the Autonomous Region of Sardinia, European Social Fund 2007-2013 - Axis IV Human Resources, Objective l.3, Line of Activity l.3.1.)

A mio nonno,
perché ne sarebbe stato orgoglioso;

ai miei genitori,
per avermi mostrato la via;

a mio fratello,
perché possa trovare la sua.

OUTLINE

INTRODUCTION

Nowadays Energy Storage Systems (ESSs) represent one of the most important and promising technology for enabling enhanced performances of a number of energy systems in both stationary and automotive applications. Considering stationary applications at first, ESS can be employed successfully for addressing several issues affecting modern power systems, such as reduced level of power quality, massive growth of distributed generation and high penetration of Renewable Energy Sources (RESs). Particularly, RESs have experienced a rapid growth in the last decade due to technological improvements, which have progressively reduced their costs and increased their efficiency at the same time. Consequently, wind and photovoltaic power plants are nowadays very widespread, which, however, introduce several problems in power system management due to their inherent poorly predictable energy production profiles, together with highly variable rates. Therefore, power systems cannot manage these intermittent power sources beyond certain limits, resulting in RES generation curtailments and, hence, in RES penetration levels lower than expected. In this context, several solutions have been proposed in the literature, among which appropriate electric vehicles charging/discharging laws or, more generally, the employment of ESSs. In particular, large ESSs can be employed as RES energy buffers, storing and then delivering the excess RES energy production. Another approach consists in employing smaller ESSs in order to mitigate RES fluctuations, directly increasing their penetration level. In any case, full RES exploitation requires the employment of appropriate scheduling and real-time control procedures, which have to handle forecasting errors and electricity market requirements. Thus, ESSs should be suitably sized and managed in order to achieve an optimal trade-off between increased performances and costs.

Regarding automotive applications, ESSs cover a fundamental role for Electric Vehicles (EVs), especially in making them more competitive compared to ICE-based vehicles. In this context, almost all the EVs on the market are equipped with high-energy density ESS only, i.e. batteries. Particularly, Lithium-ion batteries seem to be the best technology due to their high specific energy and relatively high specific power compared with other battery technologies. However, Lithium-ion batteries suffer from sudden variations of charging/discharging current, which may reduce their lifetime significantly. On the other hand, one of the most promising high-power density ESS for EVs is represented by ultra-capacitors, which can easily handle high peak power drawn and/or delivered by the electric motor

over acceleration and regenerative braking respectively. Therefore, employment of either batteries or ultra-capacitors alone results in large weight and volume in order to meet EV requirements. Consequently, academic and industrial research is focused on improving battery technologies, as well as on appropriate combinations between batteries and ultra-capacitors, i.e. on the development of suitable Hybrid Energy Storage Systems (HESSs). Particularly, HESS may bring several advantages compared to ESS, such as increased life span of battery, improved acceleration and regenerative braking performances, cost, weight and size reduction, higher efficiency, reliability and durability.

In this context, the present PhD dissertation deals with management and control of energy storage systems for both stationary and automotive applications. Chapter 1 focuses on the State-of-the-Art of ESS technologies, particularly ESSs are grouped into two main categories at first, i.e. high-energy density and high-power density ESSs. For each category, the most important ESSs are introduced and briefly described, highlighting their main advantages and drawbacks. Subsequently, an overall comparison is performed, together with some details about ESS hybridization and the most promising ESS applications. Chapter 2 regards ESS employment in stationary applications, especially for addressing RES exploitation issues and enhancing micro-grid autonomy. In this context, three different scenarios have been considered; the first one regards sizing and management of an ESS fully devoted to increase RES exploitation. For this purpose a scheduling procedure and a real-time control strategy have both been developed and combined appropriately in order to provide both energy buffering and forecasting error compensation. In the second scenario, similar issues are addressed resorting to Vehicle to Grid technology (V2G). Thus, an EV fleet is introduced, whose mobility needs are appropriately taken into account by developing a suitable mathematical model of the mobility system. Subsequently, a V2G management system is developed in order to increase RES penetration level as much as possible, thus avoiding the employment of devoted ESSs. The last scenario regards the development of an optimal EV charging strategy for increasing micro-grid autonomy. This goal has been achieved resorting to the Optimal Control Theory with the aim of reducing the energy exchanged by micro-grids with the main grid, thus increasing their self-consumption. The results obtained at system level have highlighted some criticalities in the use of EV batteries for both propulsion and power system management. In this context, an HESS may represent a viable and suitable solution. Hence, in conclusion, Chapter 3 refers to the design and management of a novel hybrid energy storage system configuration for Electric Propulsion System (EPS). Particularly, HESS management should hold the battery current as constant as possible in order to reduce its stress, thus extending the driving range and improving battery lifetime. This requires ultra-capacitors to assist the battery by handling large and sudden power fluctuations, as those occurring over acceleration and regenerative braking. Thus, mathematical modelling of each EPS unit is introduced at first, subsequently their corresponding control systems are carefully designed and integrated to each other. Finally, extensive and detailed simulation studies have been carried out, which highlight the effectiveness of the proposed HESS in reducing the peak current drawn from EV batteries.

CHAPTER 1.
ENERGY STORAGE SYSTEMS: STATE-OF-THE-ART AND FUTURE SCENARIOS

Whatever system that is able to store energy and deliver it back when needed should be called Energy Storage System (ESS). However, in this PhD dissertation, ESS denotes those energy storage systems that exchange electrical energy only, storing it into different forms (mechanical, chemical, magnetic, etc.). Such kinds of ESS are experiencing a growing interest from both academic and industrial research, especially due to technological improvements and recent environmental issues. Particularly, the on-going transformation occurring on strategic sectors, such as distributed power generation and electrified transportation, significantly relies on high-performance ESSs, which should also be characterized by moderate cost and long life expectancy. Although further improvements are required in order to meet these goals, ESSs are already successfully employed in several fields, as well documented in the technical literature [1]–[12].

Energy storage systems consist of two main stages, i.e. the power conversion system and the energy storage unit, as shown in Fig. 1.1. The power conversion system is generally represented by a Power Electronic Converter (PEC), whose duty consists of regulating ESS voltage and current levels in order to meet load and/or power supply requirements. Whereas the electrical energy conversion occurs within the energy storage unit, which is generally based on an electrochemical solution, a flywheel, a capacitor bank or a superconducting coil. At the present time there are several ESSs available on the market, which can be classified mainly as either high-energy density or high-power density ESS [13]–[19]. Particularly, high-energy density ESSs are able to provide large amount of energy but over long time periods, as occurring for the majority of electrochemical batteries. Whereas high-power density ESSs can provide much little amount of energy but in very short times, as in the case of capacitors and flywheel energy storage systems. Therefore, based on this classification, the most suitable ESS should be chosen in accordance with specific application requirements. In this context, high-energy density is fundamental in small applications, such as portable and wearable devices, where cost is frequently less important. Differently, large-scale ESS requirements strictly depend on the specific application, such as power system support or electric vehicle propulsion. It is worth noting that some large-scale applications are characterized by both high energy and power demands, thus requiring an unsuitable ESS oversizing. A viable solution consists of employing appropriate

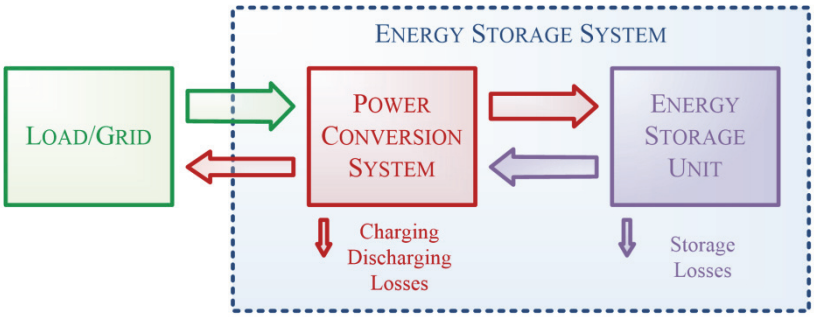

Fig. 1.1 Energy storage system stages: power conversion system and energy storage unit.

Hybrid Energy Storage Systems (HESSs), which are made up of a suitable combination of both high-energy density and high-power density ESS in order to match all the application requirements.

This Chapter presents a brief overview of the most important ESSs, which are described following the classification previously mentioned. Subsequently, they are also compared to each other in order to highlight their most important advantages and drawbacks. In addition, some HESS configurations are also presented and briefly discussed. Finally, some stationary and automotive applications are introduced, highlighting the benefits achievable by employing ESSs.

1.1 High-Energy Density ESS

Although Battery Energy Storage Systems (BESSs) are the first energy storage systems introduced in the market, they still represent the most cost-efficient high-energy density technology available today for a number of applications. This is mainly due to huge efforts of researcher all over the world in improving BESS features in terms of size, weight and costs [13]. In particular, dead weight and volume are still to be reduced, similarly full exploitation of active materials is to be attained. It is estimated that BESS energy density can be improved up to 50% within the next 10 years, also requiring the development of new materials. The achievement of all these goals will enable the employment of BESSs in a wide range of high-power applications [10].

BESS operating principle is very simple: when a load is connected to BESS terminals, it is supplied by its terminal voltage, which is generated by an internal chemical reaction. The same chemical reaction can be exploited inversely in rechargeable BESSs, when they are supplied by an external voltage source in order to restore their energy content. Depending on the materials involved in such reactions, different battery technologies can be defined, which are briefly described in the following.

1.1.1 Lead-Acid Batteries

Lead-acid battery (PbA) was invented by the French physicist Gaston Planté in 1859 and it is the oldest technology of rechargeable battery. It mainly consists of positive and negative electrodes made up of lead compounds, which are submersed into an acid electrolyte. The discharging current is generated by electron migration from the negative electrode to the positive one, whereas the charging process occurs when electrons move in the opposite direction. Positive electrodes are typically quite thin, thus they limit the battery rated power. In addition, deep charging/discharging cycles can damage the battery, active material becoming unusable. Consequently, thicker electrodes are required in order to increase the depth of discharging, but leading to increased weight [9].

Due to their inherent weightiness, PbAs have been employed in such applications where size and weight are not an issue. For examples, isolated power systems, power quality and UPS are their classical application fields. Furthermore, PbAs have dominated the market of automotive starting, lighting and ignition for decades. However, they are not suitable for load shifting or energy buffering,

their life expectancy being quite low. In addition, they require frequent maintenance in order to reinstate loss of water, which may occur due to hydrogen production during overcharges [12].

Recently, Valve-Regulated Lead-Acid Batteries (VRLA) have been developed by employing new materials, such as copper, fibres and carbon compounds. Compared to conventional PbAs, VRLAs are characterized by an increased life time (about 10 times more) and reduced weight (about 1.5 times less) [8], [9]. Consequently, they are presently used for hybrid electric vehicle propulsion, as well as for smoothing the production profile of wind power plants [10].

1.1.2 Nickel-Cadmium and Nickel-Metal-Hydride Batteries

Nickel Cadmium Battery (NiCd) was invented by the Swedish engineer Waldemar Jungner in 1899 [9]. This kind of batteries consists of a nickel-based positive electrode, a cadmium negative electrode and a potassium-based electrolyte. NiCds are characterized by a relative high energy density, low maintenance and a long life time, this last significantly depending on the depth of discharge. Consequently, NiCds have been employed for power quality and reserve services. On the other hand, their main drawbacks are memory effects, relative low efficiency and high costs. In addition, their disposal presents some environmental issues and requires complex recycling processes. These drawbacks have discouraged NiCd improvements, thus they have been replaced by Nickel-Metal-Hydride batteries (NiMHs) [8], [9].

NiMHs came on the market in the late ‘80s. Their structure is quite similar to NiCds, particularly cadmium is replaced by a metal “M”, which consists of a mixture of rare earth elements and of nickel, aluminium, cobalt or manganese. Consequently, NiMHs have been the most common power sources for the first generation of portable electronic devices. In addition, they were employed on the first generation of hybrid electric vehicles, such as Toyota Prius, due to their long life cycle and safety. However, NiMHs are not the best choice for plug-in electric vehicles, due to their relatively low specific energy and high self-discharge rate [10]. In addition, this technology is not suitable for high charging rates, because they may reduce battery capacity. For these reasons, NiMHs have now been almost totally replaced by Lithium-ion batteries in the majority of applications.

1.1.3 Lithium-ion Batteries

Lithium-ion batteries (Li-ions) were invented in 1970 by the American chemist Michael Whittingham, but the first commercial models were available only in the early 1990s. They consist of positive and negative electrodes, which are made up of graphite and lithium alloy respectively. During discharging, lithium ions migrate from the negative to the positive electrode, the opposite occurring during charging process. Li-ions are characterized by high energy density, low self-discharging rates and no memory effects, as well as very long life time and high efficiency. However, Li-ions may be damaged by heat generation due to their internal resistance. Consequently, an appropriate monitoring system is needed in order to address overcurrent and overvoltage issues [9].

Due to their excellent performances, Li-ions have been firstly employed in portable devices. Subsequently, they have become relevant also for stationary and automotive applications. Unfortunately, Li-ions suffer from sudden variations of charging/discharging current, which may reduce their lifetime significantly. Therefore, further improvements of Li-ions in terms of costs, lifetime and safety will ensure an even greater success on the market.

1.1.4 Sodium-Sulfur and Sodium-Nickel-Chloride Batteries

Sodium-Sulfur batteries (NaSs) were invented in the early 1970s and they are characterized by a high operating temperature of about 300 °C. Their composition includes sodium negative and sulphur positive electrodes, together with a beta-alumina electrolyte. During the discharging process, sodium

ions migrate through the electrolyte towards the sulphur electrode. Particularly, the electrolyte is able to conduct almost no electrons, preventing the battery from self-discharging. NaSs are characterized by high overall efficiency, long life cycle and lifetime. Some pilot projects have demonstrated their usefulness in power quality and load shifting applications. Consequently, they have been widely employed in large-scale applications, such as wind power plants and grid services, also due to their high power rate. However, NaSs have recently revealed some safety issues due to their ignition when getting in contact with water, which still need to be addressed [8], [9].

Sodium-Nickel-Chloride Batteries ($NaNiCl_2$) are quite similar to NaSs, namely the sulphur is replaced by nickel-chloride, they being characterized by similar properties and applications, such as a high operating temperature (270-350 °C). These batteries went to the market in 1995 and are better known as ZEBRAs, due to the name of the research project during which they were invented in 1985 (ZEolite Battery Research Africa Project). However, further improvements are needed in order to increase their energy density, making them appropriate for load levelling service and renewable energy sources integration [8], [9].

1.1.5 Flow Batteries

Flow Batteries (FBs) group several different technologies, which have been developed for 30 years but which are not easy available on the market. Differently from the most common BESS technologies, FBs store energy in the electrolyte solution. Particularly, the operating principle is similar to that of fuel cells: two different electrolytes are stored in two external tanks and are pumped into a cell containing a membrane, which allows the electrolytes to separate from each other. As a result, ions circulate through the electrolytes, thus generating an electrical current. An inherent advantage of this technology is that the two electrolytes are separated when the battery is completely discharged; in addition, charging/discharging processes do not affect electrolytes, leading to a long life expectancy. However, the membrane may require special disposal actions at the end of FB life time [9], [10].

Several technologies have been proposed for FBs, among which Vanadium Redox Battery (VRB) and Iron-Chromium (FeCr). The power and energy rating of FBs can be set independently: energy capacity is determined by the quantity of electrolyte stored in external tanks, whereas power rating depends on the active area of the cell stack [8]. Consequently, FBs are suitable for both energy and power applications. In spite of their low energy density and limited operating temperature range, FBs benefit from several advantages, such as long lifetime [8], flexibility and reduced emissions. For these reasons researchers are encouraged to further improve this technology in order to allow FBs to be commercialized for grid applications by 2020 [9].

1.2 High-Power Density ESS

Although there are several kinds of high-power density ESSs, all of them are characterized by poor energy density. Consequently, they can be hardly employed on their own for energy-based applications, because these lead to their excessive oversizing. The main advantage of high-power density ESSs is their capability of delivering and drawing high amount of energy in very short time, which is prevented to high-energy density ESSs. Consequently, high-power density ESSs are particularly suitable for power-based applications, such as power quality and smoothing in power systems, as well as fast acceleration and regenerative braking in propulsion systems. The most important kinds of such ESSs are capacitors, ultra-capacitors, flywheel ESSs and superconducting magnetic energy storages, which are briefly described in the following.

1.2.1 Capacitors and Ultra-capacitors

Capacitors are the only ESS technology capable to store electrical energy directly, providing high power, efficiency and very long life cycle. However, capacitors store a very little amount of energy due to their poor energy density. In order to solve this problem, research on electrochemical double-layer capacitors (EDLCs) began in 1950. As a result, EDLCs went to the market in 1978 with the name of *supercapacitors* [9]. EDLCs, which can also be called ultra-capacitors (UCs), are usually made up of two carbon electrodes, which are submersed into an electrolyte and isolated to each other by means of a porous membrane. This last prevents them from short circuits and allows ions to flow between electrodes at the same time. By connecting a voltage source to the UC terminals, an apolarized liquid is formed, storing electricity.

Compared to BESSs, UCs are able to supply energy at higher power rates, being also characterized by long life cycle and no memory effects. Thus, they are widely employed in power quality and automotive applications. Particularly, they have been successfully used on hybrid electric buses for handling small regenerative brakings, as well as in portal cranes for moving containers. Their main drawback is surely represented by the high cost per energy unit, which is about ten times that of Li-ions. Contrariwise, UCs are much more convenient in terms of cost per power unit, making them very suitable to be combined with BESSs in appropriate hybrid energy storage systems [10].

1.2.2 Flywheel Energy Storage Systems

Flywheel Energy Storage System (FESS) mainly consists of an electrical drive and a rotating mass, namely a flywheel. The drive accelerates the flywheel during the charging process, increasing its kinetic energy. Whereas FESS delivers energy to the load by decelerating the flywheel [9]. Modern FESSs can be classified into low-speed and high-speed FESSs, depending on their rotational speed [9]. Particularly, low-speed FESSs are generally heavy and cumbersome, thus they are employed for stationary applications mostly, their speed being lower than 10 krpm. Whereas high-speed FESSs are characterized by much higher rotating speed, which may even reach hundreds of krpm. This is due to their special flywheels, which are manufactured by means of composite materials [9]. Consequently, high-speed FESSs are particularly suitable for automotive applications, their energy density being generally higher than UCs.

Due to the rotating flywheel, FESSs inherently present some safety issues that require special enclosures. These are generally made up of steel sheets, which are able to contain flywheel fragments in case of breaking. In addition, the enclosure is filled with low friction gases, such as helium, which are kept at very low-pressure levels in order to improve FESS overall performances. Another important FESS components are bearings, which are the main responsible for coasting efficiency because they introduce power losses even when FESS is idle, i.e. the flywheel is pre-charged but no energy is exchanged. Consequently, appropriate design constraints must be taken into account in order to make FESSs economically feasible [9].

FESSs present several advantages compared to other ESSs, such as very high efficiency, life cycles and a life expectancy more than 15 years. In addition, they are not bounded in terms of depth of discharge and also present low environmental impact. Nowadays FESSs are employed in grid applications mostly, such as UPS, frequency regulation and renewable energy sources integration, as well as ride-through during switching between different power sources [8].

1.2.3 Superconducting Magnetic Energy Storages

The superconductivity principle was formulated in 1911 by the Dutch physicist Heike Kamerlingh Onnes, but only in 1972 it has been employed in the first ESS for power grid application [9]. A Superconducting Magnetic Energy Storage system (SMES) is mainly constituted by a

superconducting coil, a power converter and a cryogenic system. This last is required since superconducting state persists only below the critical temperature, which has to be attained using either liquid helium or nitrogen. The energy is stored in the magnetic field generated by a DC current, which flows in the coil due to the voltage supply provided by the power converter [9].

Among the ESSs, SMESs are characterized by the highest efficiency, their losses being mainly due to the power converters. In addition, SMESs are characterized by long life cycles, fast response and wide power range. Despite of these advantages, they have been used in niche applications, such as military equipment, due to the high costs related to superconductive material and cryogenic system. Recent improvements have allowed SMESs to be employed also in power system applications, such as power quality and voltage stabilization in transmission and distribution grids [9].

1.3 ESS Comparison and Hybridization

Based on ESS power and energy density, a first comparison between different ESS technologies can be performed by means of Ragone plots, as shown in Fig. 1.2. Particularly, it can be seen that Li-ions lie in the top right corner, thus they are particularly suitable for reduced-volume applications, such as portable devices, electric vehicles and other small-scale ESS applications. Whereas Pumped Hydro System (PHS) and Compressed Air Energy Storage (CAES) are characterized by both low power and energy densities, therefore they are employable for large-volume-consuming applications only. In addition, still referring to Fig. 1.2, it can be seen that FBs are characterized by lower energy density than the other kinds of batteries, which lie in the middle of the Ragone plot, as FESSs and Fuel Cells (FCs). Whereas both capacitors, UCs and SMESs have high power densities but low energy densities, revealing their usefulness for power-based applications mostly.

A more detailed ESS comparison can be carried out by referring to several ESS important features, such as those reported in Table I. Particularly, capacitors, UCs and SMESs present fast response times, which make them particularly suitable for power quality applications. Another important parameter is the cycle efficiency, which is defined as the efficiency over a full charging/discharging cycle, i.e. the share of the overall energy drawn that is delivered back by the ESS. Although all the ESS technologies here considered present quite high cycle efficiency (above 75%), research efforts are still focused on further improvements. The ESS self-discharge is one of the key aspects to be considered for determining ESS suitability in short, medium and long-term applications. Particularly,

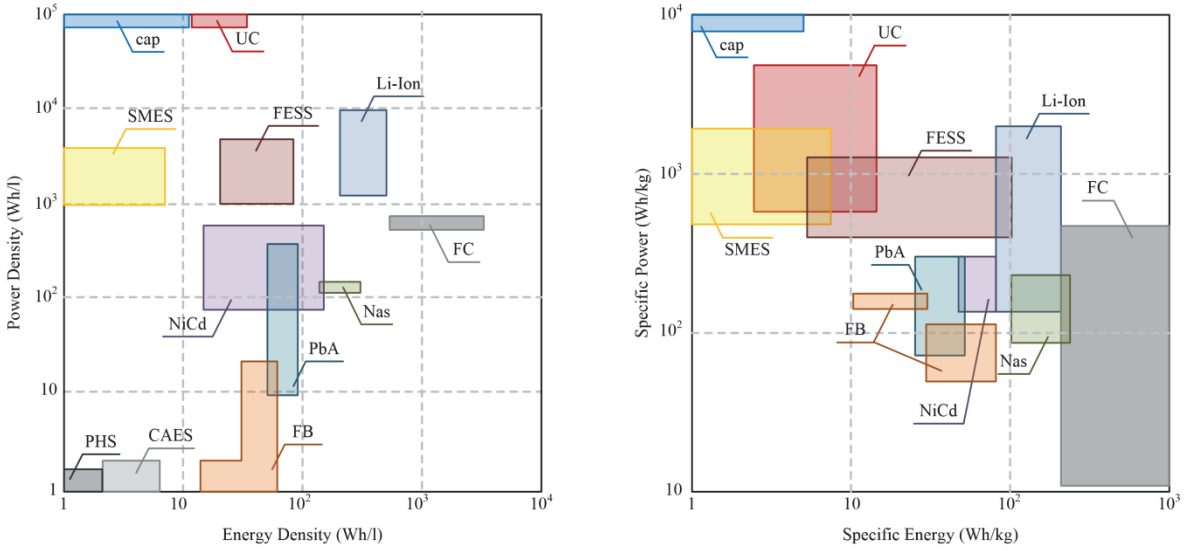

Fig. 1.2 ESS characteristics on Ragone plots, including Fuel Cell (FC), Pumped Hydro System (PHS) and Compressed Air Energy Storage (CAES).

NaSs and FBs present very small daily self-discharge, so they can be successfully employed over long-term durations (up to months), most conventional batteries being used for medium-term applications mostly (up to days). Whereas SMESs, FESSs, capacitors and UCs are eligible for short-term applications because they present very high daily self-discharge rates, i.e. they could completely release their stored energy in few hours or even shorter. In conclusion, lifetime and cycling times are very important because they affect overall investment costs, especially those related to maintenance and replacement. In this context, FESSs present high cycling times, those of capacitors, UCs and SMES being even higher. Differently, batteries are characterized by significantly lower cycling times, mainly due to chemical deterioration of their main components.

Based on both Fig. 1.2 and Table I, it is generally possible to select the best ESS for the majority of applications. However, some of them require strict specifications in terms of both energy and power densities, as well as on cost and life cycles. Consequently, a single ESS may not be able to satisfy all of them, revealing the need of combining more than one ESS technology. Particularly, the employment of ESSs with different power and energy capabilities may result in higher efficiency, longer life and an overall reduction of both size and costs. In this context, Hybrid Energy Storage Systems (HESSs) have become more and more relevant in the last decade [11], [15]–[22]. Particularly, an HESS consists of a combination of two complementary ESS technologies, i.e. a high energy and a high power density ESS, which are appropriately coupled by means of Power Electronic Converters (PECs). Several HESSs have been proposed in the literature, among which one of the most promising is surely represented by BESS coupled to UCs. Such HESS configurations can be further classified as passive, semi-active and active, depending on the number of power converters involved, as shown from Fig. 1.3 to Fig. 1.5.

Passive HESS configuration consists of a direct connection between the high-energy and the high-power density units without any additional power converter, as depicted in Fig. 1.3. In such a case, the mismatch of internal impedances of these units passively controls the amount of power that each

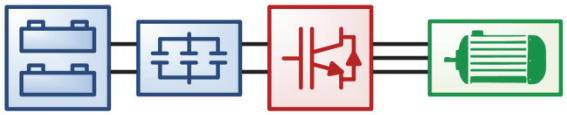

Fig. 1.3 Passive HESS topology.

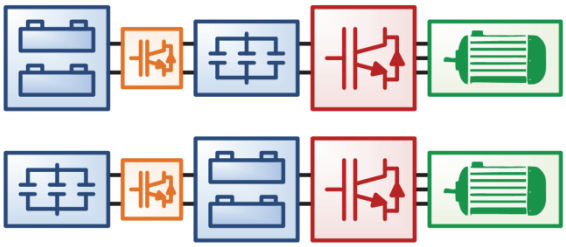

Fig. 1.4 Semi-active HESS topologies.

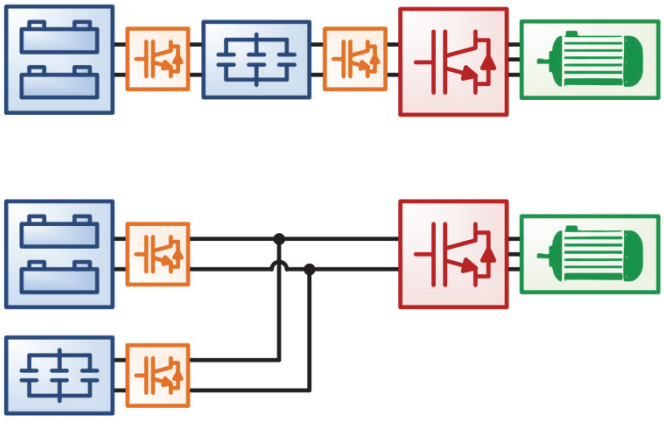

Fig. 1.5 Active HESS topologies.

TABLE I

MAIN TECHNICAL FEATURES OF ENERGY STORAGE SYSTEMS (BASED ON [8], [12], [22])

ESS TECHNOLOGY		ENERGY DENSITY [Wh/l]	POWER DENSITY [W/l]	SPECIFIC ENERGY [Wh/kg]	SPECIFIC POWER [W/kg]	RATED POWER [MW]	RATED CAPACITY [MWh]	DAILY SELF DISCHARGE [%]	LIFETIME [YEARS]	LIFE CYCLE [CYCLES]	DISCHARGE EFFICIENCY [%]	CYCLE EFFICIENCY [%]
LEAD-ACID	PbA	50-90	10-400	25-50	75-300	0-40	0.001-40	LOW 0.1-0.3	5-15	200-1800	85	63-90
NICKEL CADMIUM	NiCd	15-150	80-600	45-80	150-300	0-40	6.75	LOW 0.03-0.6	3-20	2000-3500	85	60-83
NICKEL METAL HYDRIDE	NiMH			60-80	220			HIGH	-	< 3000		50-80
LITHIUM-ION	Li-ion	150-500	1500-10000	75-200	150-2000	0-50	0-10	MEDIUM 0.1-5	5-16	1000-10000	85	75-97
LITHIUM POLYMER	Li-poly	200	250-1000					MEDIUM	-	> 1200		70
SODIUM-SULFUR	NaS	150-300	140-180	150-240	90-230	< 34	0.4-245	VERY HIGH	10-20	2500-4500	85	75-90
SODIUM NICKEL CHLORIDE	ZEBRA	-	-	100-140	150-200	50	-	VERY HIGH 15	15	2500-3000		86-88
VANADIUM REDOX	VRB	16-35	< 2	10-30	166	0-50	< 60	NEGLIGIBLE-SMALL	5-20	12000	75-82	65-85
ZINC BROMINE (FB)	ZnBr	30-65	< 25	30-80	45-100	0.05-10	0.1-4	SMALL	5-10	1500-2000	60-70	65-80
SUPERCAPACITOR	UC	10-30	100000	0.05-15	500-10000	0-0.3	0.0005	VERY HIGH 5-40	10-30	50000-100000	95-98	84-97
FLYWHEEL	FESS	20-80	1000-5000	5-100	400-1500	0.1-20	0.005-5	VERY HIGH 100	15-20	20000	90-93	90-95
SUPERCONDUCTING	SMES	0.2-6	1000-4000	0.5-75	500-2000	0.1-10	0.0008-0.015	HIGH 10-15	20-30	20000-100000	95	95-98

ESS Technology		Response Time [-]	Storage Duration	Discharge Time at Power Rate	Power Capital Cost [$/kW]	Energy Capital Cost. [$/kWh]	Maturity	Main Applications
Lead-Acid	PbA	milliseconds	Minutes-Days	Up to 10 hours	200-400	50-400	Mature	Load Leveling, Automotive, Reserve, Regulation, Power quality
Nickel Cadmium	NiCd	Milliseconds	Minutes-Days	Seconds-Hours	500-1500	400-2400	On the Market	Load Leveling,
Nickel Metal Hydride	NiMH	-	-	-	-	-	On the Market	Automotive
Lithium-ion	Li-ion	Milliseconds	Minutes-Days	Minutes-Hours	900-1600	600-3800	On the Market	Automotive
Lithium Polymer	Li-poly	-	-	-	-	-	On the Market	Automotive
Sodium-Sulfur	NaS	-	Long term	Seconds-Hours	350-3000	300-500	On the Market	Load Leveling, RES integration (smoothing & Buffering), Regulation, Reserve, Regulation
Sodium Nickel Chloride	ZEBRA	-	Seconds-Hours	Hours	-	-	On the Market	RES integration (smoothing), Load Levelling
Vanadium Redox	VRB	-	Hours-Months	Seconds-Hours	600-1500	150-1000	Early on the market	Load Leveling, RES integration (smoothing & Buffering)
Zinc Bromine	ZnBr	-	Hours-Months	Seconds-Hours	200-2500	150-1000	Demo	-
Supercapacitor	UC	Milliseconds	Seconds-Hours	Milliseconds-1 hour	100-450	300-2000	On the Market	Automotive, Regulation, Power quality
Flywheel	FESS	Seconds	Seconds-Minutes	up to 15 minutes	250-350	1000-14000	Early on the market	RES integration (smoothing), Regulation, Power quality
Superconducting	SMES	Milliseconds	Minutes-Hours	Milliseconds-up to 30 Minutes	200-500	5000-70000	Demo/Early on the market	Power quality

source delivers. In particular, UCs provide energy during rapid power variations due to their low impedance, whereas BESSs supply the steady state demand. It is worth noting that, in passive configuration, power sources must share the same voltage, which varies due to charging/discharging processes. Consequently, the power range of each source is strictly related to that of the other one, resulting in their poor exploitation. In order to improve HESS overall performances, semi-active configurations have been proposed, which are shown in Fig. 1.4. A DC/DC power converter is interposed between the power sources, allowing their partial decoupling. As a result, one of the ESS is better exploited compared to passive configuration, although the same limitations still occur on the other one. Active configurations are surely the most flexible ones due to the employment of two DC/DC converters, which allow ESSs to be managed independently, as highlighted in Fig. 1.5. Consequently, optimal HESS operation can be achieved, especially in terms of HESS power flow management. However, these configurations are very complex and costly, mainly due to additional DC/DC converters and control issues.

Summing up, HESS may bring several advantages compared to ESS, such as increased battery lifetime, improved acceleration and regenerative braking performances in propulsion applications, cost, weight and size reduction, higher efficiency, reliability and durability. It seems that DC-DC converters plays a key role in integrating and interfacing different energy sources, especially in terms of power management, flexibility and system optimization. However, since PEC employment may lead to increased cost, size and weight, suitable integrated solutions should be developed in order to manage HESS power flows optimally. In particular, researcher are focused on reducing the content of power electronics by proposing novel power converters [23], as well as integrated solutions [24]–[34].

1.4 ESS Applications

There are several applications particularly suitable for ESSs, from both technical and economic points of view. Many of them can be classified as stationary applications, such as grid services and RES exploitation; these generally require ESSs to support power system management, which is becoming a growing issue due to the diffusion of distributed generation. Another ESS application field is surely represented by electric vehicles, whose massive diffusion is expected within the next decades. In this context, ESSs cover a fundamental role for the electric propulsion system, having to properly manage acceleration, deceleration and regenerative braking. These operating conditions require both high energy and power capabilities, which are hardly matched by a single kind of ESS. Consequently, ESS management represents an actual challenge in order to further improve electric propulsion systems, increasing EV competitiveness compared to ICE-based vehicles. Finally, a promising application is the Vehicle to Grid technology, which consists of providing grid services by means of EV fleets. All these applications are briefly described in the following, highlighting their many features and opportunities.

1.4.1 Grid Services

Grid services support the electricity transfer from the production to the loads with the aim of assuring power system reliability and enhancing power quality. Although they are the same all over the world, there are no standard definitions; in fact, in some nations the same grid service has different names. The best-known services are regulation and reserve, as well as load leveling.

Load leveling briefly consists in decreasing the peak electricity demand supplied by traditional power plants (peak shaving) and increasing the peak-off demand (valley filling) at the same time. This results in shifting a certain amount of electricity delivered by traditional power plants over a defined period of time, as shown in Fig. 1.6. This is valuable because flat load dispatching is easier than

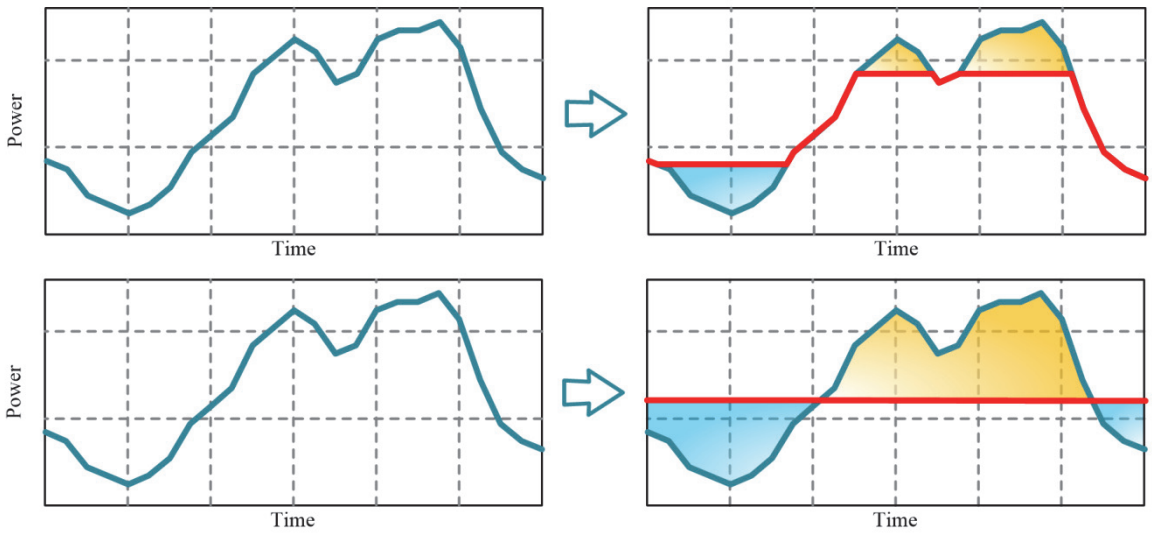

Fig. 1.6 Load leveling performances in case of small (top) and large (bottom) ESSs.

fluctuating load dispatching, simplifying forecasting and decreasing regulation needs. Although load leveling brings technical advantages, it is based on deregulation of electricity markets. In particular, profitability of such a service depends on fluctuations of energy prices. Consequently, ESS can be suitably managed in order to optimally schedule the power exchange with the grid and, thus, maximize revenues [35]–[37].

Regulation or frequency control is the grid service used by the system operator to hold frequency within a given range. This is automatically accomplished in real-time by varying some power plants' production level. In fact, they are forced by system operators to increase (regulation-up) or decrease (regulation-down) their production level [38], as shown in Fig. 1.7. Regulation revenue consists of three parts: the capacity payment, which depends on the amount of the power bid; the service payment, based on the overall exchanged energy; the opportunity cost payment, which has to account for the missing revenue due to reduced production level [39]. Such a service can be profitable if provided by appropriate ESSs with low and medium capacity but with rapid response, such as FESSs, capacitors and some kinds of batteries. These ESSs can follow the reference frequency signal more accurately than conventional generators, thus providing a higher quality of the service [40].

Although regulation and reserve would appear to be very similar, they occur in different situations: regulation has to support the system in real-time continuously, whereas reserve consists in an additional generating capacity that must be kept aside to cope with sudden power losses or load increases. Based on response time, reserve services can usually be grouped into three classes, as shown in Fig. 1.8:

- spinning reserve, which has a response time from few seconds to 5-10 min;
- supplementary reserve, which has a response time from 5-10 min to half an hour;
- backup reserve, which cannot be quickly ready, but can operate over long periods of time.

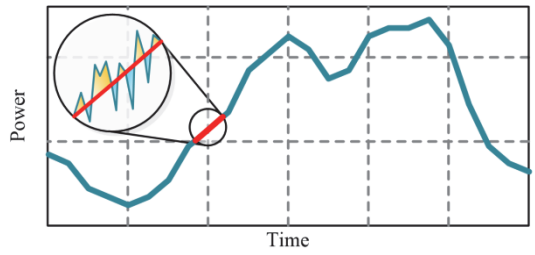

Fig. 1.7 Regulation-up and regulation-down.

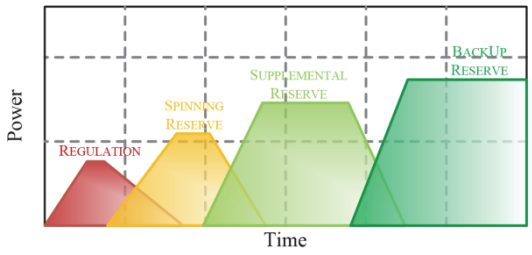

Fig. 1.8 Reserve service classification.

The above-mentioned boundaries are not standardized, thus they can change depending on the system operator [38]. Generally, spinning reserve must be able to respond very quickly, but it is not required to operate for long periods of time. In fact, spinning reserve is replaced by supplementary reserve and, in turn, by backup reserve as soon as they are available. All reserve services are remunerated for power availability and for the energy delivered. Regarding ESS technologies suitable for reserve services, they can have different characteristics depending on the specific service required. Particularly, conventional batteries have been already experimented successfully for both spinning and supplementary reserve, whereas flow batteries seem to be another promising solution. In addition, SMES and FESS may be adopted in the future as spinning reserve sources.

1.4.2 Renewable Energy Source Exploitation

In the last decade, Renewable Energy Sources (RESs) have experienced a rapid growth due to the will of reducing both the dependence on fossil sources and the emission of greenhouse gases, as well as to several technological improvements, which have progressively reduced RES costs and increased RES efficiency at the same time. Presently, wind and photovoltaic power plants cover a significant share of the overall power production and it is expected that it will increase further in the coming decades. Photovoltaic power plants have a quite regular daily cycle, their production peaks occurring about four hours before the peak load demand. Whereas wind power plant production is much more fluctuating and strongly sensitive to geographical location. However, both photovoltaic and wind power production profiles cannot be scheduled based on grid requirements only, because they inherently depend on weather conditions. Consequently, such intermittent and non-programmable power productions introduce several problems in power system management [41]. These are usually handled by conventional power plants, whose production profiles are appropriately scheduled in order to cope with RES unreliability. However, power systems cannot manage these intermittent power sources beyond certain limits, leading to RES generation curtailments and, thus, to RES penetration levels lower than expected. Several solutions that aim to increase RES integration have been proposed in the literature, among which the most promising ones resort to the employment of ESSs [42]–[50]. Particularly, as soon as RES power production exceeds about 10% of the overall one, an ESS should be required, even in presence of an ideal, widely dispatched transmission system. ESSs can increase RES power production in several ways, two examples of which are depicted in Fig. 1.9. Energy buffering is probably the most intuitive, which consists of storing the extra RES production

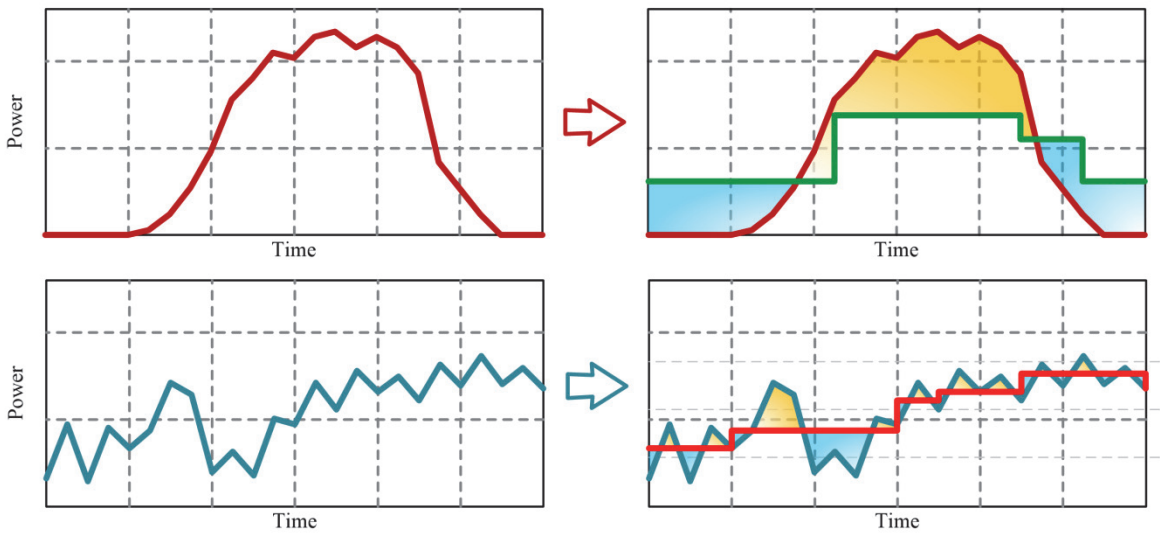

Fig. 1.9 Energy storage system applications for RES enhancement: energy buffering (on the top) and compensation of power fluctuations (on the bottom).

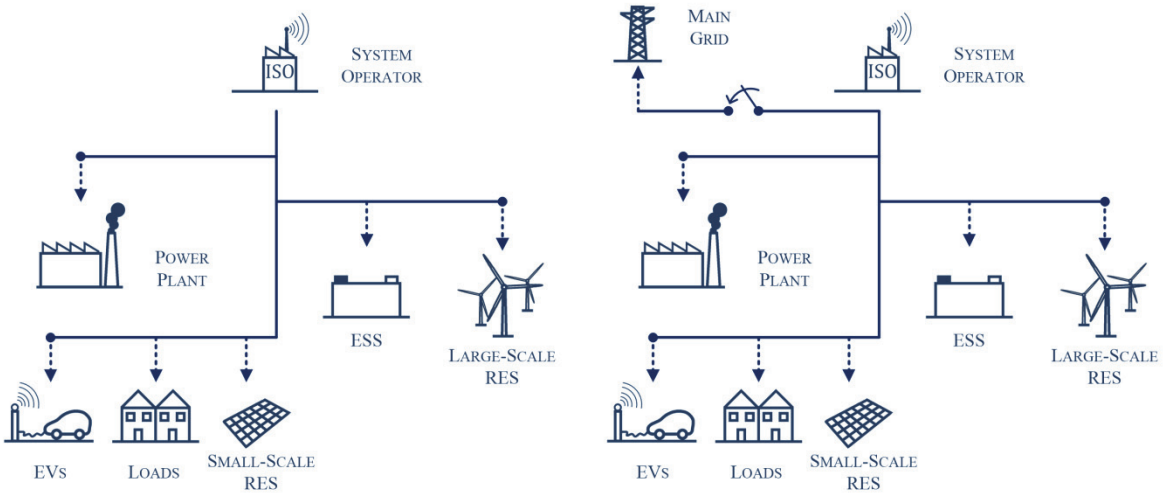

Fig. 1.10 Micro Grids examples: stand-alone MG (on the left) and grid-connected MG (on the right).

and delivering it back when required. This leads to reduce RES curtailment but generally requires large ESS capacities. Alternatively, ESS can suppress RES power fluctuations, thus increasing RES reliability. This kind of service requires ESS with high power capability and reduced capacity.

1.4.3 Smart and Micro Grids

A Smart Grid (SG) is defined as "*an electricity network that can cost efficiently integrate the behaviour and actions of all users connected to it – generators, consumers and those that do both – in order to ensure economically efficient, sustainable power system with low losses and high levels of quality and security of supply and safety*" [51]. SGs are thus characterized by a wide use of information and communication technologies in order to collect a large amount of data about production and loads. These should be elaborated automatically in order to manage the power system as a whole, increasing its overall performances in terms of efficiency, reliability and sustainability. In addition, SGs will allow the customer to be an active part of the power system, by producing electricity or providing grid services.

Micro Grids (MGs) consist of low-voltage distribution system with distributed energy resources and flexible loads. There are two types of MGs depending on their connection to the main grid, i.e. stand-alone and grid-connected MGs, examples of which are shown in Fig. 1.10. Particularly, stand-alone MGs focus on voltage and frequency control in order to guarantee their own stable operation. Whereas grid-connected MGs aim to enhance power quality and bring economic benefits, assuring a constant power flow with the main grid.

Both SGs and MGs can offer several advantages, such as increased power system reliability, energy efficiency, energy security and economic profits, mainly due to the employment of advanced RES, ESS and ICT technologies. Particularly, ESSs are widely recognized as one of their enabling technologies because they can address many issues [52]–[54], especially regarding self-consumption, stand-alone operation, autonomy and stability.

1.4.4 Electric Vehicles

Recently, Electric Vehicles (EVs) have experienced an increasing interest from both researchers and manufacturers all over the world. Particularly, EVs are very promising due to their high efficiency and low environmental impact, together with the possibility to be recharged by RES power plants directly [12]. However, ESS technologies are still poorly competitive compared to oil in terms of storage capacity. In particular, 1 litre of gasoline corresponds to about 20 kg of batteries (100 Wh/kg) for

storing the same amount of energy [10]. Consequently, EVs are characterized by limited driving range compared to ICE-based vehicles due to size and weight constraints. This is limiting their diffusion on the market.

EVs can be roughly divided into two big classes, i.e. plug-in and non-plug-in EVs, depending on their capability to be recharged by the grid. Non-plug-in EVs are essentially Hybrid EVs (HEVs), in which the propulsion is usually provided by a combination of a modest internal combustion engine and a small electric propulsion system. Particularly, the engine operates at relatively high efficiency, whereas the battery is recharged by regenerative braking or through the engine, resulting in a quite long mobility range due to the gas tank. Consequently, HEV batteries are characterized by relative low energy capacities, typically about 3 kWh, thus they are not particularly expensive. On the other hand, they should provide power up to 60 kW in order to handle peak power demands. Since the energy requirements are quite low, advanced PbAs are employed, especially in Micro-HEVs. These are not equipped with an effective electric propulsion system, but resort to an integrated starter generator for slightly improving fuel economy. Whereas in Mild and Full-HEVs the electric motor supports the vehicle over propulsion, especially at low speed, being also able to provide regenerative braking. Examples of these vehicles include Toyota Prius or Honda Insight, which both employ high-power NiMHs.

Plug-in EVs are characterized by batteries of much greater capacity than HEVs (about 30 kWh), which guarantee a larger full-electric driving range. Particularly, Battery Electric Vehicles (BEVs) are equipped with a full-electric propulsion system, thus they rely on the on-board ESS to propel the vehicle. BEVs have the advantage of a simpler drivetrain than HEVs, but ESS power and energy requirements are much more significant. Several kinds of batteries can be considered for BEVs, i.e. PbA, NiCd, NiMH, ZEBRA and Li-ion. Particularly, PbA is the most suitable choice for short-range vehicles, such as golf carts and wheelchairs, because it is a well-established technology, also presenting the lowest cost per kilowatt-hour of storage capacity. Whereas NiMH is a good choice where both EV range and performances are needed. Particularly, NiMHs can be fast recharged, so they are suitable for those vehicles that can be charged frequently, such as a commuter buses or trams. ZEBRAs have many of the attributes of NiMHs, being even characterized by a greater energy density. However, they should be kept hot, which is a major drawback especially for poorly used EVs. Finally Li-ions are considered the best solution for BEVs, due to their high energy density and power capability.

Regardless of the kind of ESSs, a single unit (batteries, supercapacitors, etc.) may be not sufficient to satisfy both dynamic and steady state EV requirements. Particularly, the battery pack needs to be oversized in order to handle the peak EV power demand, thus increasing weight, volume and cost. This also reduces battery lifetime and increases operating costs, thus preventing a massive EV diffusion on the market. An UC module can be alternatively employed, which is able to supply or drawn large power rates. However, due to its poor energy density, the UC module is able to guarantee very short driving range only [4]. Combining both batteries and UCs, the resulting HESS cannot only match both EV energy and power requirements, but also allows a suitable sizing of each ESS. Particularly, smaller batteries with lower peak-output power can be employed because UCs can manage EV high-power demand on their own for relatively short durations. Consequently, battery stress is reduced and its lifetime can be increased. Furthermore, UCs are able to recover braking energy more effectively, especially in sudden/hard braking conditions, thus further increasing fuel economy and driving range. In conclusion, HESS could benefit from increased power capabilities compared to batteries, reducing both the number and the depth of their charging/discharging cycles at the same time [4].

1.4.5 Vehicle to Grid

In order to enable their widespread use, EVs have to guarantee mobility as close as possible to that provided by ICEs, entailing cost savings at the same time. In this context, since EV battery charging period at rated power generally requires much less time than plug-in parking periods, it is possible to optimize the EV charging process from the economic point of view. In addition, EV batteries can also be employed to reduce negative impacts of EVs on power systems, even increasing their performances. This can offer EV owners the possibility to generate revenue by providing several services, while keeping their car plugged into the socket, which may lead to a rapid growth of EV use. This is defined the Vehicle to Grid (V2G) concept. In particular, V2G should be especially profitable in providing grid services, such as load leveling, regulation and reserve. Moreover, enhancing RES exploitation can be a viable alternative once the other services are saturated.

There are two ways in which an EV can operate V2G, depending on the power flow directions: when the power can flow from the grid to the EV battery only, this operating mode is usually denoted by unidirectional V2G or Grid to Vehicle (G2V). Whereas when the power can be delivered from both sides, i.e., the grid and the EV battery, such operating mode is called bidirectional V2G or, simply, V2G [55]–[58]. Although several services can be offered only by means of V2G, G2V can offer charging flexibility, load curtailment and, hence, regulation. Thus, G2V gives EV owners the opportunity to take part in the day-ahead market, buying energy and offering the so called "load only services". In addition, it is logical to suppose that G2V will be implemented earlier than V2G. This is mainly due to the fact that it can be accomplished through standard J1772 chargers that are already available on the market, avoiding additional V2G hardware requirement, costs, performances and safety issues. Moreover, G2V will not entail the overexploitation of EV batteries due to uses other than EV propulsion, whereas this issue will have to be taken into account by V2G. All these advantages result in lower implementation costs and faster returns on investment for G2V than for V2G. However, G2V cannot exploit all the benefits that V2G can; in particular, G2V can provide services during recharging mode only, thus the corresponding grid services are quite limited. Such limitation generally leads to smaller profits (about 25%) than those achievable by V2G. This last allows EV fleets to be considered as distributed ESSs, the adoption of which is widely recognized as the most important improvement of the smart grid paradigm. As a consequence, EVs will be able to address many issues, from RES integration to both SG and MG management.

Referring to V2G architectures, two main solutions have been proposed, i.e. deterministic and aggregative [59]. In the deterministic architecture shown in Fig. 1.11, V2G is provided by EVs autonomously, each of which being directly controlled and linked to the system operator by

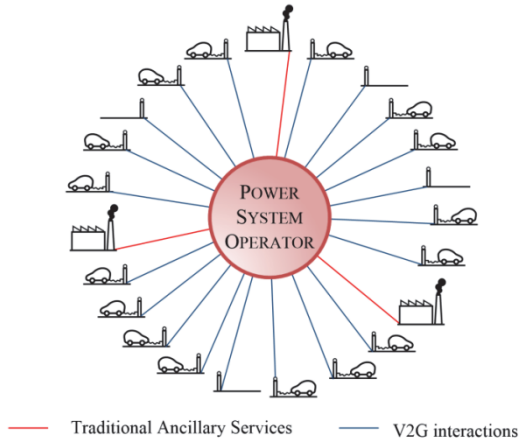

Fig. 1.11 Schematic representation of a deterministic V2G architecture. [59]

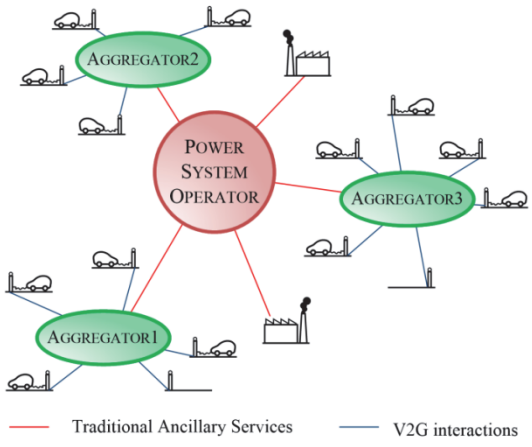

Fig. 1.12 Schematic representation of an aggregative V2G architecture. [59]

communication and power lines. Whereas the aggregative architecture consists of a framework providing V2G by means of a number of EV fleets, each of which are managed by different entities called Aggregators, as shown in Fig. 1.12. Although the first solution would appear to be simple and easy to be implemented, it prevents V2G from providing several grid services that require high power and energy minimum thresholds. On the contrary, an aggregative framework does not prevent V2G from delivering any services, but introduces additional costs. Regarding profits, availability and reliability, both solutions have been considered in order to select, from time to time, the most suitable one. Particularly, it has been proved that the availability and reliability achievable by means of the deterministic V2G architecture is about 92% and 95% in the best cases, respectively [59]. Whereas, they can both be assumed equal to 100% for the aggregative architecture, which allows the modulation of the bidding based on the state of the EV fleets. Therefore, since the availability and reliability of base load generators are about 93% and 98.9% respectively, it can be stated that an aggregative V2G architecture will be needed in order to meet industrial standards.

In conclusion, an aggregation of EVs will be needed in order to participate in the energy market. In fact, two different approaches can be followed: cost function-based power drawn scheduling and price-sensitive energy bidding. The first one, which is suitable for the deterministic V2G architecture, consists in establishing the EV charging profile based on of the energy price given by the day-ahead market and in updating it dynamically. As a result, each EV is responsible for its charging without interference from the system operator: in the hours of cheapest prices, the EV should recharge at its maximum rate. On the other hand, the price-sensitive energy bidding approach entails that the EV fleet participates in the day-ahead market and the amount of energy purchased depends on the price the EV owner is willing to pay. This approach, which is not possible for the deterministic V2G architecture, is particularly suitable for the aggregative one.

CHAPTER 2.
STATIONARY APPLICATION:
RENEWABLE ENERGY SOURCES EXPLOITATION

Renewable Energy Sources (RESs) are going to cover an important role in the future energy system. The increasing environmental awareness and the will to reduce both the dependence on fossil sources and the emission of greenhouse gases are orienting the energy policy of many governs around the world to strongly support the diffusion of RES. Consequently, this energetic transformation is going to change the role of energy infrastructure at its basic foundations, and, in particular, that of the electric power grid [60].

Presently, the electric grid has a hierarchical structure characterized by strong constraints, unidirectional energy flow and distinct differentiations in actions (generation, transmission, distribution and end use). The rapid diffusion of RES and the use of electric power grid as its main interface for the energy distribution are mining the power grid management. In fact, the increase of generation sources, their connection to the distribution network, the variability, in time and space, of energy production and consumption, make the management models presently used no more suitable, forcing towards the adoption of new paradigms of energy management. In particular, variability of power production is surely the most important issue related to RES for several reasons. First, forecasting errors on power production at any given time cause problems in scheduling the power production of conventional generators. Second, frequent fluctuations that may characterize RES power production are more difficult to be forecasted and, thus, to be compensated for by means of conventional power plants. Third, although small fluctuations can be easily overcome by conventional power plants, higher fluctuations require specific solutions [61].

All these drawbacks are usually handled by means of a suitable scheduling of conventional generators, which have to cope with load variations too. However, all operational constraints of conventional power plants have to be taken into account, in order to guarantee a reliable operation of the power system. Nevertheless, it has been shown that high RES penetration levels require supporting actions by conventional generators that are difficult to satisfy, leading to a reduction in RES exploitation [61]. Indeed, a strong RES penetration requires a more flexible power system, which represents a big challenge to face off. Therefore, in order to guarantee a factual improvement in the power system management under a high RES exploitation, novel models and configurations of

electricity distribution have been proposed, which generally resort to Energy Storage Systems (ESSs) [42], [48], [49], [62], [63]. These contribute to increase RES reliability, satisfying grid requirements at the same time. In addition, depending on their size and spread, ESSs may reduce capacity requirements of both transmission and distribution systems.

The achievement of high RES exploitation levels depends on the type of service provided by the ESS, as well as on both its size and nature [12], [48], [50], [64], [65], which are generally synthesized based on technical and/or economic optimization procedures [45]–[47], [66]. These should account for power quality, regulation and load following issues [66], [67], as well as ESS response time, charging/discharging time at rated power, cycle efficiency, life cycle assessment, working life and the control timescale required for the power grid management [48]. For smart grid applications, the use of dedicated electrochemical batteries is currently considered one of the most feasible and suitable solution. However, the integration of the electric mobility with the distribution network is considered an interesting technical solution too.

The employment of ESS for RES exploitation is investigated in this Chapter. In particular, three different approaches are presented. First, an ESS Management System (EMS) is proposed in the first section, which aims to increase the RES penetration level by both energy buffering and forecasting errors compensation. The second section presents a V2G Management System (VMS) that synthesizes the charging/discharging law of an EV fleet in order to increase RES penetration by means of energy buffering and reserve service. Finally, an optimal control strategy for EV integration into micro-grid is presented in the third section. In particular, it aims to increase energy autonomy of each micro-grid through the energy buffering provided by EVs.

2.1 ESS fully devoted to RES exploitation

A generic ESS devoted to RES exploitation can be employed as energy buffer, storing and then delivering the excess of RES energy production: this decreases the curtailments imposed by electric systems, but generally requires the employment of large ESSs. Another approach consists in employing smaller ESSs that mitigate RES fluctuations, making RES more programmable and, thus, directly increasing their penetration level. In any case, full RES exploitation requires the employment of appropriate scheduling and real-time control procedures, which have to handle forecasting errors and electricity market requirements. In this context, several ESS management strategies have been proposed in the literature for enhancing RES exploitation, many of which suggest either ESS energy buffering or forecasting error compensation. These are achieved by one-day-ahead scheduling procedures and/or real-time control algorithms with the aim of maximizing RES penetration levels and profits, mitigating RES fluctuations, as well as improving the electric grid reliability and scheduling [43]–[45], [66].

In this Section, an optimal ESS management procedure devoted to achieve a full RES exploitation is presented. Unlike other approaches previously proposed in the literature, it aims to increase the RES penetration level by both energy buffering and forecasting errors compensation. In particular, the combined RES-ESS power profile is synthesized one-day-ahead by means of an appropriate scheduling procedure, which is developed in order to minimize the RES energy production curtailments by means of ESS energy buffering. Then, a real-time control strategy is developed in order to track the scheduled power profile as well as possible, by mitigating RES forecasting errors; this results in improved RES reliability and, hence, in encouraging the increase of the RES penetration level allowed by the electric system. The worth and effectiveness of the proposed ESS management procedure is verified through a wide simulation study, which is carried out by means of the Matlab software package. Simulations refer to the case of a weakly interconnected power system, characterized by a significant share of electricity generation coming from RESs.

2.1.1 Mathematical Modelling

2.1.1.1 System Model

Referring to the schematic representation of an electric system shown in Fig. 2.1, it consists mainly of generators and loads. The first ones can be further classified as programmable or non-programmable power sources, based on the capability of regulating their power production profile. Particularly, thermal and hydro power plants are classical examples of programmable power sources because their power profile can be tuned in accordance with grid and/or load requirements. Whereas non-programmable power sources consist mainly of RES power plants, whose power profile is imposed by weather conditions mostly (sun and wind). Electric system can also include a number of ESSs with the aim of increasing system performances and reliability, such as making RES power production more programmable or providing grid services. Consequently, the power balance of such an electric system can be expressed by the following equation:

$$P_0(t) + P_{RES}(t) + S(t) + L_0(t) = 0 \tag{2.1}$$

in which P_0 and P_{RES} denotes the power delivered by programmable power sources and RES power plants respectively. Whereas S is the power exchanged by the ESS with the electric grid, L_0 being the load demand. Still referring to (2.1), it is worth noting that P_0 and P_{RES} are always positive, as well as L_0 is always negative. Whereas S can be either positive or negative in accordance with ESS operation as an additional power source or a load respectively. Particularly, the following variables can be introduced:

$$\begin{aligned} L_s(t) &= \frac{1}{2}\left(S(t) - |S(t)|\right) \\ P_s(t) &= \frac{1}{2}\left(S(t) + |S(t)|\right) \end{aligned} \tag{2.2}$$

in which $|\cdot|$ denotes the absolute value operator. As a result, L_s and P_s denote the ESS power drawn from or delivered to the electric grid respectively, as shown in Fig. 2.2. In particular, still referring to Fig. 2.2, η_c denotes the ESS charging efficiency, i.e. the share of the overall energy drawn that is effectively stored in the ESS. Similarly, η_d is the ESS discharging efficiency, which corresponds to

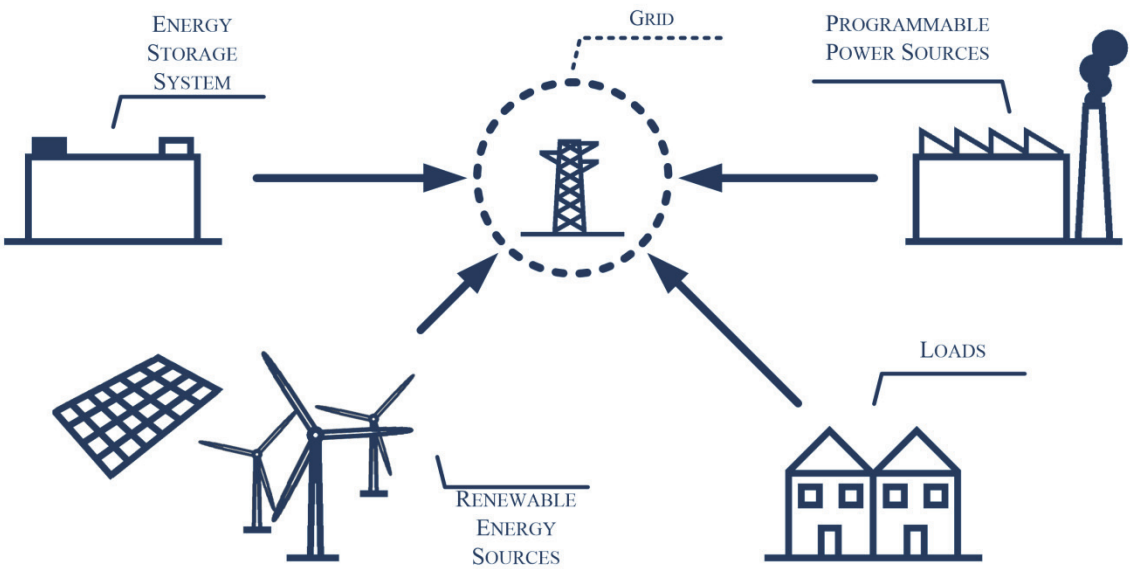

Fig. 2.1 Schematic representation of a power system with distributed ESSs.

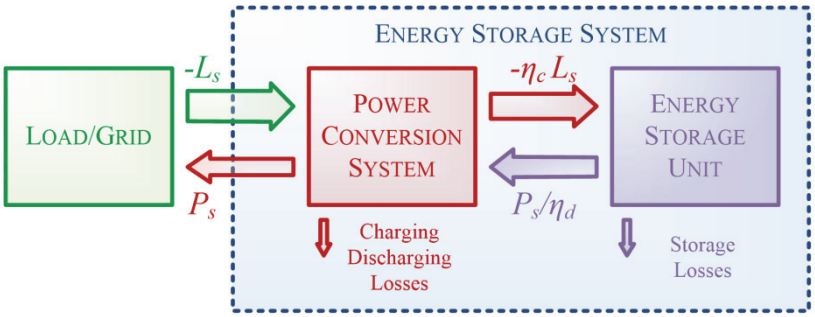

Fig. 2.2 The ESS power flows to and from the grid.

the energy effectively delivered to the grid by the ESS. It is worth noting that L_s and P_s are alternatively equal to zero, i.e. the ESS cannot draw from and deliver energy to the grid simultaneously. Therefore, based on (2.2), the power exchanged by the ESS with the grid can be expressed as:

$$S(t) = L_s(t) + P_s(t) \ . \tag{2.3}$$

In conclusion, once defined the energy exchange with the grid, the ESS energy storage level can be computed by

$$E(t) = E_0 - \int_t \left(\frac{P_s(t)}{\eta_d} + \eta_c \cdot L_s(t) \right) dt \tag{2.4}$$

in which E_0 denotes the initial energy storage level.

2.1.1.2 System Constraints

Any electric system must comply with (2.1), which entails that instantaneous power balance must always occur. Consequently, assuming no ESS, any L_0 and P_{RES} variation should be compensated by P_0. Therefore, due to the inherent, poorly predictable nature of RESs, their power production has to be assumed upper bounded as

$$P_{RES}(t) \le -(1-\sigma) \cdot L_0(t) \tag{2.5}$$

in which σ is the grid stabilization coefficient, which represents the load share that must be supplied by programmable sources in order to preserve grid stability [60], [68]. Since this coefficient is generally quite high (about 0.8), RES power production may be poorly exploited if a suitable ESS is not introduced. This can improve RES programmability, enabling lower σ values without impairing grid stability. As a consequence, (2.5) becomes

$$S_{RES}(t) \le -(1-\sigma) \cdot L_0(t) \tag{2.6}$$

in which

$$S_{RES}(t) = P_{RES}(t) + S(t) \ . \tag{2.7}$$

However, ESS power and energy exchanges must comply with the following operating constraints:

$$L(t) \le S(t) \le P(t) \tag{2.8}$$

$$E_{min} \le E(t) \le E_{max} \tag{2.9}$$

in which L and P are the maximum power drawn from the grid and deliverable to the grid by the ESS respectively. Whereas E_{max} and E_{min} are the ESS maximum and minimum energy levels respectively,

being directly proportional to the maximum and minimum ESS State of Charge (SoC) by means of the ESS rated capacity E_b. In particular, the ESS SoC should not exceed these boundaries in order to preserve its rated performances and life-time. Thus, denoting by P_b the ESS rated power, L and P can be expressed as:

$$L(t) = \begin{cases} -P_b & E(t) < E_{max} \\ 0 & otherwise \end{cases} \quad , \quad P(t) = \begin{cases} \eta_d P_b & E(t) > E_{min} \\ 0 & otherwise \end{cases} \quad . \tag{2.10}$$

As a consequence, the ESS is able to draw energy at its rated power until this does not imply exceeding E_{max}. Similarly, P is defined in accordance with the ESS rated power and E_{min}.

2.1.2 ESS Management System

The proposed ESS Management System (EMS) consists of an appropriate one-day-ahead scheduling procedure combined with a real-time control strategy, as summarized in Fig. 2.3 and Fig. 2.4. Particularly, the scheduling procedure is developed in order to minimize the RES energy production curtailments by means of ESS energy buffering. Consequently, it is carried out one-day-ahead referring to a sampling time interval T and a time horizon T_0, as shown in Fig. 2.4. Whereas the real-time control strategy is developed based on T in order to track the scheduled RES-ESS power profile as well as possible, by mitigating RES forecasting errors.

Therefore, referring to the generic time horizon d and sampling time interval k, the sampled-data model of the electric system can be easily achieved based on both (2.1) and (2.7) as

$$P_0^{(k,d)} + S_{RES}^{(k,d)} + L_0^{(k,d)} = 0 \quad , \quad S_{RES}^{(k,d)} = P_{RES}^{(k,d)} + S^{(k,d)} \quad . \tag{2.11}$$

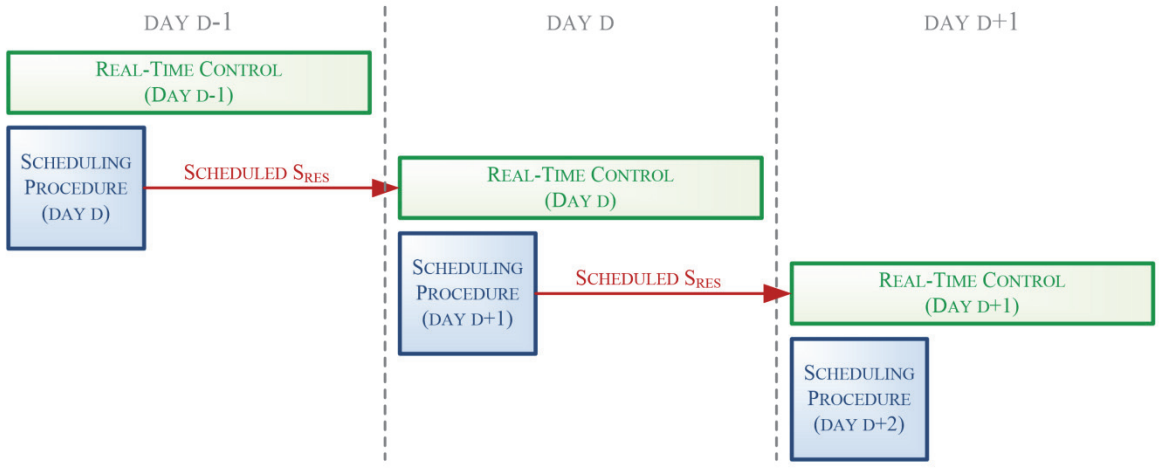

Fig. 2.3 Schematic representation of the proposed ESS Management System.

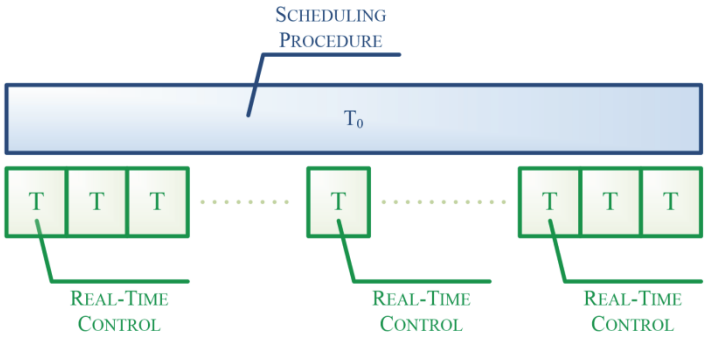

Fig. 2.4 Time horizon T_0 and sampling time interval T.

Whereas the grid stability constraint expressed by (2.6) becomes

$$S_{RES}^{(k,d)} \le -(1-\sigma)\cdot L_0^{(k,d)} \quad . \tag{2.12}$$

Referring now to the ESS, its sampled-data model can be derived from (2.4) as

$$E^{(k,d)} = E_0^{(k,d)} - \left(\frac{P_s^{(k,d)}}{\eta_d} + \eta_c \cdot L_s^{(k,d)} \right) \cdot T \quad . \tag{2.13}$$

In addition, based on both (2.8) and (2.9), the ESS operating constraints can be expressed as

$$L^{(k,d)} \le S^{(k,d)} \le P^{(k,d)} \tag{2.14}$$

in which:

$$L^{(k,d)} = max\left\{ -P_b \ , \ \frac{1}{\eta_c} \cdot \frac{E^{(k,d)} - E_{max}}{T} \right\} \quad , \quad P^{(k,d)} = min\left\{ \eta_d \cdot P_b \ , \ \eta_d \cdot \frac{E^{(k,d)} - E_{min}}{T} \right\} \quad . \tag{2.15}$$

The proposed ESS management system is described in detail in the next subsections, assuming a one-day time horizon and a sampling time interval equal to one hour. However, it is worth emphasizing that different T_0 and T can be successfully employed, particularly shorter sampling time intervals may lead to a more effective ESS management.

2.1.2.1 Scheduling procedure

Referring to the generic day *d*, the corresponding scheduling procedure is performed one-day-ahead in order to minimize the RES energy production curtailments. Therefore, referring to the generic day *d−1*, the following quantities are immediately available:

- the actual stored energy level $E^{(0,d-1)}$;
- the forecasted RES potential power profile $\tilde{P}_{RES}^{\ *}$ and load demand $\tilde{L}_0^{\ *}$, for both day *d−1* and *d*;
- the optimal combined RES-ESS power profile $S_{RES}^{\ *}$, properly synthesized the day before (*d-2*).

Unfortunately, the knowledge of the stored energy level $E^{(0,d)}$ would be required, but it is not available at the start of day *d−1*. However, this drawback can be easily overcome by employing the predicted value $\tilde{E}^{(0,d)}$ in place of the actual one, whose computation is detailed later. Then, reference is made to both the ESS and the electric grid constraints, expressed by (2.12) and (2.14) respectively. In particular, considering (2.11), such constraints can be summed up as follows:

$$\tilde{P}_{RES}^{(k,d)} + \tilde{S}^{(k,d)} \le -(1-\sigma)\cdot \tilde{L}_0^{(k,d)} \tag{2.16}$$

$$\tilde{L}^{(k,d)} \le \tilde{S}^{(k,d)} \le \tilde{P}^{(k,d)} \tag{2.17}$$

where:

$$\tilde{L}^{(k,d)} = max\left\{ -P_b \ , \ \frac{1}{\eta_c} \cdot \frac{\tilde{E}^{(k,d)} - E_{max}}{T} \right\} \quad , \quad \tilde{P}^{(k,d)} = min\left\{ \eta_d \cdot P_b \ , \ \eta_d \cdot \frac{\tilde{E}^{(k,d)} - E_{min}}{T} \right\} \quad . \tag{2.18}$$

Referring to the (S,P_{RES}) plane, (2.16) identifies the plane region highlighted in Fig. 2.5: in particular, this operating region is bounded by the straight line $\tilde{r}_0$ introduced by (2.16), together with $\tilde{r}_P$ and $\tilde{r}_L$, which correspond to the upper and lower boundaries imposed by (2.17). As a consequence, since RES power production is upper bounded by the point B̃ shown in Fig. 2.5, $\tilde{P}_{RES}$ can be chosen in accordance with

$$\tilde{P}_{RES}^{(k,d)} = min\left\{ \tilde{P}_{RES}^{*} , -(1-\sigma)\cdot \tilde{L}_0 - \tilde{L} \right\}^{(k,d)} \quad . \tag{2.19}$$

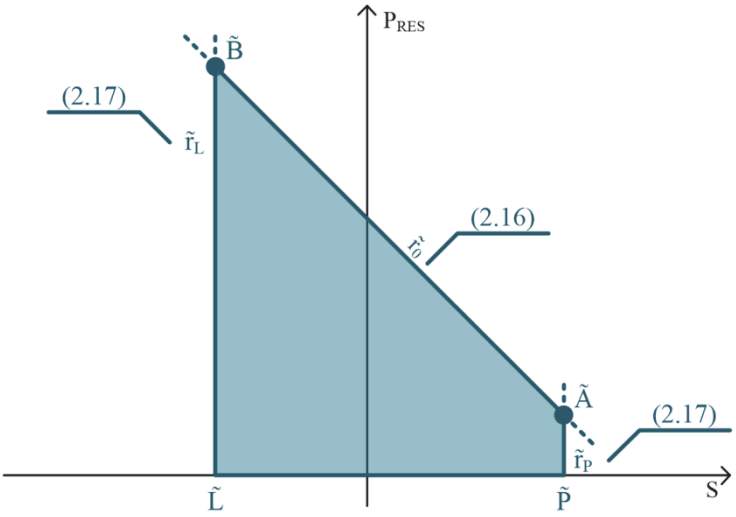

Fig. 2.5 The ESS and grid constraints representation on the (S,P_{RES}) plane.

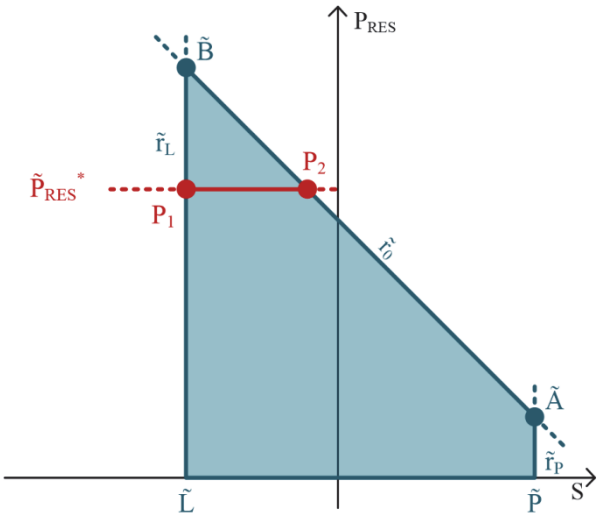

Fig. 2.6 Graphical representation of the proposed scheduling procedure in case of no RES curtailments.

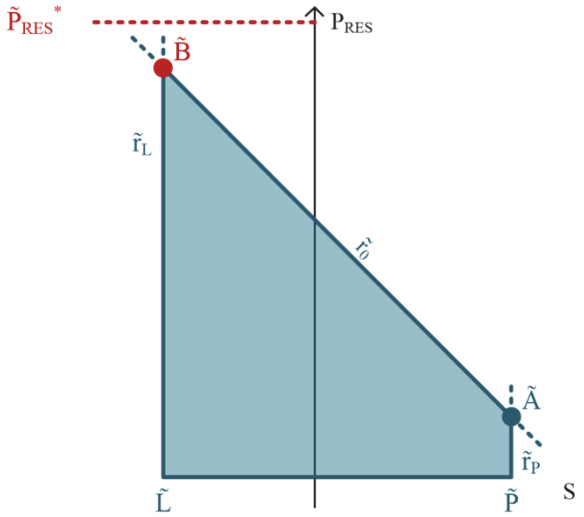

Fig. 2.7 Graphical representation of the proposed scheduling procedure in case of RES overproduction.

In particular, if $\tilde{P}_{RES}$ is equal to $\tilde{P}_{RES}^{*}$, no RES curtailments should occur. In such cases, as shown in Fig. 2.6, it is possible to select the most suitable value for $\tilde{S}$ in accordance with

$$\tilde{S}_{min}^{(k,d)} \le \tilde{S}^{(k,d)} \le \tilde{S}_{max}^{(k,d)} \tag{2.20}$$

in which $\tilde{S}_{min}$ and $\tilde{S}_{max}$ are the minimum and maximum ESS power exchange at the given $\tilde{P}_{RES}$ value:

$$\begin{aligned} \tilde{S}_{min}^{(k,d)} &= \tilde{L}^{(k,d)} \\ \tilde{S}_{max}^{(k,d)} &= min\left\{\tilde{P}^{(k,d)}, -(1-\sigma)\cdot\tilde{L}_{0}^{(k,d)} - \tilde{P}_{RES}^{(k,d)}\right\} . \end{aligned} \tag{2.21}$$

These operating conditions correspond to points P_1 and P_2 respectively, as highlighted in Fig. 2.6. Since it is suggested to maximize the combined $\tilde{S}_{RES}$ power profile and, hence, the RES power production directly delivered to the electric grid, $\tilde{S}$ is always chosen as maximum as possible in accordance with

$$\tilde{S}^{(k,d)} = \tilde{S}_{max}^{(k,d)} . \tag{2.22}$$

Referring now to a case in which $\tilde{P}_{RES}^{*}$ exceeds the point $\tilde{B}$, like that depicted Fig. 2.7, $\tilde{P}_{RES}$ and $\tilde{S}$ are uniquely determined by

$$\begin{aligned} \tilde{P}_{RES}^{(k,d)} &= -(1-\sigma)\cdot \tilde{L}_0^{(k,d)} - \tilde{L}^{(k,d)} \\ \tilde{S}^{(k,d)} &= \tilde{L}^{(k,d)} \end{aligned} \quad . \tag{2.23}$$

In conclusion, in order to carry on the proposed scheduling procedure, the ESS stored energy level has to be appropriately updated as

$$\tilde{E}^{(k+1,d)} = \tilde{E}^{(k,d)} - \left(\frac{\tilde{P}_s^{(k,d)}}{\eta_d} + \eta_c \cdot \tilde{L}_s^{(k,d)} \right) \cdot T \tag{2.24}$$

in which

$$\tilde{L}_s^{(k,d)} = \frac{1}{2}\left(\tilde{S}^{(k,d)} - \left| \tilde{S}^{(k,d)} \right| \right) \quad , \quad \tilde{P}_s^{(k,d)} = \frac{1}{2}\left(\tilde{S}^{(k,d)} + \left| \tilde{S}^{(k,d)} \right| \right) . \tag{2.25}$$

2.1.2.2 Real-time Control Strategy

The proposed real-time control strategy aims to track the optimal combined RES-ESS power profile $\tilde{S}_{RES}$, which is already synthesized one-day-ahead by the scheduling procedure. As a consequence, the following equation should be satisfied:

$$P_{RES}^{(k,d)} + S^{(k,d)} = \tilde{S}_{RES}^{(k,d)} \quad . \tag{2.26}$$

However, P_{RES} and S must be chosen also in accordance with electric system and ESS constraints, which can now be expressed as:

$$P_{RES}^{(k,d)} + S^{(k,d)} \le -(1-\sigma)\cdot \tilde{L}_0^{(k,d)} \tag{2.27}$$

$$L^{(k,d)} \le S^{(k,d)} \le P^{(k,d)} \tag{2.28}$$

where L and P are defined by (2.15) in accordance with actual ESS state of charge. Referring to Fig. 2.8, (2.26) states that the operating point should lie on the straight line $\tilde{r}_0$, whereas (2.28) imposes that the operating point must belong to the plane region bounded by r_P and r_L. These last may differ from $\tilde{r}_P$ and $\tilde{r}_L$, due to mismatches between predicted and actual ESS state of charge, as shown in Fig. 2.8. Therefore, three different situations can occur depending on the actual P_{RES}^{*} value, as shown in Fig. 2.9, Fig. 2.10 and Fig. 2.11 respectively. Particularly, firstly referring to Fig. 2.9, if P_{RES}^{*} lies below

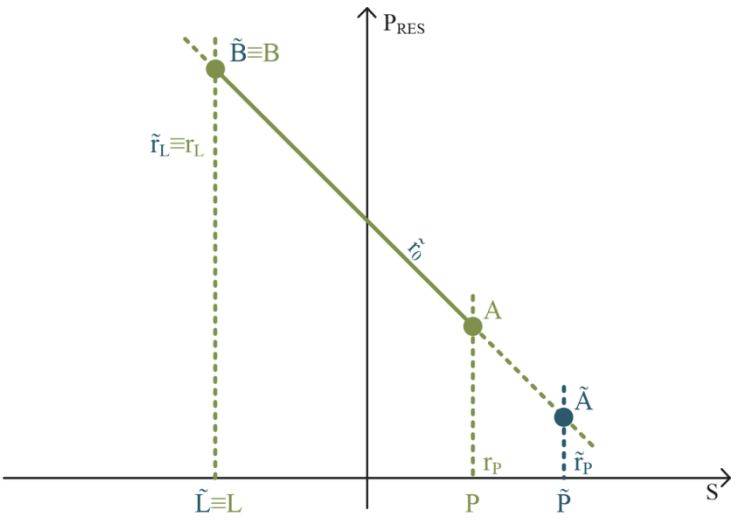

Fig. 2.8 Real-time control strategy constraints on the (S,P_{RES}) plane.

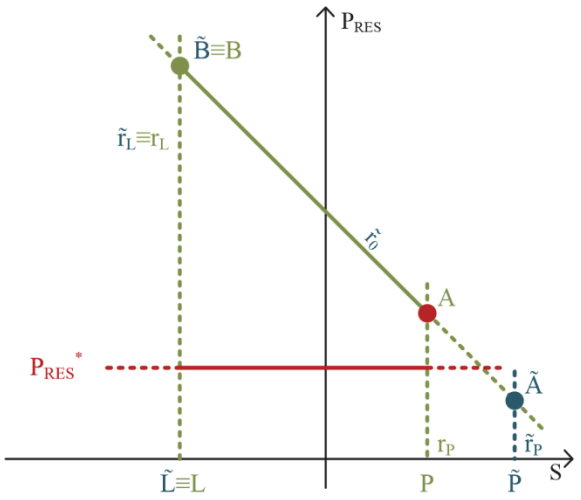

Fig. 2.9 Graphical representation of the proposed real-time control strategy in case of RES underproduction.

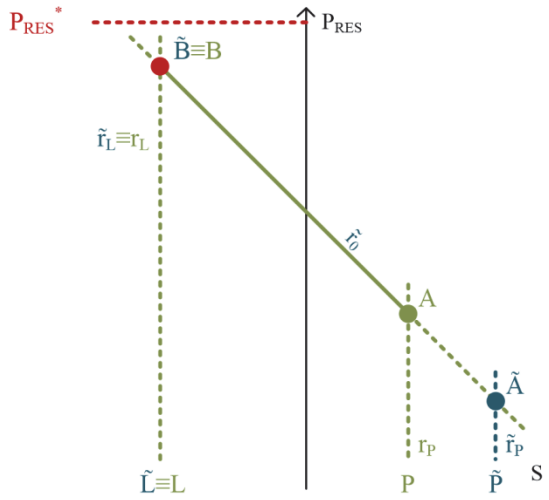

Fig. 2.10 Graphical representation of the proposed real-time control strategy in case of RES overproduction.

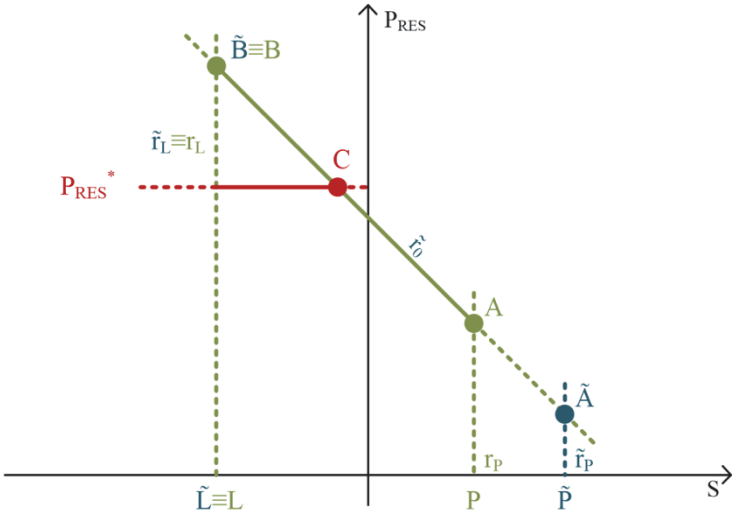

Fig. 2.11 Graphical representation of the proposed real-time control strategy in case of no RES curtailment.

the point A, P_{RES} and S must be chosen as

$$\begin{aligned} P_{RES}^{(k,d)} &= P_{RES}^{*(k,d)} \\ S^{(k,d)} &= P^{(k,d)} \end{aligned} . \tag{2.29}$$

In this case, no RES curtailment occurs, but forecasting errors prevent the real-time control strategy from successfully tracking the scheduled $\tilde{S}_{RES}$ profile, S_{RES} being lower than expected. This leads to define the RES scheduling error δ as

$$\delta^{(k,d)} = \frac{\tilde{S}_{RES}^{(k,d)} - S_{RES}^{(k,d)}}{\tilde{S}_{RES}^{(k,d)}} . \tag{2.30}$$

Otherwise, if P_{RES}^{*} exceeds its upper boundary corresponding to the point B depicted in Fig. 2.10, P_{RES} and S must be chosen as

$$\begin{aligned} P_{RES}^{(k,d)} &= -(1-\sigma)\cdot \tilde{L}_0^{(k,d)} - L^{(k,d)} \\ S^{(k,d)} &= L^{(k,d)} \end{aligned} . \tag{2.31}$$

Consequently, RES potential power production cannot be fully exploited, being partially wasted. However, since S_{RES} is equal to its scheduled value $\tilde{S}_{RES}$, no power production errors occur.

Referring to the third case, like that shown in Fig. 2.11, no RES curtailment and scheduling errors occur because P_{RES} and S can be chosen as

$$\begin{aligned} P_{RES}^{(k,d)} &= P_{RES}^{*(k,d)} \\ S^{(k,d)} &= \tilde{S}_{RES}^{(k,d)} - P_{RES}^{*(k,d)} \end{aligned} \quad . \tag{2.32}$$

In conclusion, regardless of the specific case, the RES penetration level π can be defined as

$$\pi^{(k,d)} = -\frac{S_{RES}^{(k,d)}}{\tilde{L}_0^{(k,d)}} \quad . \tag{2.33}$$

2.1.2.3 EMS Overview

A schematic representation of the proposed EMS is depicted in Fig. 2.12. It is worth noting that the scheduling procedure and the real-time control strategy operate in parallel over the generic day *d*, but they refer to different days. Firstly referring to the scheduling procedure, it aims to synthesize the optimal combined ESS-RES power profile for the day *d+1* based on the actual ESS energy storage level $E^{(0,d+1)}$. Unfortunately, since the ESS stored energy level changes in accordance with (2.13), $E^{(0,d+1)}$ can be available at the end of day *d* only, it being required by the scheduling procedure at the start of the day. Such drawback could be overcome by appropriately predicting $E^{(0,d+1)}$ as:

$$\tilde{E}^{(0,d+1)} = E^{(0,d)} - \sum_k \left(\frac{\bar{P}_s^{(k,d)}}{\eta_d} + \eta_c \cdot \bar{L}_s^{(k,d)} \right) \cdot T \tag{2.34}$$

in which $\bar{P}_s$ and $\bar{L}_s$ are determined by applying the proposed real-time procedure in advance, assuming that no forecasting errors occur in day *d*. This assumption allows the achievement of an ESS stored energy level closer to the actual one than that obtained by (2.24), avoiding cumulative errors due to forecasting errors compensation and, thus, improving the scheduling procedure performances.

Meanwhile, the optimal power profile, already synthesized by the scheduling procedure in the previous day (*d−1*), is tracked as well as possible by means of the proposed real-time control strategy, increasing RES reliability. This is carried out by compensating for the forecasting errors occurring on

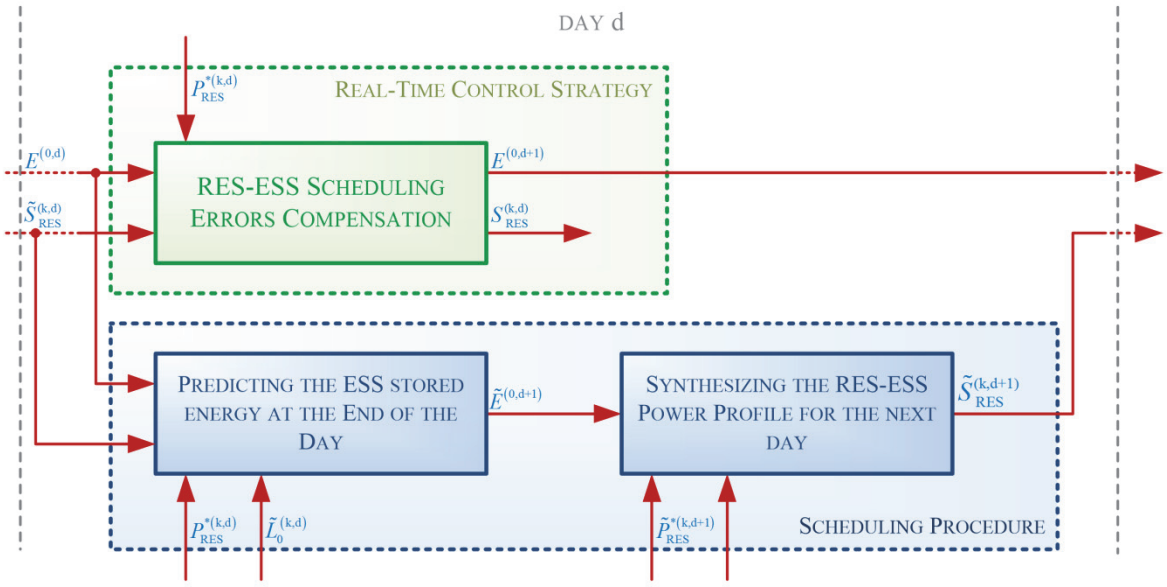

Fig. 2.12 The equivalent block control scheme of the proposed ESS management system.

the RES power production profile, whose actual potential value generally differs from the forecasted one.

In conclusion, in order to evaluate the effectiveness of the proposed EMS, two overall performance indexes can be firstly introduced as

$$\Pi = \frac{\sum_{k,d} \pi^{(k,d)} \cdot \tilde{L}_0^{(k,d)}}{\sum_{k,d} \tilde{L}_0^{(k,d)}} \tag{2.35}$$

$$\Xi = -\frac{\eta_c}{E_b} \sum_{k,d} L_s^{(k,d)} \cdot T \ . \tag{2.36}$$

In particular, Π represents the RES penetration level over a given period of time, which is upper bounded in accordance with the following equation:

$$\Pi \leq min\left\{\sigma, \Pi^*\right\} \quad , \quad \Pi^* = -\frac{\sum_{k,d} P_{RES}^{*(k,d)}}{\sum_{k,d} \tilde{L}_0^{(k,d)}} \tag{2.37}$$

in which Π^* represents the maximum RES penetration level for a given P_{RES}^*. Whereas Ξ denotes the average charging/discharging cycles performed by the ESS in the same period of time, thus accounting for ESS usage. Furthermore, in order to take into account RES scheduling and reliability, two additional indexes can be introduced as

$$\Delta = \frac{\sum_{k,d} \delta^{(k,d)} \cdot \tilde{S}_{RES}^{(k,d)}}{\sum_{\delta^{(k,d)} \neq 0} \tilde{S}_{RES}^{(k,d)}} \tag{2.38}$$

$$\Phi = \sum_{\delta^{(k,d)} \neq 0} 1 \ . \tag{2.39}$$

In particular, Δ represents the average magnitude of the scheduling error over a given time interval, which only includes the sampling time intervals in correspondence of which δ differs from zero: these are represented by the index Φ, which accounts for scheduling error occurrences.

2.1.3 Simulations

In order to evaluate the effectiveness of the proposed EMS, a simulation study is carried out by means of the Matlab Software Package. The reference energy system is the Island of Sardinia (24090 Km^2, pop. 1675411, 12 TWh annual electricity consumption), whose geographical location is highlighted in Fig. 2.13. It is characterized by a strong RES displacement and it is large enough from both demographical and geographical points of view to be a suitable benchmark for the proposed EMS. The analyzed scenario refers to the planned 2020 Sardinia Energy Target that is assumed in accordance with the European Strategic Energy Plan: in particular, it foresees almost the same annual energy consumption as that of 2011, but with a significant power increase of installed RES. Consequently, 1500 MW of installed wind power, 1000 MW of photovoltaic power and 44 MW of river hydro power have been considered, leading to a potential RES annual electricity production of about 2.51 TWh. Furthermore, the forecasting uncertainties that affect the potential RES power production have been modelled by means of a Gaussian distribution characterized by a 10% standard deviation. The simulation study is carried out by employing different ESS sizes for comparison purposes: in particular, the ESS charging/discharging efficiencies are both set equal to 0.85, whereas

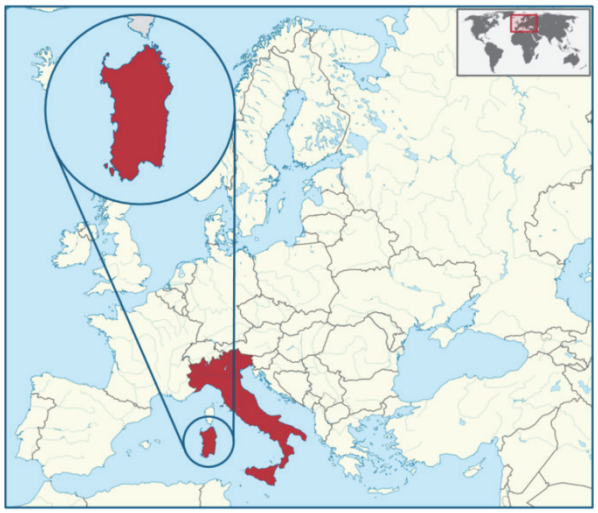

Fig. 2.13 Geographical location of the Island of Sardinia.

the following ESS sizes have been considered:

- case 0: no ESS;
- case 1: E_b = 300 MWh, P_b = 25 MW;
- case 2: E_b = 600 MWh, P_b = 50 MW;
- case 3: E_b = 1200 MWh, P_b = 100 MW;
- case 4: E_b = 2400 MWh, P_b = 200 MW.

2.1.3.1 Simulation results

The simulation results firstly refer to strict electric grid constraints, consisting in a σ value equal to 0.9. Thus, referring to a generic week, the π and δ evolutions achieved by the proposed EMS are depicted in Fig. 2.14 and Fig. 2.15 respectively. Hence, firstly referring to case 0 (no ESS), it can be seen that a large part of the potential RES power profile cannot be exploited and, hence, is wasted. In addition, the unavailability of an ESS also leads to frequent scheduling errors and, hence, to poorly predictable RES power production. Better results in terms of π can be achieved by means of the proposed EMS, as highlighted in Fig. 2.14. In fact, it can be noticed that energy buffering is able to increase RES exploitation, even if it requires large ESSs, such as that employed in case 4: this corroborates the effectiveness of the proposed scheduling procedure. Furthermore, referring to RES scheduling errors highlighted in Fig. 2.15, it can be seen that they decrease as soon as larger ESSs are employed, especially in terms of occurrences. As a result, RES power production reliability is improved, revealing the effectiveness of the proposed real-time control strategy at the same time.

Then, simulations refer to the same week, but considering the case of higher allowable RES penetration level (σ = 0.75), whose corresponding results are depicted in Fig. 2.16 and Fig. 2.17. In particular, the comparison with the previous simulation results highlights that RES curtailments are significantly reduced at σ = 0.75, even in the case 0. As a consequence, energy buffering is less required than at σ = 0.9, as can be detected by comparing Fig. 2.14 with Fig. 2.16. Furthermore, still referring to case 0, the comparison between Fig. 2.15 and Fig. 2.17 reveals less frequent RES scheduling errors at σ = 0.90 than those achieved at σ = 0.75, as expected. However, in the other cases, the proposed real-time control strategy is able to guarantee very few scheduling error occurrences, even in the case of an ESS of moderate size, such as that employed in the case 2. As a consequence, the RES power production becomes more schedulable and reliable, leading to higher RES penetration levels, without impairing the electric grid management.

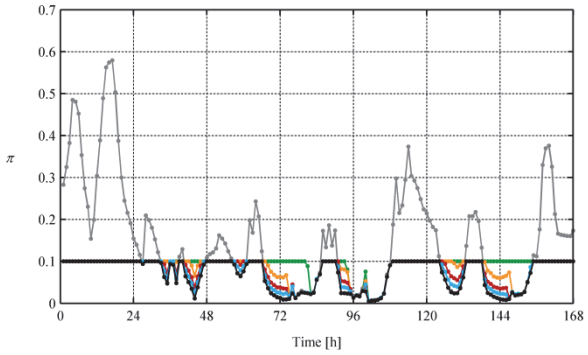

Fig. 2.14 The π evolutions over a generic week at $\sigma = 0.90$: potential (gray), cases 0 (black), 1 (blue), 2 (red), 3 (orange) and 4 (green).

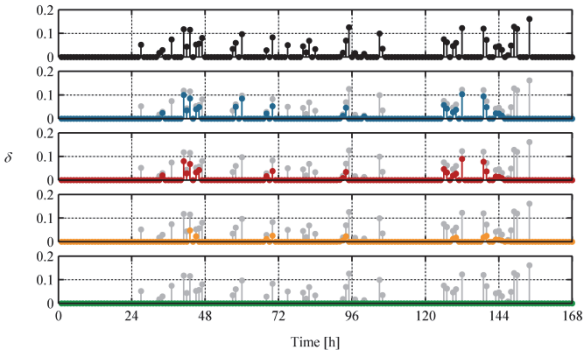

Fig. 2.15 The δ evolutions over a generic week at $\sigma = 0.90$: potential (gray), cases 0 (black), 1 (blue), 2 (red), 3 (orange) and 4 (green).

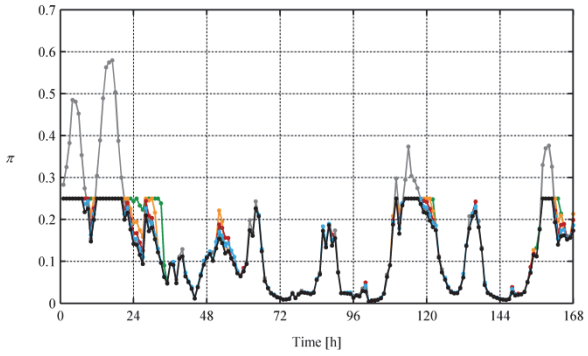

Fig. 2.16 The π evolutions over a generic week at $\sigma = 0.75$: potential (gray), cases 0 (black), 1 (blue), 2 (red), 3 (orange) and 4 (green).

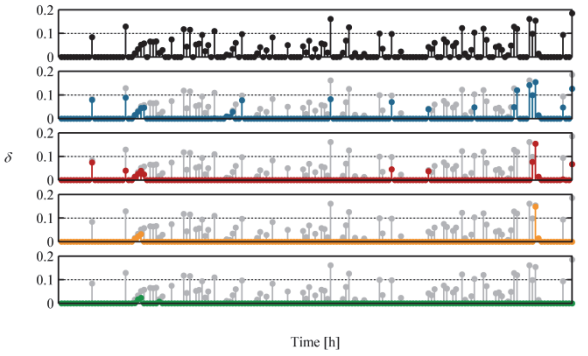

Fig. 2.17 The δ evolutions over a generic week at $\sigma = 0.75$: cases 0 (black, gray), 1 (blue), 2 (red), 3 (orange) and 4 (green).

Similar considerations can be made referring to the annual π and δ evolutions achieved at both $\sigma = 0.90$ and $\sigma = 0.75$, which are depicted in Fig. 2.18 and Fig. 2.19 and whose most significant details are summed up in Table II and Table III. In particular, firstly referring to cases 0, it can be seen that a poor RES penetration level is achieved at $\sigma = 0.90$, the scheduling errors being also quite high and frequent. Better results in terms of RES penetration level can be achieved at $\sigma = 0.75$, but this almost doubles the frequency of scheduling errors. Referring now to the results achieved by means of the proposed EMS, it can be seen that very similar and poor results can be achieved in terms of RES exploitation due to energy buffering at both $\sigma = 0.90$ and $\sigma = 0.75$, although huge ESSs are employed: it means that energy buffering does not seem a viable solution to increase the RES penetration level,

TABLE II

SIMULATIONS DETAILS (ONE YEAR, 8760 H, $\Sigma = 0.90$)

	RES EXPLOITATION				SCHEDULING ERRORS	
	PROD.	BUFF.	LOSS.	CURT.	MAGN.	FREQ.
case 0	37.9 %			62.1 %	6.6 %	1531 h
case 1	38.1 %	1.5 %	0.6 %	59.8 %	5.0 %	843 h
case 2	38.2 %	2.9 %	1.1 %	57.8 %	3.7 %	696 h
case 3	38.2 %	5.2 %	2.0 %	54.6 %	1.5 %	389 h
case 4	38.2 %	7.6 %	3.0 %	51.2 %	0.5 %	2 h

TABLE III

SIMULATIONS DETAILS (ONE YEAR, 8760 H, $\Sigma = 0.75$)

	RES EXPLOITATION				SCHEDULING ERRORS	
	PROD.	BUFF.	LOSS.	CURT.	MAGN.	FREQ.
case 0	72.1 %			27.9 %	6.5 %	2845 h
case 1	72.5 %	1.6 %	0.6 %	25.3 %	5.6 %	1152 h
case 2	72.6 %	2.6 %	1.0 %	23.8 %	5.4 %	838 h
case 3	72.6 %	4.2 %	1.6 %	21.6 %	4.4 %	585 h
case 4	72.6 %	6.4 %	2.5 %	18.5 %	3.8 %	253 h

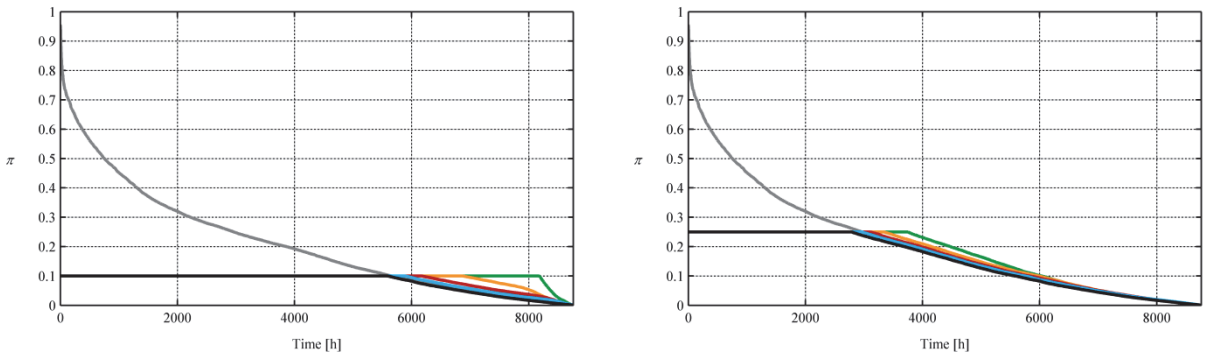

Fig. 2.18 The annual π evolutions at $\sigma = 0.90$ (on the left) and at $\sigma = 0.75$ (on the right), sorted in descending order: potential (gray), cases 0 (black), 1 (blue), 2 (red), 3 (orange) and 4 (green).

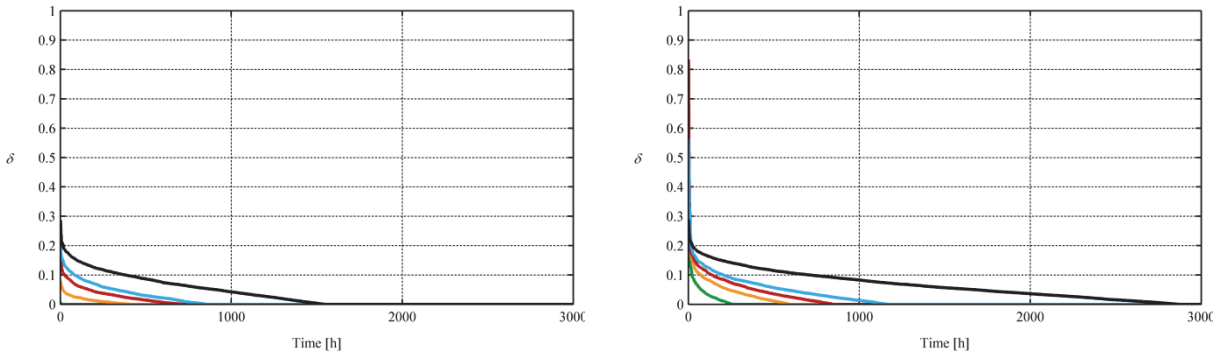

Fig. 2.19 The annual δ evolutions at $\sigma = 0.90$ (on the left) and at $\sigma = 0.75$ (on the right), sorted in descending order: cases 0 (black), 1 (blue), 2 (red), 3 (orange) and 4 (green).

being also subjected to additional losses. In contrast, very good performances can be obtained regarding the scheduling errors, especially in terms of occurrences: in fact, at $\sigma = 0.75$, the employment of a quite small ESS (case 1) allows the reduction of the scheduling errors magnitudes and occurrences, even below the values corresponding to the case 0 at $\sigma = 0.90$: this means that the proposed EMS allows the improvement of RES scheduling and reliability. As a consequence, higher RES penetration level could be allowed without impairing the electric grid stability, as pointed out previously.

In order to well evaluate the worth and the effectiveness of the proposed EMS, reference is now made to the overall performance indexes Π, Ξ, Δ and Φ, whose evolutions are depicted from Fig. 2.20 to Fig. 2.23, their values at different σ operations being resumed in Table IV. Firstly referring to the Π evolutions shown in Fig. 2.20, it can be seen that increasing the ESS size does not lead to a significantly higher RES penetration level for a given σ value: this corroborates the fact that energy buffering does not seem to significantly increase RES exploitation. Referring now to the Ξ evolutions depicted in Fig. 2.21, it can be seen that, starting from $\sigma = 1$, the ESS usage quickly increases as soon as σ decreases. This is due to the ESS energy buffering prevalence on scheduling errors compensation, leading to higher ESS charging/discharging cycles. However, when σ drops below 0.85, the ESS usage generally decreases, meaning that energy buffering is less required at medium σ operations, in correspondence of which scheduling error compensation is predominant. Finally, referring to both the Δ and Φ evolutions depicted in Fig. 2.22 and Fig. 2.23 respectively, it can be seen that scheduling errors in case 0 are quite high but slowly variable versus σ. This does not occur in the other cases, in correspondence of which, scheduling errors quickly increase as soon as σ decreases, assuming a slowly variable shape only below $\sigma = 0.6$. This is due to the fact that smaller σ values entail higher RES penetration levels permitted by the electric grid, leading to higher and more frequent scheduling errors. Furthermore, referring to Fig. 2.23, it can be seen that the employment of an ESS drastically

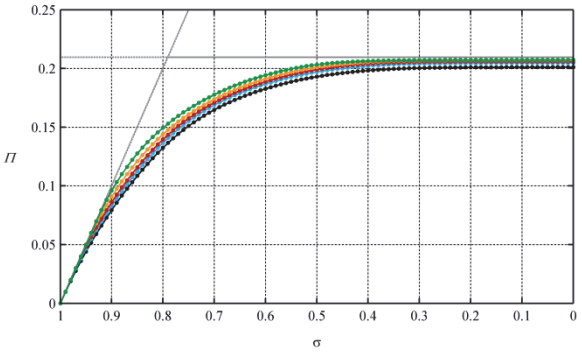

Fig. 2.20 The Π evolutions versus σ: potential (gray), case 0 (black), case 1 (blue), case 2 (red), case 3 (orange) and case 4 (green).

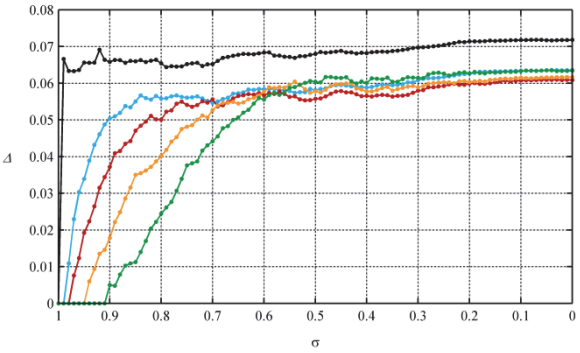

Fig. 2.22 The Δ evolutions versus σ: case 0 (black), case 1 (blue), case 2 (red), case 3 (orange) and case 4 (green).

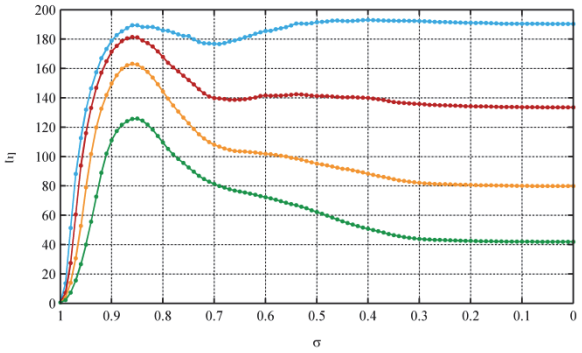

Fig. 2.21 The Ξ evolutions versus σ: case 0 (black), case 1 (blue), case 2 (red), case 3 (orange) and case 4 (green).

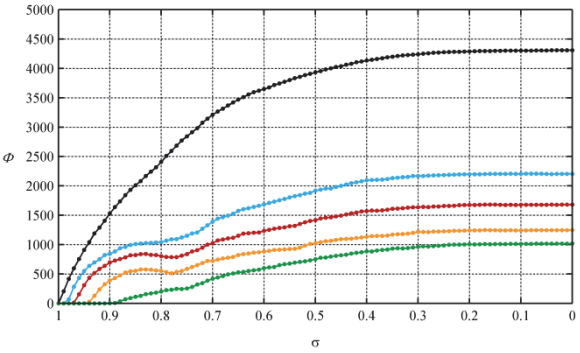

Fig. 2.23 The Φ evolutions versus σ: case 0 (black), case 1 (blue), case 2 (red), case 3 (orange) and case 4 (green).

reduces scheduling error occurrences compared to those achieved in case 0 (no ESS), even when employing quite small ESS (case 1). These results highlight the fact that the ESS can be successfully employed in order to compensate for scheduling errors in terms of magnitude, but especially in terms of occurrences.

In conclusion, simulation results have highlighted that energy buffering does not seem to be a viable solution for significantly increasing RES exploitation, unless huge ESSs are employed. On the other hand, it has been shown that excellent forecasting errors compensation can be achieved, even by resorting to ESSs of moderate size: this leads to increased RES power production scheduling and reliability, suggesting higher RES penetration levels permitted by the electric grid.

TABLE IV
SIMULATION RESULTS SUMMARY (ONE YEAR, 8760 H)

	σ = 0.90				σ = 0.85				σ = 0.80				σ = 0.75			
	Π [%]	Ξ [-]	Δ [%]	Φ [h]	Π [%]	Ξ [-]	Δ [%]	Φ [h]	Π [%]	Ξ [-]	Δ [%]	Φ [h]	Π [%]	Ξ [-]	Δ [%]	Φ [h]
case 0	7.9		6.6	1531	10.9		6.6	2012	13.3		6.5	2408	15.1		6.5	2845
case 1	8.3	179	5.0	843	11.3	189	5.5	1010	13.7	186	5.6	1043	15.5	182	5.6	1152
case 2	8.6	172	3.7	696	11.6	181	4.7	823	14.0	168	5.0	803	15.8	152	5.4	838
case 3	9.1	150	1.8	389	12.1	163	3.5	553	14.4	144	4.0	553	16.1	123	4.8	585
case 4	9.6	111	0.5	2	12.8	125	1.1	110	14.9	110	2.4	202	16.5	93	3.8	253

2.2 Vehicle to Grid

In the previous Section, the benefits provided by ESS devoted to RES exploitation have been pointed out. Hence, the analysis of the possible implementation of the proposed control algorithm to EV charging system is considered a natural prosecution of this research activity. Particularly, the spread of EVs due to the electrification of transport sector may offer a great opportunity, since battery-powered EVs may be used to support large RES integration into the power system as stated above.

The obtained results have a general validity and can be extended to other kinds of available ESSs. In particular, several studies that analyse the impact of EVs on the electric energy system have been presented. It has been shown that the benefits achievable through the increasing diffusion of EVs are superior to the criticalities introduced [69]–[71]. In addition, the previous Chapter showed that V2G may provide additional revenues to EVs owners on condition that all the issues arising from its implementation are addressed properly. The most important one is assuring V2G operation without impairing EV owners' mobility needs. For this purpose, different methodologies have been proposed in order to manage the complementary of the electric system and the mobility system needs [57], [72]–[75]. In particular, grid services at distribution level are suited for EVs massive diffusion, from technical and economic points of view. Among these, the most valuables ones are extra power supply, peak load shaving, load shifting, spinning reserve and regulation. A review of the technical literature reveals the existence of different methods to evaluate the limit of EV penetration on a defined medium voltage electric distribution system. Nevertheless, these studies are generally based on a standard centralized power system vision of the supply chain.

A novel management strategy for EV storage systems is proposed in this section. It aims to enhance the RES exploitation, prioritizing the EV mobility requirements at the same time. A mathematical model of the mobility system is firstly developed in order to estimate the amount of EVs available to exchange energy with the electric grid, together with the average state of charge of their corresponding batteries. Then, a management strategy is properly introduced in order to increase the RES energy production as much as possible, providing grid services too. The proposed management system is properly validated by means of a simulation study referred to a power system characterized by a strong RES penetration level. The simulation results highlight the effectiveness of the proposed management strategy and the potentiality of the EV storage systems in enhancing RES exploitation.

2.2.1 Mathematical Modelling

2.2.1.1 Mobility System

In order to estimate the interaction capability of the EV fleet with the electric grid, an energy model of the EV mobility system is required. Consequently, the whole EV fleet is split in three sub-fleets, as shown in Fig. 2.24: the first one (δ) represents all the EVs on the road, the second one (π) includes the

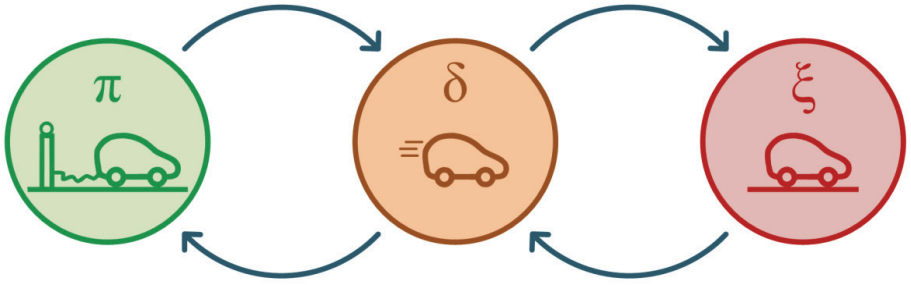

Fig. 2.24 The EV sub-fleets classification.

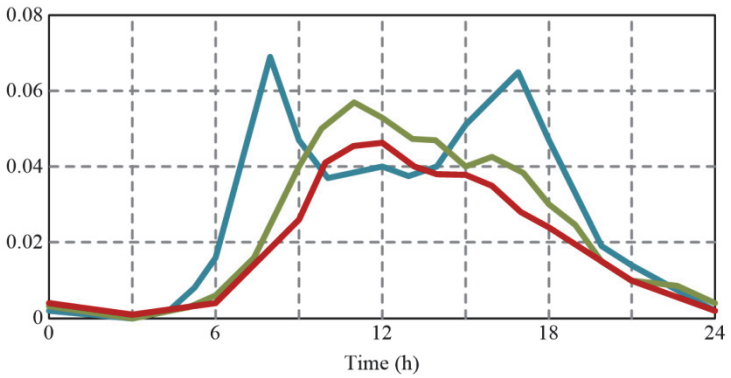

Fig. 2.25 Statistical time distribution of EVs on the road (in per unit) referred to different days: Monday-Friday (blue), Saturday (green) and Sunday (red).

EVs parked and plugged-in, whereas the last one (ξ) groups all the EVs parked and unplugged. In particular, the definition of the ξ sub-fleet is mandatory in order to account for various phenomena, especially the possibility that a parked car cannot be connected to the grid due to the lack of charging infrastructures. Then, in order to define the number of EVs belonging to each sub-fleet, reference is made to mobility habits, in particular to a statistical time distribution of the cars on the road, which has been properly deduced in [76] and reported in Fig. 2.25. Then, the remaining number of EVs are distributed into the π and ξ groups in accordance with the availability of charging infrastructures, as well as with other sociological and economic aspects.

Therefore, assuming the EV fleet made up of n_{EV} vehicles, its rated capacity and power can be computed as

$$E_b = n_{EV} \cdot e_b \tag{2.40}$$

$$P_b = n_{EV} \cdot p_b \tag{2.41}$$

in which e_b and p_b denote EV battery rated capacity and power respectively. Therefore, denoting by ε the average sub-fleet state of charge, it is possible to compute the amount of energy stored into the EV batteries of each sub-fleet at the k-th sampling time interval as

$$E_i^{(k)} = n_i^{(k)} \cdot \varepsilon_i^{(k)} \cdot e_b \quad , \quad i \in \{\pi, \delta, \xi\} \tag{2.42}$$

being n_i the number of EVs belonging to the i sub-fleet, which satisfy the following condition:

$$n_\pi^{(k)} + n_\xi^{(k)} + n_\delta^{(k)} = n_{EV} \quad . \tag{2.43}$$

The overall energy stored into EV batteries thus changes in accordance with the following relationship:

$$E_\pi^{(k+1)} + E_\delta^{(k+1)} + E_\xi^{(k+1)} = E_\pi^{(k)} + E_\delta^{(k)} + E_\xi^{(k)} - \left(F^{(k)} + \tilde{S}^{(k)}\right) \cdot T \tag{2.44}$$

where F and $\tilde{S}$ denote the average power drawn due to EV mobility and the average power exchanged with the electric grid, both referred to the sampling time interval T. Consequently, the combination between (2.44) and (2.40) yields

$$\pi^{(k+1)}\varepsilon_\pi^{(k+1)} + \delta^{(k+1)}\varepsilon_\delta^{(k+1)} + \xi^{(k+1)}\varepsilon_\xi^{(k+1)} = \pi^{(k)}\varepsilon_\pi^{(k)} + \delta^{(k)}\varepsilon_\delta^{(k)} + \xi^{(k)}\varepsilon_\xi^{(k)} - f^{(k)} - \tilde{s}^{(k)} \tag{2.45}$$

in which

$$i^{(k)} = \frac{n_i^{(k)}}{n_{EV}} \quad , \quad i \in \{\pi, \delta, \xi\} \tag{2.46}$$

$$f^{(k)} = \frac{F^{(k)} \cdot T}{E_b} \quad , \quad \tilde{s}^{(k)} = \frac{\tilde{S}^{(k)} \cdot T}{E_b} \ . \tag{2.47}$$

Unfortunately, (2.45) defines the energy evolution of the EV fleet as a whole, thus it cannot be employed for identifying those related to each sub-fleet. In this context, it is worth noting that only the π sub-fleet is able to exchange energy with the grid, acting as an equivalent ESS characterized by the following variable rated power and capacity:

$$P_b^{(k)} = n_{EV} \pi^{(k)} p_b \tag{2.48}$$

$$E_b^{(k)} = n_{EV} \pi^{(k)} e_b \ . \tag{2.49}$$

Therefore, since actual energy level of the π sub-fleet is required, (2.45) can be usefully split into the following three equations

$$\pi^{(k+1)} \varepsilon_\pi^{(k+1)} = \pi^{(k)} \varepsilon_\pi^{(k)} + d\varepsilon_\pi^{(k)} + d\varepsilon_{\pi\text{-}\delta}^{(k)} - \tilde{s}^{(k)} \tag{2.50}$$

$$\xi^{(k+1)} \varepsilon_\xi^{(k+1)} = \xi^{(k)} \varepsilon_\xi^{(k)} + d\varepsilon_\xi^{(k)} + d\varepsilon_{\xi\text{-}\delta}^{(k)} \tag{2.51}$$

$$\delta^{(k+1)} \varepsilon_\delta^{(k+1)} = \delta^{(k)} \varepsilon_\delta^{(k)} - \left(d\varepsilon_\pi^{(k)} + d\varepsilon_{\pi\text{-}\delta}^{(k)} \right) - \left(d\varepsilon_\xi^{(k)} + d\varepsilon_{\xi\text{-}\delta}^{(k)} \right) - f^{(k)} \ . \tag{2.52}$$

Firstly referring to (2.50), $d\varepsilon_\pi$ denotes the energy variation of the π sub-fleet due to a corresponding variation of its number of EVs. Assuming that each EV switching from π to δ is characterized by a given state of charge ε_0 and that no EV can switch from π to ξ, $d\varepsilon_\pi$ can be expressed as

$$d\varepsilon_\pi^{(k)} = \frac{1}{2} \left(\left(\pi^{(k+1)} - \pi^{(k)} \right) \left(\varepsilon_0^{(k)} + \varepsilon_\delta^{(k)} \right) - \left| \pi^{(k+1)} - \pi^{(k)} \right| \left(\varepsilon_0^{(k)} - \varepsilon_\delta^{(k)} \right) \right) \ . \tag{2.53}$$

Still referring to (2.50), $d\varepsilon_{\pi\text{-}\delta}$ accounts for such EV that switch between π and δ sub-fleets without varying their size. However, this phenomenon causes a variation of the sub-fleet energy level because their average states of charge generally differ from each other. Consequently, $d\varepsilon_{\pi\text{-}\delta}$ can be computed as

$$d\varepsilon_{\pi\text{-}\delta}^{(k)} = \sigma_\pi^{(k)} \left(\varepsilon_\delta^{(k)} - \varepsilon_0^{(k)} \right) \tag{2.54}$$

in which σ_π denotes the number of π *switcher pairs*, each of which moves from π to δ and viceversa, as shown in Fig. 2.26. This can be determined by introducing a turnover rate of EVs on the road (α), together with their distribution share over π (β):

$$\sigma_\pi^{(k)} = min \left\{ \pi^{(k+1)}, \pi^{(k)}, \alpha\beta\delta^{(k+1)}, \alpha\beta\delta^{(k)} \right\} \ . \tag{2.55}$$

Similarly, referring to (2.51), $d\varepsilon_\xi$ and $d\varepsilon_{\xi\text{-}\delta}$ can be computed respectively as

$$d\varepsilon_\xi^{(k)} = \frac{1}{2} \left(\left(\xi^{(k+1)} - \xi^{(k)} \right) \left(\varepsilon_\xi^{(k)} + \varepsilon_\delta^{(k)} \right) - \left| \xi^{(k+1)} - \xi^{(k)} \right| \left(\varepsilon_\xi^{(k)} - \varepsilon_\delta^{(k)} \right) \right) \tag{2.56}$$

$$d\varepsilon_{\xi\text{-}\delta}^{(k)} = \sigma_\xi^{(k)} \left(\varepsilon_\delta^{(k)} - \varepsilon_\xi^{(k)} \right) \tag{2.57}$$

in which

$$\sigma_\xi^{(k)} = min \left\{ \xi^{(k+1)}, \xi^{(k)}, \alpha(1-\beta)\delta^{(k+1)}, \alpha(1-\beta)\delta^{(k)} \right\} \ . \tag{2.58}$$

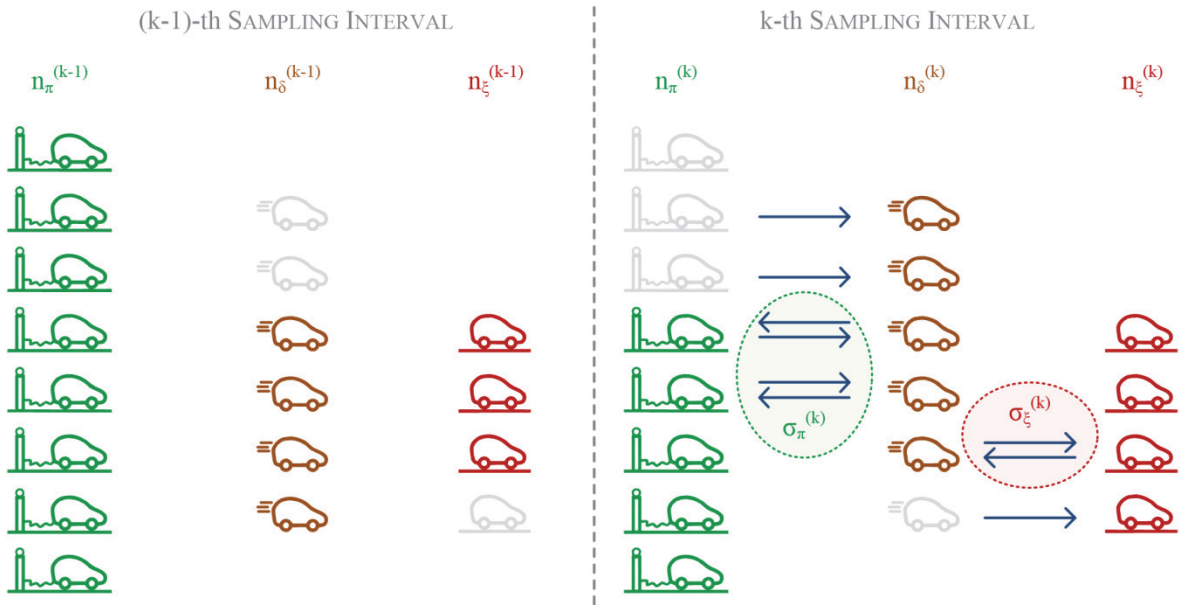

Fig. 2.26 Representation of EV sub-fleet composition over two sampling time intervals.

Therefore, substituting (2.53) through (2.58) into (2.50) through (2.52), the following system is achieved:

$$C^{(k+1)}\overline{\varepsilon}^{(k+1)} = A^{(k)}\overline{\varepsilon}^{(k)} + B^{(k)}\overline{u}^{(k)} \tag{2.59}$$

in which

$$\overline{\varepsilon}^{(k)} = \left[\varepsilon_\pi^{(k)} \quad \varepsilon_\xi^{(k)} \quad \varepsilon_\delta^{(k)}\right]^T \tag{2.60}$$

$$\overline{u}^{(k)} = \left[\tilde{s}^{(k)} \quad f^{(k)} \quad \varepsilon_0{}^{(k)}\right]^T \tag{2.61}$$

$$A^{(k)} = \begin{bmatrix} 2\pi^{(k)} & 0 & \left(\begin{array}{c}\pi^{(k+1)} - \pi^{(k)} + \\ + \left|\pi^{(k+1)} - \pi^{(k)}\right| + 2\sigma_\pi^{(k)}\end{array}\right) \\ 0 & \left(\begin{array}{c}\xi^{(k+1)} + \xi^{(k)} + \\ - \left|\xi^{(k+1)} - \xi^{(k)}\right| - 2\sigma_\xi^{(k)}\end{array}\right) & \left(\begin{array}{c}\xi^{(k+1)} - \xi^{(k)} + \\ + \left|\xi^{(k+1)} - \xi^{(k)}\right| + 2\sigma_\xi^{(k)}\end{array}\right) \\ 0 & -\left(\begin{array}{c}\xi^{(k+1)} - \xi^{(k)} + \\ - \left|\xi^{(k+1)} - \xi^{(k)}\right| - 2\sigma_\xi^{(k)}\end{array}\right) & -\left(\begin{array}{c}-2\delta^{(k)} + \pi^{(k+1)} - \pi^{(k)} + \\ + \left|\pi^{(k+1)} - \pi^{(k)}\right| + 2\sigma_\pi^{(k)} + \\ + \xi^{(k+1)} - \xi^{(k)} + \\ + \left|\xi^{(k+1)} - \xi^{(k)}\right| + 2\sigma_\xi^{(k)}\end{array}\right) \end{bmatrix} \tag{2.62}$$

$$B^{(k)} = \begin{bmatrix} -2 & \pi^{(k+1)} - \pi^{(k)} - \left|\pi^{(k+1)} - \pi^{(k)}\right| - 2\sigma_\pi^{(k)} & 0 \\ 0 & 0 & 0 \\ 0 & -\left(\pi^{(k+1)} - \pi^{(k)} - \left|\pi^{(k+1)} - \pi^{(k)}\right| - 2\sigma_\pi^{(k)}\right) & -2 \end{bmatrix} \tag{2.63}$$

$$C^{(k)} = \begin{bmatrix} 2\pi^{(k+1)} & 0 & 0 \\ 0 & 2\xi^{(k+1)} & 0 \\ 0 & 0 & 2\delta^{(k+1)} \end{bmatrix}. \tag{2.64}$$

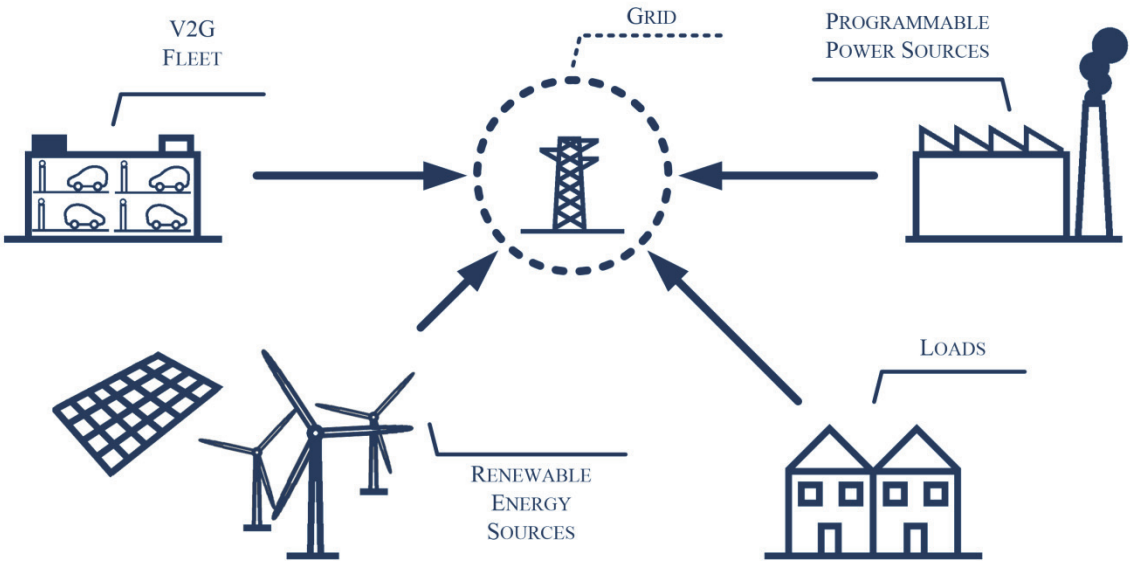

Fig. 2.27 Schematic representation of a power system characterized by a V2G fleet.

As a result, (2.59) allows the computation of the average states of charge of each sub-fleet. Consequently, based on ε_π, actual energy level of the π sub-fleet can be achieved by (2.42).

2.2.1.2 Electric System

Considering an electric system like that shown in Fig. 2.27, whose ESS is made up of EV batteries, its power balance over the generic k-th sampling time interval can be expressed as

$$P_0^{(k)} + P_{RES}^{(k)} + S^{(k)} + L_0^{(k)} = 0 \ . \tag{2.11}$$

in which P_0 and P_{RES} denotes the power delivered by programmable power sources and RES power plants respectively, L_0 being the load demand. Whereas S is the power exchanged by the ESS with the electric grid, which differs from $\tilde{S}$ because it is evaluated referring to the grid side. Consequently, S can be expressed as

$$S^{(k)} = \frac{1}{2}\left(\tilde{S}^{(k)} \left(\eta_d + \frac{1}{\eta_c} \right) - \left| \tilde{S}^{(k)} \right| \left(\eta_d - \frac{1}{\eta_c} \right) \right) \tag{2.65}$$

in which η_c and η_d denote the charging and discharging efficiency respectively. Particularly, when $\tilde{S}$ is positive, EV batteries provide energy to the grid at the following power rate:

$$P_s^{(k)} = \frac{\eta_d}{2}\left(\tilde{S}^{(k)} + \left| \tilde{S}^{(k)} \right| \right) \ . \tag{2.66}$$

Otherwise, when $\tilde{S}$ is negative, the grid recharges the EV batteries at the following power rate:

$$L_s^{(k)} = \frac{1}{2 \cdot \eta_c}\left(\tilde{S}^{(k)} - \left| \tilde{S}^{(k)} \right| \right) \ . \tag{2.67}$$

As a result, by substituting both (2.66) and (2.67) in (2.65), the following relationship is achieved:

$$S^{(k)} = L_s^{(k)} + P_s^{(k)} \ . \tag{2.68}$$

It is worth noting that S is bounded in accordance with the following constraint:

$$L^{(k)} \le S^{(k)} \le P^{(k)} \tag{2.69}$$

where

$$L^{(k)} = max\left\{-P_b^{(k)}, \frac{E_0^{(k)} - E_{max}^{(k)}}{\eta_c \cdot T}\right\} \tag{2.70}$$

$$P^{(k)} = min\left\{\eta_d \cdot P_b^{(k)}, \eta_d \cdot \frac{E_0^{(k)} - E_{min}^{(k)}}{T}\right\} \tag{2.71}$$

and

$$E_{max}^{(k)} = n_{EV}\pi^{(k)} \cdot \varepsilon_{max} e_b \tag{2.72}$$

$$E_{min}^{(k)} = n_{EV}\pi^{(k)} \cdot \varepsilon_{min} e_b \tag{2.73}$$

$$E_0^{(k)} = E_\pi^{(k+1)}\Big|_{\tilde{S}^{(k)}=0} \ . \tag{2.74}$$

Considering now grid stability issues, they should account not only for the poorly predictable nature of RES, but also for EV mobility needs and uncertainties. Therefore, the two dimensionless coefficients μ and v are appropriately introduced: particularly, μ accounts for reliability of the power delivered by the EV batteries, whereas v represents the share of the power drawn by EV batteries for mobility needs. Based on these considerations, RES power production is upper bounded in accordance with the following relationship:

$$P_{RES}^{(k)} + \left(1-\mu^{(k)}\right)P_s^{(k)} + \left(1-v^{(k)}\right)L_s^{(k)} \le -\left(1-\sigma\right)\cdot\left(L_0^{(k)} + v^{(k)} \cdot L_{s,k}\right) + \frac{P_\Gamma^{(k)}}{\rho} \tag{2.75}$$

where σ is the grid stabilization coefficient, which represents the load share that must be supplied by programmable sources in order to preserve grid stability [60], [68]. Particularly, focusing on the first side of (2.75), the second term is the unreliable power delivered by EV batteries, the third term denoting their deferrable power drawn. Whereas P_Γ is the power deliverable by EV batteries for reserve service, ρ being the dimensionless reserve allocation coefficient (≤ 1). Particularly, P_Γ is upper bounded as follow:

$$P_\Gamma^{(k)} \le P^{(k)} - P_s^{(k)} - \frac{P^{(k)}}{L^{(k)}} \cdot v^{(k)} L_s^{(k)} \ . \tag{2.76}$$

As a result, (2.75) lower bounds the reserve service for a given RES power production as follow:

$$\rho \cdot \left(P_{RES}^{(k)} + \left(1-\mu^{(k)}\right)P_s^{(k)} + \left(1-\sigma\cdot v^{(k)}\right)L_s^{(k)} + \left(1-\sigma\right)L_0^{(k)}\right) \le P_\Gamma^{(k)} \ . \tag{2.77}$$

Consequently, by properly combining (2.76) with (2.77), the upper bound of the RES energy production can be achieved:

$$P_{RES}^{(k)} \le -\left(1 + \frac{1}{\rho} - \mu^{(k)}\right)P_s^{(k)} - \left(1 + \frac{v^{(k)}P^{(k)}}{\rho L^{(k)}} - \sigma v^{(k)}\right)L_s^{(k)} + \frac{P^{(k)}}{\rho} - \left(1-\sigma\right)L_0^{(k)} \ . \tag{2.78}$$

Referring to the (S,P_{RES}) plane, both (2.69) and (2.78) combine to identify the plane region highlighted in Fig. 2.28, whose points satisfy all the constraints previously introduced. Such operating region is bounded by the straight lines r_P and r_L, which correspond to the upper and lower boundaries imposed by (2.69), and by the straight lines r_μ and r_v, both introduced by (2.78). Particularly, when S is positive, it equals P_s, L_s being zero. Consequently, r_μ occurs, which is defined by the following equation:

$$P_{RES}^{(k)} = -\left(1+\frac{1}{\rho}-\mu^{(k)}\right)S^{(k)} + \frac{P^{(k)}}{\rho} - (1-\sigma)L_0^{(k)} \quad . \tag{2.79}$$

The opposite occurs when S is negative, thus (2.78) leads to define r_v as

$$P_{RES}^{(k)} = -\left(1+\frac{\nu^{(k)}P^{(k)}}{\rho L^{(k)}} - \sigma\nu^{(k)}\right)S^{(k)} + \frac{P^{(k)}}{\rho} - (1-\sigma)L_0^{(k)} \quad . \tag{2.80}$$

Hence, it is worth noting that the slopes of r_μ and r_v depend on μ and ν respectively, whose variations lead to r_μ and r_v rotation around the point A, as shown in Fig. 2.28. Particularly, counter clockwise rotation always occurs for r_μ if μ increases, as detectable by (2.79). It means that increased reliability of the power delivered by EV batteries leads to an increased share of the load demand supplied by RES, as expected. Similar considerations can be made for r_v, particularly counter clockwise rotation occurs for increasing ν but on condition that

$$\frac{P^{(k)}}{\rho L^{(k)}} < \sigma \tag{2.81}$$

However, in this case, RES exploitation capability decreases as v increases because EV batteries are less available for providing both deferrable load and reserve service.

In conclusion, it is also worthy of note that the point A does not depend on μ and v, as pointed out by the following equations

$$S^{(k)} = 0 \quad , \quad P_{RES}^{(k)} = \frac{P^{(k)}}{\rho} - (1-\sigma)L_0^{(k)} \quad . \tag{2.82}$$

2.2.2 V2G Management System

The proposed V2G Management System (VMS) is summed up in Fig. 2.29. It aims to define the most suitable V2G operation (S) in real-time in order to enable full RES exploitation, guaranteeing EV mobility needs at the same time. Particularly, the proposed VMS should enable P_{RES} to track a given potential RES power production profile P_{RES}^* as well as possible; in addition, VMS has also to guarantee a suitable tracking of S^*, which is synthesized based on EV mobility requirements.

Hence, referring to the generic k-th sampling time interval, P_{RES} must be chosen in accordance with

$$P_{RES}^{(k)} = min\left\{P_{RES}^{*(k)}, \hat{P}_{RES}^{(k)}\right\} \tag{2.83}$$

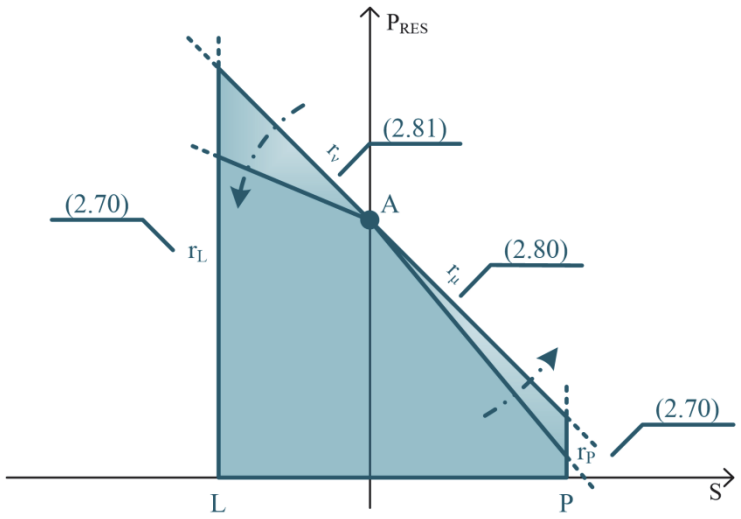

Fig. 2.28 ESS and electric grid constraints representations on the (S,P_{RES}) plane.

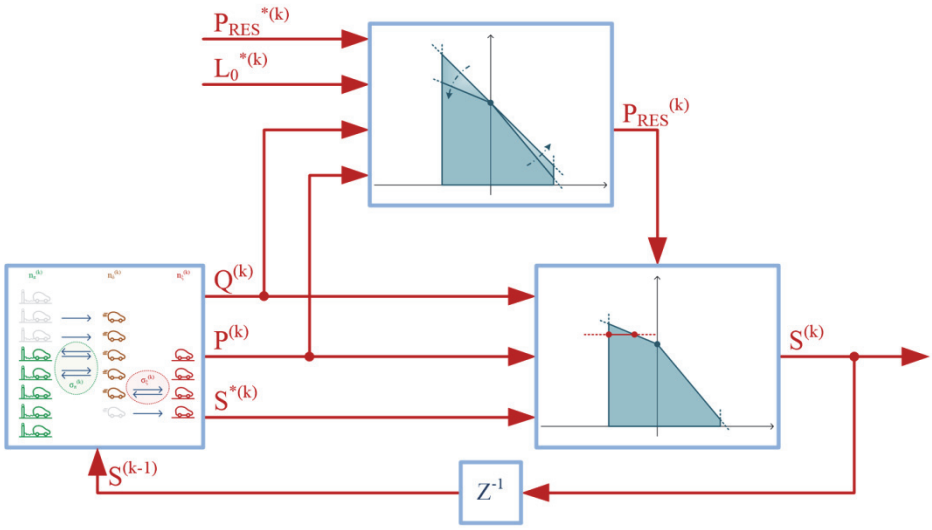

Fig. 2.29 Equivalent block control scheme of the proposed V2G management system.

in which P_{RES}^{*} is the given potential RES power production profile, whereas $\hat{P}_{RES}$ is determined in accordance with (2.78) as

$$\hat{P}_{RES}^{(k)} = -(1-\sigma)L_0^{(k)} + \frac{P^{(k)}}{\rho} + max\left\{-\left(1-\sigma v^{(k)}\right)L^{(k)} - v^{(k)}\frac{P^{(k)}}{\rho}, 0\right\}. \tag{2.84}$$

Particularly, if P_{RES} equals P_{RES}^{*}, it means that all potential RES power production can be delivered to the electric grid. In such cases, like that shown in Fig. 2.30, S can be chosen in accordance with the following constraint

$$S_{min}^{(k)} \le S^{(k)} \le S_{max}^{(k)} \tag{2.85}$$

where S_{min} and S_{max} correspond to the points P_1 and P_2 shown in Fig. 2.30. Therefore, S is chosen as close as possible to S^{*} in order to reinstate EV mobility consumption. Consequently, once both P_{RES} and S are chosen, the power required by reserve service can be easily computed as

$$P_{\Gamma}^{(k)} = min\left\{0, \frac{1}{\rho}\left(P_{RES}^{(k)} + \left(1-\mu^{(k)}\right)P_s^{(k)} + \left(1-\sigma\right)L_0^{(k)} + \left(1-\sigma v^{(k)}\right)L_s^{(k)}\right)\right\} \tag{2.86}$$

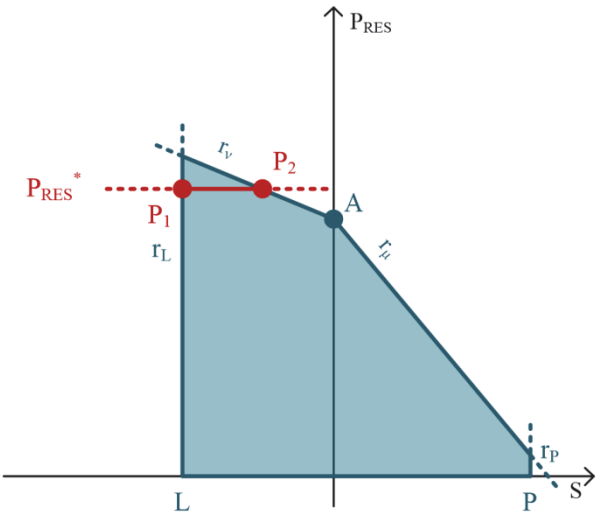

Fig. 2.30 Graphical representation of the proposed V2G management strategy: no RES curtailment.

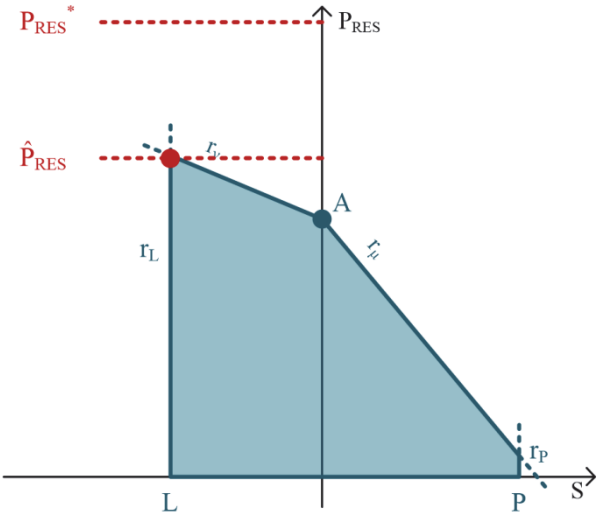

Fig. 2.31 Graphical representation of the proposed V2G management strategy: RES curtailments.

Otherwise, when P_{RES}^{*} exceeds $\hat{P}_{RES}$, it means that potential RES power production cannot be fully exploited and, thus, it is partially wasted. In such cases, like that depicted in Fig. 2.31, S is univocally determined by substituting $\hat{P}_{RES}$ in (2.80), as well as the required reserve service.

Based on the proposed VMS, the potential RES power production can be split as

$$P_{RES}^{*(k)} = P_{RES}^{(k)} + P_{RES,w}^{(k)} \tag{2.87}$$

in which $P_{RES,w}$ denotes the RES power production curtailments due to system constraints. Furthermore, actual RES power production can be expressed as a sum of three terms:

$$P_{RES}^{(k)} = P_{RES,d}^{(k)} + P_{RES,\Gamma}^{(k)} + P_{RES,l}^{(k)} \quad . \tag{2.88}$$

Particularly, $P_{RES,d}$ represents the RES power production delivered to the electric grid directly, $P_{RES,\Gamma}$ is its increase due to the reserve service provided by EV batteries, $P_{RES,l}$ being the RES power production drawn by EVs. In addition, $P_{RES,l}$ can be further expressed as

$$P_{RES,l}^{(k)} = -\frac{\Theta}{\Lambda} \cdot P_{RES,l}^{(k)} + \left(1 + \frac{\Theta}{\Lambda}\right) \cdot P_{RES,l}^{(k)} \tag{2.89}$$

in which Θ is the overall EV consumption within a given time horizon, whereas Λ represents the total energy drawn by EV batteries in the same period of time:

$$\begin{aligned} \Theta &= \frac{\mathrm{T}}{\eta_c} \cdot \sum_k F^{(k)} \\ \Lambda &= \mathrm{T} \cdot \sum_k L_s^{(k)} \quad . \end{aligned} \tag{2.90}$$

Particularly, the first term of (2.89) accounts for EV energy reinstatement coming from RES that is due to EV mobility consumption only. Whereas the second term represents EV battery usage as energy buffer. Consequently, it is possible to define an appropriate performance index Ψ as follow:

$$\Psi = \frac{\sum_k \left(P_{RES,d}^{(k)} + P_{RES,\Gamma}^{(k)} - \frac{\Theta}{\Lambda} \cdot P_{RES,l}^{(k)} + \eta_c \eta_d \cdot \left(1 + \frac{\Theta}{\Lambda}\right) \cdot P_{RES,l}^{(k)} \right)}{\sum_k P_{RES}^{*(k)}} \quad . \tag{2.91}$$

In particular, Ψ consists of the ratio between the RES energy production effectively exploited and the corresponding potential one, the last terms of the numerator being properly weighted in accordance with the energy buffer efficiency. As a consequence, higher Ψ values entail less RES curtailments and, thus, a better RES exploitation. In conclusion, the overall EV batteries usage can be also considered by introducing the index Φ as follow:

$$\Phi = \frac{\eta_c \cdot \Lambda}{n_{EV} \cdot e_b} \quad . \tag{2.92}$$

This index denotes the average number of charging/discharging cycles that are performed by a single EV battery within the given time horizon.

2.2.3 Simulations

In order to validate the proposed VMS, a simulation study is performed by means of the Matlab software package. The Sardinia island is assumed as the reference system because it is characterized by a huge potential RES power production. Particularly, two scenarios have been analysed, as detailed in Table V: the first one refers to the 2009 Electrical Energy Sardinia database, whereas the second one refers to a hypothetical 2020 Sardinia Energy target, which is developed in accordance with the

TABLE V
SIMULATION SCENARIOS

		2009	2020
YEARLY LOAD DEMAND	[TWh]	12	12
WIND POWER PLANTS	[MW]	600	2000
PHOTOVOLTAIC POWER PLANTS	[MW]	40	400
RIVER HYDRO POWER	[MW]	44	44

European Strategic Energy Plan. In both scenarios, the stabilization and the reserve allocation coefficients (σ and ρ) are set constant to 0.9 and 0.1 respectively. Thus, the procedure described in the previous section is recursively employed for different sizes of the EV fleet in terms of number of vehicles (n_{EV}) and their corresponding rated power (p_b). Thus, a variable number of EVs between 10^3 and $2 \cdot 10^4$ is considered, which correspond to 0.1 and 2 per cent of the overall Sardinian car fleet respectively. In addition, p_b varies between 1 kW and 20 kW, in accordance with commercial charging power rates. Differently, e_b is assumed equal to 30 kWh in accordance with the average capacity of commercial EV.

Regarding EV mobility, an average daily distance of 35 km is assumed for each EV, based on which it is possible to determine the corresponding daily energy consumption. This is properly distributed over each sampling time interval in accordance with the statistical time distribution of vehicles on the road, which is already depicted in Fig. 2.25. Furthermore, suitable reference profiles for EV fleet state of charge have been introduced, which account for different daily habits, as shown in Fig. 2.32. In addition, the average state of charge of each EV coming from the π sub-fleet (ε_0) is set to 0.8 in order to guarantee EV mobility needs. Finally, μ and ν coefficients properly vary in accordance with the average state of charge of the π sub-fleet, as shown in Fig. 2.33.

2.2.3.1 *Simulation results*

Referring to the first scenario (2009), the case of 5000 EVs and 2 kW rated power is considered at first, whose simulation results over a generic week is reported in Fig. 2.34 and Fig. 2.35. In particular, focusing on the overall RES power production, it can be seen that $P_{RES,d}$ is slightly predominant over $P_{RES,\Gamma}$, $P_{RES,l}$ being quite negligible. This means that providing reserve service by means of EV batteries leads to an increased RES exploitation than that achievable resorting to energy buffering, preserving EV batteries usage at the same time. Nevertheless, it is worth noting that $P_{RES,w}$ is quite high, denoting that the EV fleet is still undersized in order to fully exploit such a potential RES power

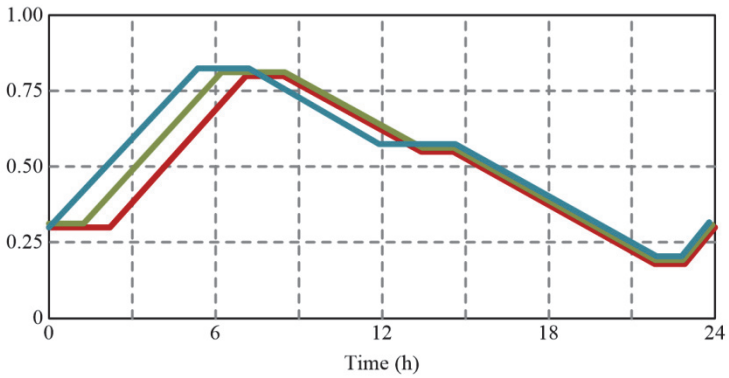

Fig. 2.32 Evolution of reference EV fleet state of charge referred to different days: Monday-Friday (blue), Saturday (green) and Sunday (red).

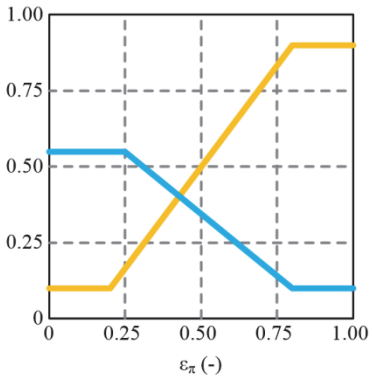

Fig. 2.33 Evolution of μ (orange) and ν (cyan) coefficients.

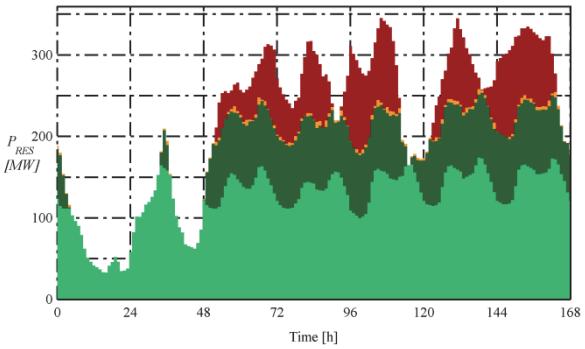

Fig. 2.34 The P_{RES} time evolution at 2009 in case of n_{EV} = 5000 and p_b = 2 kW: $P_{RES,d}$ (light green), $P_{RES,\Gamma}$ (dark green), $P_{RES,l}$ (orange) and $P_{RES,w}$ (red).

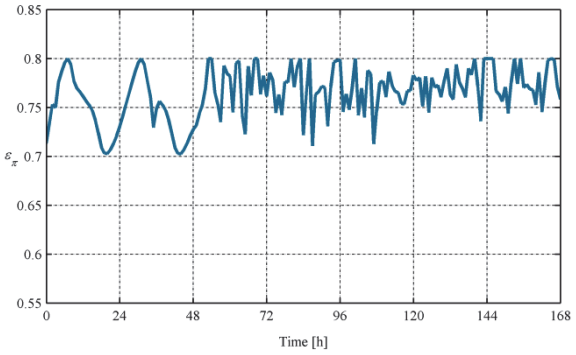

Fig. 2.35 The ε_π time evolution at 2009 in case of n_{EV} = 5000 and p_b = 2 kW.

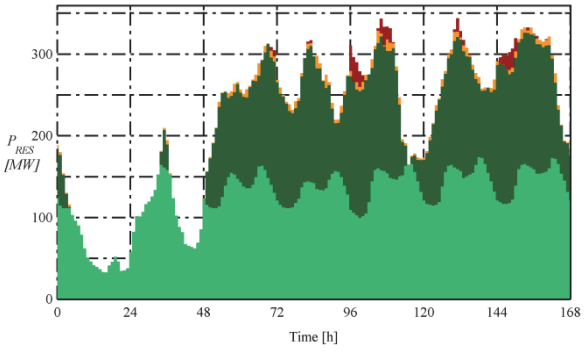

Fig. 2.36 The P_{RES} time evolution at 2009 in case of n_{EV} = 5000 and p_b = 4 kW: $P_{RES,d}$ (light green), $P_{RES,\Gamma}$ (dark green), $P_{RES,l}$ (orange) and $P_{RES,w}$ (red).

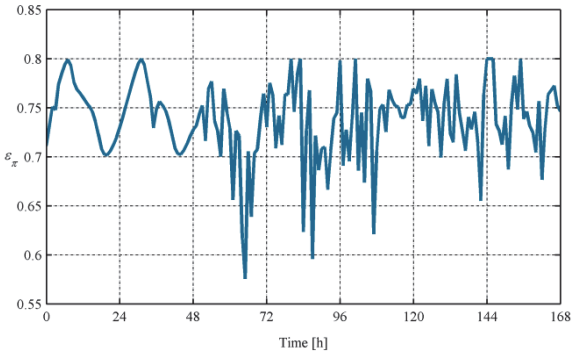

Fig. 2.37 The ε_π time evolution at 2009 in case of n_{EV} = 5000 and p_b = 4 kW.

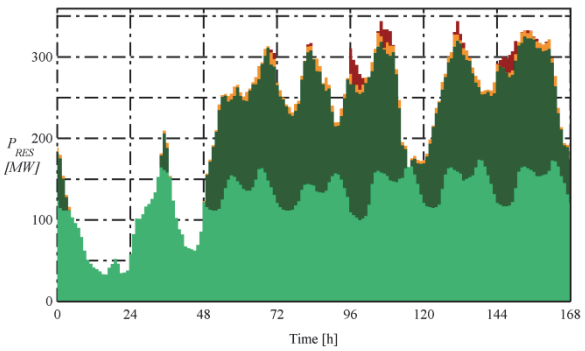

Fig. 2.38 The P_{RES} time evolution at 2009 in case of n_{EV} = 10000 and p_b = 2 kW: $P_{RES,d}$ (light green), $P_{RES,\Gamma}$ (dark green), $P_{RES,l}$ (orange) and $P_{RES,w}$ (red).

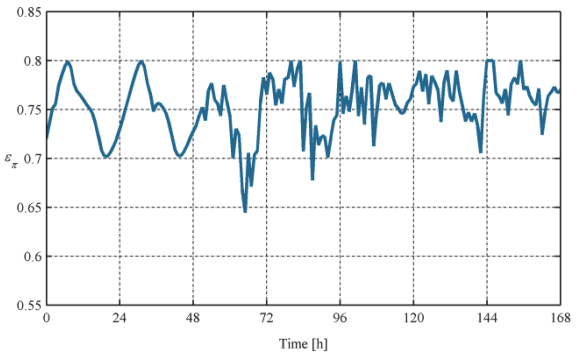

Fig. 2.39 The ε_π time evolution at 2009 in case of n_{EV} = 10000 and p_b = 2 kW.

production. Considering now the corresponding evolution of the average state of charge of the π sub-fleet reported in Fig. 2.35, it can be seen that it stands firmly around 0.75, being not subjected to significant fluctuations. This means that EV mobility is not impaired by V2G operations, although this produces a high frequency ripple on ε_π.

Considering now the same number of EVs but doubling p_b (from 2 to 4 kW), significant improvements in RES exploitation is achieved, as shown in Fig. 2.36. This is mainly due to the increased availability of the reserve service provided by EV batteries, as highlighted by the higher $P_{RES,\Gamma}$ share. The corresponding ε_π evolution is depicted in Fig. 2.37, whose comparison with Fig. 2.35 reveals an increase of the ripple magnitude occurring on ε_π. This phenomenon is due to the increased p_b value, which leads to a more significant energy buffering.

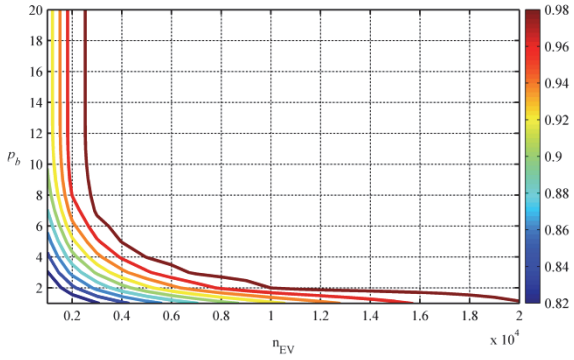

Fig. 2.40 The yearly Ψ loci at 2009 on the (n_{EV},p_b) plane.

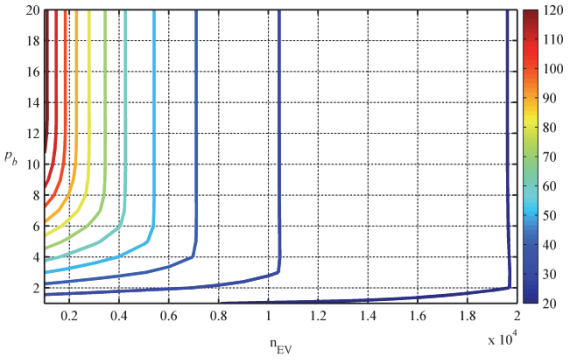

Fig. 2.41 The yearly Φ loci at 2009 on the (n_{EV},p_b) plane.

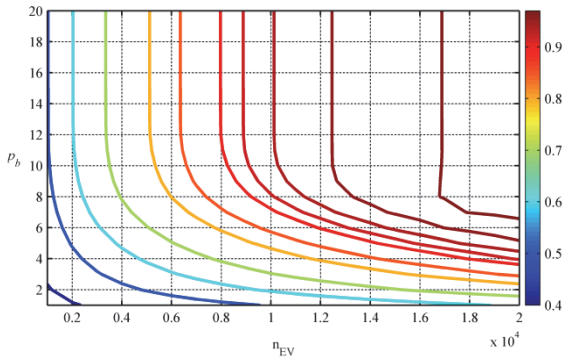

Fig. 2.42 The yearly Ψ loci at 2020 on the (n_{EV},p_b) plane.

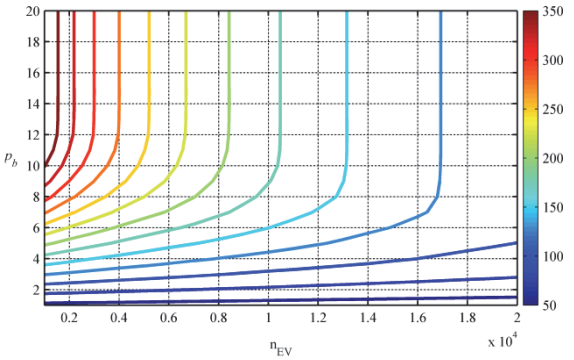

Fig. 2.43 The yearly Φ loci at 2020 on the (n_{EV},p_b) plane.

Very similar results in terms of RES exploitation is achieved by employing 10000 EVs with a rated charging/discharging power of 2 kW, as shown in Fig. 2.38. However, in this case, the ripple occurring on ε_π is much smoother than that achieved in the previous case, as detectable by Fig. 2.39. This is due to both the increased number of EVs and the lower p_b value.

The overall simulation results achieved for the 2009 scenario are depicted in Fig. 2.40 and Fig. 2.41, which refer to the Ψ and Φ loci on the (n_{EV}, p_b) plane respectively. The hyperbolic nature of the Ψ loci reveals that high p_b values entail a relatively small number of EVs in order to achieve a given RES exploitation. The same result can be also obtained resorting to lower p_b and higher n_{EV}. As a result, an unplanned increase of p_b and/or n_{EV} does not always assure better RES exploitations. In addition, referring to the Φ loci depicted in Fig. 2.41, it can be seen that EV battery usage decreases as n_{EV} increases.

Similar remarks can be made for the 2020 scenario, whose corresponding simulation results are depicted in Fig. 2.42 and Fig. 2.43, although some differences occur. These are mainly due to the huge potential RES power production assumed for the 2020 scenario, which leads to lower Ψ and higher Φ values, as expected. The comparison between the two scenarios can be better performed referring to both Table VI and Table VII, which summarize the Ψ and Φ values achieved in correspondence of some (n_{EV}, p_b) pairs of values. The comparison highlights that the proposed VMS allows the exploitation of significant potential RES power production by means of reasonable amounts of EVs, even in case of domestic charging/discharging power rates. Furthermore, such results can be achieved without significantly increasing the charging/discharging cycles.

In conclusion, it can be stated that providing grid services by means of EV batteries allows a better RES exploitation than that achievable by means of energy buffering, preserving EV battery usage at the same time. This corroborates the results achieved in the previous section, which refers to the case of a devoted ESS.

TABLE VI

THE PERFORMANCE INDEX Ψ AT 2009 (2020)

n_{EV} \ p_b	2 kW	4 kW	8 kW	12 kW	20 kW
1000	0.800 (0.395)	0.836 (0.425)	0.890 (0.478)	0.906 (0.496)	0.906 (0.496)
5000	0.915 (0.506)	0.981 (0.612)	0.988 (0.757)	0.988 (0.794)	0.989 (0.795)
10000	0.980 (0.612)	0.988 (0.764)	0.988 (0.918)	0.988 (0.939)	0.989 (0.937)
15000	0.988 (0.696)	0.988 (0.861)	0.989 (0.968)	0.989 (0.968)	0.989 (0.968)
20000	0.988 (0.763)	0.988 (0.923)	0.989 (0.970)	0.989 (0.970)	0.989 (0.970)

TABLE VII

THE EVS BATTERIES EXPLOITATION INDEX Φ AT 2009 (2020)

n_{EV} \ p_b	2 kW	4 kW	8 kW	12 kW	20 kW
1000	74 (138)	116 (219)	159 (361)	175 (424)	175 (426)
5000	73 (130)	99 (191)	105 (278)	105 (305)	105 (306)
10000	72 (124)	83 (170)	83 (223)	83 (233)	83 (233)
15000	71 (118)	76 (155)	76 (188)	76 (189)	76 (189)
20000	70 (114)	72 (143)	72 (161)	72 (162)	72 (162)

2.3 Micro Smart Grids

The previous section has highlighted the improvements of power system performances provided by V2G in terms of RES exploitation. However, a large number of EVs will require the implementation of appropriate management strategies in order to share large power and energy flows properly [39]. In fact, although a single EV is not able to significantly affect the power system operation, large fleets can cause considerable side effects. Consequently, in recent years, many studies have been carried out to assert EV impact on the electric grid. Some of them state that the charging process of a limited amount of EVs will not require significant grid re-arrangements and new power plants [59], [77]–[80]. However, the impact of EV diffusion depends on the features of the electricity network that feeds EVs, together with their charging system. In addition, even if the total impact of the extra load due to EV charging does not negatively affect the production side, the same might not be said for the grid side. In fact, due to the distributed nature of such loads, a number of problems can occur locally, such as overloads or power quality issues [81]. The EV diffusion process could also badly affect the hourly power request, especially regarding the increase of peak electricity demand [77].

All these considerations highlight the need of suitable EV charging laws, which unavoidably have to take into account EV owners' habits. The EV charging strategies reported in the literature can be mainly categorized as follows [77], [70]:

- dumb charging, which consists in fully recharging EVs at rated power whenever they are plugged-in;
- delayed charging, which entails a time delay between the EV plug-in and the start of its recharging in order to minimize electricity costs;
- smart charging, which consists in recharging EVs on the basis of the needs of both the owners and the system operator.

If dumb charging is employed, EV owners are totally free to plug-in and charge their vehicles whenever they want. The other charging strategies can be performed either manually by the user or automatically. In the first case, each EV owner is able to set the way in which the vehicle is recharged. Such choice may be influenced by the system operator by means of appropriate incentive policies, such as dual tariff programs. In the second case, which mostly implies smart charging operation, an active management system with a hierarchical structure establishes the charging profile in order to maximize economic and/or technical benefits for both the electric grid and the owners [78]. Although all the above-mentioned charging strategies can presently be afforded by the system

operator, a large number of EVs will not be able to charge simultaneously and/or at their maximum rate. As a consequence, smart charging laws will be unavoidable [82]. In particular, they will be able not only to avoid negative impact on the electric grid, but also to guarantee its better performances. Regarding this, it has been shown that a smart charging strategy allows integration of a number of EVs several times greater than that achievable by dumb charging [70]. In addition, notwithstanding an increasing number of EVs, nodes voltage and congestion levels do not increase due to the implementation of more sophisticated charging strategies. Moreover, losses can decrease and valleys can be filled at the same time [70].

The effectiveness of smart charging strategies will strongly depend on the charging infrastructures, and their geographical distribution. In fact, appropriate planning of the charging station allocation will increase EV availability for V2G, making it more flexible and reliable at the same time and overcoming the EV drivers "range anxiety" issue. In this context, it has been proved that wide distribution of charging stations, e.g., home, work and shopping centers, will bring more benefits than high power recharge rates [77]. Furthermore, wide distribution of charging stations will extend the EV charging process throughout the day, reducing the peak load by 20%-35%.

Consequently, the increase of the number of EVs will require the development of novel paradigms based on distributed and self-standing power [83]. Among these paradigms, the management of the power system as a cluster of micro-grids (MGs) is considered a promising solution [84]–[88]. In this context, an optimal charging strategy for V2G operation of an EV fleet is presented in this section. In particular, the proposed charging strategy aims to exploit V2G operation in order to increase MGs autonomy, in terms of both time and space energy demand.

2.3.1 Mathematical Modelling

Referring to the schematic representation of a Micro-Grid (MG) shown in Fig. 2.44, it generally consists of both industrial and residential loads, as well as small-scale distributed power plants. In addition, it may be characterized by stationary ESS and/or an EV fleet providing V2G services. Consequently, its power balance can be expressed as

$$P(t)+S(t)+L(t)+G(t)=0 \tag{2.93}$$

in which P and L is MG power production and load demand respectively, S is the power supplied or drawn by the ESSs, G being the power exchanged by the MG with the main grid. In this context, it is

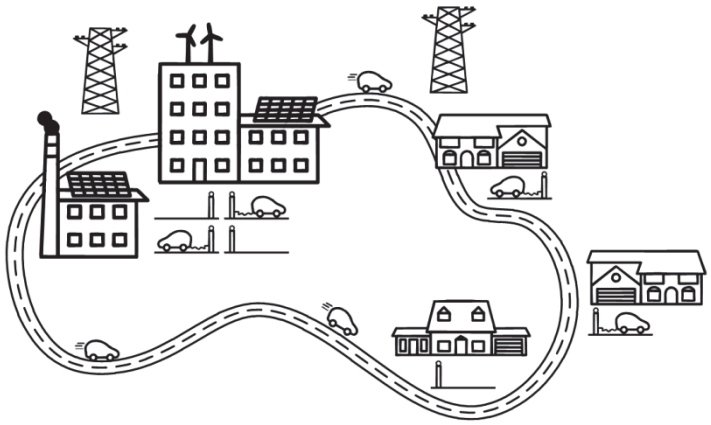

Fig. 2.44 Schematic representation of a micro-grid.

worth noting that the EV fleet acts as a distributed ESS, so its contribution to the MG power generation and/or drawn is accounted by S directly. Similarly, P accounts for both programmable and RES power plants. Based on these considerations, S and P can be further defined as

$$S(t) = S_{ESS}(t) + S_{V2G}(t) \tag{2.94}$$

$$P(t) = P_0(t) + P_{RES}(t) \tag{2.95}$$

where S_{ESS} and S_{V2G} denotes the power exchanged by the ESS and the EV fleet respectively, whereas P_0 and P_{RES} are the power production related to programmable and RES power plants respectively. Furthermore, assuming that the EV fleet is made up of n_{EV} vehicles, S_{V2G} can be split into several terms, each of which denotes the power exchanged by a single EV:

$$S_{V2G}(t) = \sum_{j=1}^{n_{EV}} s_j(t) \ . \tag{2.96}$$

Focusing now on the single j-th EV, the time evolution of the energy stored in its battery can be expressed as

$$\dot{e}_j(t) = -\left(\frac{p_{s,j}(t)}{\eta_d} + \eta_c \cdot l_{s,j}(t) \right) - f_j(t) \tag{2.97}$$

where f is the EV consumption due to its mobility needs, η_d and η_c are the discharging and charging efficiency respectively. Whereas p_s and l_s denote the power delivered to and drawn from the MG, which are defined as

$$p_{s,j}(t) = \frac{1}{2}\left(s_j(t) + \left| s_j(t) \right| \right) \quad , \quad l_{s,j}(t) = \frac{1}{2}\left(s_j(t) - \left| s_j(t) \right| \right) \ . \tag{2.98}$$

The V2G operation provided by the EV fleet is constrained by both energy and power limits occurring on each EV. Thus, still referring to the j-th EV, such limits can be expressed as

$$e_{min,j}(t) \le e_j(t) \le e_{max,j}(t) \tag{2.99}$$

$$l_j(t) \le s_j(t) \le p_j(t) \ . \tag{2.100}$$

Particularly, e_{min} and e_{max} are the minimum and maximum allowable energy level, which are imposed in order to preserve both EV battery rated performance and lifetime, as well as to guarantee an appropriate energy reserve for daily mobility needs. Whereas l and p depend also on the EV charging rate (p_b) as

$$l_j(t) = \begin{cases} -p_b & e_j(t) < e_{max,j} \\ 0 & otherwise \end{cases} \quad , \quad p_j(t) = \begin{cases} \eta_d p_b & e_j(t) > e_{min,j} \\ 0 & otherwise \end{cases} \ . \tag{2.101}$$

2.3.2 Optimal EV Charging Strategy

2.3.2.1 Problem Statement

Referring to Fig. 2.45, a generic micro-grid cluster made up of a number of MGs (n_{MG}) is considered. It is assumed that all its MGs are connected to the main grid and they share the same EV fleet. Consequently, based on (2.93), (2.94) and (2.95), the power balance condition of the i-th MG is expressed as

$$R^{(i)}(t) + S_{V2G}^{(i)}(t) + G^{(i)}(t) = 0 \tag{2.102}$$

where R denotes the residual power of each MG:

$$R^{(i)}(t) = P_0^{(i)}(t) + P_{RES}^{(i)}(t) + S_{ESS}^{(i)}(t) + L^{(i)}(t) \ . \tag{2.103}$$

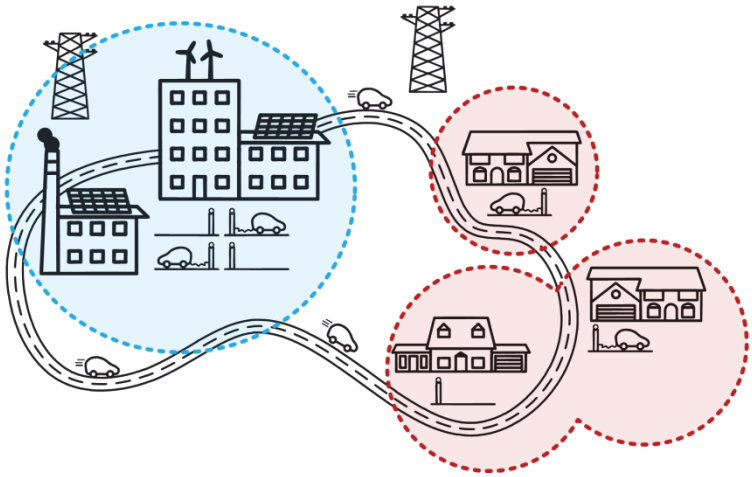

Fig. 2.45 Schematic representation of a generic micro-grid cluster.

Particularly, R can be either positive or negative depending on MG overproduction or underproduction respectively. It is worth noting that such a power unbalance is generally handled by the main grid if no V2G operation is provided. Based on (2.102), the overall power balance of the MG cluster can be thus expressed as

$$\bar{R}(t)+\bar{S}_{V2G}(t)+\bar{G}(t)=0 \tag{2.104}$$

where

$$\bar{R}(t)=\sum_{i}^{n_{MG}} R^{(i)}(t) \quad , \quad \bar{S}_{V2G}(t)=\sum_{i}^{n_{MG}} S_{V2G}^{(i)}(t) \quad , \quad \bar{G}(t)=\sum_{i}^{n_{MG}} G^{(i)}(t) \ . \tag{2.105}$$

Based on (2.104), the MG cluster can be defined fully autonomous if $\bar{G}$ is equal to zero within any given time horizon T_f. It means that the EV fleet should be managed in order to compensate for $\bar{R}$. Consequently, a suitable objective function could be introduced as

$$\bar{\Phi}=\int_{0}^{T_f} \bar{G}^2(t)dt \ . \tag{2.106}$$

Unfortunately, (2.106) does not account for power unbalances of each MG, which may force the main grid to provide an appropriate power supply and/or drawn. Particularly, some G can occur, even if $\bar{G}$ is equal to zero, meaning that the main grid must provide a power buffering service. This drawback could be overcome by introducing a most suitable objective function than (2.106), which is defined as follow:

$$\Phi=\int_{0}^{T_f} \sum_{i}^{n_{MG}} \left(G^{(i)}(t)\right)^2 dt \ . \tag{2.107}$$

As a result, (2.107) accounts not only for MG power unbalances as a whole, but also for their geographical distribution within the MG cluster. Consequently, its minimization leads to a more autonomous MG cluster in terms of both time and space than that achievable by minimizing (2.106). In this context, V2G represents an ideal solution, because an EV fleet is able to compensate for power unbalances in different places due to its itinerant nature.

2.3.2.2 Problem Formulation

In order to minimize (2.107), the Optimal Control Theory is employed. Consequently, in order to well identify input and state variables of the MG cluster, (2.102) is better expressed as

$$G^{(i)} = -\left(R^{(i)} + S_{V2G}^{(i)}\right) \tag{2.108}$$

in which S_{V2G} can be expressed in accordance with (2.96) as

$$S_{V2G}^{(i)} = \sum_{j=1}^{n_{EV}} s_j^{(i)} \quad . \tag{2.109}$$

In addition, it is worth noting that each EV can be connected to only one MG at a time; alternatively, it can be on the road. Consequently, the following equation can be introduced

$$s_j = \sum_{i=1}^{n_{MG}} s_j^{(i)} \quad . \tag{2.110}$$

Based on (2.110), it can be stated that each input variable consists of the power exchanged by the j-th EV with the i-th MG. Whereas the generic state variable corresponds to the energy level of the j-th EV, which can be expressed in accordance with both (2.97) and (2.98) as

$$\dot{e}_j = -\alpha \cdot \sum_{i=1}^{n_{MG}} s_j^{(i)} - \beta \cdot \sum_{i=1}^{n_{MG}} \left| s_j^{(i)} \right| - f_j \tag{2.111}$$

in which

$$\alpha = \frac{1}{2}\left(\frac{1}{\eta_d} + \eta_c\right) \quad , \quad \beta = \frac{1}{2}\left(\frac{1}{\eta_d} - \eta_c\right) . \tag{2.112}$$

Once input and state variables are identified, the corresponding operating constraints must be considered. Particularly, based on (2.100) and (2.101), input constraints can be expressed as

$$l_j^{(i)} \le s_j^{(i)} \le p_j^{(i)} \tag{2.113}$$

in which

$$l_j^{(i)} = \begin{cases} -p_b^{(i)} & e_j < e_{max,j} \\ 0 & otherwise \end{cases} \quad , \quad p_j^{(i)} = \begin{cases} \eta_d p_b^{(i)} & e_j > e_{min,j} \\ 0 & otherwise \end{cases} . \tag{2.114}$$

Whereas state constraints can be determined based on (2.99), but expressed as

$$c_j \le 0 \quad , \quad c_j = \left(e_j - e_{min,j}\right)\left(e_j - e_{max,j}\right) . \tag{2.115}$$

Based on all these considerations, it is now possible to introduce both the Hamiltonian and the augmented Hamiltonian functions, which are defined respectively as

$$H = \sum_{i}^{n_{MG}} \left(G^{(i)}(t)\right)^2 + \sum_{j}^{n_{EV}} \lambda_j \dot{e}_j \tag{2.116}$$

$$\bar{H} = H + \sum_{j}^{n_{EV}} \mu_j \dot{c}_j \tag{2.117}$$

in which λ and μ are appropriate Lagrange multipliers and

$$\dot{c}_j = -\left(2e_j - e_{min,j} - e_{max,j}\right) \cdot \left(\alpha \cdot \sum_{i=1}^{n_{MG}} s_j^{(i)} + \beta \cdot \sum_{i=1}^{n_{MG}} \left| s_j^{(i)} \right| + f_j \right) . \tag{2.118}$$

Particularly, λ must satisfy the following equation

$$\dot{\lambda}_j = \begin{cases} -\dfrac{\partial H}{\partial e_j} \; for \; c_j < 0 \\ -\dfrac{\partial \bar{H}}{\partial e_j} \; for \; c_j = 0 \end{cases} \quad , \quad \lambda_j\left(T_f\right) = k_j \tag{2.119}$$

whereas μ can be determined in accordance with

$$\lambda_j\left(t_0^-\right) = \lambda_j\left(t_0^+\right) + \frac{\partial}{\partial e_j}\sum_j^{n_{EV}} \mu_j \dot{c}_j\left(t_0\right) \; . \tag{2.120}$$

Particularly, referring to (2.119), k should be generally equal to zero if the final state is not constrained. Whereas t_0 introduced in (2.120) denotes a switching time instant, in correspondence of which at least one c_j equals zero.

In conclusion, the optimal values of input variables can be synthesized in accordance with the Pontryagin's Minimum Principle, which requires that the Hamiltonian function is minimized within the input boundaries:

$$s_j^{(i)} = s_j^{(i)*} \quad , \quad H\left(s_j^{(i)*}\right) = min\left\{H\left(s_j^{(i)}\right)\right\}\Big|_{l_j^{(i)} \le s_j^{(i)} \le p_j^{(i)}} \; . \tag{2.121}$$

2.3.2.3 Case Study

The proposed OCS has been synthesized referring to a simple case, i.e. an MG cluster made up of two MGs and characterized by a single EV only, as shown in Fig. 2.46. Particularly, the W MG is assumed to be an industrial/commercial area, whereas the H MG consists of a single house. Therefore, (2.107) becomes

$$\Phi = \int_0^{T_f} \left(\left(G^{(W)}\right)^2 + \left(G^{(H)}\right)^2\right) dt \tag{2.122}$$

where, due to the presence of only one EV, G can be further expressed as

$$G^{(W)} = -\left(R^{(W)} + s^{(W)}\right) \tag{2.123}$$

$$G^{(H)} = -\left(R^{(H)} + s^{(H)}\right) \; . \tag{2.124}$$

In addition to W and H, another virtual MG can be introduced (R), which accounts for the EV on the road. Consequently, EV power exchange and energy level can be expressed as

$$s = s^{(W)} + s^{(H)} + s^{(R)} \tag{2.125}$$

$$\dot{e} = -\alpha \cdot \left(s^{(W)} + s^{(H)} + s^{(R)}\right) - \beta \cdot \left(\left|s^{(W)}\right| + \left|s^{(H)}\right| + \left|s^{(R)}\right|\right) - f \; . \tag{2.126}$$

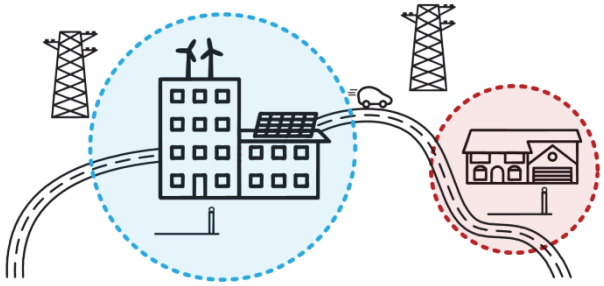

Fig. 2.46 Schematic representation of the case study: W MG (cyan) and H MG (red).

These are constrained respectively as

$$l^{(W)} \le s^{(W)} \le p^{(W)} \quad , \quad l^{(H)} \le s^{(H)} \le p^{(H)} \quad , \quad s^{(R)} = 0 \tag{2.127}$$

$$c \le 0 \quad , \quad c = \left(e - e_{min}\right)\left(e - e_{max}\right) . \tag{2.128}$$

In particular, when the EV is on the road, its power exchange is always equal to zero, as stated by (2.127). Therefore, over such operating conditions, no control action can be performed. However, since (2.128) must be always satisfied, this requires that the proposed OCS guarantees an appropriate energy level at the start of each trip in order to satisfy EV mobility needs, without violating (2.128).

Based on these considerations, the time horizon T_f can be split in a number of time intervals, depending on which micro-grid hosts the EV, as shown in Fig. 2.47. Furthermore, each H or W time intervals can be further split into two or more sub-intervals based on (2.128). Particularly, OFF sub-intervals are characterized by a constant EV energy level that must be equal to either its maximum or minimum value. Consequently, no power can be exchanged with the hosting MG over such periods of time, the EV being idle. Otherwise, ON sub-intervals occur, in correspondence of which the EV is able to provide V2G operation to the hosting MG. It is worth noting that such classification is not necessary for R intervals due to the mobility consumption f, which surely differs from zero. In addition, it is also worthy of note that ON and OFF sub-intervals arise from the application of the Optimal Control Theory, which identifies the most appropriate switching time instants by means of (2.120) in order to minimize Φ throughout T_f.

Thus, over the generic ON sub-interval, only the Hamiltonian function must be considered:

$$H = \left(G^{(W)}\right)^2 + \left(G^{(H)}\right)^2 + \lambda \dot{e} \tag{2.129}$$

where

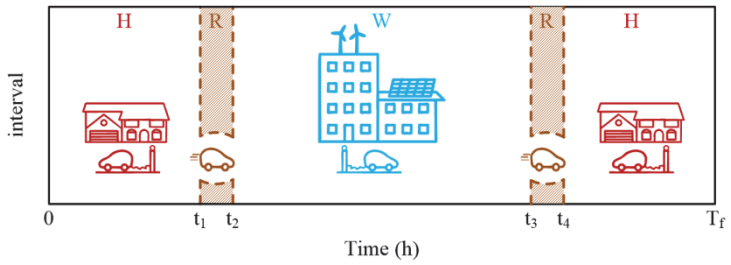

Fig. 2.47 H, W and R time intervals.

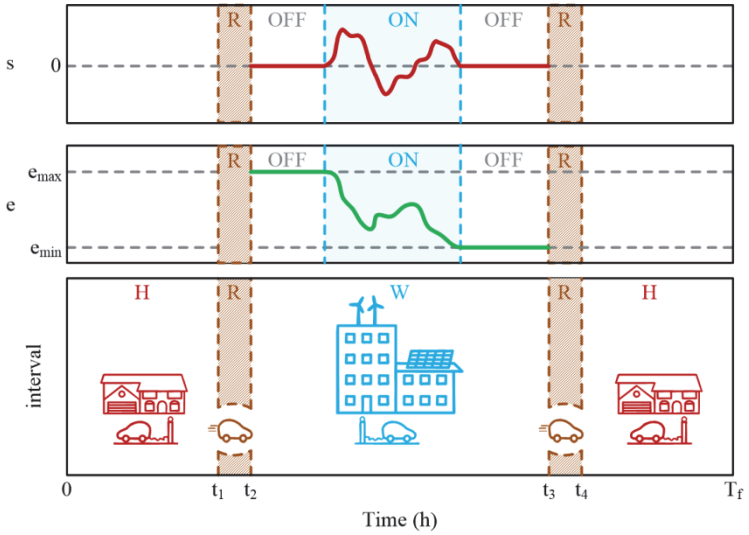

Fig. 2.48 ON and OFF time intervals.

$$\dot{e} = -\alpha \cdot s^{(W,H)} - \beta \cdot \left| s^{(W,H)} \right| \quad , \quad l^{(W,H)} \le s^{(W,H)} \le p^{(W,H)} \quad . \tag{2.130}$$

In addition:

$$c < 0 \quad \Rightarrow \quad \dot{\lambda} = 0 \quad \Rightarrow \quad \lambda = \Lambda = cost. \; . \tag{2.131}$$

Therefore, in order to minimize *H*, its partial derivatives with respect to *s* is considered:

$$\frac{\partial H}{\partial s^{(W,H)}} = 2\left(R^{(W,H)} + s^{(W,H)} \right) - \Lambda \cdot \left(\alpha + \sigma^{(W,H)} \beta \right) \quad , \quad \sigma^{(W,H)} = sign\left(s^{(W,H)} \right) \tag{2.132}$$

As a consequence, the optimal input profiles should be chosen in accordance with

$$s^{(W,H)} = max\left\{ l^{(W,H)}, min\left\{ s_0^{(W,H)}, p^{(W,H)} \right\} \right\} \tag{2.133}$$

in which

$$s_0^{(W,H)} = -R^{(W,H)} + \frac{\Lambda}{2} \cdot \left(\alpha + \sigma_0^{(W,H)} \beta \right) \tag{2.134}$$

It is worth noting that Λ should be ideally equal to zero, leading to compensate the residual power of the MG hosting the EV at the maximum extent. Unfortunately, this hardly occurs without violating (2.128). Therefore, as soon as *c* equals zero at t_0, an OFF sub-interval occurs, during which:

$$c = 0 \quad \Rightarrow \quad e = e_{min,max} = cost \quad \Rightarrow \quad \dot{e} = 0 \quad \Rightarrow \quad s^{(W,H)} = 0 \quad . \tag{2.135}$$

Consequently

$$\bar{H} = H = \left(R^{(W)} \right)^2 + \left(R^{(H)} \right)^2 \tag{2.136}$$

$$\dot{\lambda} = 0 \quad \Rightarrow \quad \lambda = \bar{\Lambda} = cost. \; . \tag{2.137}$$

Therefore, considering (2.120), the following result is achieved

$$\Lambda = \bar{\Lambda} \quad , \quad s^{(W,H)}\Big|_{t0} = 0 \quad , \quad e\big|_{t0} = e_{min,max} \quad . \tag{2.138}$$

Thus, based on of (2.138), it is possible to compute both Λ and t_0.

Finally, during a generic R time interval:

$$s^{(R)} = 0 \quad \Rightarrow \quad \dot{e} = -f \tag{2.139}$$

$$c < 0 \quad \Rightarrow \quad \dot{\lambda} = 0 \quad \Rightarrow \quad \lambda = \Lambda^{(R)} = cost. \; . \tag{2.140}$$

Consequently:

$$H = \left(R^{(W)} \right)^2 + \left(R^{(H)} \right)^2 - \Lambda^{(R)} f \quad . \tag{2.141}$$

It is worth noting that, in this case, Λ is undetermined. However, such a value is unnecessary because no control action has to be synthesized, i.e. *s* is always equal to zero. Therefore, if (2.128) is satisfied, no further actions are required. Otherwise, the Λ value determined in the previous sub-intervals must be adapted in order to guarantee an adequate energy level for the EV trip, as already stated before.

2.3.2.4 Performance Indexes

In order to evaluate the effectiveness of the proposed OCS in mitigating the energy exchange with the main grid, it is possible to introduce the following performance indexes:

$$\Psi = \sqrt{\frac{\Phi}{T_f}} \tag{2.142}$$

$$\Gamma_{+}^{(i)} = \frac{1}{2}\int_{0}^{T_f}\left(G^{(i)} + \left|G^{(i)}\right|\right)dt \tag{2.143}$$

$$\Gamma_{-}^{(i)} = \frac{1}{2}\int_{0}^{T_f}\left(G^{(i)} - \left|G^{(i)}\right|\right)dt \ . \tag{2.144}$$

Particularly, (2.143) and (2.144) define the energy delivered and drawn by the main grid to/from the i-th MG respectively. Consequently, each MG gross and net energy exchange can be expressed as:

$$\Delta\Gamma^{(i)} = \int_{0}^{T_f}\left|G^{(i)}\right|dt = \Gamma_{+}^{(i)} - \Gamma_{-}^{(i)} \tag{2.145}$$

$$\Sigma\Gamma^{(i)} = \int_{0}^{T_f} G^{(i)}dt = \Gamma_{+}^{(i)} + \Gamma_{-}^{(i)} \ . \tag{2.146}$$

As a result, (2.145) allows the computation of the overall energy flowing through the connections between each MG and the main grid. Consequently, this index is particularly suitable for measuring how much the main grid acts as an energy buffer towards each MG. Whereas MG autonomy in terms of energy consumption can be better estimated by means of (2.146).

Similar considerations can be made for the energy exchange between each MG and the EV, leading to define the following indexes:

$$\Omega_{+}^{(i)} = \frac{1}{2}\int_{0}^{T_f}\left(s^{(i)} + \left|s^{(i)}\right|\right)dt \tag{2.147}$$

$$\Omega_{-}^{(i)} = \frac{1}{2}\int_{0}^{T_f}\left(s^{(i)} - \left|s^{(i)}\right|\right)dt \tag{2.148}$$

$$\Delta\Omega^{(i)} = \int_{0}^{T_f}\left|s^{(i)}\right|dt = \Omega_{+}^{(i)} - \Omega_{-}^{(i)} \tag{2.149}$$

$$\Sigma\Omega^{(i)} = \int_{0}^{T_f} s^{(i)}dt = \Omega_{+}^{(i)} + \Omega_{-}^{(i)} \tag{2.150}$$

Particularly, assuming that no V2G services are provided, Ω_{+} is zero, whereas Ω_{-} consists of EV consumption reinstatement due to its mobility needs.

2.3.3 Simulations

The proposed OCS is implemented in the Matlab environment referring to the simple case study previously analysed. Thus, firstly referring to the W MG, both micro-wind and PV power plants have been considered, which are characterized by 3 kW and 10 kW rated power respectively. Whereas no power plants have been considered for the H MG, its residual power being thus equal to its load demand. Particularly, the peak load demand of the H MG is set to 6 kW, whereas that of the W MG is 15 kW. Regarding the EV, its main parameters are summarized in Table VIII. Particularly, an EV battery capacity of 30 kWh is considered, whose operating range should be limited to increase its

TABLE VIII
EV MAIN PARAMETERS

	pb	e_b	e_{min}	e_{max}	η_c	η_d
VALUE	3	30	6	24	0.90	0.85
UNITS	[kW]	[kWh]	[kWh]	[kWh]	[-]	[-]

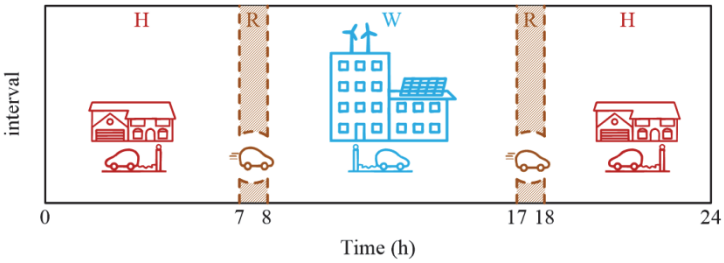

Fig. 2.49 EV daily habits over a working day.

lifetime. Thus, e_{min} and e_{max} are set to 20% and 80% of the rated capacity respectively. In addition, the rated charging/discharging power is set to 3 kW for both W and H, whereas the overall charging and discharging efficiency are set to 0.90 and 0.85 respectively. Finally, the EV consumption is set to 0.2 kWh/km.

Simulations are performed assuming a time horizon equal to 24 hours, whereas the sampling time interval is chosen equal to 1 minute. Consequently, EV daily habits over a generic working day is considered and shown in Fig. 2.49. Hence, two different scenarios have been introduced, each of which refers to different RES power productions. Particularly, the first scenario (S-1) refers to a sunny and poorly windy day, which corresponds to a significant RES power production profile, as shown in Fig. 2.50. Whereas the second scenario (S-2) is characterized by a much lower MG power production profile, as frequently occurs during fall or winter months. Each scenario also refers to its own load demand profiles, which are depicted in Fig. 2.51 and Fig. 2.52 for W and H MG respectively.

In order to test the effectiveness of the proposed OCS, its performances are compared to those achievable by means of an EV Dumb Charging Strategy (DCS). This consists of recharging the EV battery at its rated power as soon as it is plugged into the socket, until e_{max} is reached. Whereas the initial and final energy levels are imposed equal to 50% of the rated capacity in order to avoid high average states of charge, which badly affect the battery lifetime [89].

2.3.3.1 Simulations Results

Simulation results firstly refer to the S-1 scenario, whose corresponding residual power profiles are depicted in Fig. 2.53. In particular, the $R^{(W)}$ evolution highlights that overproduction occurs in the middle of the day due to an excess RES power production compared to the W load demand. Whereas $R^{(H)}$ is always negative because it perfectly matches the H load demand, no power plants being considered for the H MG.

Simulation results achieved by employing the DCS are depicted in Fig. 2.54. It can be seen that only two charging periods occur, each of which immediately after the end of the corresponding trip. Consequently, this leads to increased power drawn of W and H MG respectively. Referring to the first charging period, it can be seen that DCS does not exploit W overproduction properly, it mostly occurring later in the day. Similar consideration can be made to the second charging periods, which unsuitably increases the peak of the H load demand. These results reveal the poor performances achievable by DCS in compensating for MG residual powers, as expected.

Much better results are achieved by means of the proposed OCS, as highlighted by Fig. 2.55. It shows that charging and discharging periods alternatively occur in accordance with V2G operations. Particularly, EV battery discharges at first in order to compensate for H residual power; this is performed optimally accounting for the incoming trip, at the end of which the energy level is almost equal to e_{min}. It is worth noting that such operation also takes into account W residual power, which is mitigated shortly as the EV plugs at W, until e_{min} is reached. The subsequent EV charging is appropriately delayed in order to exploit W overproduction at the maximum extent, in accordance

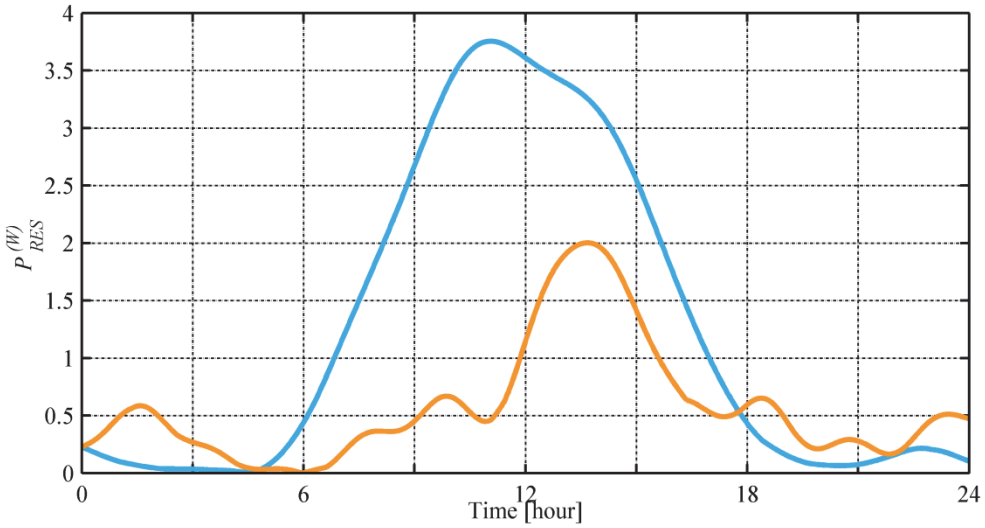

Fig. 2.50 The forecasted daily evolution of $P_{RES}^{(W)}$ over S-1 (cyan) and S-2 (orange), in pu with respect to the EV rated power.

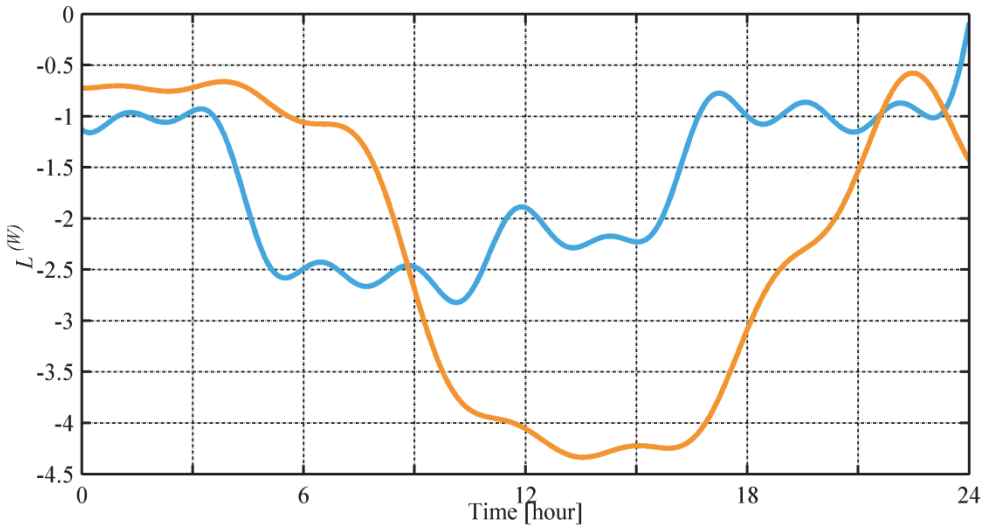

Fig. 2.51 The forecasted daily evolution of $L^{(W)}$ over S-1 (cyan) and S-2 (orange), in pu with respect to the EV rated power.

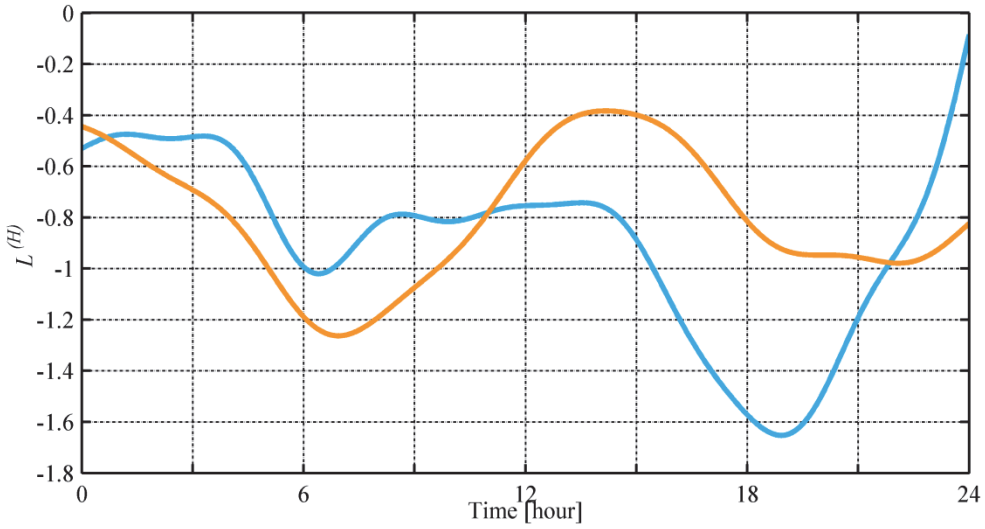

Fig. 2.52 The forecasted daily evolution of $L^{(H)}$ over S-1 (cyan) and S-2 (orange), in pu with respect to the EV rated power.

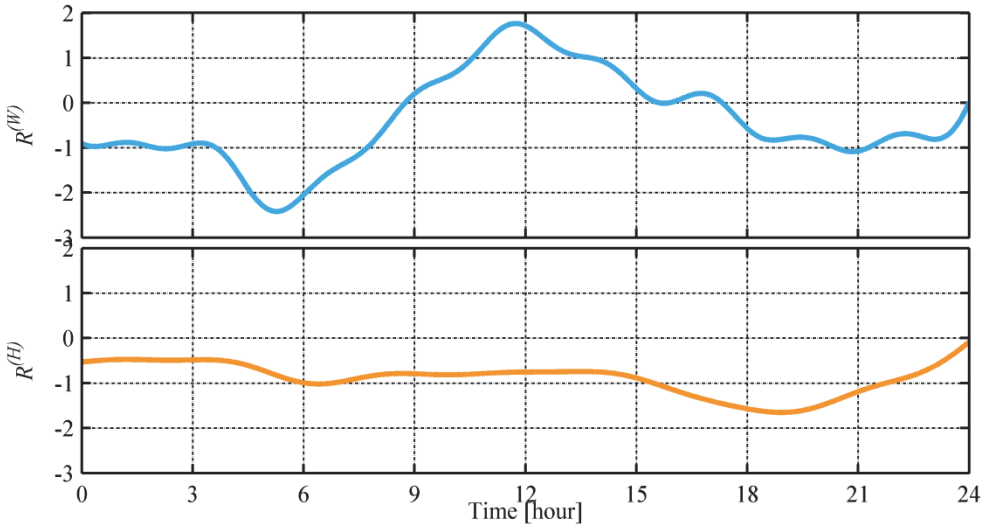

Fig. 2.53 The daily evolution of residual powers referred to S-1: $R^{(W)}$ (cyan) and $R^{(H)}$ (orange), in pu with respect to the EV rated power.

with EV power and energy constraints. Particularly, it is worth noting that the EV battery fully recharges even beyond W overproduction, which cannot be fully exploited due to the power limitation constraint. Such operation is required by the subsequent trip and H time interval, in correspondence of which the EV battery acts as an energy buffer in order to optimally compensate for the H residual power.

The overall simulation results achieved over S-1 are summarized in Table IX. Particularly, referring to the index Ψ, it can be seen that the proposed OCS enables a significant reduction compared to case 0 (no EV). This is due to the optimal distribution of EV charging throughout the day, which decreases peak power exchanged by both W and H MGs with the main grid. Differently, DCS leads to an increased Ψ compared to case 0; this occurs mainly because DCS is unable to provide V2G services, i.e. no discharging is allowed. In addition, the uncontrolled EV charging at rated power increases peak power demand, especially at H, leading to quite poor performances.

The effectiveness of the proposed OCS is also corroborated by the energy indexes reported in Table IX. Firstly referring to the case 0, it can be seen that some overproduction occurs (about 20 kWh), which, however, is much less than the energy drawn by the MG cluster (about 110 kWh). Consequently, the net energy drawn is about 90 kWh, whereas the gross energy exchange is quite higher, it being about 130 kWh. It means that the main grid acts as an energy buffer, drawing and then delivering back the MG cluster overproduction during the day. This phenomenon less occurs when the single EV is introduced. Particularly, over DCS, only a minor exploitation of MG overproduction is achieved, benefits coming mainly from the increased MG energy drawn due to EV mobility consumption. Much better results are achieved by the proposed OCS, which enables an almost full exploitation of MG overproduction. Consequently, net and gross energy exchanges are quite similar to each other, revealing a reduced need of energy buffering provided by the main grid. Such a service is successfully provided by the EV, leading to a slight increase in the overall MG energy drawn.

TABLE IX
OVERALL PERFORMANCE INDEXES FOR SCENARIO S-1

		Ψ [kW_{eq}]	Γ_+ [kWh]	Γ_- [kWh]	$\Sigma\Gamma$ [kWh]	$\Delta\Gamma$ [kWh]	Ω_+ [kWh]	Ω_- [kWh]	$\Delta\Omega$ [kWh]	$\Sigma\Omega$ [kWh]	Losses [kWh]
OVERALL	NO EV	4.37	112.7	-19.5	93.2	132.2	-	-	-	-	-
	DCS	4.86	125.5	-16.6	108.9	142.1	0	-15.7	15.7	-15.7	-3.7
	OCS	3.95	114.1	-3.8	110.3	117.9	4.8	-22.0	26.8	-17.2	-5.2

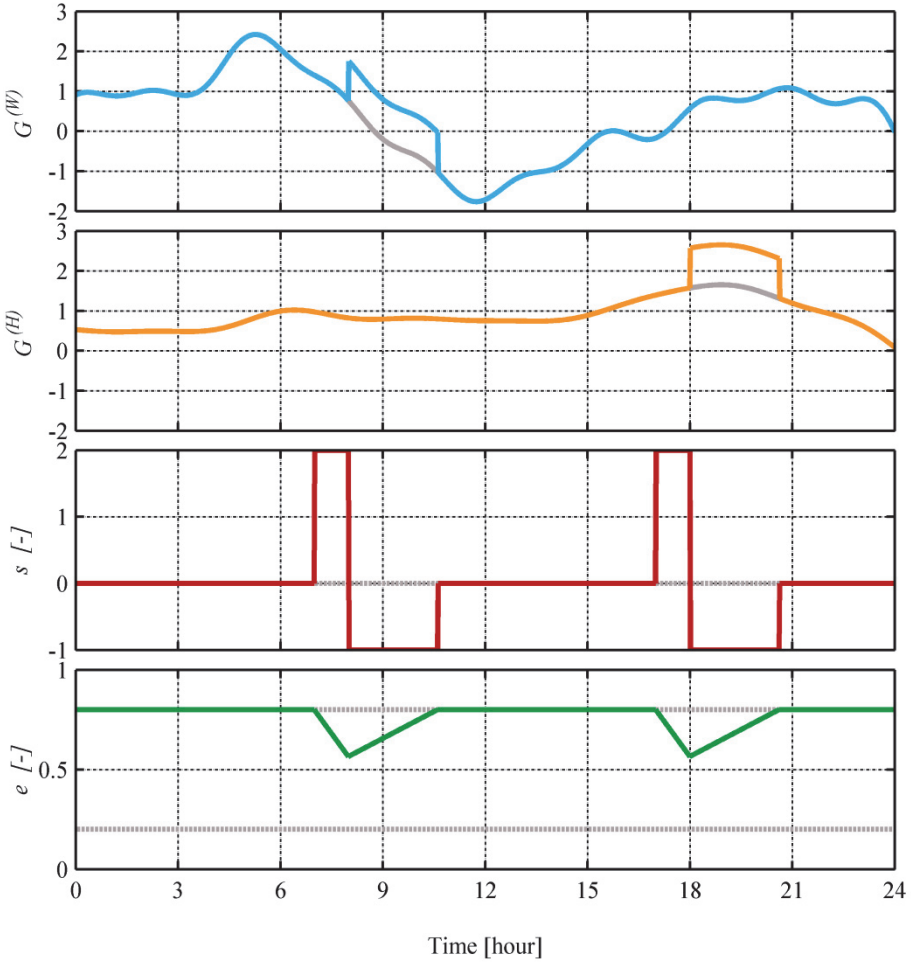

Fig. 2.54 DCS overall results achieved over S-1: no EV (grey), $G^{(W)}$ (cyan), $G^{(H)}$ (orange), s (red), e (green), in pu with respect to the EV rated power and capacity.

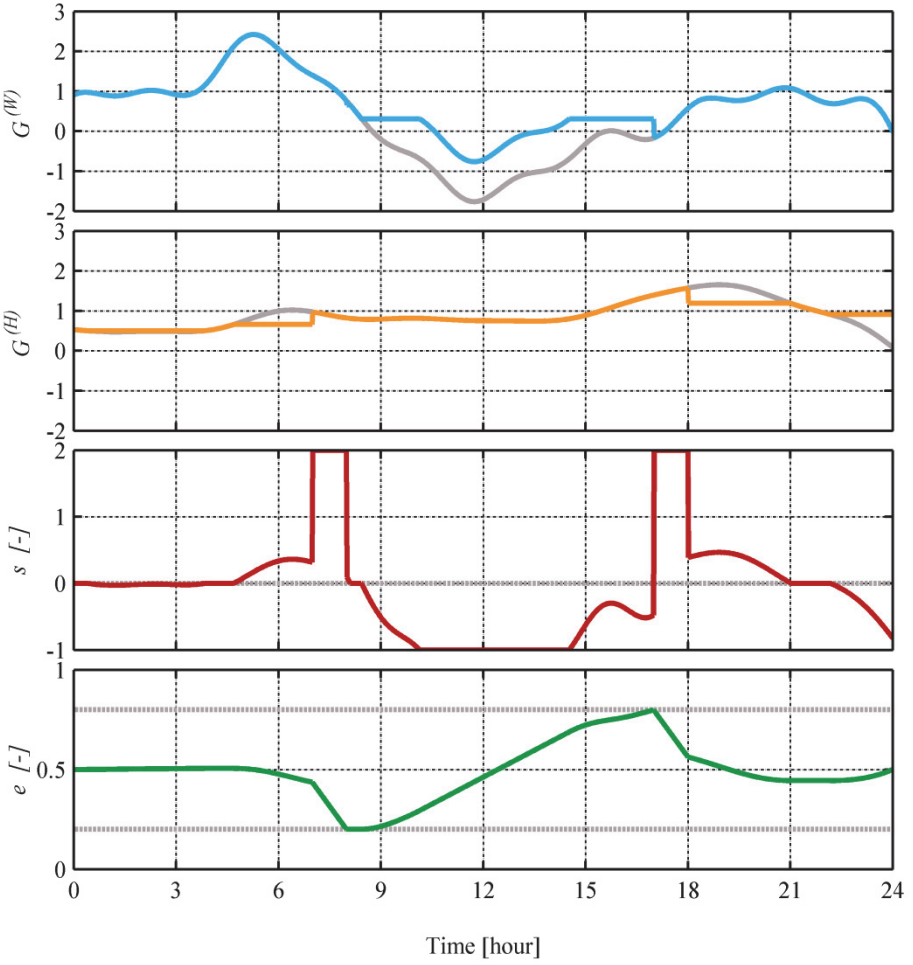

Fig. 2.55 OCS overall results achieved over S-1: no EV (grey), $G^{(W)}$ (cyan), $G^{(H)}$ (orange), s (red), e (green), in pu with respect to the EV rated power and capacity.

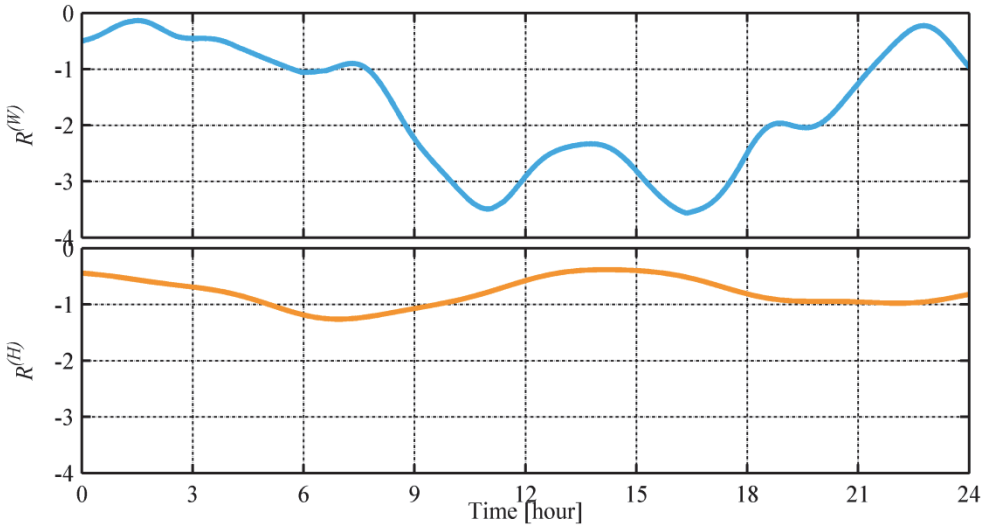

Fig. 2.56 The daily evolution of residual powers referred to S-2: $R^{(W)}$ (cyan) and $R^{(H)}$ (orange), in pu with respect to the EV rated power.

Different considerations can be made for the second scenario (S-2), as highlighted by Fig. 2.56 through Fig. 2.58, as well as by Table X. Particularly, no MG overproduction occurs over S-2, as easily detectable in Fig. 2.56. However, this does not affect DCS performance significantly because it inherently poorly exploits MG overproduction, as stated in the previous case. Consequently, an increase in peak load demand at both W and H occurs, as shown in Fig. 2.57. Differently, the proposed OCS span the EV charging optimally in order to reduce the W peak load demand as depicted in Fig. 2.58. Such a peak shaving is achieved resorting to an appropriate energy buffering which requires increased peaks of H load demand. However, these are still lower than the W ones, revealing the effectiveness of the proposed OCS.

Such performances are further corroborated referring to Table X. Particularly, increased Ψ values are achieved over both DCS and OCS compared to case 0, as well as both net and gross energy exchange. This is due to the increased MG energy drawn caused by the EV mobility consumption. However, it is worth noting that the proposed OCS is able to manage EV charging optimally in order to minimize its impact on the power drawn of the MG cluster and, thus, on the main grid. Consequently, the OCS makes the second scenario comparable in terms of power exchange with the same without EV.

In conclusion, it can be stated that the proposed OCS allows the optimal management of an EV fleet in providing V2G services within a given MG cluster. Particularly, it has been shown that EV mobility can be optimally exploited in terms of both time and space, mitigating EV charging issues and, eventually, reducing main grid support actions.

TABLE X
OVERALL PERFORMANCE INDEXES FOR SCENARIO S-2

		Ψ [kW_{eq}]	Γ_+ [kWh]	Γ_- [kWh]	$\Sigma\Gamma$ [kWh]	$\Delta\Gamma$ [kWh]	Ω_+ [kWh]	Ω_- [kWh]	$\Delta\Omega$ [kWh]	$\Sigma\Omega$ [kWh]	Losses [kWh]
OVERALL	NO EV	6.58	179.5	0	179.5	179.5	-	-	-	-	-
	DCS	7.20	195.2	0	195.2	195.2	0	-15.7	15.7	15.7	-3.7
	OCS	6.77	196.6	0	196.6	196.6	4.8	-21.6	26.1	-17.1	-5.1

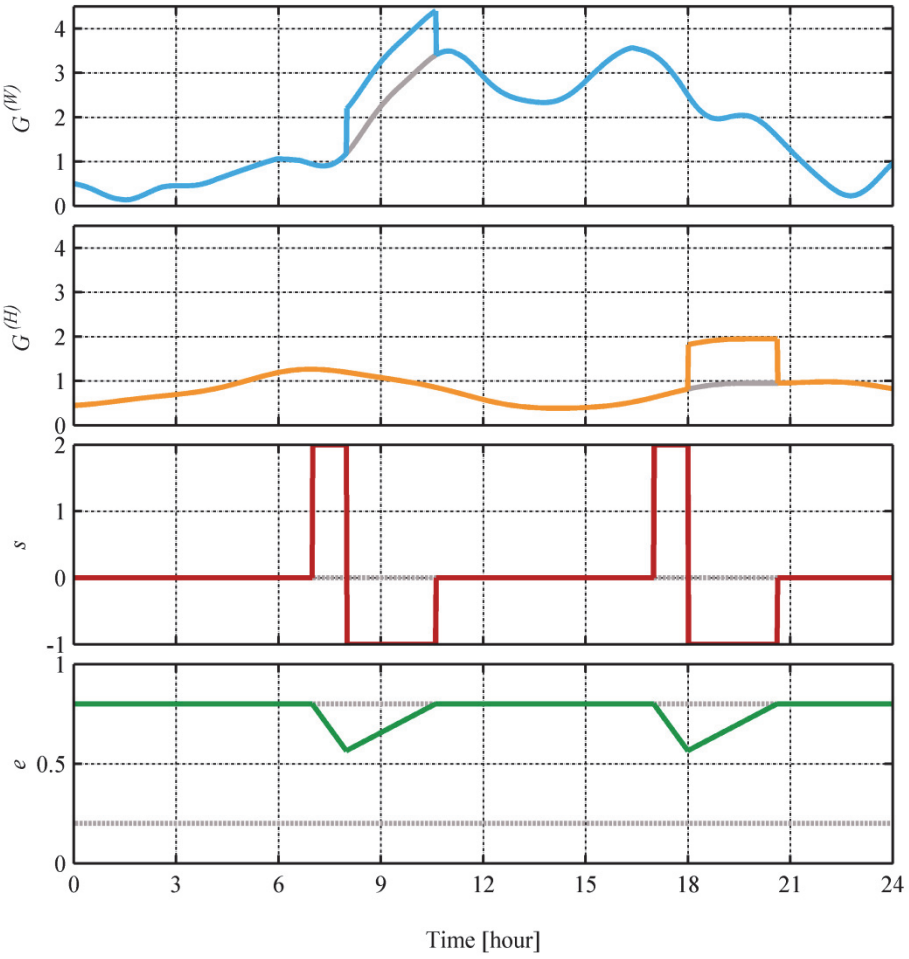

Fig. 2.57 DCS overall results achieved over S-2: no EV (grey), $G^{(W)}$ (cyan), $G^{(H)}$ (orange), s (red), e (green), in pu with respect to the EV rated power and capacity.

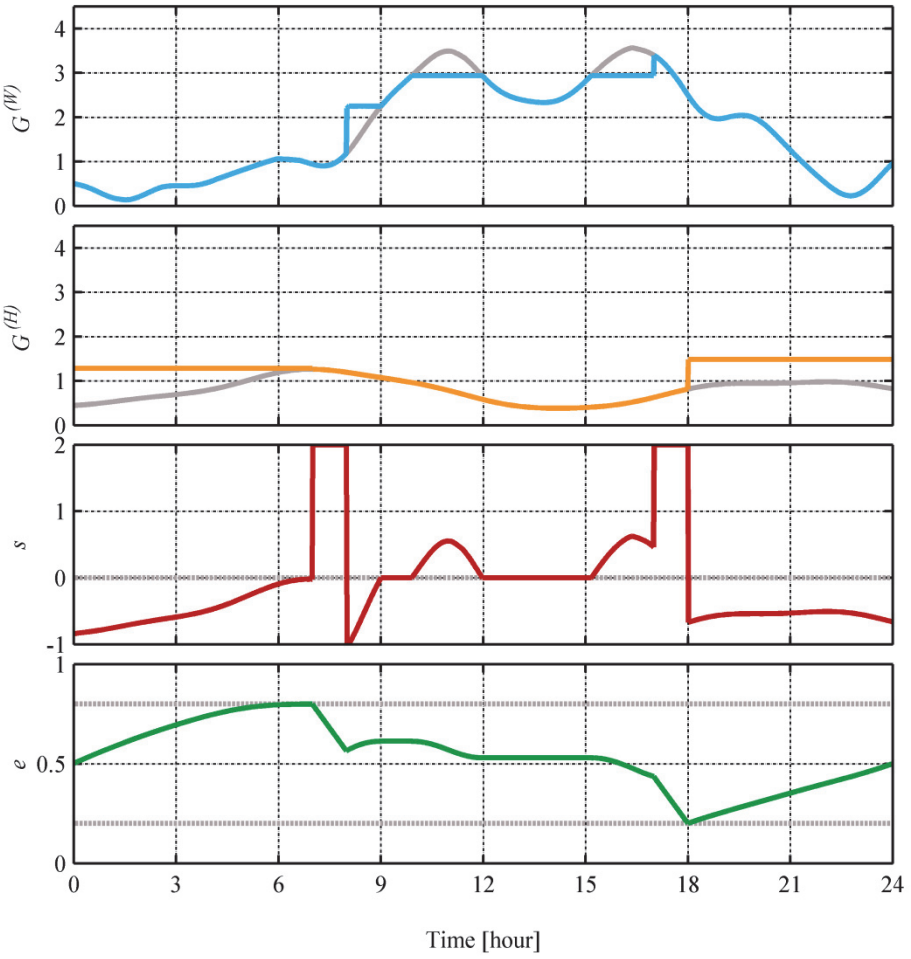

Fig. 2.58 OCS overall results achieved over S-2: no EV (grey), $G^{(W)}$ (cyan), $G^{(H)}$ (orange), s (red), e (green), in pu with respect to the EV rated power and capacity.

CHAPTER 3.
AUTOMOTIVE APPLICATION:
ELECTRIC PROPULSION SYSTEM FOR ELECTRIC VEHICLES

Electric Propulsion System (EPS) for Electric Vehicles (EVs) consists mainly of an electric propulsion motor (EPM) and an Energy Storage System (ESS), which are appropriately coupled through a number of Power Electronic Converters (PECs), as shown in Fig. 3.1. Particularly, ESS has to supply EPM over propulsion, being also able to store the energy recovered by the EPM over regenerative braking. Both these goals are carried out through one or more PECs, which are driven in accordance with EPM and ESS control units [5]–[7].

Firstly focusing on EPM, its main requirements are ruggedness, high torque to inertia ratio, high torque density, wide speed and constant-power speed ranges, low noise, little or no maintenance, small size, ease of control and low cost. Several types of electrical machines have been considered for EPM, such as induction, permanent magnet, switched reluctance and synchronous reluctance machines. At the present time, the majority of commercially available EVs employs either induction or permanent magnet synchronous machines; particularly, interior permanent magnet synchronous machine is widely used as EPM (Toyota Prius, Ford Escape, Chevy Volt, etc.) because of its high efficiency, torque and power density, as well as wide speed range due to its high flux-weakening capability. However, due to the great concern about the availability of rare earth-based magnets and their increasing cost, research is currently focused on the development of EPM with reduced or no magnet content, but still capable of assuring high performances. In this context, a viable solution could be represented by enclosing a small amount of permanent magnets in synchronous reluctance machines, making their performances similar to interior permanent magnet synchronous machines. Such a solution seems to be very promising for future EPMs, especially in terms of reduced costs. [19], [20], [90]–[92]

Regarding PECs for EPS, one of their main tasks is to enable an appropriate supply for the EPM. In this context, current EVs use two-level inverter topologies, which represent a well-established technology in several application fields. However, three-level inverters seem particularly suitable for EVs because they are characterized by lower switching losses. In fact, this converters topology reduces voltage stresses of power semiconductor devices and, in turn, the acoustic noise.

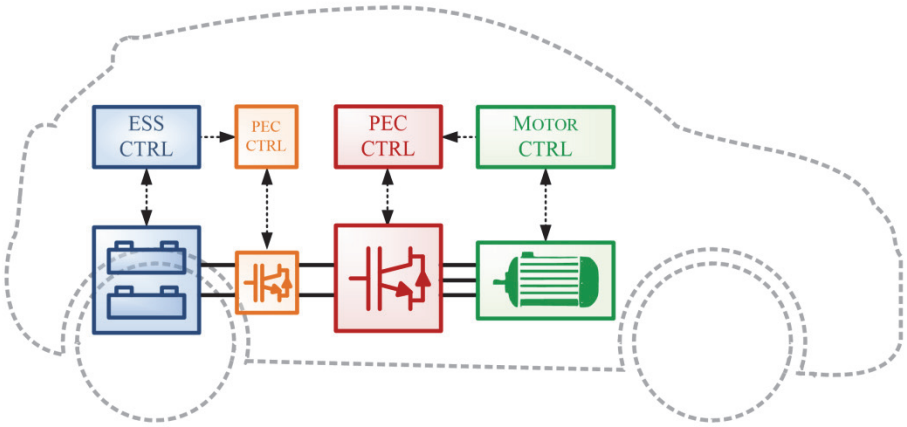

Fig. 3.1 Main components of an electric propulsion system: electric propulsion motor (green), energy storage system (blue) and power electronic converters (red and orange).

In addition, the increased number of voltage steps allows reduction of both total harmonic distortion and electromagnetic interference emissions compared to two-level inverters. Thus, many EV manufacturing companies are managing to replace their two-level inverters with three-level ones in order to increase EPS performances [18]–[20], [92]–[94].

Regarding ESSs, academic and industrial research is focused on improving battery technologies, as well as on appropriate combinations between BT and UC, i.e. on the development of suitable Hybrid Energy Storage Systems (HESSs) [13]–[20]. In this context, it seems that DC-DC converters play a key role in integrating and interfacing different energy sources, especially in terms of power management, flexibility and system optimization. However, since PEC employment may lead to increased cost, size and weight, suitable integrated solutions should be developed in order to manage HESS power flows optimally without resorting to DC-DC converters [15], [19], [24]–[33], [95], [96].

Another fundamental component of EPS is the management system, which should guarantee an appropriate supervision and coordination of the several control units devoted to drive each EPS component. This task could be made even harder by the employment of an HESS, which requires an efficient management of power flows through different ESSs in order increase EPS overall performances and efficiency. Particularly, HESS management should hold the battery current as constant as possible in order to reduce its stress, extending the driving range and improving battery lifetime. This requires UCs to assist the battery by handling large and sudden power fluctuations, as those occurring over acceleration, regenerative braking and fast charging. In this context, a number of HESS management strategies have been proposed in the literature, which can be classified as non-demand prediction and demand prediction. The first ones resort to previous and actual EPS status in order to select the most suitable scenario following either deterministic or non-deterministic approaches. Particularly, deterministic approaches are more simple and easy to be implemented, but they require prior information regarding driving pattern, as well as good knowledge of system structure and model. Thus, instantaneous speed represents a very important reference for managing HESS power flow optimally; in particular, at low speed operation, UCs should be well charged for upcoming acceleration, whereas they should be sufficiently discharged at high speed operation in order to handle regenerative braking on their own mostly. Differently, non-deterministic approaches are based on stochastic and heuristic methods, thus system optimization strictly depends on their tuning and training. Improved HESS power flow management could be attained resorting to demand prediction algorithms, although accurate predictions of driving parameters (speed, acceleration, terrain information, etc.) are difficult to be achieved. In this context, traffic flow models or forecasting methods could be used, as well as on board navigation and sensor systems. At the present time, it

seems that there is no universal solution for HESS management strategy, as also pointed out by significant research efforts spent on this topic. In this context, HESS management could benefit from a more integrated control with both EPM and PEC, leading to the development of suitable management and control system. [14], [15], [19], [20], [25], [28], [34], [97]–[105]

In this context, a novel HESS topology for EPS is proposed in this chapter, which consists of a suitable integration among a battery pack, an UC-capacitor module and a three-phase Neutral-Point Clamped Converter (NPC). Particularly, the high integration with the NPC allows HESS to benefit from the advantages of active configurations without the need of any additional PECs. Therefore, UC voltage can vary within a wide range, thus enabling its full exploitation. In addition, the proposed HESS configuration also prevents batteries from handling sudden high power fluctuations, preserving its rated performances and extending its life. All these goals will be achieved also by means of suitable management and control strategies, which will be implemented through the NPC.

The chapter is structured as follows: mathematical modelling of each EPS component are introduced appropriately in the first section. Based on these, novel EPS control systems are then developed in order to guarantee suitable EPS performances, especially regarding the management of HESS energy flows, all this being presented in the second section. Finally, the third section reports both numerical functionality tests and simulations on the EPS, which highlight the effectiveness of the proposed HESS configuration.

3.1 Mathematical Modelling

This section addresses the mathematical model of each EPS component, namely the Surface-Mounted Permanent Magnet Synchronous Machine (SPM), the Three-Phase Neutral-Point Clamped Converter (NPC) and the Hybrid Energy Storage System (HESS). Particularly, SPM mathematical model is briefly introduced in the first subsection, since it is already pointed out in many books and papers in the literature. Similarly, NPC mathematical model is presented shortly in the second subsection, although some differences occur compared to NPC modelling presented in the literature. Whereas much more attention is given to the HESS mathematical modelling due to the novelty of the proposed configuration, which allows a partial decupling between DC-link voltage and energy content: this aspect is thus investigated in detail in the third subsection.

3.1.1 Permanent Magnet Synchronous Machine

Referring to the schematic representation of a three-phase SPM depicted in Fig. 3.2, where *{a,b,c}* denote the phases of stator winding, the SPM electrical equations can be expressed as [106]

$$v_n = r\,i_n + L\frac{di_n}{dt} + \frac{d\lambda_n}{dt} \quad , \qquad n \in \{a,b,c\} \tag{3.1}$$

in which r and L denote the phase resistance and the synchronous inductance, whereas v_n and i_n are phase voltages and currents respectively, λ_n being the magnetic flux linkages due to permanent magnets [107]. It is worth noting that (3.1) is assumed in conditions of negligible magnetic anisotropy and saturation effects of the electrical machine, as generally occurs for SPM. Thus, it is possible to define voltage, current and flux space vectors based on their corresponding phase quantities as

$$x_{\alpha\beta} = \frac{2}{3}\left(x_a + x_b\, e^{j\frac{2}{3}\pi} + x_c\, e^{j\frac{4}{3}\pi} \right) \quad , \quad x \in \{v,i,\lambda\} \quad . \tag{3.2}$$

Therefore, by substituting (3.1) in (3.2) and assuming each λ_n sine-shaped, the continuous-time electrical equation of SPM in the stationary αβ reference frame can be achieved as

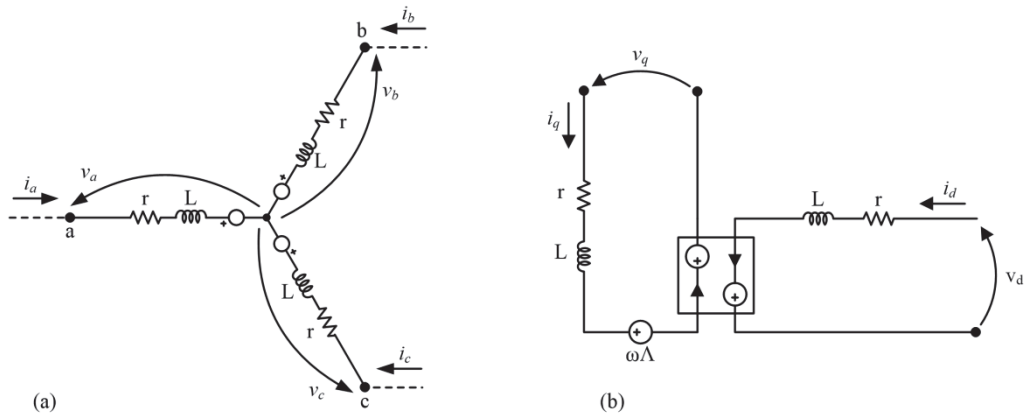

Fig. 3.2 Schematic representation of a three-phase SPM: abc and dq equivalent circuits (on the left and on the right respectively).

$$v_{\alpha\beta} = r\, i_{\alpha\beta} + L\frac{di_{\alpha\beta}}{dt} + \frac{d\lambda_{\alpha\beta}}{dt} \quad , \qquad \lambda_{\alpha\beta} = \Lambda e^{j\theta} \tag{3.3}$$

where the constant Λ denotes the magnitude of the flux linkage vector, whereas θ is the electrical rotor position. Moving from the stationary αβ to the synchronous dq reference frame, (3.3) can be replaced by

$$v_{dq} = \left(r + j\omega L\right) i_{dq} + L\frac{di_{dq}}{dt} + j\omega\Lambda \tag{3.4}$$

whose circuital representation is depicted in Fig. 3.2, whereas ω is the electrical rotor speed and

$$x_{dq} = x_{\alpha\beta}\, e^{-j\theta} \quad , \quad x \in \{v, i, \lambda\} \ . \tag{3.5}$$

Finally, denoting by p the number of pole pairs, SPM electromagnetic torque T_e and electromechanical power P_m can be expressed respectively as

$$T_e = \frac{3}{2} p\Lambda \cdot i_q \quad , \quad P_m = \frac{3}{2}\omega\Lambda \cdot i_q \ . \tag{3.6}$$

It is worth nothing that (3.4) is more suitable than (3.3) for designing SPM control algorithms, as just stated before. In fact, referring to (3.6), appropriate torque control can be achieved by controlling i_q directly, thus justifying the employment of the dq reference frame in place of the stationary αβ one. Finally, mechanical equation of the SPM can be introduced as

$$T_e = J\frac{d\omega_m}{dt} + D\,\omega_m + T_l \tag{3.7}$$

in which ω_m is the rotor speed, J and D are the inertia and viscous damping factor respectively, T_l being the load torque.

3.1.2 Neutral Point Clamped Converter

Referring to the schematic representation of a Three-Level Neutral Point Clamped Converter (NPC) shown in Fig. 3.3, it can be seen that each of its leg consists of four switches and two clamping diodes [108], [109]. Furthermore, the DC-link consists of high-side and low-side capacitors, whose voltages are denoted by V_H and V_L respectively. Denoting by V_x the voltage of the generic phase x referred to the neutral point N, three different leg states can be defined, i.e. H, L and M, depending on the switching states S, as pointed out in Table XI. In particular, the H state occurs when the upper two switches are ON simultaneously, V_x being equal to V_H. Similarly, the L state means that the lower two

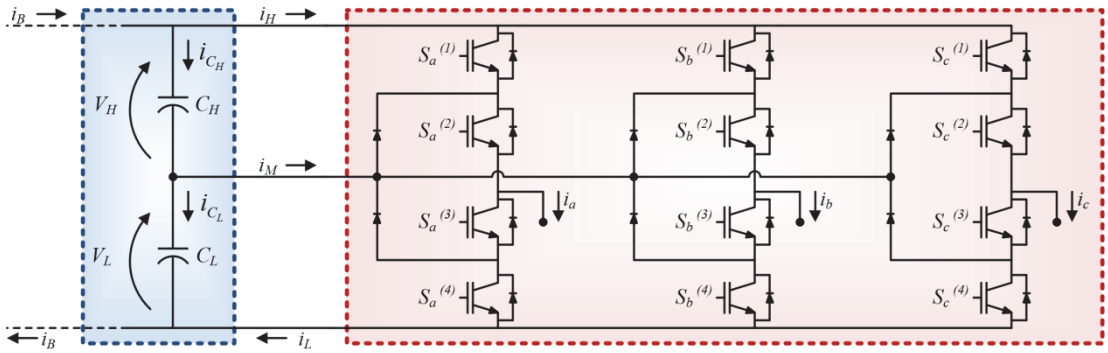

Fig. 3.3 A three-phase three-level Neutral Point Clamped Converter (red box) and its DC-link (blue box).

switches are ON and, thus, V_x is equal to $-V_L$. Finally, the M state occurs when the two central switches are ON, so the phase terminal is directly coupled to the neutral point, V_x being equal to zero. Consequently, the per unit phase terminal voltage can be defined as:

$$v_x = \delta_H v_H - \delta_L v_L \quad , \quad \begin{matrix} x \in \{a,b,c\} \\ \delta \in \{\alpha,\beta,\gamma\} \end{matrix} \tag{3.8}$$

where δ_H and δ_L denote the duty cycles of the H and L states of the leg x, $\{\alpha,\beta,\gamma\}$ being the duty cycles of the legs $\{a,b,c\}$ respectively. Furthermore, v_H and v_L are the per unit capacitor voltages, which are defined as

$$v_H = \frac{V_H}{V_H + V_L} \quad , \quad v_L = \frac{V_L}{V_H + V_L} \ . \tag{3.9}$$

Still referring to (3.8), the duty cycles of each leg must satisfy the following equation:

$$\delta_H + \delta_M + \delta_L = 1 \quad , \quad \delta \in \{\alpha,\beta,\gamma\} \ . \tag{3.10}$$

Thus, based on both (3.8) and (3.10), the generic phase terminal v_x is bounded in accordance with

$$-v_L \le v_x \le v_H \quad , \quad x \in \{a,b,c\} \ . \tag{3.11}$$

Considering now the per unit chain voltages, they can be expressed as

$$\begin{aligned} v_{ab} &= v_a - v_b \\ v_{bc} &= v_b - v_c \\ v_{ca} &= v_c - v_a \ . \end{aligned} \tag{3.12}$$

Based on (3.12), the chain voltage space vector can be thus introduced as

$$v_{ch} = \frac{2}{3}\left(v_{ab} + v_{bc} \cdot e^{j\frac{2}{3}\pi} + v_{ca} \cdot e^{j\frac{4}{3}\pi} \right) \ . \tag{3.13}$$

TABLE XI
SWITCHING AND LEG STATES

LEG STATE	SWITCHING STATES				V_x
	$S_x^{(1)}$	$S_x^{(2)}$	$S_x^{(3)}$	$S_x^{(4)}$	
H	1	1	0	0	V_H
M	0	1	1	0	*0*
L	0	0	1	1	$-V_L$

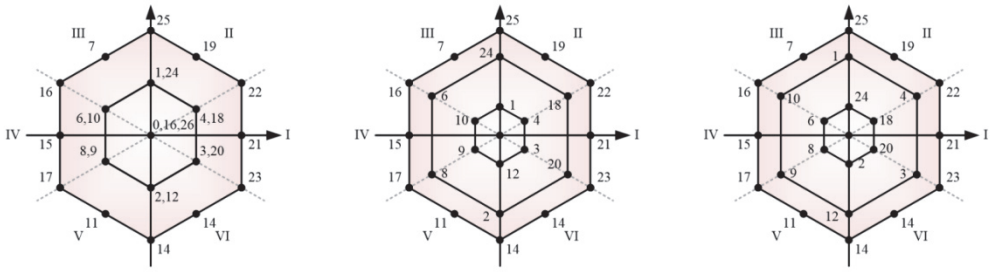

Fig. 3.4 Voltage space vector locus of an NPC in case of voltage equalization (left), V_H higher than V_L (middle) and V_H lower than V_L (right).

As a consequence, considering all combinations of the leg states, it is possible to determine the fundamental voltage space vectors applicable by the NPC, as shown in both Fig. 3.4 and Table XII. Particularly, they are achieved by assuming that each leg is characterized by one leg state only, i.e. two of δ_H, δ_M and δ_L are equal to zero, the other one being equal to one. Still referring to Fig. 3.4, it can be seen that some fundamental vectors are redundant when the NPC is perfectly equalized, i.e. V_H equals V_L. Such phenomenon much less occurs in case of voltage unbalance, in correspondence of which only zero voltage vectors are overlapped. In addition, based on (3.11), it can be stated that each space vector that lies within the hexagon depicted in Fig. 3.4 can be achieved by a suitable choice of the duty cycles of each leg, obviously in accordance with (3.10). Finally, DC-link current relationships can be expressed as

$$\begin{aligned} i_H &= \alpha_H\, i_a + \beta_H\, i_b + \gamma_H\, i_c \\ i_M &= \alpha_M\, i_a + \beta_M\, i_b + \gamma_M\, i_c \\ i_L &= -\left(\alpha_L\, i_a + \beta_L\, i_b + \gamma_L\, i_c\right) \end{aligned} \tag{3.14}$$

TABLE XII
NPC VOLTAGE SPACE VECTORS

	a	b	c	v_{ch}		a	b	c	v_{ch}		a	b	c	v_{ch}
0	M	M	M	0	9	L	M	M	$\frac{2}{\sqrt{3}}\, V_L \measuredangle \frac{7}{6}\pi$	18	H	M	M	$\frac{2}{\sqrt{3}}\, V_H \measuredangle \frac{\pi}{6}$
1	M	M	L	$\frac{2}{\sqrt{3}}\, V_L \measuredangle \frac{\pi}{2}$	10	L	M	L	$\frac{2}{\sqrt{3}}\, V_L \measuredangle \frac{5}{6}\pi$	19	H	M	L	$V_H + V_L \measuredangle \frac{\pi}{3}$
2	M	M	H	$\frac{2}{\sqrt{3}}\, V_H \measuredangle \frac{3}{2}\pi$	11	L	M	H	$V_H + V_L \measuredangle \frac{4}{3}\pi$	20	H	M	H	$\frac{2}{\sqrt{3}}\, V_H \measuredangle \frac{11}{6}\pi$
3	M	L	M	$\frac{2}{\sqrt{3}}\, V_L \measuredangle \frac{11}{6}\pi$	12	L	L	M	$\frac{2}{\sqrt{3}}\, V_L \measuredangle \frac{3}{2}\pi$	21	H	L	M	$V_H + V_L$
4	M	L	L	$\frac{2}{\sqrt{3}}\, V_L \measuredangle \frac{\pi}{6}$	13	L	L	L	0	22	H	L	L	$\frac{2}{\sqrt{3}}\, (V_H + V_L) \measuredangle \frac{\pi}{6}$
5	M	L	H	$V_H + V_L \measuredangle \frac{5}{3}\pi$	14	L	L	H	$\frac{2}{\sqrt{3}}\, (V_H + V_L) \measuredangle \frac{3}{2}\pi$	23	H	L	H	$\frac{2}{\sqrt{3}}\, (V_H + V_L) \measuredangle \frac{11}{6}\pi$
6	M	H	M	$\frac{2}{\sqrt{3}}\, V_H \measuredangle \frac{5}{6}\pi$	15	L	H	M	$V_H + V_L \measuredangle \pi$	24	H	H	M	$\frac{2}{\sqrt{3}}\, V_H \measuredangle \frac{\pi}{2}$
7	M	H	L	$V_H + V_L \measuredangle \frac{2}{3}\pi$	16	L	H	L	$\frac{2}{\sqrt{3}}\, (V_H + V_L) \measuredangle \frac{5}{6}\pi$	25	H	H	L	$\frac{2}{\sqrt{3}}\, (V_H + V_L) \measuredangle \frac{\pi}{2}$
8	M	H	H	$\frac{2}{\sqrt{3}}\, V_H \measuredangle \frac{7}{6}\pi$	17	L	H	H	$\frac{2}{\sqrt{3}}\, (V_H + V_L) \measuredangle 7\frac{\pi}{6}$	26	H	H	H	0

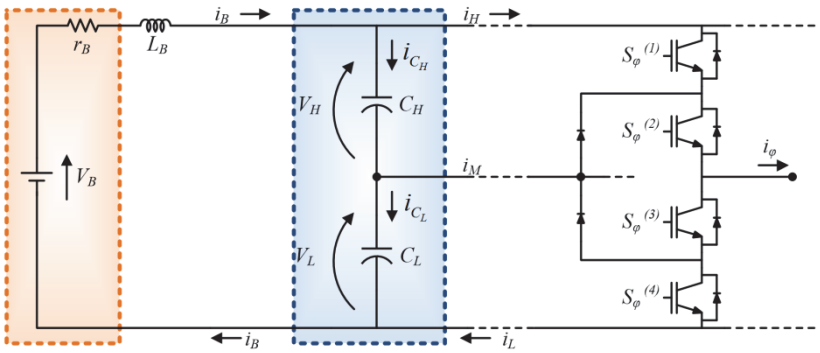

Fig. 3.5 Schematic representation of the proposed hybrid energy storage system: battery pack (orange) and capacitor module (blue)..

3.1.3 Hybrid Energy Storage System

The Hybrid Energy Storage System (HESS) considered in this work consists of an UC-capacitor module and a battery pack, as shown in Fig. 3.5. Particularly, the UC-capacitor module is made up of both high-side and low-side DC-link capacitors, whose corresponding equations can be expressed as:

$$C_H \frac{dV_H}{dt} = i_B - i_H \quad , \quad C_L \frac{dV_L}{dt} = i_B - i_L \tag{3.15}$$

in which i_B denotes the current drawn from or delivered to the battery pack. This last is modelled by means of a constant DC voltage source (V_B) and a parasitic series resistance (r_B), leading to the following equation:

$$V_B = r_B i_B + L_B \frac{di_B}{dt} + V_{DC} \tag{3.16}$$

where L_B denotes the inductance of the input filter of the NPC, V_{DC} being the overall DC-link voltage:

$$V_{DC} = V_H + V_L \ . \tag{3.17}$$

Therefore, by combining (3.15) to each other the following result is achieved

$$C_{DC} \frac{dV_{DC}}{dt} = i_B - i_{DC} \quad , \quad i_{DC} = c_H i_H + c_L i_L \tag{3.18}$$

in which i_{DC} and C_{DC} denote the equivalent DC-link current and series capacitance respectively, whereas c_H and c_L are the per unit capacitance:

$$C_{DC} = \frac{C_H C_L}{C_H + C_L} \quad , \quad c_H = \frac{C_H}{C_H + C_L} \quad , \quad c_L = \frac{C_L}{C_H + C_L} \ . \tag{3.19}$$

Considering now the energy stored in the UC-capacitor module, it can be expressed as

$$E_{DC} = \frac{1}{2} C_H V_H^2 + \frac{1}{2} C_L V_L^2 \ . \tag{3.20}$$

Hence, based on (3.17), (3.20) can be further expressed as

$$E_{DC} = \frac{1}{2} C_H V_H^2 + \frac{1}{2} C_L \left(V_{DC} - V_H \right)^2 \tag{3.21}$$

Consequently, by defining the energy base value and the unbalance capacity factor respectively as

$$\hat{E}_{DC} = \frac{1}{2} C_L V_{DC}^2 \tag{3.22}$$

$$\zeta = \frac{c_H}{c_L} \tag{3.23}$$

the per unit energy of the capacitor module can be easily achieved as

$$e_{DC} = \zeta v_H^2 + \left(1 - v_H\right)^2 \quad . \tag{3.24}$$

Referring to the (v_H,e_{DC}) plane, (3.24) identify a parabola as highlighted in Fig. 3.6. Particularly, when ζ is equal to 1, i.e. high-side and low-side capacitances are equal to each other, the minimum energy stored in the DC-link occurs when it is perfectly equalize:

$$v_H = v_L = \frac{1}{2} \quad , \quad e_{DC} = e_{DC,min} = \frac{1}{2} \quad . \tag{3.25}$$

Whereas when ζ differs from one, the minimum energy value is achieved for unbalanced DC-link voltages:

$$v_H = \frac{1}{1+\zeta} \quad , \quad v_L = \frac{\zeta}{1+\zeta} \quad , \quad e_{DC} = e_{DC,min} = \frac{\zeta}{1+\zeta} \quad . \tag{3.26}$$

Based on all these considerations, it can be stated that ζ values greater than one are suitable for exploiting DC-link capabilities as energy buffer, for given V_{DC} and energy base values. Consequently, DC-link voltage unbalances are required in order to vary the energy stored in the UC-capacitor module, without affecting its overall voltage. Such energy variations can be determined by considering the time derivative of (3.20), appropriately combined with (3.15), leading to

$$\frac{dE_{DC}}{dt} = V_{DC}\left(i_B - i_p\right) \tag{3.27}$$

in which i_p is the equivalent "power" current, which is proportional to the power drawn by the NPC load:

$$i_p = v_H i_H + v_L i_L \quad . \tag{3.28}$$

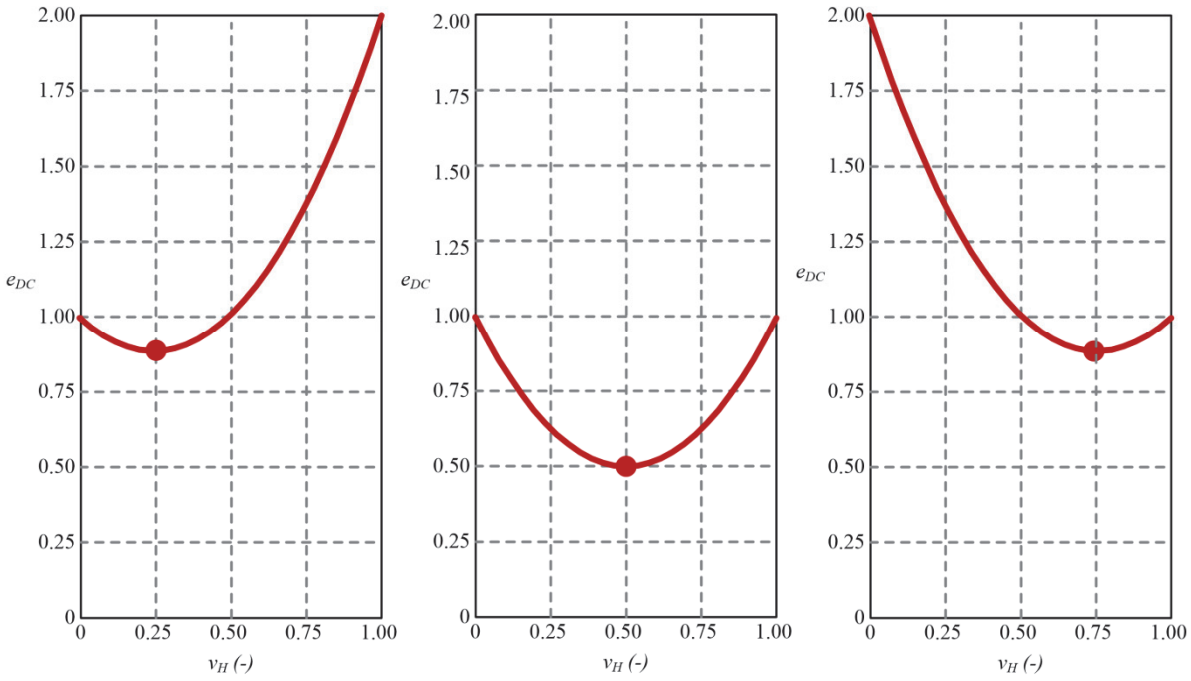

Fig. 3.6 DC-link energy evolution versus v_H at constant DC-link voltage: ζ > 1 (on the left), ζ = 1 (in the middle), ζ < 1 (on the right).

3.2 Electric Propulsion System Control

This section presents the design of the EPS control system, whose schematic representation is depicted in Fig. 3.7. This consists of a number of control units, which have been developed with the aim of controlling SPM, NPC and HESS with a given order of priority. Particularly, SPM control system is characterized by the highest level of priority because propulsion performances must be guaranteed in any case. Such a control system guarantees SPM speed, torque and current regulations, characterized by increasing dynamic performances. Whereas HESS control system has to manage the energy flows among the battery pack and the UC-capacitor module in accordance with SPM requirements, it being thus characterized by a lower level of priority. Finally, NPC control system has to synthesize the most suitable PWM pattern in order to satisfy both SPM and HESS requirements. When this cannot occur, NPC control has to prioritize SPM requirements compared to HESS needs, which are thus satisfied to the maximum extent.

3.2.1 SPM Control

The overall control scheme of the SPM used as EV propulsion motor is depicted in Fig. 3.8. It consists mainly of an inner current control loop and an outer speed control loop. Although a speed loop is generally not required in vehicular applications, it is particularly useful to emulate EV drivers in tracking given speed profiles, such as those provided by standard driving cycles [110]–[112]. As a result, a suitable reference torque profile is achieved, which emulates that imposed by the vehicle driver. Based on the reference torque profile, different reference currents can be synthesized in accordance with a number of SPM control strategies (constant torque angle, constant mutual flux linkage, unity power factor, etc.). Once reference current profiles have been achieved, they should be tracked appropriately by means of the corresponding dq current control system. This has to synthesize the most suitable reference voltage space vector based on both actual and reference current values, as shown in Fig. 3.8. As a result, reference chain voltages are achieved, whose implementation is carried out by the NPC control system, also in accordance with HESS needs.

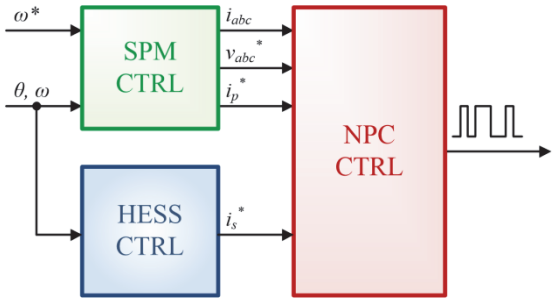

Fig. 3.7 An overview of the proposed EPS control system.

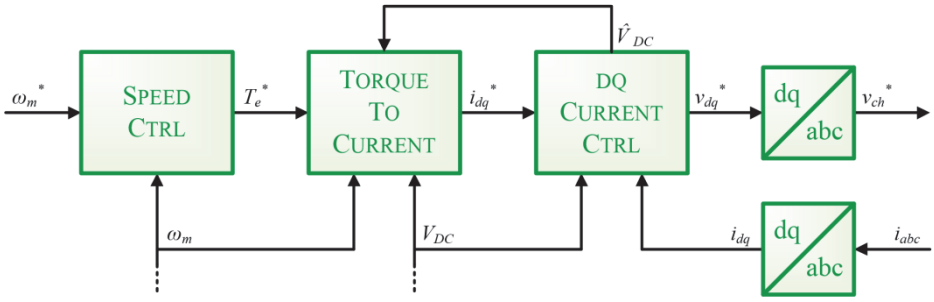

Fig. 3.8 Overall SPM block control scheme.

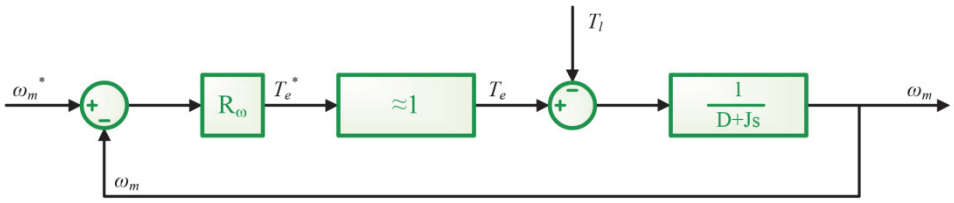

Fig. 3.9 The simplified speed control loop.

3.2.1.1 Speed Control System

The speed control system is synthesized referring to the equivalent speed control loop depicted in Fig. 3.9. Particularly, this is achieved based on (3.7) and assuming that torque control is accomplished within very short periods compared to those required by speed regulation. Consequently, reference and actual torque profiles can be considered superimposed, leading to the following open-loop transfer function:

$$G_\omega(s) = \frac{\Omega_m}{\Delta\Omega_m} = R_\omega(s) \cdot \frac{1}{J} \cdot \frac{1}{(s - z_m)} \quad , \quad z_m = -\frac{D}{J} \ . \tag{3.29}$$

Based on (3.29), a PI regulator can be employed, whose transfer function can be expressed as

$$R_\omega(s) = k_p^{(\omega)} \frac{(s - z_\omega)}{s} \quad , \quad z_\omega = -\frac{k_i^{(\omega)}}{k_p^{(\omega)}} \ . \tag{3.30}$$

Particularly, in order to simplify (3.29), the integral gain can be chosen in accordance with the following relationship:

$$k_i^{(\omega)} = k_p^{(\omega)} \frac{D}{J} \ . \tag{3.31}$$

Consequently, by substituting (3.31) and (3.30) in (3.29), this last becomes

$$G_\omega(s) = \frac{k_p^{(\omega)}}{J} \cdot \frac{1}{s} \ . \tag{3.32}$$

Therefore, the corresponding closed-loop transfer function can be expressed as

$$\frac{\Omega_m}{\Omega_m^*} = \frac{k_p^{(\omega)}}{J s + k_p^{(\omega)}} \ . \tag{3.33}$$

Finally, based on (3.33), it is possible to choose the proportional gain in accordance with the desired closed-loop bandwidth (f_c), leading to:

$$k_p^{(\omega)} = 2\pi f_c J \ \Rightarrow \ k_i^{(\omega)} = 2\pi f_c D \ . \tag{3.34}$$

In conclusion, a schematic representation of the PI-based speed regulator is depicted in Fig. 3.10. It

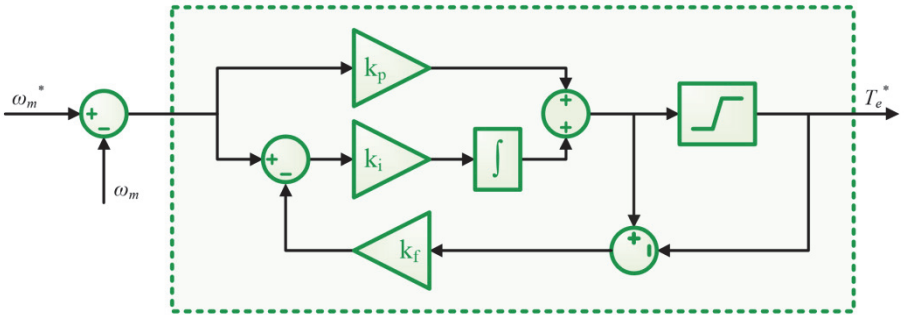

Fig. 3.10 Schematic representation of the PI-based speed control regulator.

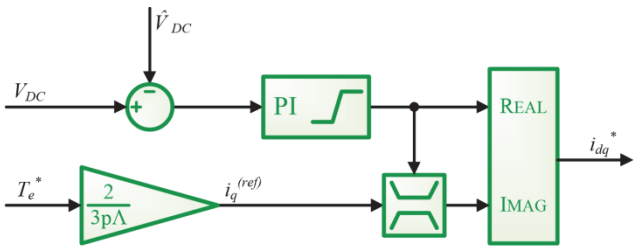

Fig. 3.11 Schematic representation of the MTPA block.

can be seen that it encloses an appropriate anti-windup filter, i.e. the back-calculation method is employed [113], [114], whose gain is chosen as

$$k_f^{(\omega)} = \frac{1}{k_p^{(\omega)}} \quad . \tag{3.35}$$

3.2.1.2 Current Control Strategy

Based on the reference torque, the dq reference current profiles have been synthesized in accordance with the Maximum Torque Per Ampere control strategy (MTPA). This generally represents the most suitable choice because it allows SPM to deliver the maximum torque for a given rated current. Referring thus to (3.6), MTPA consists of driving the SPM torque by means of the q current vector component, simultaneously holding the d current component constant at zero. Consequently, dq reference current profiles can be easily achieved as

$$i_{dq}^{*} = j\frac{2T_e^{*}}{3p\Lambda} \quad . \tag{3.36}$$

However, at high-speed operation, d current components different from zero could be needed due to DC-link voltage saturation, leading to flux-weakening operation [128]. This is appropriately guaranteed resorting to the well-known voltage follower based on a PI voltage compensator [114], [116], [113], as shown in Fig. 3.11. Particularly, negative d current components are injected appropriately as soon as the required DC-link voltage ($\hat{V}_{DC}$) exceeds the actual value (V_{DC}). Such operation is performed by means of a PI regulator, whose anti-windup method and gains have been set in accordance with the design suggestions reported in [113], [114], [116]. As a result, a good trade-off between dynamic and flux-weakening performances is achieved, leading to:

$$i_d^{*} = k_p^{(v)}\left(\hat{V}_{DC} - V_{DC}\right) + k_i^{(v)}\int\left(\hat{V}_{DC} - V_{DC}\right)dt \quad , \quad -I_{max} \le i_d^{*} \le 0 \quad . \tag{3.37}$$

Consequently, the reference q current profile can be determined based on both (3.36) and (3.37) as

$$i_q^{*} = \frac{2T_e^{*}}{3p\Lambda} \quad , \quad -\sqrt{I_{max}^2 - \left(i_d^{*}\right)^2} \le i_q^{*} \le \sqrt{I_{max}^2 - \left(i_d^{*}\right)^2} \quad . \tag{3.38}$$

3.2.1.3 dq Current Control System

The dq reference current profiles have to be tracked by means of an appropriate current control system, which can be designed differently, depending on the chosen control technique (linear, hysteresis, model predictive control, etc.). Particularly, linear control through PI regulators generally provides good steady state performances and a fair insensitivity to model parameter variations and uncertainties. Thus, it is particularly suitable for vehicular applications, also because these are relatively low demanding in terms of current dynamic performances. Consequently, a PI-based current control system is employed, which is designed based on the equivalent current control loop

depicted in Fig. 3.12. Particularly, $\tilde{v}_{dq}$ is introduced in accordance with the so-called feedback linearization method as:

$$\tilde{v}_{dq} = v_{dq} - j\omega\left(Li_{dq} + \Lambda\right) . \tag{3.39}$$

Consequently, based on (3.39), (3.4) becomes

$$\tilde{v}_{dq} = r\, i_{dq} + L\frac{di_{dq}}{dt} . \tag{3.40}$$

As a result, the open-loop transfer function can be expressed as

$$G_{dq}(s) = \frac{I_{dq}}{\Delta I_{dq}} = R_{dq}(s)\cdot\frac{1}{L}\cdot\frac{1}{(s - z_e)} \quad , \quad z_e = -\frac{r}{L} . \tag{3.41}$$

Based on (3.41), a PI regulator can be successfully employed for each current control loop, whose gains can be determined in accordance with the same procedure followed for the speed control system design. Therefore, proportional, integral and anti-windup gains can be chosen respectively as

$$k_p^{(dq)} = 2\pi f_c^{(dq)} L \quad , \quad k_i^{(dq)} = 2\pi f_c^{(dq)} r \quad , \quad k_f^{(dq)} = \frac{1}{k_p^{(dq)}} . \tag{3.42}$$

It is worth noting that $f_c^{(dq)}$ must be much greater than $f_c^{(w)}$ (10 times more) in order to allow current regulation to occur almost instantaneously compared to the speed one.

The overall structure of the dq current control system is resumed in Fig. 3.13. It can be seen that (3.39) is properly employed in order to synthesize the reference voltage space vector. This last is also constrained by DC-link voltage saturation, based on which the back-calculation method is employed, as for the speed control system. In addition, the required DC-link voltage is also considered in order to determine the most suitable d reference current profile, as detailed before.

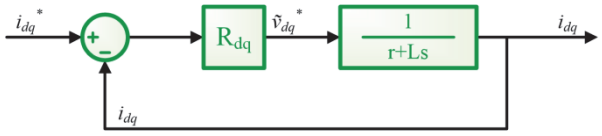

Fig. 3.12 Current control loop.

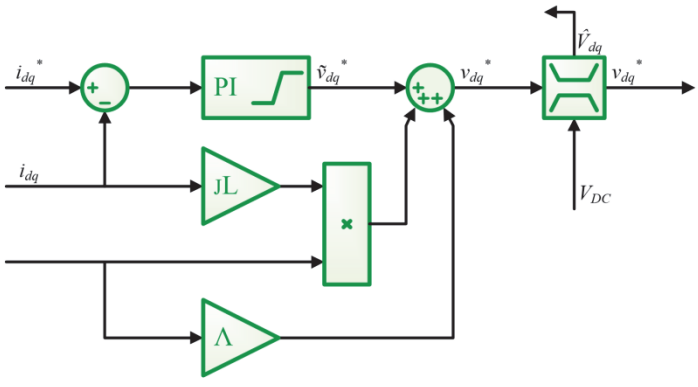

Fig. 3.13 Overall dq current control system.

3.2.2 NPC Control

The NPC control has been developed with the aim of satisfying both SPM and HESS requirements. Particularly, regarding the SPM, such requirements consist of only applying the reference chain voltages, which are appropriately synthesized by the SPM control in accordance with speed and/or torque demand. Whereas HESS requirements are represented by DC-link voltage regulation needs, based on which both battery current and DC-link energy content can be successfully controlled, as detailed in the following subsection.

All these goals can be achieved resorting to suitable PWM patterns. Their development firstly requires the definition of suitable voltage sectors (σ_v) in accordance with the binary signs of reference chain voltages $\{s_{ab}^*, s_{bc}^*, s_{ca}^*\}$, as summed up in Table XIII. Consequently, a new set of indexes $\{u,v,w\}$ can be introduced, each of which alternatively denotes one of the phase terminals $\{a,b,c\}$ over each voltage sector, in accordance with Table XIV. As a result, based on both Table XIII and Table XIV, it is possible to state that v_{uv} always represents the voltage of maximum magnitude, v_{vw} and v_{wu} being always opposite to v_{uv}:

$$\begin{aligned} &|v_{uv}| \geq |v_{vw}| \quad , \quad |v_{uv}| \geq |v_{wu}| \\ &s_{uv} = \overline{s}_{vw} = \overline{s}_{wu} \ . \end{aligned} \tag{3.43}$$

Consequently, (3.8) and (3.11) become respectively

$$v_x = \delta_H v_H - \delta_L v_L \quad , \quad \begin{matrix} x \in \{u,v,w\} \\ \delta \in \{\varphi,\psi,\xi\} \end{matrix} \tag{3.44}$$

$$-v_L \leq v_x \leq v_H \quad , \quad x \in \{u,v,w\} \tag{3.45}$$

where $\{\varphi,\psi,\xi\}$ replace $\{\alpha,\beta,\gamma\}$ in denoting the duty cycles of the legs $\{u,v,w\}$. Furthermore, (3.10) can now be expressed as

$$\delta_H + \delta_M + \delta_L = 1 \quad , \quad \delta \in \{\varphi,\psi,\xi\} \ . \tag{3.46}$$

Finally, based on (3.44), (3.12) and (3.14) become

$$\begin{aligned} v_{uv} &= (\varphi_H - \psi_H) v_H - (\varphi_L - \psi_L) v_L \\ v_{vw} &= (\psi_H - \xi_H) v_H - (\psi_L - \xi_L) v_L \\ v_{wu} &= (\xi_H - \varphi_H) v_H - (\xi_L - \varphi_L) v_L \end{aligned} \tag{3.47}$$

$$\begin{aligned} i_H &= \varphi_H i_u + \psi_H i_v + \xi_H i_w \\ i_M &= \varphi_M i_u + \psi_M i_v + \xi_M i_w \\ i_L &= -(\varphi_L i_u + \psi_L i_v + \xi_L i_w) \ . \end{aligned} \tag{3.48}$$

In conclusion, based on both (3.47) and (3.48), it can be stated that different combinations of $\{\varphi,\psi,\xi\}$ may lead to the same chain voltages but to different DC-link currents. Such property can thus be suitably exploited in order to regulate DC-link voltages without affecting SPM requirements, as carried out in developing both HML and PS-PWM patterns.

TABLE XIII
VOLTAGE SECTORS

s_{ab}	0	0	1	1	1	0
s_{bc}	1	0	0	0	1	1
s_{ca}	1	1	1	0	0	0
σ_v	I	II	III	IV	V	VI

TABLE XIV
PHASE TERMINAL INDEXES

σ_v	I	II	III	IV	V	VI
u	a	c	b	a	c	b
v	b	a	c	b	a	c
w	c	b	a	c	b	a

TABLE XV
CURRENT SECTORS

s_u	0	0	1	1	1	0
s_v	1	0	0	0	1	1
s_w	1	1	1	0	0	0
σ_i	I	II	III	IV	V	VI

3.2.2.1 HML-PWM

The HML-PWM is a PWM-based modulator for an NPC that consists of selecting the most suitable PWM pattern in order to proper manage the DC-link capacitor voltages. This is developed in accordance with a binary signal ε that is provided by the HESS control. Particularly, ε is high when high-side capacitor needs to be charged; otherwise ε is low. Such a DC-link voltage regulation must be performed also by taking into account the reference chain voltages provided by the SPM control, whose achievement is mandatory.

Thus, referring to both Table XIII and Table XIV, only odd voltage sectors are considered at first (I, III, V), in correspondence of which v_{uv} is always positive. Consequently, based on (3.47), both φ_L and ψ_H are always imposed equal to zero. This is done because these duty cycles do not contribute to the achievement of a positive v_{uv} value. As a result, (3.47) becomes

$$\begin{aligned} v_{uv}^{*} &= \varphi_H v_H + \psi_L v_L \\ v_{vw}^{*} &= -\psi_L v_L - \left(\xi_H v_H - \xi_L v_L\right) \\ v_{wu}^{*} &= -\varphi_H v_H + \left(\xi_H v_H - \xi_L v_L\right) . \end{aligned} \tag{3.49}$$

Whereas high-side and low-side DC-Link currents can be determined from (3.48) as

$$\begin{aligned} i_H &= \varphi_H \cdot i_u + \xi_H \cdot i_w \\ i_L &= -\left(\psi_L \cdot i_v + \xi_L \cdot i_w\right) . \end{aligned} \tag{3.50}$$

Thus, based on ε, different choices of all the remaining duty cycles have to be performed. Particularly, if ε is high, i_H has to be minimized in order to recharge or less discharge C_H to the maximum extent, by satisfying (3.49) at the same time. Otherwise, i.e. ε is low, i_H has to be maximized, always in accordance with (3.49). Both these goals require the knowledge of the signs of actual phase currents, as easily detectable from (3.50). Therefore, actual current sectors (σ_i) can be defined in accordance with the binary signs of the actual phase currents $\{s_u, s_v, s_w\}$, as pointed out in Table XV. Consequently, it is possible to select the remaining duty cycles properly in accordance with both ε and σ_i, leading to twelve different cases.

Firstly referring to the case O.0.I (σ_v = I/III/V, ε = 0, σ_i = I), (3.49) and (3.50) highlight the need of maximizing φ_H, which can thus be computed as

$$\varphi_H^{*} = \frac{1}{v_H} min\left\{v_{uv}^{*}, v_H\right\} . \tag{3.51}$$

Consequently, based on (3.49), ψ_L can be immediately determined as

$$\psi_L^{*} = \frac{1}{v_L} max\left\{0, v_{uv}^{*} - v_H\right\} . \tag{3.52}$$

As a result, by substituting (3.51) and (3.52) in (3.49), both ξ_H and ξ_L can be achieved as

$$\xi_H^{*} = \frac{1}{v_H} max\left\{0, v_{wu}^{*} + min\left\{v_{uv}^{*}, v_H\right\}\right\} . \tag{3.53}$$

$$\xi_L^{*} = \frac{1}{v_L} max\left\{0, -\left(v_{wu}^{*} + v_H\right)\right\} . \tag{3.54}$$

Similar considerations can be made also for even voltage sectors (II, IV, VI), in correspondence of which v_{uv} is always negative. Consequently, both φ_H and ψ_L are always set at zero, thus (3.47) and (3.48) become

$$\begin{aligned} v_{uv}^{*} &= -\varphi_L v_L - \psi_H v_H \\ v_{vw}^{*} &= \psi_H v_H - \left(\xi_H v_H - \xi_L v_L\right) \\ v_{wu}^{*} &= \varphi_L v_L + \left(\xi_H v_H - \xi_L v_L\right) \end{aligned} \tag{3.55}$$

$$\begin{aligned} i_H &= \psi_H \cdot i_v + \xi_H \cdot i_w \\ i_L &= -\left(\varphi_L \cdot i_u + \xi_L \cdot i_w\right) \end{aligned} \tag{3.56}$$

Considering now the case E.0.III (σ_v = II/IV/VI, ε = 0, σ_i = III), ψ_H needs to be maximized in order to discharge C_H as much as possible, leading to

$$\psi_H^{*} = \frac{1}{v_H} min\left\{-v_{uv}^{*}, v_H\right\} \ . \tag{3.57}$$

Consequently, all the other duty cycles can be computed as

$$\varphi_L^{*} = \frac{1}{v_L} max\left\{0, -\left(v_{uv}^{*} + v_H\right)\right\} \tag{3.58}$$

$$\xi_H^{*} = \frac{1}{v_H} max\left\{0, -v_{vw}^{*} + min\left\{-v_{uv}^{*}, v_H\right\}\right\} \tag{3.59}$$

$$\xi_L^{*} = \frac{1}{v_L} max\left\{0, v_{vw}^{*} - v_H\right\} \ . \tag{3.60}$$

As a result, based on both these cases, it is possible to define the H-PWM pattern in accordance with the following relationships.

$$\varphi_H^{*} = \frac{1}{v_H} max\left\{0, min\left\{v_{uv}^{*}, v_H\right\}\right\} \tag{3.61}$$

$$\varphi_L^{*} = \frac{1}{v_L} max\left\{0, -\left(v_{uv}^{*} + v_H\right)\right\} \tag{3.62}$$

$$\psi_H^{*} = \frac{1}{v_H} max\left\{0, min\left\{-v_{uv}^{*}, v_H\right\}\right\} \tag{3.63}$$

$$\psi_L^{*} = \frac{1}{v_L} max\left\{0, -\left(v_{uv}^{*} - v_H\right)\right\} \tag{3.64}$$

$$\xi_H^{*} = \frac{1}{v_H} max\left\{0, min\left\{-v_{vw}^{*} + \psi_H v_H, v_{wu}^{*} + \varphi_H v_H\right\}\right\} \tag{3.65}$$

$$\xi_L^{*} = \frac{1}{v_L} max\left\{0, v_{vw}^{*} - v_H, -\left(v_{wu}^{*} + v_H\right)\right\} \ . \tag{3.66}$$

A schematic representation of the H-PWM is depicted in Fig. 3.14. It allows φ_H or ψ_H maximization depending on the voltage sector for any ε and σ_i values. Therefore, it can be successfully employed for discharging C_H in cases O.0.I and E.0.III, as just highlighted. However, it is worth nothing that it can be also employed for different combinations of ε and σ_i, may leading to C_H discharging.

A similar procedure can be followed for defining the L-PWM, whose schematic representation is shown in Fig. 3.15. Particularly, it allows ψ_L or φ_L maximization in correspondence of odd and even voltage sectors respectively, in accordance with the following relationships:

$$\varphi_H^{*} = \frac{1}{v_H} max\left\{0, v_{uv}^{*} - v_L\right\} \tag{3.67}$$

$$\varphi_L^* = \frac{1}{v_L} max\left\{0, min\left\{-v_{uv}^*, v_L\right\}\right\} \tag{3.68}$$

$$\psi_H^* = \frac{1}{v_H} max\left\{0, -\left(v_{uv}^* + v_L\right)\right\} \tag{3.69}$$

$$\psi_L^* = \frac{1}{v_L} max\left\{0, min\left\{v_{uv}^*, v_L\right\}\right\} \tag{3.70}$$

$$\xi_H^* = \frac{1}{v_H} max\left\{0, -\left(v_{vw}^* + v_L\right), v_{wu}^* - v_L\right\} \tag{3.71}$$

$$\xi_L^* = \frac{1}{v_L} max\left\{0, min\left\{v_{vw}^* + \psi_L v_L, -v_{wu}^* + \varphi_L V_L\right\}\right\} \ . \tag{3.72}$$

Unfortunately, H-PWM and L-PWM are not able to maximize or minimize i_H for all combinations of σ_v, ε, σ_i. This can be proved by referring to the case O.0.II (σ_v = I/III/V, ε = 0, σ_i = II), in correspondence of which voltage and current equations are still expressed by (3.49) and (3.50) respectively. Particularly, φ_H can be still maximized, as in case O.0.I, but this must not imply increasing ξ_H. This occurs because i_w is negative and characterized by a magnitude greater than i_u, thus, ξ_H should be minimized. In addition, also ξ_L should be minimized in order to increase φ_H as much as possible. Based on these considerations, the M-PWM shown in Fig. 3.16 can be introduced, which allows both ξ_H and ξ_L minimization in accordance with the following relationships:

$$\varphi_H^* = \frac{1}{v_H} max\left\{0, min\left\{-v_{wu}^* + \xi_H v_H, v_H\right\}\right\} \tag{3.73}$$

$$\varphi_L^* = \frac{1}{v_L} max\left\{0, min\left\{v_{wu}^* + \xi_L v_L, v_L\right\}\right\} \tag{3.74}$$

$$\psi_H^* = \frac{1}{v_H} max\left\{0, min\left\{v_{vw}^* + \xi_H v_H, v_H\right\}\right\} \tag{3.75}$$

$$\psi_L^* = \frac{1}{v_L} max\left\{0, min\left\{-v_{vw}^* + \xi_L v_L, v_L\right\}\right\} \tag{3.76}$$

$$\xi_H^* = \frac{1}{v_H} max\left\{0, -\left(v_{vw}^* + v_L\right), v_{wu}^* - v_L\right\} \tag{3.77}$$

$$\xi_L^* = \frac{1}{v_L} max\left\{0, v_{vw}^* - v_H, -\left(v_{wu}^* + v_H\right)\right\} \ . \tag{3.78}$$

In conclusion, H-PWM, L-PWM and M-PWM base equations are summarized in Table XVI through Table XVIII, whereas the overall scheme of the proposed HML-PWM is depicted in Fig. 3.17. In particular, based on $\{\varepsilon,\sigma_v,\sigma_i\}$, H-PWM, L-PWM and M-PWM are alternatively employed in order to provide suitable C_H charging or discharging, as pointed out in Table XIX. It is worth noting that any PWM patterns guarantees the achievement of the reference chain voltages, thus prioritizing SPM requirements compared to DC-link voltage regulation needs.

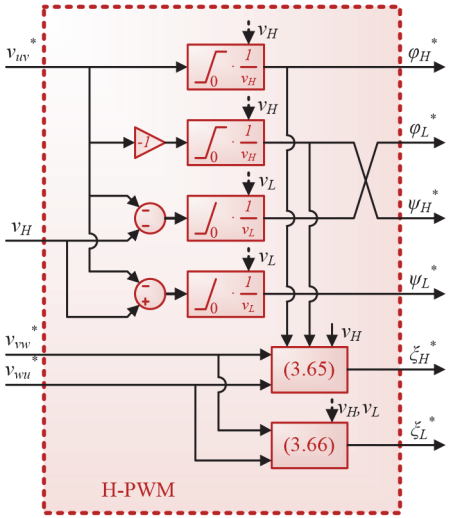

Fig. 3.14 Schematic representation of the H-PWM.

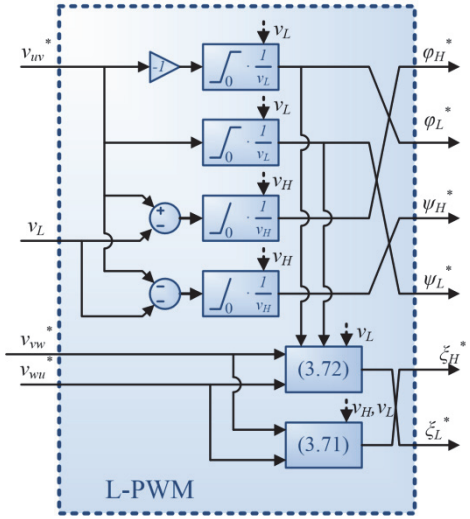

Fig. 3.15 Schematic representation of the L-PWM.

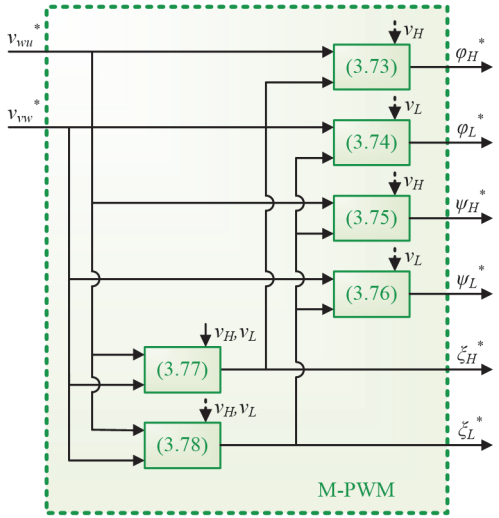

Fig. 3.16 Schematic representation of the M-PWM.

TABLE XVI
H-PWM PATTERNS

φ_H	$\frac{1}{v_H} max\{0, min\{v_{uv}^*, v_H\}\}$	(3.61)
φ_L	$\frac{1}{v_L} max\{0, -(v_{uv}^* + v_H)\}$	(3.62)
ψ_H	$\frac{1}{v_H} max\{0, min\{-v_{uv}^*, v_H\}\}$	(3.63)
ψ_L	$\frac{1}{v_L} max\{0, -(v_{uv}^* - v_H)\}$	(3.64)
ξ_H	$\frac{1}{v_H} max\{0, min\{-v_{vw}^* + \psi_H v_H, v_{wu}^* + \varphi_H v_H\}\}$	(3.65)
ξ_L	$\frac{1}{v_L} max\{0, v_{vw}^* - v_H, -(v_{wu}^* + v_H)\}$	(3.66)

TABLE XVII
L-PWM PATTERNS

φ_H	$\frac{1}{v_H} max\{0, v_{uv}^* - v_L\}$	(3.67)
φ_L	$\frac{1}{v_L} max\{0, min\{-v_{uv}^*, v_L\}\}$	(3.68)
ψ_H	$\frac{1}{v_H} max\{0, -(v_{uv}^* + v_L)\}$	(3.69)
ψ_L	$\frac{1}{v_L} max\{0, min\{v_{uv}^*, v_L\}\}$	(3.70)
ξ_H	$\frac{1}{v_H} max\{0, -(v_{vw}^* + v_L), v_{wu}^* - v_L\}$	(3.71)
ξ_L	$\frac{1}{v_L} max\{0, min\{v_{vw}^* + \psi_L v_L, -v_{wu}^* + \varphi_L V_L\}\}$	(3.72)

TABLE XVIII
M-PWM PATTERNS

φ_H	$\frac{1}{v_H} max\{0, min\{-v_{wu}^* + \xi_H v_H, v_H\}\}$	(3.73)
φ_L	$\frac{1}{v_L} max\{0, min\{v_{wu}^* + \xi_L v_L, v_L\}\}$	(3.74)
ψ_H	$\frac{1}{v_H} max\{0, min\{v_{vw}^* + \xi_H v_H, v_H\}\}$	(3.75)
ψ_L	$\frac{1}{v_L} max\{0, min\{-v_{vw}^* + \xi_L v_L, v_L\}\}$	(3.76)
ξ_H	$\frac{1}{v_H} max\{0, -(v_{vw}^* + v_L), v_{wu}^* - v_L\}$	(3.77)
ξ_L	$\frac{1}{v_L} max\{0, v_{vw}^* - v_H, -(v_{wu}^* + v_H)\}$	(3.78)

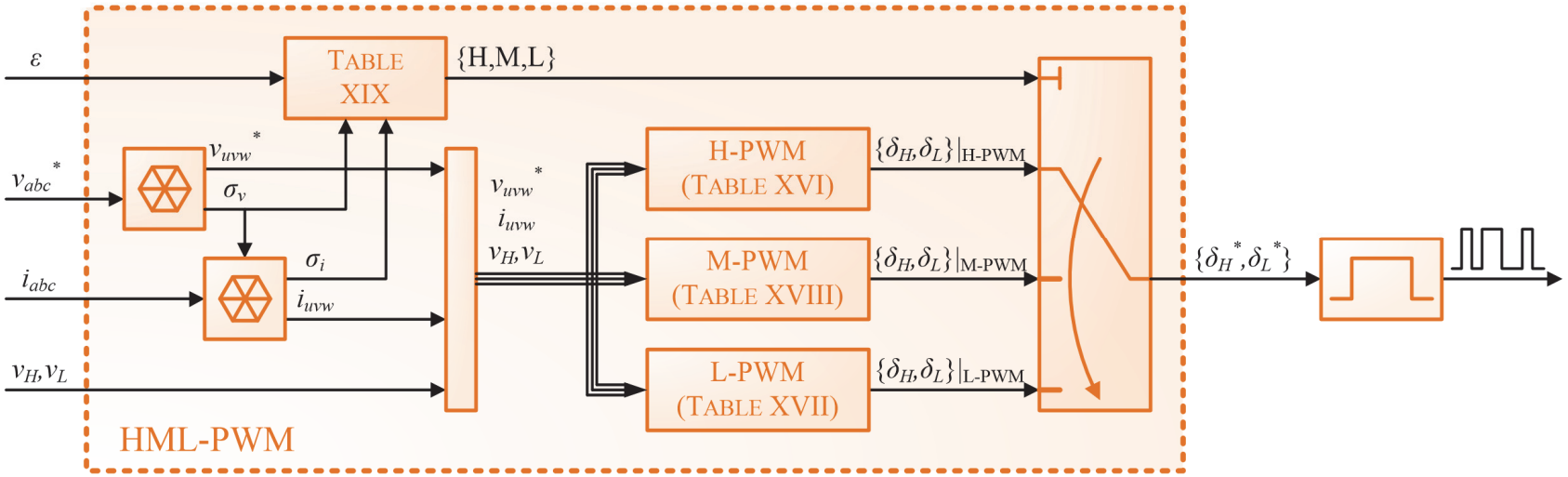

Fig. 3.17 Equivalent block control scheme of the proposed HML-PMW.

TABLE XIX
HML-PWM

$\varepsilon = 0$		σ_i					
		I	II	III	IV	V	VI
σ_v	I	H-PWM	M-PWM	L-PWM	L-PWM	H-PWM	H-PWM
	II	L-PWM	M-PWM	H-PWM	H-PWM	H-PWM	L-PWM
	III	H-PWM	M-PWM	L-PWM	L-PWM	H-PWM	H-PWM
	IV	L-PWM	M-PWM	H-PWM	H-PWM	H-PWM	L-PWM
	V	H-PWM	M-PWM	L-PWM	L-PWM	H-PWM	H-PWM
	VI	L-PWM	M-PWM	H-PWM	H-PWM	H-PWM	L-PWM

$\varepsilon = 1$		σ_i					
		I	II	III	IV	V	VI
σ_v	I	L-PWM	H-PWM	H-PWM	H-PWM	M-PWM	L-PWM
	II	H-PWM	H-PWM	H-PWM	H-PWM	M-PWM	H-PWM
	III	L-PWM	H-PWM	H-PWM	H-PWM	M-PWM	L-PWM
	IV	H-PWM	H-PWM	H-PWM	H-PWM	M-PWM	H-PWM
	V	L-PWM	H-PWM	H-PWM	H-PWM	M-PWM	L-PWM
	VI	H-PWM	H-PWM	H-PWM	H-PWM	M-PWM	H-PWM

3.2.2.2 PS-PWM

The HML-PWM described in the previous subsection allows DC-link regulation by charging or discharging the high-side capacitor as needed. This goal is achieved through a binary signal ε, based on which i_H is maximized or minimized, as occurs in hysteresis-based control system. Although such a procedure is quite simple and easy to be implemented, it inherently introduces high-frequency current and voltage ripple, especially at steady state operation. As a consequence, high-frequency currents harmonics may arise, leading to capacitor over-stresses and/or electromagnetic compatibility issues. These drawbacks can be both overcome by designing another PWM pattern that enables a fine regulation of DC-link voltages by means of DC-link currents. These last should thus be driven appropriately, avoiding their maximization or minimization when unnecessary.

Based on the previous consideration, a novel PWM pattern has been developed with the aim of guaranteeing improved performances compared to HML-PWM. Thus, considering the per unit reference chain voltages in the *uvw* frame, they can be expressed as

$$\begin{aligned} v_{uv}^{*} &= v_u - v_v \\ v_{vw}^{*} &= v_v - v_w \\ v_{wu}^{*} &= v_w - v_u \end{aligned} \tag{3.79}$$

in which the phase terminal voltages boundaries are still expressed by (3.45), which is reported below for convenience purposes:

$$-v_L \le v_x \le v_H \quad , \quad x \in \{u,v,w\} \ . \tag{3.45}$$

Therefore, based on (3.79), v_u and v_v can be expressed as:

$$\begin{aligned} v_u &= -v_{wu}^{*} + v_w \\ v_v &= v_{vw}^{*} + v_w \ . \end{aligned} \tag{3.80}$$

Thus, the substitution of (3.80) in (3.45) yields

$$v_{w,min} \le v_w \le v_{w,max} \tag{3.81}$$

where:

$$\begin{aligned} v_{w,min} &= max\left\{v_{wu}^{*}, -v_{vw}^{*}\right\} - v_L \\ v_{w,max} &= min\left\{v_{wu}^{*}, -v_{vw}^{*}\right\} + v_H \, . \end{aligned} \tag{3.82}$$

As a result, based on (3.81), it can be stated that the reference chain voltages can be successfully achieved for any v_w lying within $[v_{w,min}, v_{w,max}]$. Consequently, v_w can be suitably chosen in accordance with (3.81) in order to satisfy DC-link voltage regulation needs at the maximum extent. For this purpose, reference can be made to both i_H and i_L, which are expressed as

$$\begin{aligned} i_H &= \varphi_H \, i_u + \psi_H \, i_v + \xi_H \, i_w \\ i_L &= -\left(\varphi_L \, i_u + \psi_L \, i_v + \xi_L \, i_w\right) \end{aligned} \tag{3.83}$$

where each duty cycle contributes to the corresponding phase terminal voltage in accordance with (3.44), as reported below for convenience purposes:

$$v_x = \delta_H v_H - \delta_L v_L \quad , \quad \begin{matrix} x \in \{u,v,w\} \\ \delta \in \{\varphi,\psi,\xi\} \end{matrix} \tag{3.44}$$

Particularly, assuming that H and L states of each leg cannot occur over the same sampling time interval, δ_H and δ_L are equal to zero alternatively:

$$\delta_H \cdot \delta_L = 0 \quad , \quad \delta \in \{x, y, z\} . \tag{3.84}$$

It is worth noting that such an assumption does not affect the phase terminal voltages, which are still bounded in accordance with (3.45). Thus, based on both (3.44) and (3.84), the following relationships can be introduced:

$$\delta_H = \frac{|v_x| + v_x}{2 v_H} \ , \ \delta_L = \frac{|v_x| - v_x}{2 v_L} \quad , \quad \begin{matrix} x \in \{u, v, w\} \\ \delta \in \{\varphi, \psi, \xi\} \end{matrix} . \tag{3.85}$$

Consequently, by substituting (3.85) in (3.83), i_H and i_L can be further expressed as:

$$\begin{matrix} i_H = \dfrac{1}{2 v_H} \left(\sum\limits_x |v_x| i_x + \sum\limits_x v_x i_x \right) \\ i_L = -\dfrac{1}{2 v_L} \left(\sum\limits_x |v_x| i_x - \sum\limits_x v_x i_x \right) \end{matrix} \quad , \quad x \in \{u, v, w\} . \tag{3.86}$$

Based on (3.86), it is possible to introduce two additional DC-link currents, i.e. i_p and i_s, which are defined respectively as

$$\begin{matrix} i_p = v_H i_H + v_L i_L = \sum\limits_x v_x i_x \\ i_s = v_H i_H - v_L i_L = \sum\limits_x |v_x| i_x \end{matrix} \quad , \quad x \in \{u, v, w\} . \tag{3.87}$$

It is worth noting that i_p represents the equivalent power current drawn by the NPC load, as already defined in (3.28). Hence, by substituting (3.80) in (3.87), the following results are achieved:

$$\begin{matrix} i_p = -v_{wu}^* i_u + v_{vw}^* i_v + v_w \left(i_u + i_v + i_w \right) \\ i_s = \left| -v_{wu}^* + v_w \right| \cdot i_u + \left| v_{vw}^* + v_w \right| \cdot i_v + \left| v_w \right| \cdot i_w \end{matrix} . \tag{3.88}$$

Thus, focusing on i_p at first, it can be stated that it does not generally depend on v_w because the sum of the phase currents is equal to zero in an isolated star-connected three-phase system, as occurring in the majority of applications. Consequently, i_s can be controlled by v_w in accordance with DC-link voltage regulation needs, without affecting the power exchange between the NPC and its load.

In order to perform an i_s control, the following relationships can be considered:

$$i_s = \left| -v_{wu}^* + v_w \right| \cdot i_u + \left| v_{vw}^* + v_w \right| \cdot i_v + \left| v_w \right| \cdot i_w \tag{3.89}$$

$$v_{w,min} \le v_w \le v_{w,max} . \tag{3.81}$$

Therefore, both voltage and current sectors must be considered, as for the HML-PWM. Particularly, over odd voltage sectors (σ_v = I,III,V), (3.82) becomes

$$\begin{matrix} v_{w,min} = -v_{vw}^* - v_L \\ v_{w,max} = v_{wu}^* + v_H \end{matrix} \tag{3.90}$$

whereas over even voltage sectors (σ_v = II,IV,VI), (3.82) is expressed as

$$\begin{matrix} v_{w,min} = v_{wu} - v_L \\ v_{w,max} = -v_{vw} + v_H \end{matrix} . \tag{3.91}$$

As a consequence, based on either (3.90) or (3.91), the i_s evolution versus v_w can be achieved for each (σ_v,σ_i) pair of values, as pointed out in Table XX and highlighted in Fig. 3.18 through Fig. 3.29.

Particularly, it can be seen that minimum and maximum values of i_s are generally achieved in correspondence of either $v_w^{(+)}$ and $v_w^{(-)}$, which are defined respectively as

$$\begin{aligned} v_w^{(+)} &= max\left\{v_{wu}^*, -v_{vw}^*\right\} \\ v_w^{(-)} &= min\left\{v_{wu}^*, -v_{vw}^*\right\} \ . \end{aligned} \tag{3.92}$$

Consequently, if at least one of these values lies within [$v_{w,min}$,$v_{w,max}$], it means that a *plateau* region occurs, as highlighted in Table XXI and Table XXII, as well as in Fig. 3.18 through Fig. 3.29. Over such operating regions, any further variation of v_w does not affect i_s because the sum of the phase currents equals zero, as assumed previously. However, it is worth noting that, referring to the II and V current sector, minimum and maximum values of i_s occur when v_w is zero, as shown in Fig. 3.19, Fig. 3.22, Fig. 3.25 and Fig. 3.28. These also highlight that a given i_s value (i_s^*) may correspond to two different v_w values, i.e. v_w^* and $\tilde{v}_w$. In such cases, v_w^* should be chosen because it lies within the v_w interval that guarantees a linear control of i_s within its full range. This interval can be identified by introducing the following binary variable:

$$\sigma_0 = sign\left\{\left|i_s\left(v_{w,max}\right) - i_s\left(0\right)\right| - \left|i_s\left(v_{w,min}\right) - i_s\left(0\right)\right|\right\} \ . \tag{3.93}$$

In conclusion, based on all the previous considerations, the PS-PWM pattern can be introduced as in Fig. 3.30. Particularly, for any given v_{ch}^* and i_s^*, the most suitable v_w^* can be chosen in accordance with Table XX. Once v_w^* is determined, it is then possible to compute the other phase terminal voltages by means of (3.80) and, thus, all the H and L duty cycles by means of (3.85).

The PS-PWM just described enables an appropriate regulation of i_s, by means of which HESS requirements can be satisfied at the maximum extent. However, in order to further increase i_s regulation capability, (3.84) should not be assumed. This means that both H and L states may both occur over a sampling time interval. Therefore, the duty cycles of each leg can be expressed as

$$\delta_H = \overline{\delta}_H + \tilde{\delta}_H \quad , \quad \delta_L = \overline{\delta}_L + \tilde{\delta}_L \quad , \quad \delta \in \{\varphi, \psi, \xi\} \tag{3.94}$$

where $\overline{\delta_H}$ and $\overline{\delta_L}$ are chosen in accordance with (3.84), whereas $\tilde{\delta}_H$ and $\tilde{\delta}_L$ denote additional duty cycles, which must satisfy the following relationship

$$v_H \tilde{\delta}_H - v_L \tilde{\delta}_L = 0 \quad , \quad \delta \in \{\varphi, \psi, \xi\} \ . \tag{3.95}$$

TABLE XX
v_w^* EXPRESSION FOR ODD AND EVEN VOLTAGE SECTORS

σ_i	σ_v = I, III, V	σ_i	σ_v = II, IV, VI
I IV	$\frac{1}{2} max\left\{v_{wu}^* + \frac{i_s^* + v_{vu}^* i_v}{i_u}, -v_{vw}^* - \frac{i_s^* + v_{wu}^* i_u}{i_v}\right\}$	I IV	$\frac{1}{2} min\left\{v_{wu}^* - \frac{i_s^* - v_{vu}^* i_v}{i_u}, -v_{vw}^* + \frac{i_s^* - v_{wu}^* i_u}{i_v}\right\}$
II V	$-\frac{1}{2}\left(v_{vw}^* + \frac{i_s^* + v_{wu}^* i_u}{i_v}\right)$, $for\ \sigma_0 = 0$ $\frac{1}{2}\left(v_{wu}^* + \frac{i_s^* + v_{vu}^* i_v}{i_u}\right)$, $for\ \sigma_0 = 1$	II V	$-\frac{1}{2}\left(v_{wu}^* - \frac{i_s^* - v_{vu}^* i_v}{i_u}\right)$, $for\ \sigma_0 = 0$ $\frac{1}{2}\left(-v_{vw}^* + \frac{i_s^* - v_{wu}^* i_u}{i_v}\right)$, $for\ \sigma_0 = 1$
III VI	$\frac{1}{2} min\left\{v_{wu}^* + \frac{i_s^* + v_{vu}^* i_v}{i_u}, -v_{vw}^* - \frac{i_s^* + v_{wu}^* i_u}{i_v}\right\}$	III VI	$\frac{1}{2} max\left\{v_{wu}^* - \frac{i_s^* - v_{vu}^* i_v}{i_u}, -v_{vw}^* + \frac{i_s^* - v_{wu}^* i_u}{i_v}\right\}$

TABLE XXI

i_s EXPRESSIONS OVER ODD SECTORS

$v^*_{wu} \cdot i_u - v^*_{vw} \cdot i_v$	$v_{w,min} \le v_w \le -v^*_{vw}$
$-v^*_{wu} \cdot i_u - v^*_{vw} \cdot i_v + 2 \cdot v_w \cdot i_u$	$-v^*_{vw} < v_w \le 0$
$-v^*_{wu} \cdot i_u - v^*_{vw} \cdot i_v - 2 \cdot v_w \cdot i_v$	$0 < v_w \le v^*_{wu}$
$-v^*_{wu} \cdot i_u + v^*_{vw} \cdot i_v$	$v^*_{wu} < v_w \le v_{w,max}$

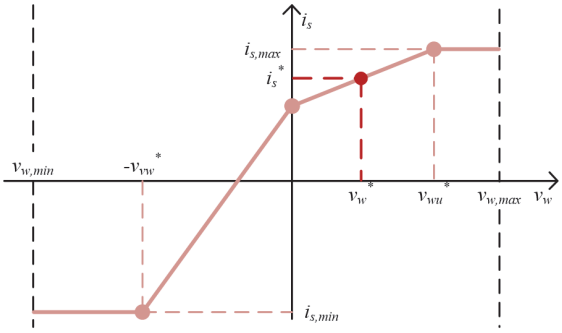

Fig. 3.18 The i_s evolution over any odd voltage sector and first current sectors.

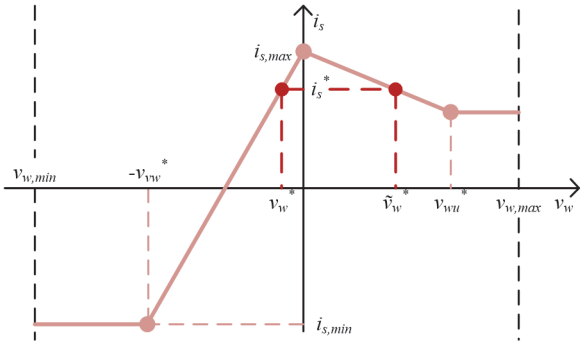

Fig. 3.19 The i_s evolution over any odd voltage sector and second current sectors.

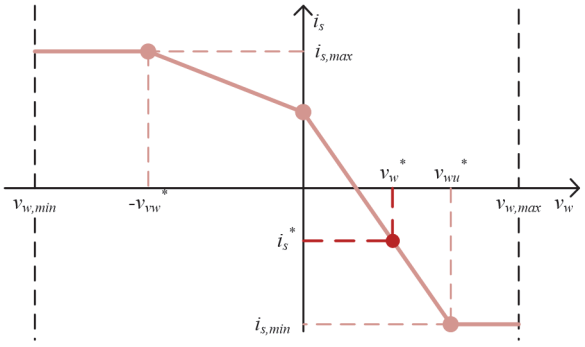

Fig. 3.20 The i_s evolution over any odd voltage sector and third current sectors.

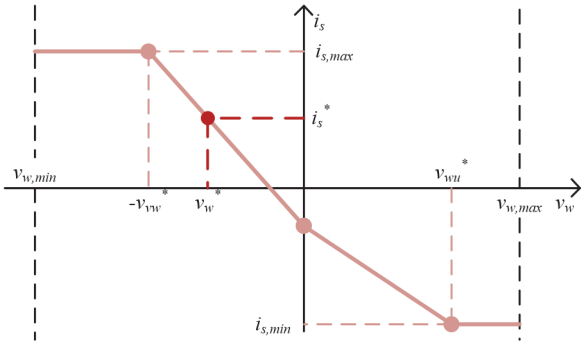

Fig. 3.21 The i_s evolution over any odd voltage sector and fourth current sectors.

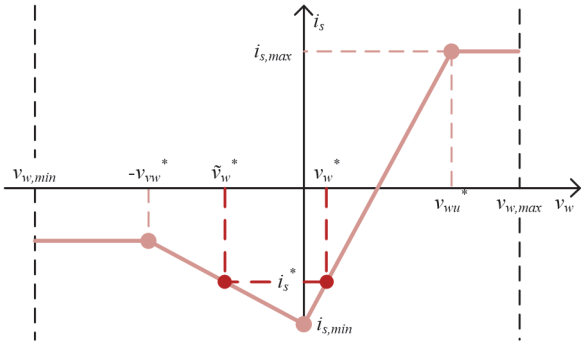

Fig. 3.22 The i_s evolution over any odd voltage sector and fifth current sectors.

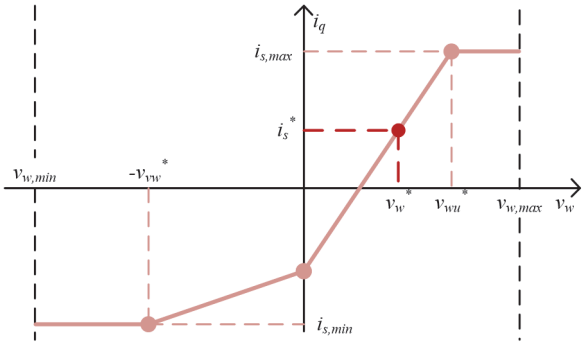

Fig. 3.23 The i_s evolution over any odd voltage sector and sixth current sectors.

TABLE XXII

i_s EXPRESSIONS OVER EVEN SECTORS

$v_{wu} \cdot i_u - v_{vw} \cdot i_v$	$v_{w,min} \le v_w \le v_{wu}$
$v_{wu} \cdot i_u + v_{vw} \cdot i_v + 2 \cdot v_w \cdot i_v$	$v_{wu} < v_w \le 0$
$v_{wu} \cdot i_u - v_{vw} \cdot i_v - 2 \cdot v_w \cdot i_u$	$0 < v_w \le -v_{vw}$
$-v_{wu} \cdot i_u + v_{vw} \cdot i_v$	$-v_{vw} < v_w \le v_{w,max}$

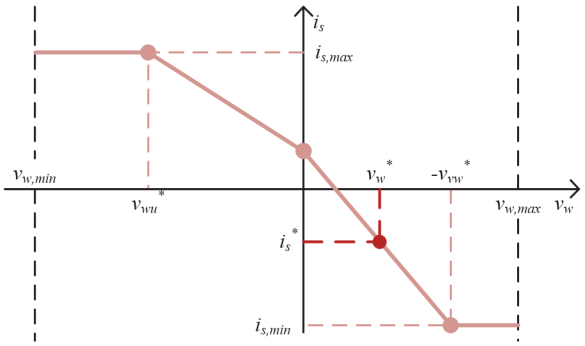

Fig. 3.24 The i_s evolution over any even voltage sector and first current sectors.

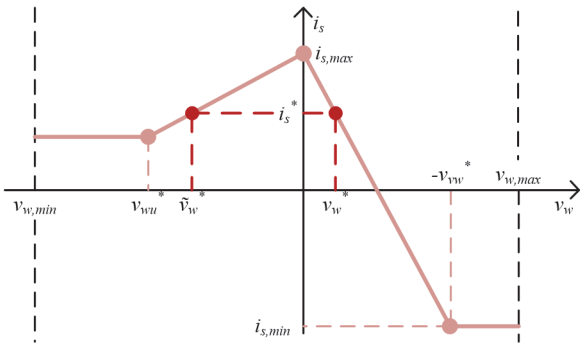

Fig. 3.25 The i_s evolution over any even voltage sector and second current sectors.

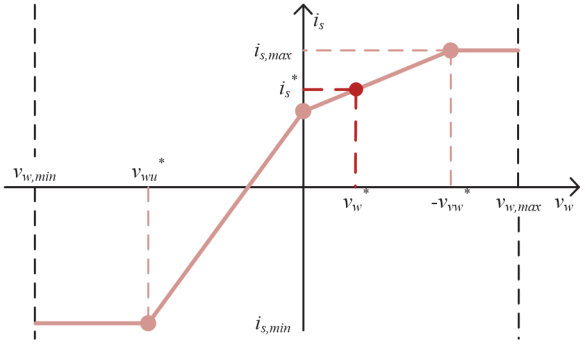

Fig. 3.26 The i_s evolution over any even voltage sector and third current sectors.

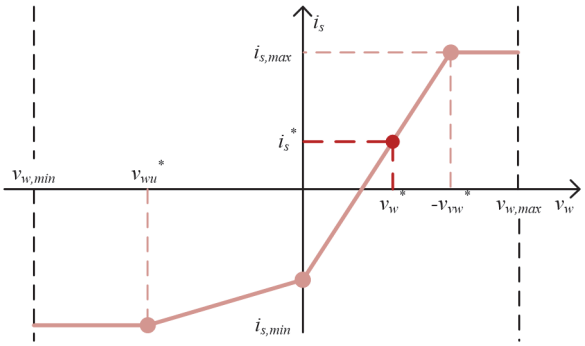

Fig. 3.27 The i_s evolution over any even voltage sector and fourth current sectors.

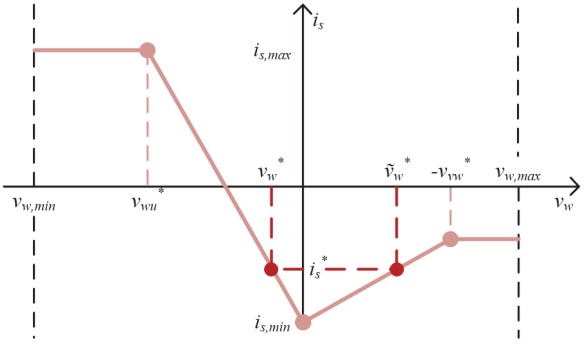

Fig. 3.28 The i_s evolution over any even voltage sector and fifth current sectors.

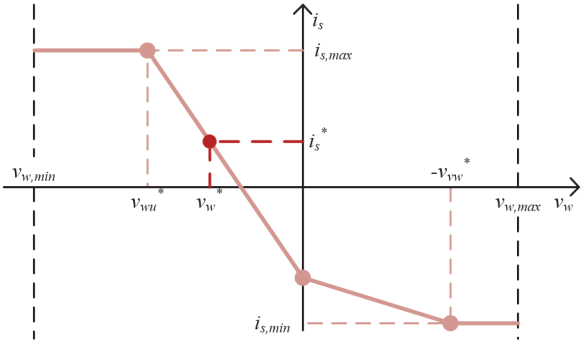

Fig. 3.29 The i_s evolution over any even voltage sector and sixth current sectors.

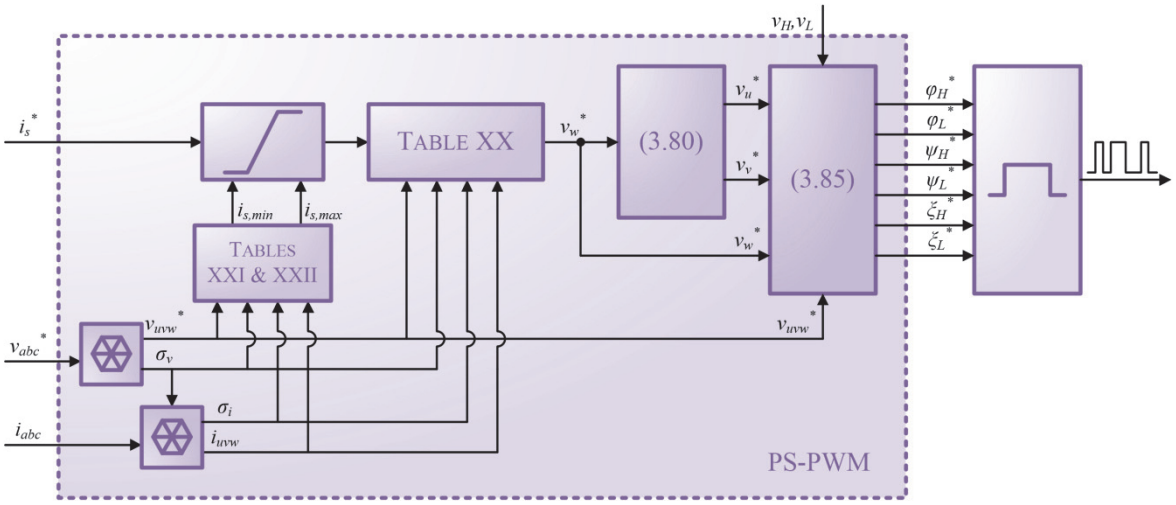

Fig. 3.30 Equivalent block control scheme of the proposed PS-PWM.

Consequently, based on (3.44) and (3.95), it can be stated that additional duty cycles do not contribute to phase terminal voltages and, thus, to the achievement of the reference chain voltages. Furthermore, considering (3.46), additional duty cycles are bounded in accordance with the following inequality:

$$\tilde{\delta}_H + \tilde{\delta}_L \le 1 - \left(\bar{\delta}_H + \bar{\delta}_L\right) \quad , \quad \delta \in \{\varphi, \psi, \xi\} \ . \tag{3.96}$$

As a result, by substituting (3.94) in (3.83), DC-link currents can be expressed as

$$\begin{aligned} i_H &= \bar{i}_H + \sum_{\delta,x} \tilde{\delta}_H i_x \\ i_L &= \bar{i}_L - \sum_{\delta,x} \tilde{\delta}_L i_x \end{aligned} \tag{3.97}$$

where $\bar{\imath}_H$ and $\bar{\imath}_L$ are still expressed as in (3.86). Therefore, by combining (3.97) with (3.87), i_p and i_s can now be expressed as

$$\begin{aligned} i_p &= \bar{i}_p \\ i_s &= \bar{i}_s + \tilde{i}_s \end{aligned} \tag{3.98}$$

in which

$$\tilde{i}_s = \sum_{\delta,x} \left(v_H \tilde{\delta}_H + v_L \tilde{\delta}_L\right) i_x \quad , \quad x \in \{u, v, w\} \ . \tag{3.99}$$

It is worth noting that the introduction of addition duty cycles does not affect i_p due to (3.95), as expected. Furthermore, by combining (3.95) with (3.99) and (3.96), the following results are achieved:

$$\tilde{i}_s = 2 v_H \sum_{\delta,x} \tilde{\delta}_H i_x \quad , \quad x \in \{u, v, w\} \tag{3.100}$$

$$\tilde{\delta}_H \le v_L \left(1 - \bar{\delta}_H - \bar{\delta}_L\right) \quad , \quad \delta \in \{\varphi, \psi, \xi\} \ . \tag{3.101}$$

In conclusion, based on both (3.100) and (3.101), the i_s boundaries can be usefully extended, thus enabling i_s regulation over a wider range. However, it is worth noting that PS-PWM should resort to additional duty cycles only when needed because they increase the number of commutation within the sampling time interval, thus leading to increased switching losses.

3.2.3 HESS Control

The HESS control system has been developed in order to manage the energy flows among the battery and the UC-capacitor module appropriately. Particularly, during SPM acceleration, the UC-capacitor module should supply the majority of the SPM energy demand. Similarly, during regenerative braking, it should store most of the energy recovered by the SPM. Consequently, the battery should supply steady state SPM energy demand only, thus appropriately preserving its rated performances and extending its life.

All these goals can be achieved by means of the control architecture shown in Fig. 3.31. It consists of three control loops, which allow the regulation of DC-link energy content, battery current and overall DC-link voltage simultaneously. Particularly, the outer loop aims to synthesize the most suitable reference battery current in order to achieve a given reference DC-link energy level. This is done based on both (3.27) and (3.16), which are reported below for convenience purpose:

$$\frac{dE_{DC}}{dt} = V_{DC}\left(i_B - i_p\right) \tag{3.27}$$

$$V_B = r_B i_B + L_B \frac{di_B}{dt} + V_{DC} \ . \tag{3.16}$$

It is worth noting that the reference DC-link energy level should vary in accordance with SPM operating conditions, i.e. it should decrease as SPM speed increases in order to charge or discharge the UC-capacitor module as desired. Particularly, at low speed operation, ultra-capacitors should be well charged for upcoming acceleration, whereas they should be sufficiently discharged at high speed operation in order to handle regenerative braking on their own mostly.

Once the reference battery current is achieved, it is then tracked by means of the intermediate control loop, which determines a suitable reference profile for the overall DC-link voltage based on (3.16). Subsequently, the inner control loop synthesizes the corresponding equivalent DC-link current profile in accordance with:

$$C_{DC}\frac{dV_{DC}}{dt} = i_B - i_{DC} \quad , \quad i_{DC} = c_H i_H + c_L i_L \ . \tag{3.18}$$

Finally, based on both i_{DC} and i_p, it is possible to determine the corresponding reference input value for the PS-PWM as

$$i_s^* = i_p \frac{c_L v_H + c_H v_L}{c_L v_H - c_H v_L} - 2\, i_{DC} \frac{2\, v_H v_L}{c_L v_H - c_H v_L} \ . \tag{3.102}$$

In conclusion, it is worth noting that (3.27), (3.16) and (3.18) highlight a significant coupling among E_{DC}, V_{DC} and i_B. Consequently, HESS control system design is harder to be accomplished compared to SPM control, in which speed and currents are quite decupled. In this context, it is also worthy of note that the employment of an NPC for interfacing the HESS with the SPM allows a partial decupling

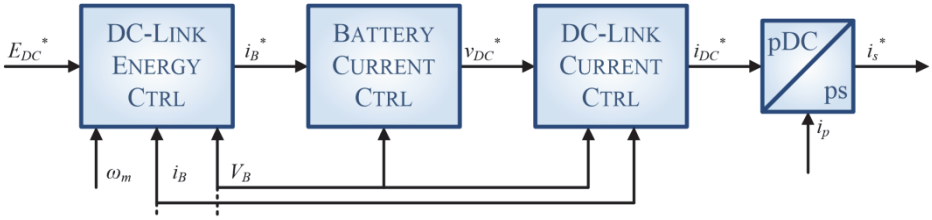

Fig. 3.31 The overall HESS control system.

between E_{DC} and V_{DC}, which cannot be achieved resorting to conventional two-level converters. The designing of each HESS control loop is detailed in the following subsections.

3.2.3.1 DC-link Energy Control System

A schematic representation of the energy control loop is depicted in Fig. 3.32, where P_B and P denote battery and SPM power respectively:

$$P_B = V_{DC} i_B \tag{3.103}$$

$$P = V_{DC} i_p = V_H i_H + V_L i_L \ . \tag{3.104}$$

In addition, it is assumed that both battery current and DC-link current control loops are quite faster than the energy loop so that their closed-loop transfer functions can be both neglected. Consequently, referring to Fig. 3.32, the energy closed-loop transfer function can be expressed as

$$W_E(s) = \frac{E_{DC}}{E_{DC}^*} = \frac{R_E(s)}{s + R_E(s)} P_B - \frac{1}{s + R_E(s)} P \ . \tag{3.105}$$

Hence, based on (3.105), a PI regulator is needed in order to guarantee an appropriate tracking of the reference DC-link energy profile. Therefore, R_E should be chosen as:

$$R_E(s) = k_p^{(E)} + \frac{k_i^{(E)}}{s} \ . \tag{3.106}$$

Thus, by substituting (3.106) in (3.105), the following equation is achieved

$$W_E(s) = \frac{k_p^{(E)} s + k_i^{(E)}}{s^2 + k_p^{(E)} s + k_i^{(E)}} P_B - \frac{s}{s^2 + k_p^{(E)} s + k_i^{(E)}} P \ . \tag{3.107}$$

Based on (3.107), both k_p and k_i can be chosen in accordance with the following relationships:

$$k_p^{(E)} = 4\pi f_c^{(E)} \ \Rightarrow \ k_i^{(E)} = \left(2\pi f_c^{(E)}\right)^2 \ . \tag{3.108}$$

The equivalent block control scheme of the energy control system is depicted in Fig. 3.33. Particularly, once P_B^* is achieved, the corresponding i_B^* can be determined by substituting (3.16) in (3.103), leading to

$$P_B^* = i_B^* \cdot \left(V_B - r_B i_B^* - L_B \frac{di_B^*}{dt} \right) \ . \tag{3.109}$$

Furthermore, assuming L_B negligible, i_B^* can be expressed as

$$i_B^* = \frac{V_B}{2r_B} - \sqrt{\left(\frac{V_B}{2r_B}\right)^2 - \frac{P_B^*}{r_B}} \ . \tag{3.110}$$

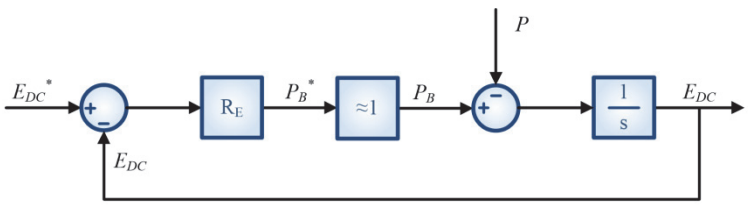

Fig. 3.32 Schematic representation of the energy control loop.

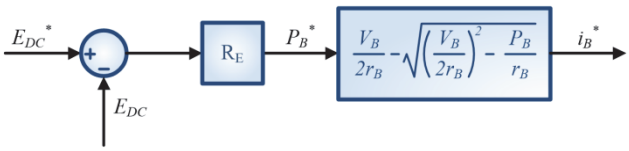

Fig. 3.33 Equivalent block control scheme of the energy control system.

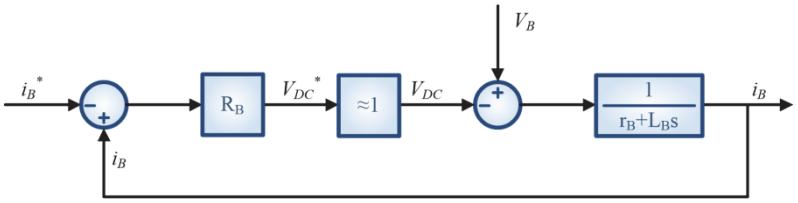

Fig. 3.34 Battery current control loop.

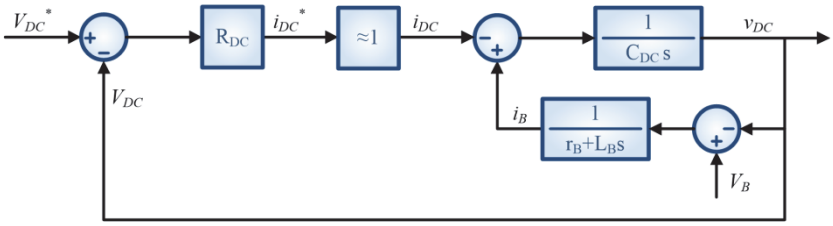

Fig. 3.35 DC-link voltage loop.

3.2.3.2 Battery Current Control System

The battery current control system can be designed based on the corresponding closed-control loop depicted in Fig. 3.34. Particularly, DC link voltage control is assumed almost instantaneous so that its transfer function is safely neglected. As a consequence, the battery current control loop is quite similar to the SPM speed control loop, thus leading to employ the same design solutions. Particularly, a PI regulator is employed, whose transfer function can be expressed as

$$R_B(s)=k_p^{(B)}\frac{(s-z_B)}{s}\quad,\quad z_B=-\frac{k_i^{(B)}}{k_p^{(B)}} \tag{3.111}$$

In addition, proportional and integral gains have been chosen in accordance with the following relationships:

$$k_p^{(B)}=2\pi f_c^{(B)}L_B\ \Rightarrow\ k_i^{(B)}=2\pi f_c^{(B)}r_B \tag{3.112}$$

As a result, open-loop and closed-loop transfer functions can be achieved respectively as:

$$G_B(s)=\frac{k_p^{(B)}}{L_B}\cdot\frac{1}{s} \tag{3.113}$$

$$W_B(s)=\frac{I_B}{I_B^*}=\frac{k_p^{(B)}}{L_B s+k_p^{(B)}} \tag{3.114}$$

3.2.3.3 DC-link Voltage Control System

The DC-link voltage control system has been developed based on the corresponding loops depicted in Fig. 3.35. Particularly, the inner feed-forward loop can be simplified by introducing the following transfer function:

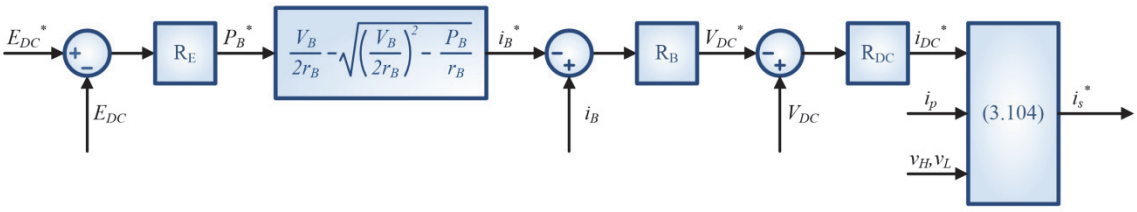

Fig. 3.36 The overall HESS control system

$$W(s)=\frac{V_{DC}}{-I_{DC}}=\frac{1}{C_{DC}}\cdot\frac{s-z_B}{(s-p_1)(s-p_2)} \quad , \quad z_B=-\frac{r_B}{L_B} \quad , \quad p_{12}=-\frac{z_B}{2}\pm\sqrt{\left(\frac{z_B}{2}\right)^2-\frac{1}{C_{DC}L_B}} \quad . \tag{3.115}$$

A PI regulator is then introduced, whose transfer function can be expressed as:

$$R_{DC}(s)=k_p^{(DC)}\frac{(s-z_{DC})}{s} \quad , \quad z_{DC}=-\frac{k_i^{(DC)}}{k_p^{(DC)}} \quad . \tag{3.116}$$

As a consequence, the open loop transfer function of the overall DC-link voltage loop can be expressed as:

$$G_{DC}(s)=\frac{V_{DC}}{\Delta V_{DC}}=-\frac{k_p^{(DC)}}{C_{DC}}\cdot\frac{(s-z_{DC})(s-z_B)}{s(s-p_1)(s-p_2)} \quad . \tag{3.117}$$

It is thus possible to select the most suitable values of the proportional and integral gains in order to simplify (3.117) further. In addition, such a choice must guarantee that the DC-link voltage control system is quite faster than the other ones, i.e. battery current and energy control systems.

In conclusion, it is worth noting that DC-link voltage is driven by means of i_{DC}, which can be instantaneously varied by the NPC control. Particularly, NPC control system is fed by i_s^*, which can be determined by means of both i_{DC}^* and i_p^* as in (3.102). As a result, the overall HESS control can be represented as in Fig. 3.36

3.3 Simulations

In order to verify the performances of the proposed EPS, a number of simulation studies are carried out in the Matlab Simulink environment referring to the set-up shown in Fig. 3.37. This consists mainly of an SPM, an NPC and the proposed HESS, whose parameters and rated values are reported in Table XXIII. Focusing on the SPM at first, its inertia coefficient has been set in order to guarantee its acceleration at rated torque from zero to 2500 rpm within 1 second. Whereas the damping factor has been chosen in order to achieve a Constant-Power Speed Ratio equal to 2, SPM rated power being

TABLE XXIII
EPS PARAMETERS AND RATED VALUES

	SPM								
	r	L	p	Λ	J	D	$T_{e,n}$	$\omega_{m,n}$	I_n
VALUE	0.125	1.9	5	0.201	0.121	0.030	31.5	2500	21
UNITS	Ω	mH	-	V·s	Kg·m^2	Nm·s	Nm	rpm	A
	NPC					HESS			
	V_n	I_n	V_{DC}	f_c	V_B	r_B	L_B	C_H	C_L
VALUE	600	50	560	20	560	0.400	1.5	6	0.470
UNITS	V	A	V	kHz	V	Ω	mH	mF	mF

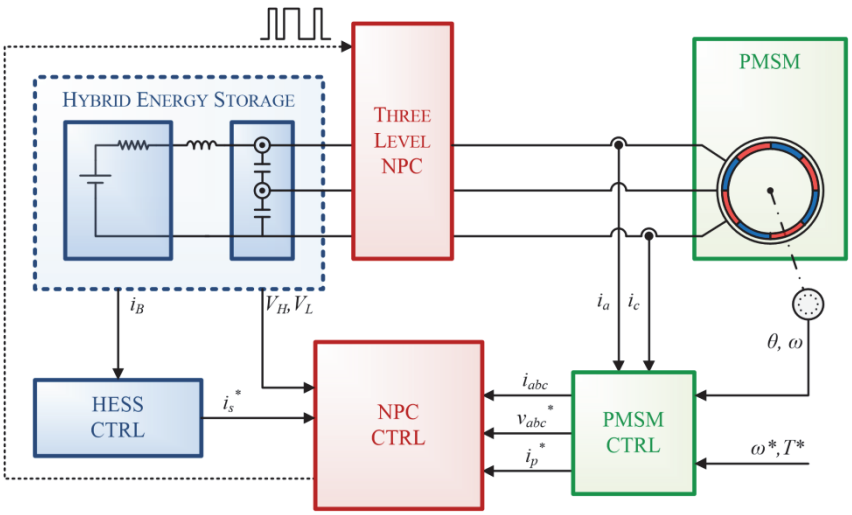

Fig. 3.37 EPS simulation set-up.

about 8.25 kW. These choices have been made in order to emulate realistic EPS operating conditions as much as possible, keeping simulation times relatively short. Considering now the NPC, it consists mainly of 12 IGBTs and 6 clamping diodes, whose rated voltage and current are reported in Table XXIII. In addition, the overall DC-link voltage has been set to 560 V, whereas the switching frequency has been set to about 20 kHz, the sampling time interval being 51.2 μs. The NPC is linked to the proposed HESS directly, which consists of a battery pack and an UC-capacitor module, whose main details are reported in Table XXIII. Particularly, the UC-capacitor module has been sized in order to deliver the energy needed for accelerating the SPM up to the half of the rated speed. In this context, it is worth noting that the high-side capacitor is about 13 times greater than the low-side one, in accordance with the design suggestions introduced in previous subsections.

Simulations regard both suitable functionality tests and overall EPS performances over different operating conditions. Particularly, functionality tests have been performed in order to preliminary highlight the superior performances achievable by PS-PWM compared to HML-PWM, thus justifying the employment of the former in the proposed EPS. Therefore, reference has been made to the set-up shown in Fig. 3.38, in which the proposed HESS is replaced by a three-phase rectifier, the overall DC-link voltage being about 560 V. Whereas the SPM and NPC parameters and rated values are still reported in Table XXIII, except for both J and D. These last have been appropriately decreased in order to shorten simulation times as needed. Finally, C_H and C_L are both set equal to 470 μF because there is no need of exploiting DC-link energy content over functionality tests on PS-PWM and HML-PWM.

3.3.1 Functionality Tests

Functionality tests regard numeric simulations of both HML-PWM and PS-PWM in order to highlight the superior performances achievable by the latter, as stated previously. Thus, focusing on HML-PWM at first, it has been tested in equalizing DC-link voltages. For this purposes, the binary signal ε is determined through a hysteresis regulator, which is fed by the difference between high-side and low-side DC-link voltages, as shown in Fig. 3.39. Consequently, any voltage unbalance that exceeds a given threshold is counteracted by an appropriate commutation of ε. In this context, it is worth noting that positive and negative thresholds can be set both at zero, meaning that no voltage unbalances are allowed. However, such a solution may lead to increased current ripple, which, in turn, may overstress DC-link capacitors.

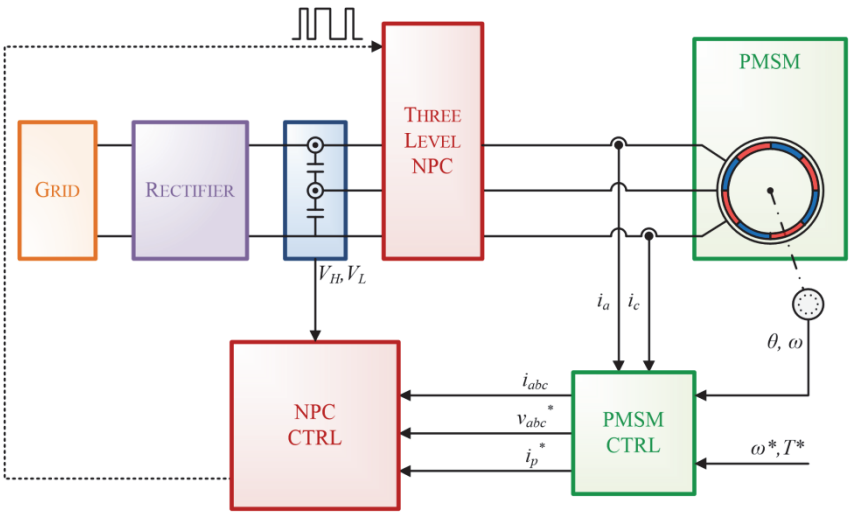

Fig. 3.38 Functionality test set-up.

Considering now PS-PWM, its effectiveness is verified referring to the same scenario as that of HML-PWM for comparison purposes. Therefore, i_s^* needs to be synthesized based on DC-link voltage unbalance (V_M), as shown in Fig. 3.40. Particularly, the reference voltage unbalance is set to zero in order to provide DC-link voltage equalization. Hence, by subtracting (3.15) to each other, the following result is achieved:

$$\frac{dV_M}{dt} = \frac{i_M}{C} \tag{3.118}$$

where V_M and i_M denote the DC-link voltage and current unbalance respectively:

$$\begin{aligned} V_M &= V_H - V_L \\ i_M &= -(i_H - i_L) \end{aligned} \quad . \tag{3.119}$$

As a result, (3.118) suggests that DC-link voltage unbalance can be suitably controlled by means of i_M. Consequently, i_M^* can be determined by means of DC-link voltage unbalance error through a simple proportional regulator, whose gain can be appropriately set in order to impose the desired dynamic performances. It is worth noting that only a proportional regulator is employed because i_M^* has to be held constant at zero when V_M^* is achieved. Once i_M^* is determined, the corresponding i_s^* can be easily achieved as:

$$i_s^* = (v_H - v_L) \cdot i_p + (2 v_H v_L) \cdot i_M^* \quad . \tag{3.120}$$

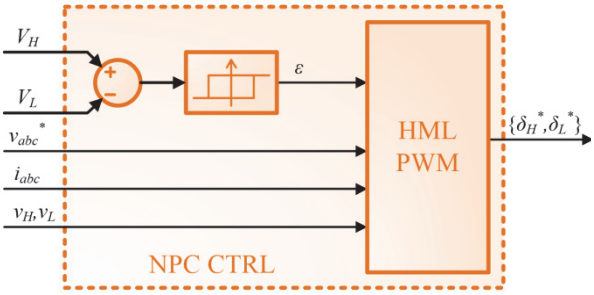

Fig. 3.39 Equivalent block control scheme of the proposed HML-PWM for DC-link voltage equalization.

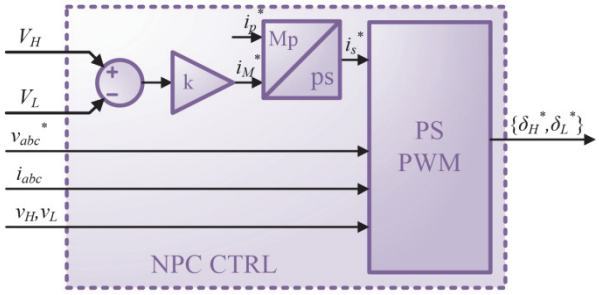

Fig. 3.40 Equivalent block control scheme of the proposed PS-PWM for DC-link voltage equalization.

In order to test the effectiveness of the proposed HML-PWM in equalizing the DC-link voltages, initial voltage unbalances are imposed. In particular, two different situations have been considered: in the first one (case I), v_H and v_L are set equal to 0.55 and 0.45 p.u. respectively, whereas they are set at 0.47 and 0.53 p.u. in case II. Simulations refer to the SPM start-up, thus, starting from rest, a step reference torque is imposed, equal to the rated one. Consequently, the torque is quickly driven to its reference value, as shown in Fig. 3.41. Then, it is successfully held constant, while the rotor speed increases up to its rated value, which is achieved after about 0.08 s. The corresponding phase current evolutions are depicted in Fig. 3.42. Referring to both Fig. 3.41 and Fig. 3.42, it can be stated that almost the same evolutions are achieved in case I and case II, meaning that DC-link voltage equalization provided by HML-PWM does not affect SPM performances significantly, as expected.

The corresponding DC-link voltage evolutions are shown in Fig. 3.43, whereas the duty cycles of each leg are depicted in Fig. 3.44. In spite of different DC-link voltage unbalances, it can be seen that voltage equalization is accomplished in both cases. However, some differences occur, particularly DC-link voltage equalization is achieved later in case I than in case II, due to the more significant initial voltage unbalance. In addition, referring to case I, the employment of L states is avoided at first, i.e. $\{\alpha_L,\beta_L,\gamma_L\}$ are held constant at zero, as shown in Fig. 3.44. This is due to the need of discharging C_H as much as possible, v_H being greater than v_L, as highlighted in Fig. 3.43. As the rotor speed increases, the employment of L states becomes unavoidable, due to the increased SPM voltage requirement. However, this does not prevent the accomplishment of the equalization process, at the end of which H and L states occur equally. Similarly, in case II, the proposed equalization algorithm firstly resorts to L states mostly in order to discharge C_L as much as possible, v_L being greater than v_H. Subsequently, as soon as the equalization process is accomplished, L and H states occur equally, as in case I.

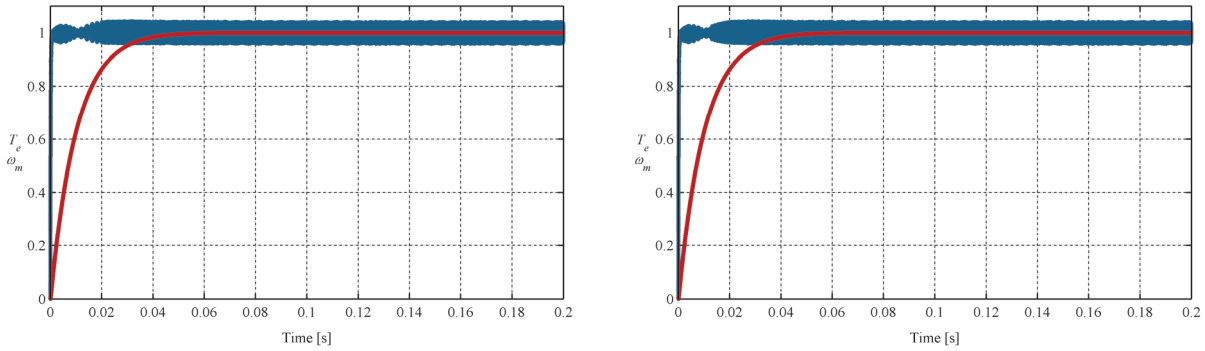

Fig. 3.41 Torque (blue) and rotor speed (red) evolutions (in p.u.) at the SPM start-up in case I (on the left) and in case II (on the right).

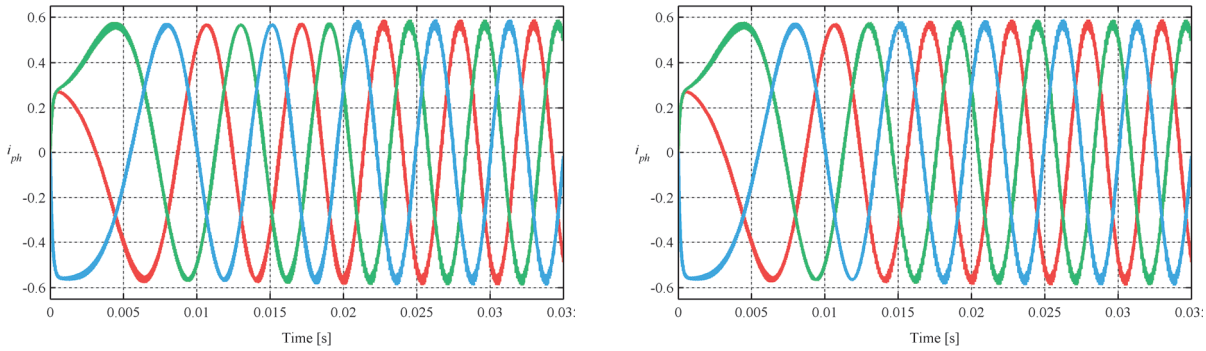

Fig. 3.42 Phase current evolutions (in p.u.) at the SPM start-up in case I (on the left) and in case II (on the right).

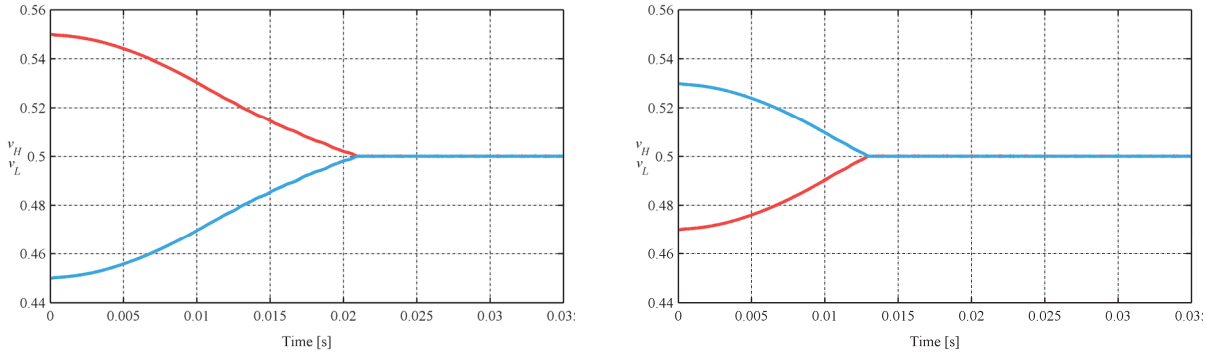

Fig. 3.43 DC-link voltage evolutions (in p.u.) across C_H (red) and C_L (cyan) at the SPM start-up in case I (on the left) and in case II (on the right).

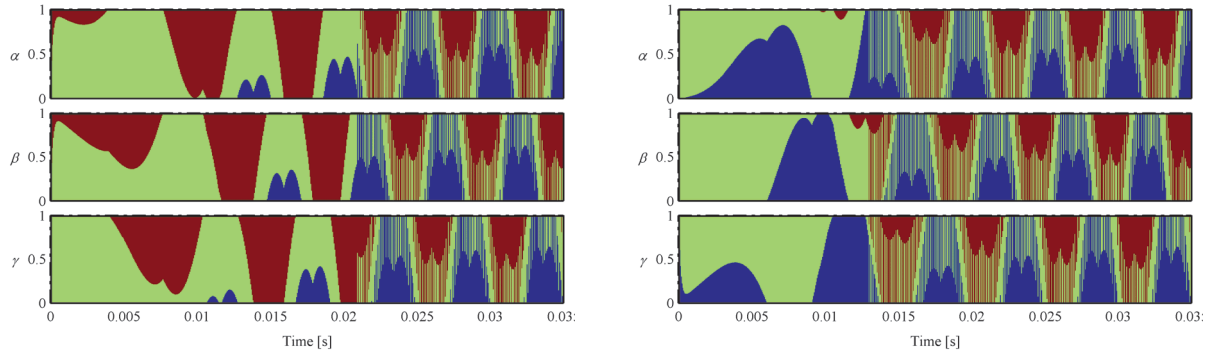

Fig. 3.44 Duty cycle evolutions at the SPM start-up in case I (on the left) and in case II (on the right): α_H, β_H, γ_H (red), α_M, β_M, γ_M (green) and α_L, β_L, γ_L (blue).

Simulations then regard DC-link voltage equalization achievable by means of PS-PWM, particularly a comparison with HML-PWM is carried out in order to highlight the superior performances of the former. Thus, reference is still made to the same SPM start-up but to a different initial DC-link voltage unbalance, i.e. v_H and v_L start from 0.6 and 0.4 p.u. respectively for both PS-PWM and HML-PWM.

The overall simulation results are reported from Fig. 3.45 to Fig. 3.49. Firstly focusing on DC-link voltage evolutions depicted in Fig. 3.45, it can be seen that the equalization process is accomplished very similarly in both cases, although it is slightly delayed by PS-PWM compared to HML-PWM. This is due to the employment of a proportional regulator, whose dynamic performances are slightly lower than that achievable by means of a hysteresis regulator. However, as soon as DC-link voltage equalization is achieved, HML-PWM introduces high current ripple on both high-side and low-side capacitors, as shown in Fig. 3.46. Such a current ripple leads to improper exploitation of DC-link capacitors, which is appropriately avoided in case of PS-PWM. Such an improvement is due to the more accurate control of DC-link currents provided by PS-PWM, as well highlighted by the i_s evolutions shown in Fig. 3.47. Particularly, over the equalization process, both HML-PWM and PS-PWM are characterized by almost the same i_s evolution, it being upper bounded by its maximum threshold. However, as soon as DC-link voltage equalization is almost accomplished, i_s is successfully driven to zero by PS-PWM, its ripple being quite negligible. Whereas the hysteretic nature of HML-PWM introduces high frequency ripple on i_s.

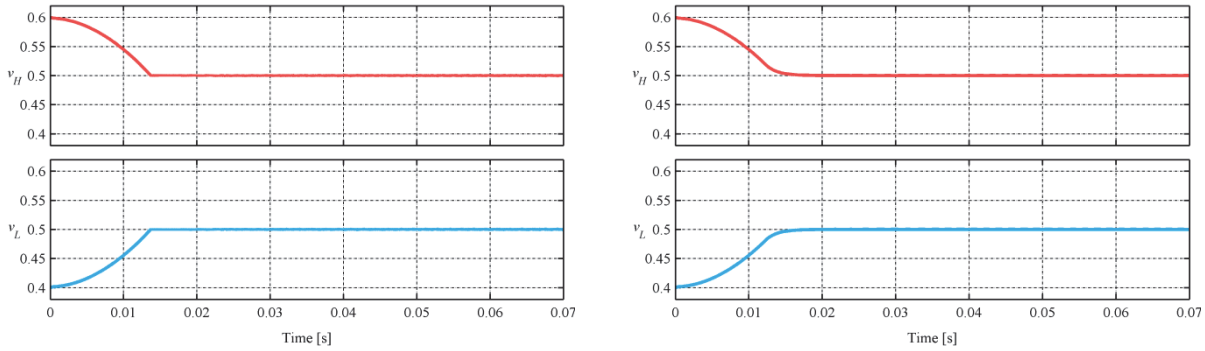

Fig. 3.45 DC-link voltage evolutions achieved by HML-PWM (on the left) and PS-PWM (on the right): high-side capacitor (red) and low-side capacitor (cyan).

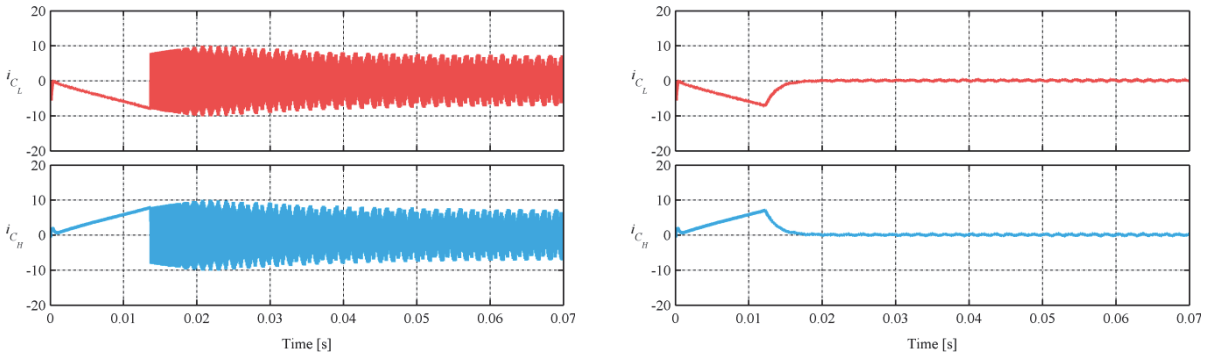

Fig. 3.46 DC-link capacitor current evolutions achieved by HML-PWM (on the left) and PS-PWM (on the right): high-side capacitor (red) and low-side capacitor (cyan).

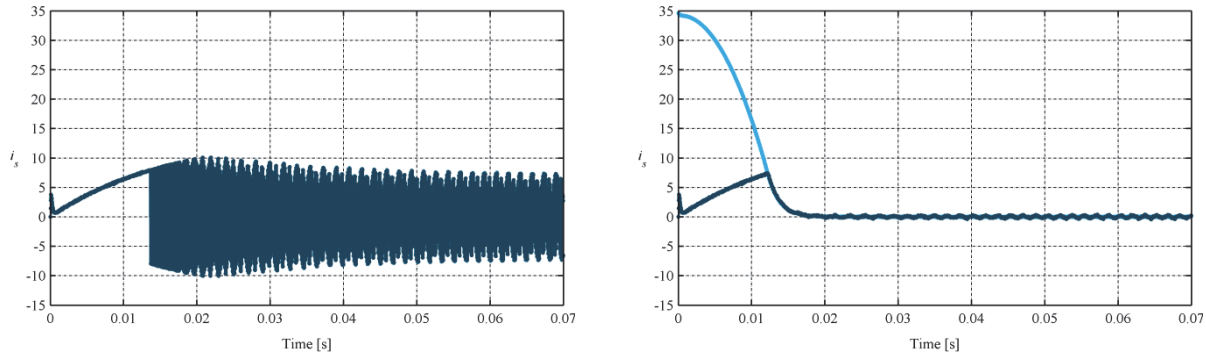

Fig. 3.47 DC-link equivalent current i_s evolutions achieved by HML-PWM (on the left) and PS-PWM (on the right): actual (blue) and reference (cyan).

Focusing now on SPM performances, reference can be made to torque and speed evolutions at first, which are depicted in Fig. 3.48, the corresponding phase current evolutions being depicted in Fig. 3.49. It can be seen that all the evolutions are almost superimposed over the equalization process, as expected. Whereas, once DC-link voltage equalization is accomplished, higher torque and current ripple occur by means of PS-PWM than that achieved by HML-PWM. This phenomenon is related to the different duty cycles synthesized by PS-PWM compared to HML-PWM, which are both shown in Fig. 3.50. Particularly, once achieved, DC-link voltage equalization requires high-side and low-side capacitors to be exploited equally as in a pure series connection. This goal is well achieved by PS-PWM, leading to short duty cycles and maximum magnitude of voltage pulses applied to the SPM. Whereas HML-PWM fully exploits high-side and low-side capacitors alternatively, leading to larger voltage pulses of reduced magnitude compared to PS-PWM. However, it is worth noting that the

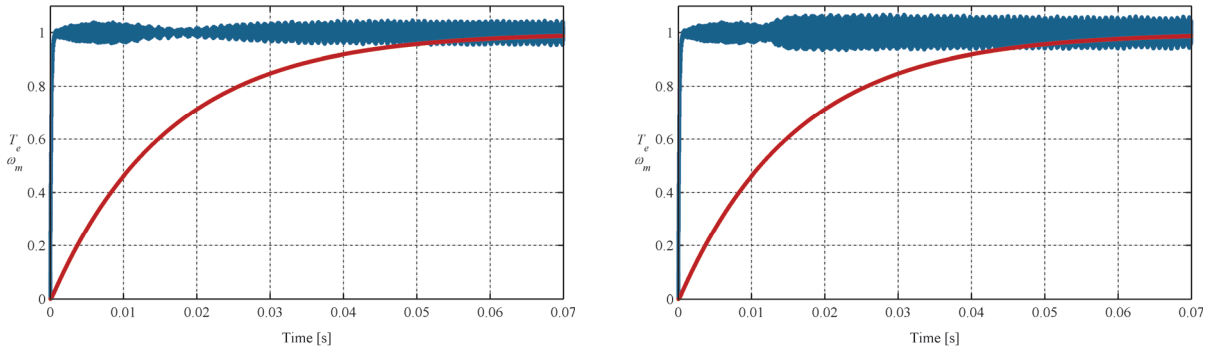

Fig. 3.48 SPM torque (blue) and speed (red) evolutions achieved by HML-PWM (on the left) and PS-PWM (on the right).

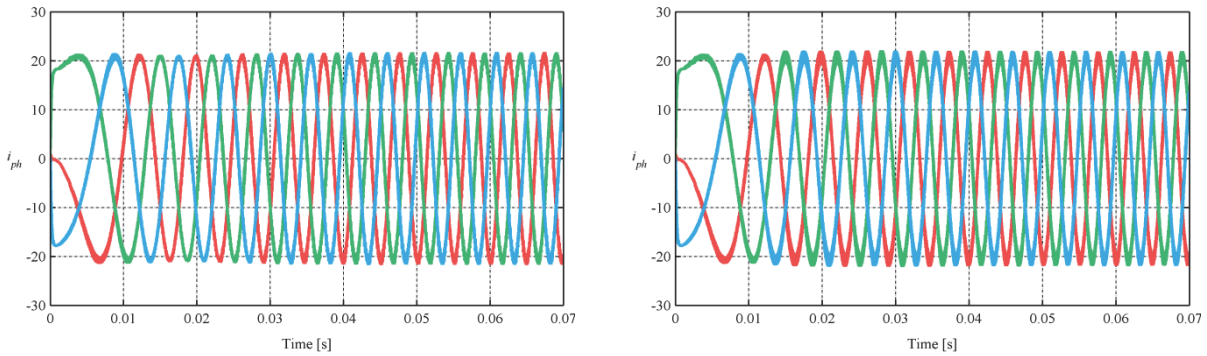

Fig. 3.49 Phase currents evolutions achieved by HML-PWM (on the left) and PS-PWM (on the right).

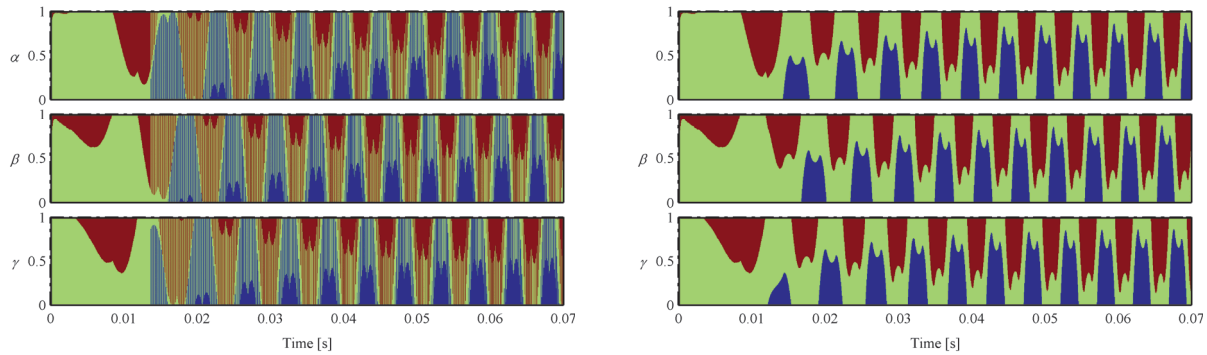

Fig. 3.50 Duty cycle evolutions achieved by HML-PWM (on the left) and PS-PWM (on the right): δ_H (red), δ_M (green) and δ_L (blue).

increased ripple achieved by PS-PWM on both torque and phase currents are quite small, if compared to the ripple reduction achieved on capacitor currents.

Steady state performances achievable by both HML-PWM and PS-PWM are evidenced in Fig. 3.51 through Fig. 3.56. Particularly, it can be seen that PS-PWM reduces capacitor voltage and current ripple, this last being about 15 times less than that occurring by HML-PWM. In addition, although torque and current ripple achieved by HML-PWM are lower than by PS-PWM, they seem quite irregular, thus denoting a lower frequency content. As a result, based on all the previous consideration can be stated that PS-PWM guarantees superior performances compared to HML-PWM, especially in terms of capacitor current ripple reduction.

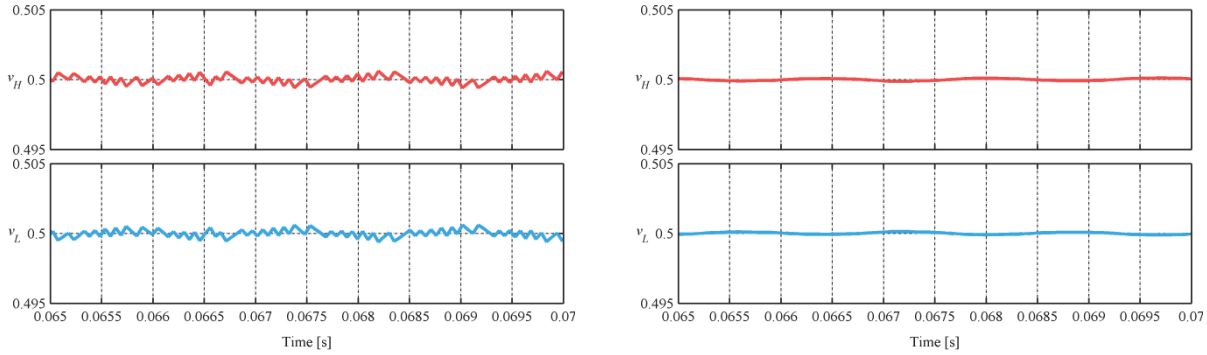

Fig. 3.51 Zoomed sight of Fig. 3.45 at steady state operation for both HML-PWM (on the left) and PS-PWM (on the right): high-side (red) and low-side (cyan) DC-link capacitor voltages.

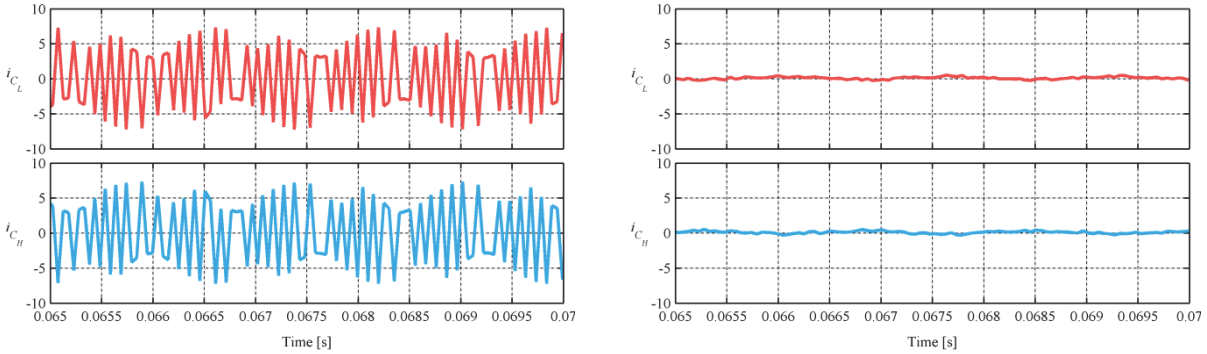

Fig. 3.52 Zoomed sight of Fig. 3.46 at steady state operation for both HML-PWM (on the left) and PS-PWM (on the right): high-side (red) and low-side (cyan) capacitor currents.

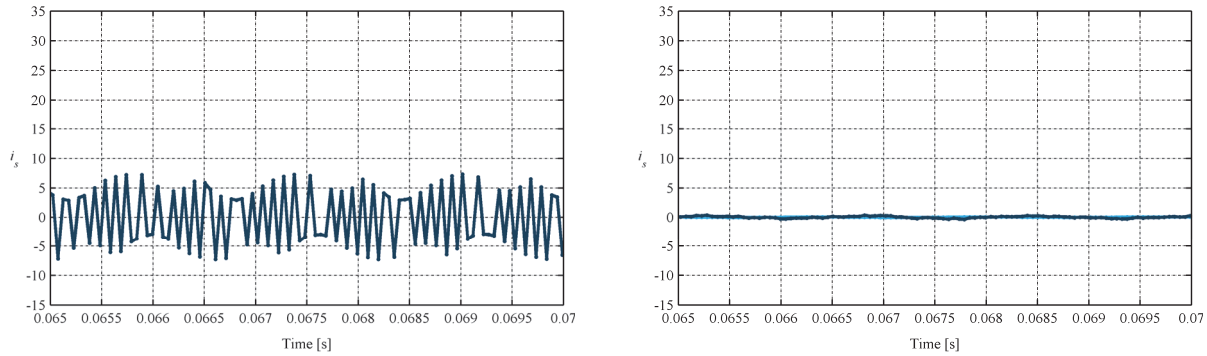

Fig. 3.53 Zoomed sight of Fig. 3.47 at steady state operation for both HML-PWM (on the left) and PS-PWM (on the right): actual (blue) and reference (cyan) i_s.

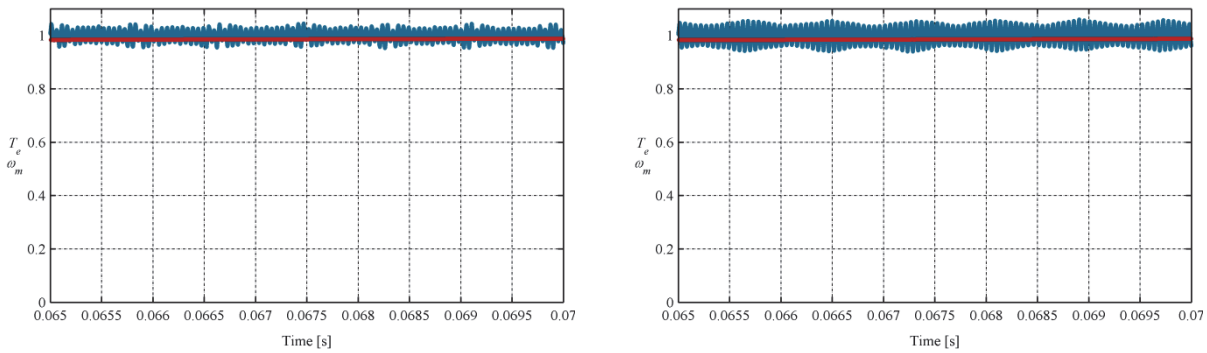

Fig. 3.54 Zoomed sight of Fig. 3.48 at steady state operation for both HML-PWM (on the left) and PS-PWM (on the right): SPM torque (blue) and speed (red).

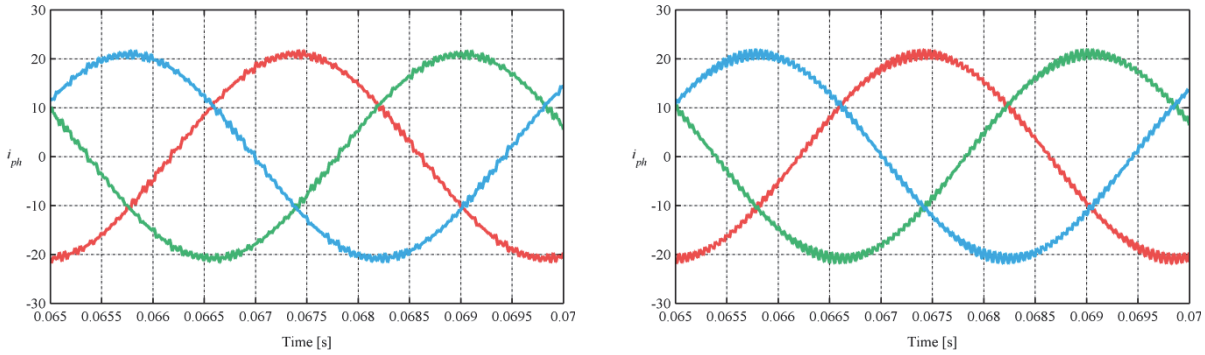

Fig. 3.55 Zoomed sight of Fig. 3.49 at the steady state operation for both HML-PWM (on the left) and PS-PWM (on the right).

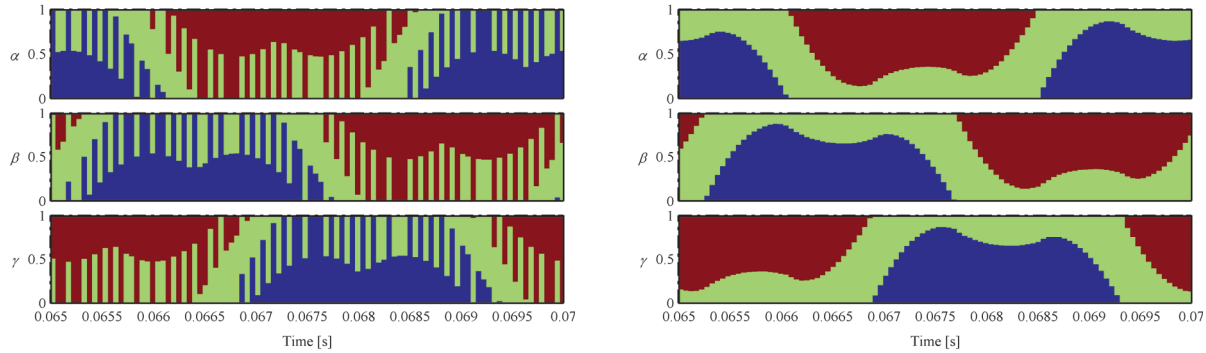

Fig. 3.56 Zoomed sight of Fig. 3.50 at steady state operation for both HML-PWM (on the left) and PS-PWM (on the right): δ_H (red), δ_M (green) and δ_L (blue).

3.3.2 EPS Simulation Results

The simulation study on the proposed EPS consists of a sudden start-up followed by an equally sudden stop. These are both emulated by means of suitable step reference speed variations; particularly, starting from rest, a reference speed value equal to half of the rated one is imposed. Subsequently, after steady state operation is reached, the reference speed value is suddenly switched to zero in order to stop the SPM. Regarding the initial DC-link voltages, v_H and v_L are set to 0.8 and 0.2 respectively, the overall DC-link voltage being equal to V_B. This results in an appropriate pre-charging of the UC-capacitor module, which is assumed to be carried out previously.

Simulation results firstly focus on SPM start-up, whose torque and speed evolutions are depicted in Fig. 3.57 and Fig. 3.58 respectively. Particularly, SPM torque is suddenly driven to its rated value in order to accelerate the SPM to the maximum extent, in accordance with the reference speed value. Subsequently, when the rotor speed reaches about 80 per cent of the reference value, the SPM torque slowly decreases in accordance with its reference value in order to achieve the reference speed value within 1 s, as imposed over the design stage. Focusing on Fig. 3.57, it is worth noting that reference and actual torque evolution are almost superimposed, due to the high dynamic performances provided by the dq current regulators compared with those required by the speed control system. Considering now HESS performances, reference can be made to the evolutions of the DC-link energy content depicted in Fig. 3.59, whereas battery and power current evolutions are shown in Fig. 3.60. It can be seen that DC-link energy content decreases as SPM speed increases, well tracking its reference value. This last varies with the actual SPM speed in order to allow the UC-capacitor module to deliver the energy required for accelerating the SPM. Consequently, a relative low power drawn is required from the battery pack, as detectable by comparing the i_p and i_B evolutions

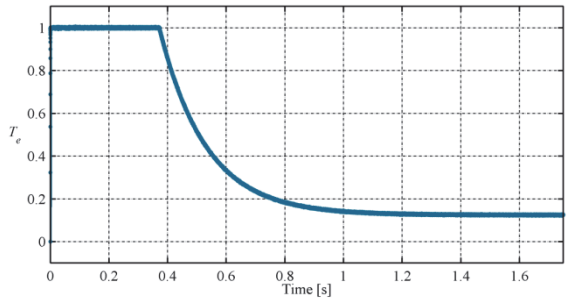

Fig. 3.57 SPM torque evolutions over acceleration: actual (blue) and reference (cyan) profile.

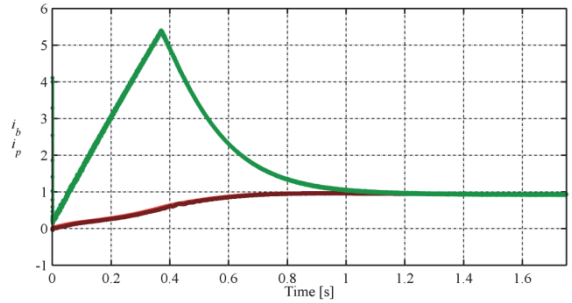

Fig. 3.60 Battery and power current evolutions over acceleration: i_p (green), actual (brown) and reference (red) i_B profiles.

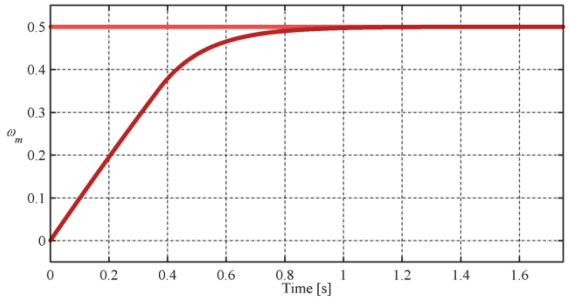

Fig. 3.58 Rotor speed evolutions over acceleration: actual (dark red) and reference (light red) profile.

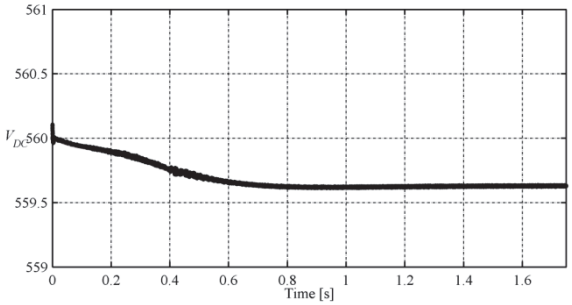

Fig. 3.61 DC-link voltage evolutions over acceleration: actual (black) and reference (grey) profiles.

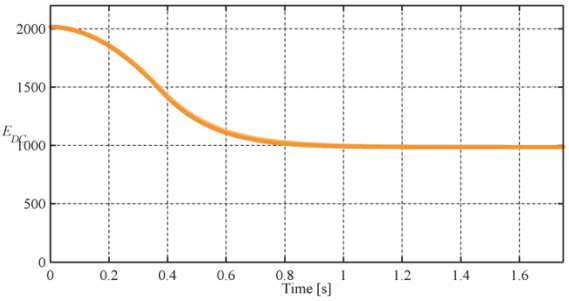

Fig. 3.59 DC-link energy content evolutions over acceleration: actual (orange) and reference (yellow) profile.

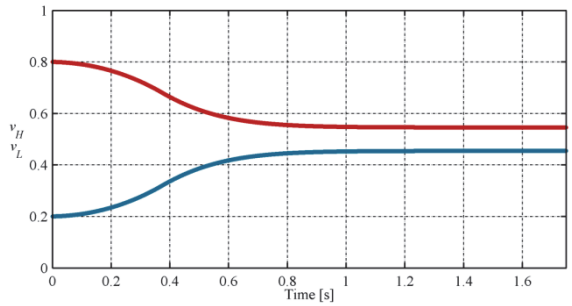

Fig. 3.62 DC-link capacitor voltage evolutions over acceleration: v_H (red) and v_L (blue) profiles.

shown in Fig. 3.60. However, it is worth noting that E_{DC} decreases slightly faster than its reference value because it accounts for both electrical and mechanical losses occurring on the NPC and SPM. Whereas these are not considered in imposing the reference E_{DC} profile, whose reduction accounts for kinetic energy stored by the SPM only. As soon as the SPM speed reaches about 80 per cent of the reference value, i_p decreases due to SPM torque reduction, slowly converging to i_B. This last presents a little overshoot due to the need of covering the energy deficit occurring on the DC-link, as previously mentioned. As a result, at steady state operation, the battery pack supplies the SPM on its own, thus the UC-capacitor module does not deliver energy further, as well highlighted in Fig. 3.59. Focusing now on DC-link voltage evolutions depicted in Fig. 3.61 and Fig. 3.62, it can be seen that V_{DC} slightly decreases in order to increase the current drawn from the battery pack, as shown in Fig. 3.61. Much more significant variations occur on both v_H and v_L, particularly v_H drops from 0.80 to about 0.55, while v_L increases from 0.20 to about 0.45, as highlighted in Fig. 3.62. This is due to the need of discharging C_H for delivering the energy required by SPM acceleration, thus preventing the battery pack to deliver high peak currents.

.

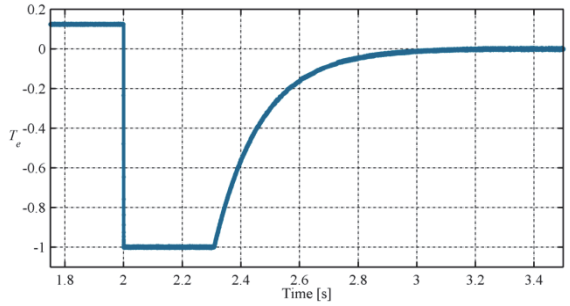

Fig. 3.63 SPM torque evolutions over deceleration: actual (blue) and reference (cyan) profile.

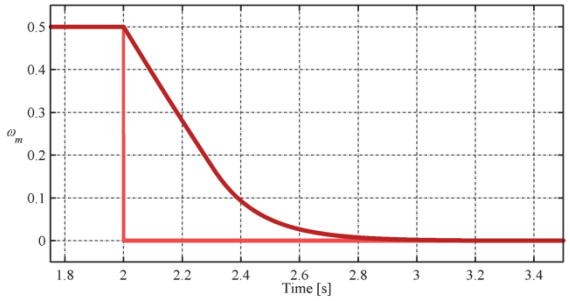

Fig. 3.64 Rotor speed evolutions over deceleration: actual (dark red) and reference (light red) profile.

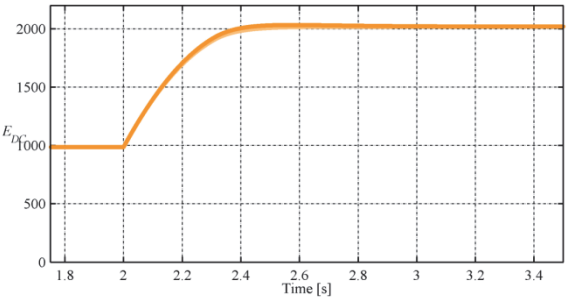

Fig. 3.65 DC-link energy content evolutions over deceleration: actual (orange) and reference (yellow) profile.

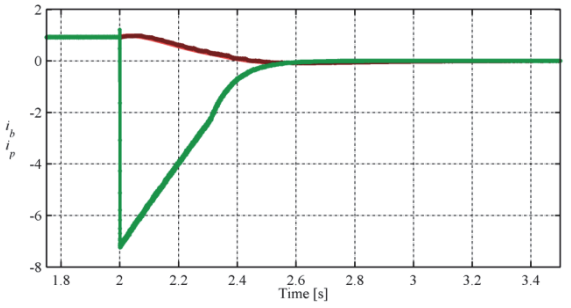

Fig. 3.66 Battery and power current evolutions over deceleration: i_p (green), actual (brown) and reference (red) i_B profiles.

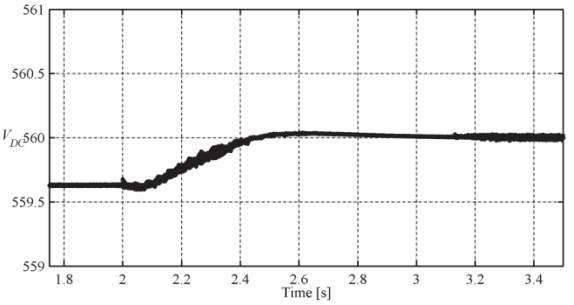

Fig. 3.67 DC-link voltage evolutions over deceleration: actual (black) and reference (grey) profiles.

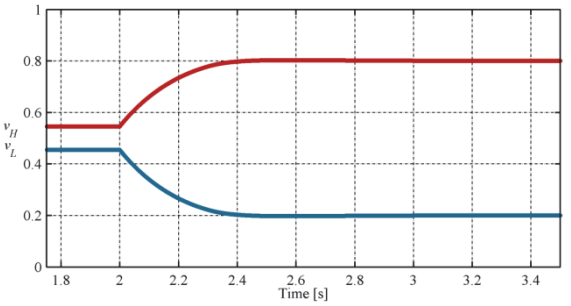

Fig. 3.68 DC-link capacitor voltage evolutions over deceleration: v_H (red) and v_L (blue) profiles.

After 2 s, the reference speed value is suddenly reduced to zero in order to stop the SPM. Consequently, SPM provides an appropriate braking torque in order to reduce its speed within 1 s, as shown in both Fig. 3.63 and Fig. 3.64. Also in this case, reference and actual torque values are almost superimposed, revealing the effectiveness of the SPM current control system. Considering now the DC-link energy content evolutions depicted in Fig. 3.65, it can be seen that the reference value increases slightly faster than the actual one at first. As a result, a DC-link energy deficit is detected, which leads to further increase battery current drawn, as shown in Fig. 3.66. However, as the actual DC-link energy content approaches its reference profile, i_B is slightly reduced down to zero, the UC-capacitor module being then recharged by the SPM mostly. At steady state operation, DC-link energy content is fully restored; this is mainly due to energy recovered by the SPM over regenerative braking, as well highlighted by the i_p evolution shown in Fig. 3.66. Considering now the DC-link voltage evolutions depicted in both Fig. 3.67 and Fig. 3.68, it can be seen that the overall V_{DC} slowly increases up to its rated value, while v_H and v_L are driven to their corresponding initial value by means of the

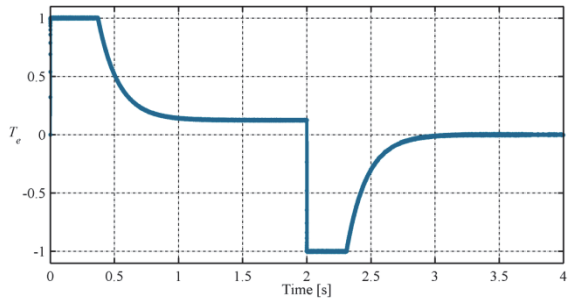

Fig. 3.69 Overall SPM torque evolution: actual (blue) and reference (cyan) profile.

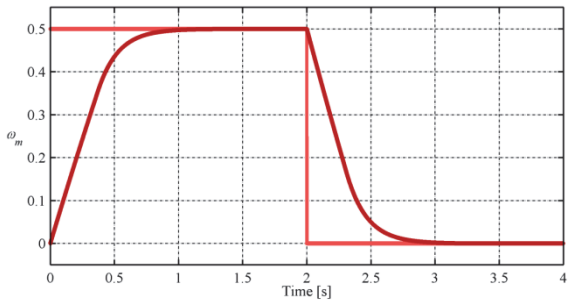

Fig. 3.70 Overall rotor speed: actual (dark red) and reference (light red) profile.

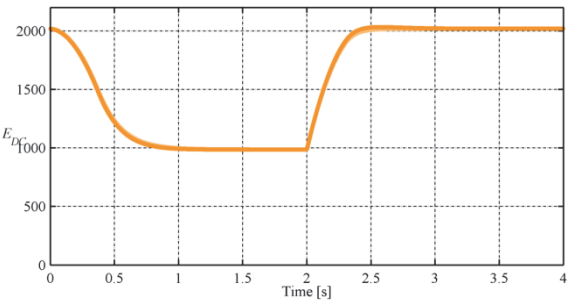

Fig. 3.71 Overall DC-link energy content: actual (orange) and reference (yellow) profile.

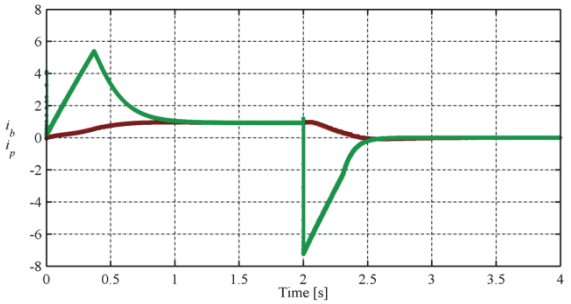

Fig. 3.72 Overall battery and power current: i_p (green), actual (brown) and reference (red) i_B profiles.

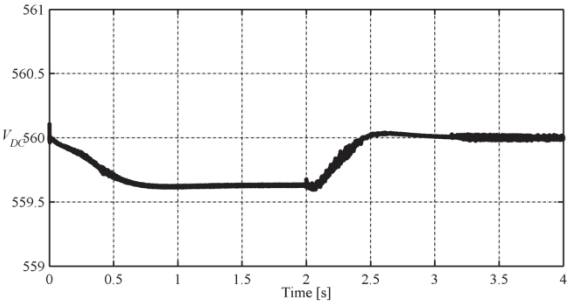

Fig. 3.73 Overall DC-link voltage: actual (black) and reference (grey) profiles.

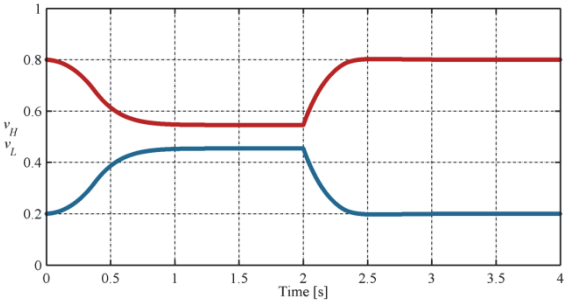

Fig. 3.74 Overall DC-link capacitor voltages: v_H (red) and v_L (blue) profiles.

NPC control. The overall simulation results regarding both SPM acceleration and deceleration are resumed from Fig. 3.69 to Fig. 3.74.

In conclusion, the energy flows achieved over both acceleration and deceleration are depicted in Fig. 3.75. It can be seen that over acceleration, all the energy stored by the SPM comes from the UC-capacitor module, whereas the battery pack delivers the amount of energy needed to cover the overall EPS losses. These last are mainly due to mechanical friction, although some losses also occur on SPM, NPC and battery. Similar considerations can be made referring to SPM deceleration, particularly the energy initially stored in the UC-capacitor module is fully reinstated by both the SPM and the battery pack. This last still provide some energy in order to compensate for EPS losses, which are much less than over acceleration. As a result, it can be stated that the proposed EPS operates as expected, both in terms of peak current drawn from the battery pack and amount of energy exchanged by the DC-link.

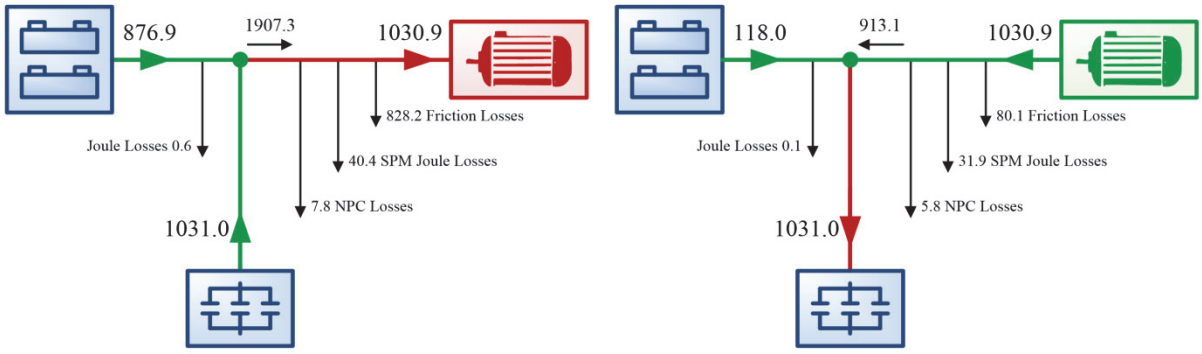

Fig. 3.75 Energy flows achieved over acceleration (on the left) and deceleration (on the right).

CONCLUSION

This PhD dissertation has presented a number of scenarios in which Energy Storage Systems (ESSs) can be usefully employed for increasing energy system performances. Particularly, after introducing the State-of-the-Art of ESS technologies (Chapter 1), reference has been made to some stationary and automotive applications. Stationary applications have regarded Renewable Energy Sources (RESs) exploitation issues and EV integration within micro-grids (Chapter 2). It has been shown that ESSs are particularly useful in compensating for RES forecasting errors, whereas they are much less effective as energy buffers. In addition, Vehicle to Grid (V2G) has also been revealed as an alternative and viable solution for increasing RES penetration level and micro-grid autonomy, even in presence of small EV fleets. The promising results obtained in the energy management of power systems by means of the use of V2G and G2V paradigm have suggested the integration of Electric Vehicles (EVs) into the power system. This requires that EV energy storage systems should satisfy both electric propulsion and power system requirements. With this aim, the design and management of a novel Hybrid Energy Storage System (HESS) for EVs has been considered (Chapter 3). Particularly, the proposed configuration allows the reduction of the peak current delivered by EV batteries, thus preserving their rated performances and increasing their lifetime. This goal has been achieved by means of a suitable management of the energy flows provided by the HESS, leading to a good exploitation of the proposed topology. The effectiveness of the proposed solutions has been verified through several extensive simulation studies, which have been carried out in the Matlab environment.

In conclusion, it can be stated that all cases have revealed the need of carefully sizing and managing ESSs in order to achieve optimal results. In this context, it is worth noting that the employment of large ESS easily leads to enhanced performances but also to significant increased costs. This drawback cannot be sustained, especially in automotive applications, in which EV competitiveness is strictly related to a decrease of ESS size, weight and costs. On the other hand, small ESSs do not generally guarantee the same performances but they can be quite similar if optimal management and control strategies are employed. These last thus will cover a fundamental role in making ESS more widespread, enabling an optimal trade-off among increased performances, costs, management and control issues.

REFERENCES

[1] F. S. Barnes and J. G. Levine, *Large Energy Storage Systems Handbook*. CRC Press, 2011.

[2] R. A. Huggins, *Energy Storage*. Boston, MA: Springer US, 2010.

[3] P. J. Grbovic, *Ultra-capacitors in Power Conversion Systems: Applications, Analysis, and Design from Theory to Practice*. Wiley-IEEE Press, 2014.

[4] A. Emadi, *Advanced Electric Drive Vehicles*. CRC Press, 2015.

[5] S. S. Williamson, *Energy Management Strategies for Electric and Plug-in Hybrid Electric Vehicles*. New York, NY: Springer New York, 2013.

[6] L. Guzzella and A. Sciarretta, *Vehicle Propulsion Systems*. Berlin, Heidelberg: Springer Berlin Heidelberg, 2013.

[7] M. Ehsani, Y. Gao, and A. Emadi, *Modern Electric, Hybrid Electric, and Fuel Cell Vehicles: Fundamentals, Theory, and Design, Second Edition*. CRC Press, 2009.

[8] B. Zakeri and S. Syri, "Electrical energy storage systems: A comparative life cycle cost analysis," *Renew. Sustain. Energy Rev.*, vol. 42, pp. 569–596, Feb. 2015.

[9] V. A. Boicea, "Energy Storage Technologies: The Past and the Present," *Proc. IEEE*, vol. 102, no. 11, pp. 1777–1794, Nov. 2014.

[10] M. S. Whittingham, "History, Evolution, and Future Status of Energy Storage," *Proc. IEEE*, vol. 100, no. Special Centennial Issue, pp. 1518–1534, May 2012.

[11] G. Ren, G. Ma, and N. Cong, "Review of electrical energy storage system for vehicular applications," *Renew. Sustain. Energy Rev.*, vol. 41, pp. 225–236, Jan. 2015.

[12] S. Vazquez, S. M. Lukic, E. Galvan, L. G. Franquelo, and J. M. Carrasco, "Energy Storage Systems for Transport and Grid Applications," *IEEE Trans. Ind. Electron.*, vol. 57, no. 12, pp. 3881–3895.

[13] U.S. Department of Energy (DOE), Office of Energy Efficiency & Renewable Energy (EERE), and Vehicle Technologies Office (VTO), "Energy Storage R&D," 2013.

[14] H. Xiaoliang, J. M. A. Curti, and H. Yoichi, "Energy management strategy with optimized power interface for the battery supercapacitor hybrid system of Electric Vehicles," in *Proc. of 39th Annual Conference of the IEEE Industrial Electronics Society (IECON 2013)*, 2013, pp. 4635–4640.

[15] F. Ju, Q. Zhang, W. Deng, and J. Li, “Review of structures and control of battery-supercapacitor hybrid energy storage system for electric vehicles,” in *Proc. of IEEE International Conference on Automation Science and Engineering (CASE 2014)*, 2014, pp. 143–148.

[16] S. Lu, K. A. Corzine, and M. Ferdowsi, “A New Battery/Ultracapacitor Energy Storage System Design and Its Motor Drive Integration for Hybrid Electric Vehicles,” *IEEE Trans. Veh. Technol.*, vol. 56, no. 4, pp. 1516–1523, Jul. 2007.

[17] D. Zhu, S. Yue, S. Park, Y. Wang, Naehyuck Chang, and M. Pedram, “Cost-effective design of a hybrid electrical energy storage system for electric vehicles,” in *Proc. of International Conference on Hardware/Software Codesign and System Synthesis (CODES+ISSS 2014)*, 2014, pp. 1–8.

[18] L. Kumar, K. K. Gupta, and S. Jain, “Power electronic interface for vehicular electrification,” in *Proc. of IEEE International Symposium on Industrial Electronics (ISIE 2013)*, 2013, pp. 1–6.

[19] U.S. Department of Energy (DOE), “Advanced Power Electronics and Electric Motors Program,” 2013.

[20] U.S. Department of Energy (DOE), “EV Everywhere Grand Challenge: DOE’s 10-Year Vision for Plug-in Electric Vehicles.” [Online]. Available: http://energy.gov/eere/vehicles/ev-everywhere-grand-challenge-does-10-year-vision-plug-electric-vehicles. [Accessed: 27-Feb-2015].

[21] S. Fiorenti, J. Guanetti, Y. Guezennec, and S. Onori, “Modeling and experimental validation of a Hybridized Energy Storage System for automotive applications,” *J. Power Sources*, vol. 241, pp. 112–120, Nov. 2013.

[22] X. Luo, J. Wang, M. Dooner, and J. Clarke, “Overview of current development in electrical energy storage technologies and the application potential in power system operation,” *Appl. Energy*, vol. 137, pp. 511–536, Jan. 2015.

[23] H. Tao, J. L. Duarte, and M. A. M. Hendrix, “Multiport converters for hybrid power sources,” in *Proc. of IEEE Power Electronics Specialists Conference (PESC 2008)*, 2008, pp. 3412–3418.

[24] O. C. Onar and A. Khaligh, “A Novel Integrated Magnetic Structure Based DC/DC Converter for Hybrid Battery/Ultracapacitor Energy Storage Systems,” *IEEE Trans. Smart Grid*, vol. 3, no. 1, pp. 296–307, Mar. 2012.

[25] G. Guidi, T. M. Undeland, and Y. Hori, “Effectiveness of supercapacitors as power-assist in pure ev using a sodium-nickel chloride battery as main energy storage,” in *Proc. of 24th International Battery, Hybrid and Fuel Cell Electric Vehicle Symposium (EVS-24)*, 2009.

[26] Y.-J. Lee, A. Khaligh, and A. Emadi, “Advanced Integrated Bidirectional AC/DC and DC/DC Converter for Plug-In Hybrid Electric Vehicles,” *IEEE Trans. Veh. Technol.*, vol. 58, no. 8, pp. 3970–3980, Oct. 2009.

[27] J.-S. Lai and D. J. Nelson, “Energy Management Power Converters in Hybrid Electric and Fuel Cell Vehicles,” *Proc. IEEE*, vol. 95, no. 4, pp. 766–777, Apr. 2007.

[28] A. Ostadi and M. Kazerani, “A Comparative Analysis of Optimal Sizing of Battery-only, Ultracapacitor-only, and Battery-Ultracapacitor Hybrid Energy Storage Systems for a City Bus,” *Veh. Technol. IEEE Trans. On*, vol. PP, no. 99, pp. 1–1, 2014.

[29] H.-W. He, R. Xiong, and Y.-H. Chang, “Dynamic Modeling and Simulation on a Hybrid Power System for Electric Vehicle Applications,” *Energies*, vol. 3, no. 11, pp. 1821–1830, Nov. 2010.

[30] A. Khaligh and Z. Li, “Battery, Ultracapacitor, Fuel Cell, and Hybrid Energy Storage Systems for Electric, Hybrid Electric, Fuel Cell, and Plug-In Hybrid Electric Vehicles: State of the Art,” *IEEE Trans. Veh. Technol.*, vol. 59, no. 6, pp. 2806–2814, Jul. 2010.

[31] M.-E. Choi, S.-W. Kim, and S.-W. Seo, “Energy Management Optimization in a Battery/Supercapacitor Hybrid Energy Storage System,” *IEEE Trans. Smart Grid*, vol. 3, no. 1, pp. 463–472, Mar. 2012.

[32] L. Gao, R. A. Dougal, and S. Liu, “Power enhancement of an actively controlled battery/ultracapacitor hybrid,” *IEEE Trans. Power Electron.*, vol. 20, no. 1, pp. 236–243, Jan. 2005.

[33] M. Ortuzar, J. Moreno, and J. Dixon, "Ultracapacitor-Based Auxiliary Energy System for an Electric Vehicle: Implementation and Evaluation," *IEEE Trans. Ind. Electron.*, vol. 54, no. 4, pp. 2147–2156, Aug. 2007.

[34] G. Livint and A.-G. Stan, "Control strategies for hybrid electric vehicles with two energy sources on board," in *Proc. of International Conference and Exposition on Electrical and Power Engineering (EPE 2014)*, 2014, pp. 142–147.

[35] Electric Power Research Institute (EPRI), "Program on Technology Innovation: Advanced Sodium Sulfur (NaS) Battery Energy Storage System - 2006 Annual Report," Dec. 2007.

[36] Metropolitan Transit Authority (MTA), "MTA LI BUS And NYPA Install First Sodium Sulfur Battery Energy Storage System In State," 09-Jan-2009. [Online]. Available: http://www.mta.info/press-release/mta-headquarters/mta-li-bus-and-nypa-install-first-sodium-sulfur-battery-energy. [Accessed: 25-Mar-2015].

[37] G. Sliker, "Long Island Bus. NaS Battery Energy Storage Project," presented at the DOE Peer Review. Energy Storage & Power Electronics Systems Research Program, Washington, DC, 29-Sep-2009.

[38] I. Kuzle, D. Bosnjak, and S. Tesnjak, "An overview of ancillary services in an open market environment," in *Proc. of IEEE Mediterranean Conference on Control Automation (MED 2007)*, Athens (Greece), 2007, pp. 1–6.

[39] A. De Los Rios, J. Goentzel, K. E. Nordstrom, and C. W. Siegert, "Economic analysis of vehicle-to-grid (V2G)-enabled fleets participating in the regulation service market," in *Proc. of IEEE PES Innovative Smart Grid Technologies (ISGT 2012)*, 2012, pp. 1–8.

[40] U.S. Department of Energy (DOE), "DOE/EPRI 2013 Electricity Storage Handbook in Collaboration with NRECA," Jul. 2013.

[41] J. C. Smith, S. Beuning, H. Durrwachter, E. Ela, D. Hawkins, B. Kirby, W. Lasher, J. Lowell, K. Porter, K. Schuyler, and P. Sotkiewicz, "Impact of variable renewable energy on US electricity markets," in *Proc. of IEEE Power and Energy Society General Meeting (PESGM 2010)*, 2010, pp. 1–12.

[42] Y. S. Wong, L. L. Lai, S. Gao, and K. T. Chau, "Stationary and mobile battery energy storage systems for smart grids," in *Proc. of 4th International Conference on Electric Utility Deregulation and Restructuring and Power Technologies (DRPT 2011)*, 2011, pp. 1–6.

[43] Y. Yuan, Q. Li, and W. Wang, "Optimal operation strategy of energy storage unit in wind power integration based on stochastic programming," *IET Renew. Power Gener.*, vol. 5, no. 2, pp. 194–201, Mar. 2011.

[44] K. Heussen, S. Koch, A. Ulbig, and G. Andersson, "Unified System-Level Modeling of Intermittent Renewable Energy Sources and Energy Storage for Power System Operation," *IEEE Syst. J.*, vol. 6, no. 1, pp. 140–151, Mar. 2012.

[45] T. K. A. Brekken, A. Yokochi, A. von Jouanne, Z. Z. Yen, H. M. Hapke, and D. A. Halamay, "Optimal Energy Storage Sizing and Control for Wind Power Applications," *IEEE Trans. Sustain. Energy*, vol. 2, no. 1, pp. 69–77, Jan. 2011.

[46] Y. Makarov, P. Du, M. C. W. Kintner-Meyer, C. Jin, and H. Illian, "Optimal size of energy storage to accommodate high penetration of renewable resources in WECC system," in *Proc. of Innovative Smart Grid Technologies (ISGT 2010)*, 2010, pp. 1–5.

[47] M. Kintner-Meyer, C. Jin, P. Balducci, M. Elizondo, X. Guo, T. Nguyen, F. Tuffner, and V. Viswanathan, "Energy storage for variable renewable energy resource integration - A regional assessment for the Northwest Power Pool (NWPP)," in *Proc. of IEEE Power Systems Conference and Exposition (PSCE 2011)*, 2011, pp. 1–7.

[48] M. Swierczynski, R. Teodorescu, C. N. Rasmussen, P. Rodriguez, and H. Vikelgaard, "Overview of the energy storage systems for wind power integration enhancement," in *Proc. of IEEE International Symposium on Industrial Electronics (ISIE 2010)*, 2010, pp. 3749–3756.

[49] M. H. Nehrir, C. Wang, K. Strunz, H. Aki, R. Ramakumar, J. Bing, Z. Miao, and Z. Salameh, "A Review of Hybrid Renewable/Alternative Energy Systems for Electric Power Generation: Configurations, Control, and Applications," *IEEE Trans. Sustain. Energy*, vol. 2, no. 4, pp. 392–403, Oct. 2011.

[50] B. V. Mathiesen and H. Lund, "Comparative analyses of seven technologies to facilitate the integration of fluctuating renewable energy sources," *IET Renew. Power Gener.*, vol. 3, no. 2, pp. 190–204, Jun. 2009.

[51] European Union (EU), "Standardization Mandate to European Standardisation Organisations (ESOs) to support European Smart Grid deployment." 01-Mar-2011.

[52] U.S. Department of Energy (DOE), "The Smart Grid: An Introduction." .

[53] European Technology Platform for the electricity networks of the future (ETP), "Vision and Strategy for European Electricity Networks of the Future." 2006.

[54] European Technology Platform for the electricity networks of the future (ETP), "Strategic Research Agenda 2035." 2012.

[55] W. Kempton and J. Tomić, "Vehicle-to-grid power fundamentals: Calculating capacity and net revenue," *J. Power Sources*, vol. 144, no. 1, pp. 268–279, Jun. 2005.

[56] W. Kempton and J. Tomić, "Vehicle-to-grid power implementation: From stabilizing the grid to supporting large-scale renewable energy," *J. Power Sources*, vol. 144, no. 1, pp. 280–294, Giugno 2005.

[57] W. Kempton and A. Dhanju, "Electric Vehicles with V2G: Storage for Large-Scale Wind Power," *Wind. Int.*, Mar. 2006.

[58] J. Tomić and W. Kempton, "Using fleets of electric-drive vehicles for grid support," *J. Power Sources*, vol. 168, no. 2, pp. 459–468, Jun. 2007.

[59] C. Quinn, D. Zimmerle, and T. H. Bradley, "The effect of communication architecture on the availability, reliability, and economics of plug-in hybrid electric vehicle-to-grid ancillary services," *J. Power Sources*, vol. 195, no. 5, pp. 1500–1509, Mar. 2010.

[60] H. Lund, Ed., *Renewable Energy Systems. The Choice and Modeling of 100% Renewable Solutions.* Boston: Academic Press, 2010.

[61] G. Boyle, Ed., *Renewable Electricity and the Grid: The Challenge of Variability*. London; Sterling, VA: Routledge, 2009.

[62] M. Beaudin, H. Zareipour, A. Schellenberglabe, and W. Rosehart, "Energy storage for mitigating the variability of renewable electricity sources: An updated review," *Energy Sustain. Dev.*, vol. 14, no. 4, pp. 302–314, Dec. 2010.

[63] D. U. Sauer, M. Kleimaier, and W. Glaunsinger, "Relevance of energy storage in future distribution networks with high penetration of renewable energy sources," in *Proc. of 20th International Conference and Exhibition on Electricity Distribution (CIRED 2009)*, 2009, pp. 1–4.

[64] G. Coppez, S. Chowdhury, and S. P. Chowdhury, "Impacts of energy storage in distributed Power Generation: A review," in *Proc. of IEEE International Conference on Power System Technology (POWERCON 2010)*, 2010, pp. 1–7.

[65] J. A. Martinez, "Modeling and characterization of energy storage devices," in *Proc. of IEEE Power and Energy Society General Meeting (PESGM 2011)*, 2011, pp. 1–6.

[66] S. G. Goyena and O. A. Sádaba, "Sizing and analysis of big scale and isolated electric systems based on renewable sources with energy storage," in *Proc. of IEEE PES/IAS Conference on Sustainable Alternative Energy (SAE 2009)*, IEEE PES/IAS Conference on Sustainable Alternative Energy (SAE), 2009, pp. 1–7.

[67] J. Lassila, J. Haakana, V. Tikka, and J. Partanen, "Methodology to Analyze the Economic Effects of Electric Cars as Energy Storages," *IEEE Trans. Smart Grid*, vol. 3, no. 1, pp. 506–516, Mar. 2012.

[68] A. Franco and P. Salza, "Strategies for optimal penetration of intermittent renewables in complex energy systems based on techno-operational objectives," *Renew. Energy*, vol. 36, no. 2, pp. 743–753, Feb. 2011.

[69] J. A. P. Lopes, F. J. Soares, P. M. R. Almeida, P. C. Baptista, C. M. Silva, and T. L. Farias, "Quantification of technical impacts and environmental benefits of electric vehicles integration on electricity grids," in *Proc. of 8th International Symposium on Advanced Electromechanical Motion Systems Electric Drives Joint Symposium (ELECTROMOTION 2009)*, 2009, pp. 1–6.

[70] J. A. P. Lopes, F. J. Soares, and P. M. R. Almeida, "Integration of Electric Vehicles in the Electric Power System," *Proc. IEEE*, vol. 99, no. 1, pp. 168–183, Jan. 2011.

[71] K. Clement-Nyns, E. Haesen, and J. Driesen, "The Impact of Charging Plug-In Hybrid Electric Vehicles on a Residential Distribution Grid," *IEEE Trans. Power Syst.*, vol. 25, no. 1, pp. 371–380, Feb. 2010.

[72] A. T. Al-Awami and E. Sortomme, "Coordinating Vehicle-to-Grid Services With Energy Trading," *IEEE Trans. Smart Grid*, vol. 3, no. 1, pp. 453–462, Mar. 2012.

[73] F. K. Tuffner and M. Kintner-Meyer, "Using electric vehicles to mitigate imbalance requirements associated with an increased penetration of wind generation," in *Proc. of IEEE Power and Energy Society General Meeting (PESGM 2011)*, 2011, pp. 1–8.

[74] C. Ahn, C.-T. Li, and H. Peng, "Optimal decentralized charging control algorithm for electrified vehicles connected to smart grid," *J. Power Sources*, vol. 196, no. 23, pp. 10369–10379, Dec. 2011.

[75] K. J. Dyke, N. Schofield, and M. Barnes, "The Impact of Transport Electrification on Electrical Networks," *IEEE Trans. Ind. Electron.*, vol. 57, no. 12, pp. 3917–3926, Dec. 2010.

[76] UK Department for Transport, "Statistics at DFT - Department for Transport - GOV.UK." [Online]. Available: https://www.gov.uk/government/organisations/department-for-transport/about/statistics. [Accessed: 16-Mar-2015].

[77] C. Weiller, "Plug-in hybrid electric vehicle impacts on hourly electricity demand in the United States," *Energy Policy*, vol. 39, no. 6, pp. 3766–3778, Jun. 2011.

[78] C. Quinn, D. Zimmerle, and T. H. Bradley, "An Evaluation of State-of-Charge Limitations and Actuation Signal Energy Content on Plug-in Hybrid Electric Vehicle, Vehicle-to-Grid Reliability, and Economics," *IEEE Trans. Smart Grid*, vol. 3, no. 1, pp. 483–491, Mar. 2012.

[79] Electric Power Research Institute (EPRI), "Environmental Assessment of Plug-In Hybrid Electric Vehicles, Volume 1: Nationwide Greenhouse Gas Emissions," 2007.

[80] C. Guille and G. Gross, "A conceptual framework for the vehicle-to-grid (V2G) implementation," *Energy Policy*, vol. 37, no. 11, pp. 4379–4390, Nov. 2009.

[81] S. Shahidinejad, S. Filizadeh, and E. Bibeau, "Profile of Charging Load on the Grid Due to Plug-in Vehicles," *IEEE Trans. Smart Grid*, vol. 3, no. 1, pp. 135–141, Mar. 2012.

[82] Y. Hermans, B. Le Cun, and A. Bui, "Individual decisions amp; schedule planner in a Vehicle-to-grid context," in *Proc. of IEEE International Electric Vehicle Conference (IEVC 2012)*, 2012, pp. 1–6.

[83] D. P. Tuttle and R. Baldick, "The Evolution of Plug-In Electric Vehicle-Grid Interactions," *IEEE Trans. Smart Grid*, vol. 3, no. 1, pp. 500–505, Mar. 2012.

[84] W. Su and J. Wang, "Energy Management Systems in Microgrid Operations," *Electr. J.*, vol. 25, no. 8, pp. 45–60, Oct. 2012.

[85] R. H. Lasseter, "Smart Distribution: Coupled Microgrids," *Proc. IEEE*, vol. 99, no. 6, pp. 1074–1082, Jun. 2011.

[86] R. H. Lasseter and P. Paigi, "Microgrid: a conceptual solution," in *Proc. of IEEE 35th Annual Power Electronics Specialists Conference (PESC 2004)*, 2004, vol. 6, pp. 4285–4290 Vol.6.

[87] S. X. Chen, H. B. Gooi, and M. Q. Wang, "Sizing of Energy Storage for Microgrids," *IEEE Trans. Smart Grid*, vol. 3, no. 1, pp. 142–151, Mar. 2012.

[88] S. Teleke, M. E. Baran, S. Bhattacharya, and A. Q. Huang, "Rule-Based Control of Battery Energy Storage for Dispatching Intermittent Renewable Sources," *IEEE Trans. Sustain. Energy*, vol. 1, no. 3, pp. 117–124, Oct. 2010.

[89] G. Lacey, T. Jiang, G. Putrus, and R. Kotter, “The effect of cycling on the state of health of the electric vehicle battery,” in *Proc. of 48th International Universities Power Engineering Conference (UPEC 2013)*, 2013, pp. 1–7.

[90] J. de Santiago, H. Bernhoff, B. Ekergård, S. Eriksson, S. Ferhatovic, R. Waters, and M. Leijon, “Electrical Motor Drivelines in Commercial All-Electric Vehicles: A Review,” *IEEE Trans. Veh. Technol.*, vol. 61, no. 2, pp. 475–484, Feb. 2012.

[91] I. Boldea, L. N. Tutelea, L. Parsa, and D. Dorrell, “Automotive Electric Propulsion Systems With Reduced or No Permanent Magnets: An Overview,” *Ind. Electron. IEEE Trans. On*, vol. 61, no. 10, pp. 5696–5711, Oct. 2014.

[92] K. Rajashekara, “Present Status and Future Trends in Electric Vehicle Propulsion Technologies,” *IEEE J. Emerg. Sel. Top. Power Electron.*, vol. 1, no. 1, pp. 3–10, Mar. 2013.

[93] A. Choudhury, P. Pillay, and S. S. Williamson, “Comparative Analysis Between Two-Level and Three-Level DC/AC Electric Vehicle Traction Inverters Using a Novel DC-Link Voltage Balancing Algorithm,” *Emerg. Sel. Top. Power Electron. IEEE J. Of*, vol. 2, no. 3, pp. 529–540, Sep. 2014.

[94] H. Zhang, L. M. Tolbert, and B. Ozpineci, “Impact of SiC Devices on Hybrid Electric and Plug-In Hybrid Electric Vehicles,” *IEEE Trans. Ind. Appl.*, vol. 47, no. 2, pp. 912–921, Mar. 2011.

[95] A. Di Napoli, F. Crescimbini, F. Guilii Capponi, and L. Solero, “Control strategy for multiple input DC-DC power converters devoted to hybrid vehicle propulsion systems,” in *Proc. of IEEE International Symposium on Industrial Electronics (ISIE 2002)*, 2002, vol. 3, pp. 1036–1041 vol.3.

[96] K. Mikkelsen, “Design and evaluation of hybrid energy storage systems for electric powertrains,” 2010.

[97] B. Hredzak, V. G. Agelidis, and M. Jang, “A Model Predictive Control System for a Hybrid Battery-Ultracapacitor Power Source,” *IEEE Trans. Power Electron.*, vol. 29, no. 3, pp. 1469–1479, Mar. 2014.

[98] X. Liu, Q. Zhang, and C. Zhu, “Design of battery and ultracapacitor multiple energy storage in hybrid electric vehicle,” in *Proc. of IEEE Vehicle Power and Propulsion Conference (VPPC 2009)*, 2009, pp. 1395–1398.

[99] L. Wang, J., E.G. Collins, and H. Li, “Optimal Design and Real-Time Control for Energy Management in Electric Vehicles,” *IEEE Trans. Veh. Technol.*, vol. 60, no. 4, pp. 1419–1429, May 2011.

[100] S. Buller, M. Thele, R. W. A. A. De Doncker, and E. Karden, “Impedance-based simulation models of supercapacitors and Li-ion batteries for power electronic applications,” *IEEE Trans. Ind. Appl.*, vol. 41, no. 3, pp. 742–747, May 2005.

[101] A. C. Baisden and A. Emadi, “ADVISOR-based model of a battery and an ultra-capacitor energy source for hybrid electric vehicles,” *IEEE Trans. Veh. Technol.*, vol. 53, no. 1, pp. 199–205, Jan. 2004.

[102] E. Ozatay, B. Zile, J. Anstrom, and S. Brennan, “Power distribution control coordinating ultracapacitors and batteries for electric vehicles,” in *Proc. of American Control Conference (ACC 2004)*, 2004, vol. 5, pp. 4716–4721 vol.5.

[103] O. Laldin, M. Moshirvaziri, and O. Trescases, “Predictive Algorithm for Optimizing Power Flow in Hybrid Ultracapacitor/Battery Storage Systems for Light Electric Vehicles,” *Power Electron. IEEE Trans. On*, vol. 28, no. 8, pp. 3882–3895, Aug. 2013.

[104] M.-E. Choi and S.-W. Seo, “Robust energy management of a battery/supercapacitor Hybrid Energy Storage System in an electric vehicle,” in *Proc. of IEEE International Electric Vehicle Conference (IEVC 2012)*, 2012, pp. 1–5.

[105] J. Moreno, M. E. Ortuzar, and J. W. Dixon, “Energy-management system for a hybrid electric vehicle, using ultracapacitors and neural networks,” *IEEE Trans. Ind. Electron.*, vol. 53, no. 2, pp. 614–623, Apr. 2006.

[106] A. Serpi, G. Gatto, A. Damiano, and I. Marongiu, “Model Predictive Control with Input and Output Constraints,” in *Model Predictive Control: Theory, Practices and Future Challenges*, Hauppauge, New York: Nova Science Pub Inc, 2015.

[107] R. Krishnan, *Permanent Magnet Synchronous and Brushless DC Motor Drives*. CRC Press, 2009.

[108] B. Wu, *High-Power Converters and AC Drives*. Wiley, 2006.

[109] A. Nabae, I. Takahashi, and H. Akagi, "A New Neutral-Point-Clamped PWM Inverter," *IEEE Trans. Ind. Appl.*, vol. IA-17, no. 5, pp. 518–523, Sep. 1981.

[110] S. Stockar, V. Marano, M. Canova, G. Rizzoni, and L. Guzzella, "Energy-Optimal Control of Plug-in Hybrid Electric Vehicles for Real-World Driving Cycles," *IEEE Trans. Veh. Technol.*, vol. 60, no. 7, pp. 2949–2962, Sep. 2011.

[111] S. Campanari, G. Manzolini, and F. Garcia de la Iglesia, "Energy analysis of electric vehicles using batteries or fuel cells through well-to-wheel driving cycle simulations," *J. Power Sources*, vol. 186, no. 2, pp. 464–477, Jan. 2009.

[112] T. J. Barlow, S. Latham, I. S. McCrae, and P. G. Boulter, "A reference book of driving cycles for use in the measurement of road vehicle emissions." UK Department of Transport, 2009.

[113] P.-Y. Lin and Y.-S. Lai, "Voltage Control Technique for the Extension of DC-Link Voltage Utilization of Finite-Speed SPMSM Drives," *IEEE Trans. Ind. Electron.*, vol. 59, no. 9, pp. 3392–3402, Sep. 2012.

[114] T.-S. Kwon and S.-K. Sul, "Novel Antiwindup of a Current Regulator of a Surface-Mounted Permanent-Magnet Motor for Flux-Weakening Control," *IEEE Trans. Ind. Appl.*, vol. 42, no. 5, pp. 1293–1300, Sep. 2006.

[115] A. Damiano, G. Gatto, I. Marongiu, A. Perfetto, and A. Serpi, "Operating Constraints Management of a Surface-Mounted PM Synchronous Machine by Means of an FPGA-Based Model Predictive Control Algorithm," *IEEE Trans. Ind. Inform.*, vol. 10, no. 1, pp. 243–255, Feb. 2014.

[116] D. S. Maric, S. Hiti, C. C. Stancu, J. M. Nagashima, and D. B. Rutledge, "Two flux weakening schemes for surface-mounted permanent-magnet synchronous drives. Design and transient response considerations," in *Proc. of IEEE International Symposium on Industrial Electronics (ISIE 1999)*, 1999, vol. 2, pp. 673–678 vol.2.

PUBLICATIONS

[1] A. Damiano, I. Marongiu, **M. Porru**, A. Serpi, "Electric Vehicle energy storage management for Renewable Energy Sources exploitation", *in Proc. of IEEE International Electric Vehicle Conference (IEVC 2012)*, Greenville (USA), 4-8 Mar. 2012

[2] A. Damiano, G. Gatto, I. Marongiu, **M. Porru**, A. Serpi, "The Plug-In Electric Vehicles Role in Smart Grid Development: a Survey", *in Proc. of European Electric Vehicle Congress 2012*, Brussels (Belgium), 19-21 Nov. 2012.

[3] A. Damiano, I. Marongiu, **M. Porru**, A. Serpi, "A suitable PWM for DC-link voltage equalization of Three-Level Neutral-Point Clamped Converters", *in Proc. 39th Annual Conference of the IEEE Industrial Electronics Society (IECON 2013)*, Vienna (Austria), Nov. 10-13, 2013.

[4] A. Damiano, I. Marongiu, A. Monni, **M. Porru**, "Design of a 10 MW multi-phase PM synchronous generator for direct-drive wind turbines", *in Proc. 39th Annual Conference of the IEEE Industrial Electronics Society (IECON 2013)*, Vienna (Austria), Nov. 10-13, 2013.

[5] A. Damiano, G. Gatto, I. Marongiu, **M. Porru**, A. Serpi, "Vehicle-to-Grid Technology: State-of-the-Art and Future Scenarios", *Journal of Energy and Power Engineering (JEPE)*, vol. 8, no. 1, pp. 152-165, Jan. 2014.

[6] A. Damiano, G. Gatto, I. Marongiu, **M. Porru**, A. Serpi, "Real-Time Control Strategy of Energy Storage Systems for Renewable Energy Sources Exploitation", *IEEE Trans. Sustainable Energy*, vol. 5, no. 2, pp.567-576, Apr. 2014

[7] **M. Porru**, A. Serpi, I. Marongiu, A. Damiano, "An Improved DC-Link Voltage Equalization for Three-Level Neutral-Point Clamped Converters", *in Proc. 10th Conference on Ph.D. Research in Microelectronics and Electronics (PRIME 2014),* Grenoble (France), June 30 – July 3, 2014.

[8] **M. Porru**, A. Serpi, I. Marongiu, A. Damiano, "A Novel DC-link Voltage and Current Control Algorithm for Neutral-Point-Clamped Converters", *in Proc. 40th Annual Conference of the IEEE Industrial Electronics Society (IECON 2014)*, Dallas (USA), Oct. 30 - Nov. 1, 2014.

[9] M. Musio, **M. Porru**, A. Serpi, I. Marongiu, A. Damiano, "Optimal Electric Vehicle Charging Strategy for Energy Management in Microgrids", *in Proc. of 2nd IEEE International Electric Vehicle Conference (IEVC 2014)*, Florence (Italy), Dec. 17-19, 2014.

AWARDS

[1] A. Damiano, I. Marongiu, **M. Porru**, A. Serpi , Second Prize Paper Award from the Power Electronic Technical Committee of the IEEE Industrial Electronics Society at the 39th IECON.

[2] **M. Porru**, Bronze Leaf Certificate at the IEEE 10th Conference on Ph.D Research in Microelectronics and Electronics (PRIME 2014).